UNIVERSITA' DEGLI STUDI DELL'INSUBRIA

Dipartimento di Scienza ed Alta Tecnologia

Dottorato in Fisica e Astrofisica

Development of a Silicon Photomultiplier based innovative and low cost Positron Emission Tomography scanner

Advisor:

Prof. Massimo CACCIA

Tutor:

Dott. Romualdo SANTORO

Doctoral Dissertation of:

Valentina AROSIO

2013-2016

Contents

List of Figures

List of Tables

Introduction

The Silicon Photomultiplier (SiPM) is a state-of-the-art semiconductor photodetector consisting of a high density matrix (up to 10^4) of independent pixels of micro-metric dimension (from 10 μm to 100 μm) which form a macroscopic unit of 1 to 6 mm^2 area. Each pixel is a single-photon avalanche diode operated with a bias voltage of a few volts above the breakdown voltage. When a charge carrier is generated in a pixel by an incoming photon or a thermal effect, a Geiger discharge confined to that pixel is initiated and an intrinsic gain of about 10^6 is obtained. The output signal of a pixel is the same regardless of the number of interacting photons and provide only a binary information. Since the pixels are arranged on a common Silicon substrate and are connected in parallel to the same readout line, the SiPM combined output response corresponds to the sum of all fired pixel currents. As a result, the SiPM as a whole is an analogue detector, which can measure the incoming light intensity.

Nowadays a great number of companies are investing increasing efforts in SiPM detector performances and high quality mass production. SiPMs are in rapid evolution and benefit from the tremendous development of the Silicon technology in terms of cost production, design flexibility and performances. They have reached a high single photon detection sensitivity and photon detection efficiency, an excellent time resolution, an extended dynamic range. They require a low bias voltage and have a low power consumption, they are very compact, robust, flexible and cheap. Considering also their intrinsic insensitivity to magnetic field they result to have an extremely high potential in fundamental and applied science (particle and nuclear physics, astrophysics, biology, environmental science and nuclear medicine) and industry.

The SiPM performances are influenced by some effects, as saturation, afterpulsing and crosstalk, which lead to an inherent non-proportional response with respect to the number of incident photons. Consequently, it is not trivial to relate the measured electronic signal to the corresponding light intensity. Since for most applications it is desirable to qualify the SiPM response (i.e in order to properly design a detector for a given application, perform corrections on measurements or on energy spectra, calibrate a SiPM for low light measurements, predict detector performance) the implementation of characterization procedures plays a key role.

The SiPM field of application that has been considered in this thesis is the Positron Emission Tomography (PET). PET represents the most advanced in-vivo nuclear imaging modality: it provides functional information of the physiological and molecular processes of organs and tissues. Thanks to its diagnostic power, PET has a recognized superiority over all other imaging modalities in oncology, neurology and cardiology. SiPMs are usually successfully

employed for the PET scanners because they allow the measurement of the Time Of Flight of the two coincidence photons to improve the signal to noise ratio of the reconstructed images. They also permit to perfectly combine the functional information with the anatomical one by inserting the PET scanner inside the Magnetic Resonance Imaging device.

Recently, PET technology has also been applied to preclinical imaging to allow non invasive studies on small animals. The increasing demand for preclinical PET scanner is driven by the fact that small animals host a large number of human diseases. In-vivo imaging has the advantage to enable the measurement of the radiopharmaceutical distribution in the same animal for an extended period of time. As a result, PET represents a powerful research tool as it offers the possibility to study the abnormalities at the origin of a disease, understand its dynamics, evaluate the therapeutic response and develop new drugs and treatments. However, the cost and the complexity of the preclinical scanners are limiting factors for the spread of PET technology: 70-80% of small-animal PET is concentrated in academic or government research laboratories.

The EasyPET concept proposed in this Thesis, protected under a patent filed by Aveiro University, aims to achieve a simple and affordable preclinical PET scanner. The innovative concept is based on a single pair of detector kept collinear during the whole data acquisition and a moving mechanism with two degrees of freedom to reproduce the functionalities of an entire PET ring. The main advantages are in terms of the reduction of the complexity and cost of the PET system. In addition the concept is bound to be robust against acollinear photoemission, scatter radiation and parallax error. The sensitivity is expected to represent a fragility due to the reduced geometrical acceptance. This drawback can be partially recovered by the possibility to accept Compton scattering events without introducing image degradation effects, thanks to the sensor alignment.

A 2D imaging demonstrator has been realized in order to assess the EasyPET concept and its performance has been analyzed in this Thesis to verify the net balance between competing advantages and drawbacks. The demonstrator had a leading role in the outreach activity to promote the EasyPET concept and a significant outcome is represented by the new partners that recently joined the collaboration. The EasyPET has been licensed to Caen S.p.a. and, thanks to the participation of Nuclear Instruments to the electronic board re-designed, a new prototype has been realized with additional improvements concerning the mechanics and the control software. In this Thesis the prototype functionalities and performances are reported as a result of a commissioning procedure. The EasyPET will be commercialized by Caen S.p.a. as a product for the educational market and it will be addressed to high level didactic laboratories to show the operating principles and technology behind the PET imaging.

The topics mentioned above will be examined in depth in the following Chapters according to the subsequent order. In Chapter 1 the Silicon Photomultiplier will be described in detail, from their operating principle to their main application fields passing through the advantages and the drawback effects connected with this type of sensor. Chapter 2 is dedicated to a SiPM standard characterization method based on the staircase and resolving power measurement. A more refined analysis involves the Multi-Photon spectrum, obtained by integrating the SiPM response to a light pulse. It exploits the SiPM single photon sensitivity and its photon number resolving capability to measure some of its properties of general interest for a multitude of potential applications, disentangling the

features related to the statistics of the incident light. Chapter 3 reports another SiPM characterization method which implements a post-processing of the digitized SiPM waveforms with the aim of extracting a full picture of the sensor characteristics from a unique data-set. The procedure is very robust, effective and semi-automatic and suitable for sensors of various dimensions and produced by different vendors. Chapter 4 introduces the Positron Emission Tomography imaging: its principle, applications, related issues and state of the art of PET scanner will be explained. Chapter 5 deals with the preclinical PET, reporting the benefits and the technological challenges involved, the performance of the commercially available small animal PET scanners, the main applications and the frontier research in this field. In Chapter 6 the EasyPET concept is introduced. In particular, the basic idea behind the operating principle, the design layout and the image reconstruction will be illustrated and then assessed through the description and the performance analysis of the EasyPET proof of concept and demonstrator. The effect of the use of different sensor to improve the light collection and the coincidence detection efficiency, together with the analysis of the importance of the sensor and the crystal alignment will be reported in Chapter 7. The design, the functionalities and the commissioning of the EasyPET prototype addressed to the educational market will be defined in Chapter 8. Finally, Chapter 9 contains a summary of the conclusions and an outlook of the future research studies.

Chapter 1

Silicon Photomultipliers

Silicon Photomultipliers (SiPMs) are state-of-the-art light sensors featuring single photon detection sensitivity, high photon detection efficiency, unprecedented photon number resolving capability, excellent time resolution and extended dynamic range. Thanks to their compactness, robustness, insensitivity to magnetic field, low operating voltages and low power consumption, SiPMs have an extremely high potential in fundamental and applied science and industry. SiPMs benefit from the rapid evolution of the Silicon technology and the investment of different companies in terms of cost production, design flexibility, detector performances and high quality mass production, becoming the natural choice for an increasing number of applications.

1.1 SiPM operating principle

SiPM consists of a matrix of independent micro-cell with densities up to 10^4 per mm^2 arranged on a common substrate, with a common load and connected in parallel to a single readout output. Figure 1.1 is an illustrative picture of the SiPM operating principle. Each cell is formed out of an avalanche photodiode and a polysilicon quench resistor connected in series. The photodiode is operated in a limited Geiger-Müller regime and it is biased with few volts above its breakdown voltage (30-100 V depending on the producer). A charge carrier generated in the depletion region by photon absorption, thermal excitation or released by a silicon impurity reaches the photodiode junction volume by drift or diffusion. In this region the high electric field induces charge multiplication by impact ionization and a self-sustaining breakdown avalanche with a gain of about 10^6 occurs in that cell. In order to interrupt the avalanche development a built in quench resistor induces a drop in the operating voltage, restores the initial bias condition and enables the cell to be sensitive to new incoming photons [1], [2], [3], [4].

This intrinsic charge amplification mechanism ensures high sensitivity to the single photon, since only one charge carrier needs to be generated in the depletion region to detect the light pulse. As a consequence, each pixel gives rise to the same signal with 10^6 gain despite of the number of primary carriers created in its depletion region.

Actually each SiPM pixel is a binary device but the SiPM as a whole constitutes an analogue detector; the independently operating pixels are connected to
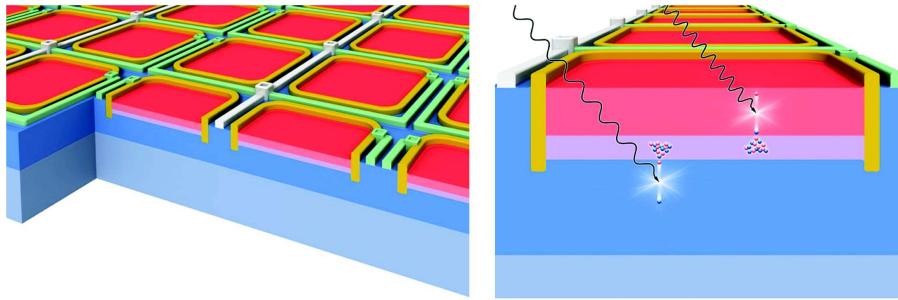
Figure 1.1: An artist's view of the SiPM structure and operating principle.

the same readout line and the combined output signal corresponds to the sum of all fired pixel signals. In practice, by counting the number of fired cells the SiPM can provide an information about the the intensity of the incoming light.

Figure 1.2(a) shows the typical response by a SiPM to light pulses emitted by a LED: each band of traces corresponds to a different number of fired cells, proportional to the number of impinging photons. Because of the high gain compared to the noise level, traces are well separated, providing a photon number resolved detection of the light field [5].
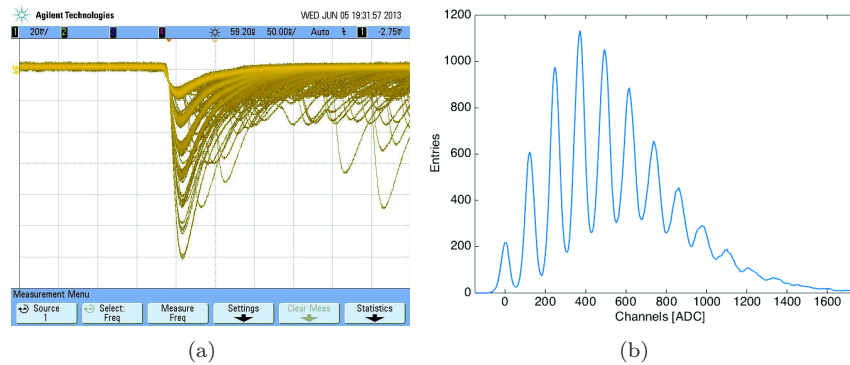
Figure 1.2: Response of an Hamamatsu SiPM (S10362-11-100C) illuminated by a LED: (a) output at the oscilloscope and (b) integrated and digitized signal.

The high photon number resolving capability can also be observed in Figure 1.2(b), displaying the spectrum of the SiPM response to a high statistics of pulses emitted by a LED: every entry corresponds to the digitized released charge, measured integrating the cells current during a pre-defined time interval [5]. The events trigger is provided by the LED itself, resulting to be synchronous to the light pulse. The well separated peaks correspond to different number of cells fired at the same time and their areas are related to the Poisson statistical property of the light source. In particular, the peak at 0 corresponds to no detected photons and its width σ_0 measures the noise of the system, i.e. the stochastic fluctuations in the output signal in absence of any stimulus. The width of the peak corresponding to one detected photon, σ_1, is slightly bigger. Despite of the fact that the pixel structure is produced with high uniformity and the SiPM

response homogeneity is high, yielding an excellent photoelectron resolution, the number of electrons generated in avalanches of various cells can have a difference of about 10% [4]. Since fired cells are randomly distributed in the detector sensitive area, residual differences in the gain become evident broadening the peak and adding an extra contribution with respect to the 0 peak width. As a consequence, the peak width is increasing with the number $N_{firedcell}$ of fired cells with a growth expected to follow a $\sqrt{N_{firedcell}}$ law, eventually limiting the maximum number M of resolved peaks. In order to quantify the capability to resolve neighboring peaks in a spectrum, the resolving power R is defined as [6]:

$$R = \frac{\Delta_{pp}}{\sigma_{gain}},\tag{1.1}$$

where Δ_{pp} is the peak-to-peak distance in the spectrum and $\sigma_{gain} = \sqrt{\sigma_1^2 - \sigma_0^2}$ accounts for the cell to cell gain fluctuations. Applying the Sparrow criterion, according to which two peaks are no longer resolved as long as the dip half way between them ceases to be visible in superposed curves, M is given by $R^2/4$ [7].

Topology

The schematic structure of the avalanche microcell of a SiPM is shown in Figure 1.3 and presents the configuration n^+-p-π-p^+.
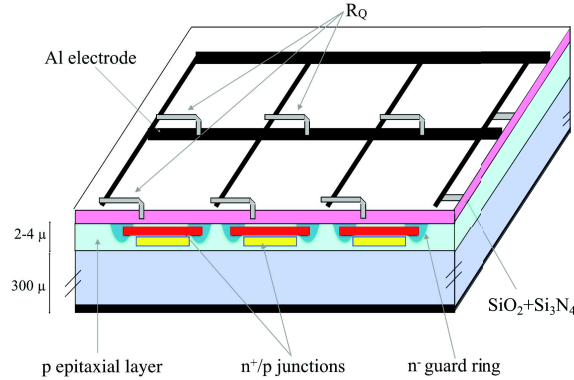
Figure 1.3: The structure of a SiPM with n^+-p-π-p^+ configuration.

The n^+ side is thin (0.1-1.5 μm) and is the one which receives light through a window. Than there are three p-type layers of different doping levels to suitably modify the field distribution across the structure. The Geiger mode discharge occurs in the thin (0.7-0.8m) region between the n^+ and p layers, created thanks to the high electric fields (3-5$\cdot$10^5 V/cm). A few micron of slightly p-type doping π epitaxial layer is deposited on the heavily doped p^+ substrate ($\approx$ 300 μm thick). The absorption of photons of $\lambda \approx 400$ nm takes place mainly in this π layer. The nearly uniform field here separates the electron-hole pairs and drifts them towards the n^+ and p^+ sides, respectively. When the drifting electron reach the junction volume it is accelerated by the high fields to sufficiently large kinetic energy to further cause impact ionization and initiate a breakdown avalanche. In Figure 1.4 is reported the behavior of the electric field [8].
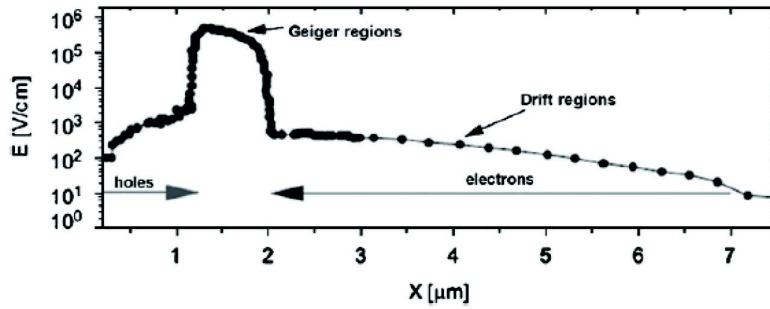
Figure 1.4: The electric field is at a maximum at the n^+-p junction, decreases slowly in the epitaxial layer and then vanishes in the p^+ substrate [8].

On the cell surface a thin metal layer is placed (≈ 0.01 μm) with an antireflection coating. Above the n^+ region, a polysilicon resistive SiO_2 layer (thickness ≈ 0.15 μm, $\rho \approx 10^5$-$10^7 \Omega$/cm) electrically decouples adjacent cells and limits the Geiger breakdown propagation by a local reduction of the electric field. The uniformity of the electric field within a pixel is guaranteed by the edge structure of n^- guard rings around each pixel. Recently, these structures are replaced by a Metal Quench Resistor (MQR) to increase the sensor active area [9]. All cells are connected in parallel by alluminum strips to a common bias line.

SiPMs are produced with different cell size, typically ranging between 10 μm and 100 μm, shown in Figure 1.5(a). Cells are arranged to form macroscopic unit (Figure 1.5(b)) of areas from 1x1 mm^2 up to 6x6 mm^2. Arrays up to 24x24 mm^2 active area have been engineered by a few companies, relying on four side buttable sensors with Through Silicon Via interconnection technology [10].

10 µm   15 µm   25 µm   50 µm

(a)

(b)
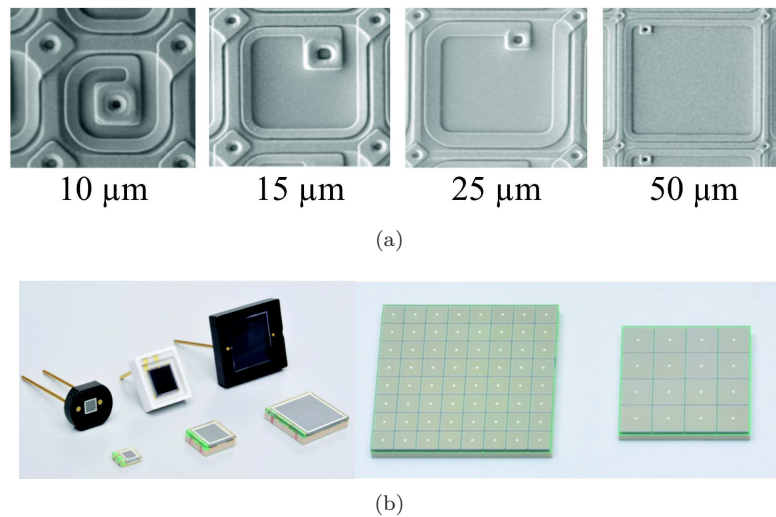
Figure 1.5: (a) Microphotograph of different cell size SiPM with MQR. (b) Hamamatsu SiPM of area of 1x1mm^2, 3x3 mm^2 and 6x6 mm^2 and arrays of 8x8 and 4x4 elements for a total active area of 24x24 mm^2 and 12x12 mm^2 [11].

Electrical model

A schematic representation of the sensor is shown in Figure 1.6. Each single cell photodiodes, labelled as D, has in series a quenching resistor R_Q. The pre-breakdown state corresponds to the switch in the OFF condition, with the junction capacitance C_D charged at $V > V_{bd}$, where V_{bd} is the breakdown voltage and V is the operating voltage [12].

When a carrier traverses the high-field region and initiate an avalanche discharge the new state of the system goes in the ON condition. A voltage source V_{bd} and a series resistor R_S, including both the resistance of the neutral regions inside the silicon as well as the space charge resistance, are added to the circuit in parallel to the diode capacitance. C_D discharges through the series resistance down to the breakdown voltage with a time constant $\tau_D = R_S C_D$ [12].

As the voltage across C_D decreases, the current flows through the quenching resistance and through the diode, tending to the asymptotic value of $(V - V_{bd})/(R_Q + R_S)$. In this final phase, if R_Q is high enough (some hundreds of kΩ), the diode current is so low (below 10-20 μA) that a statistical fluctuation brings the instantaneous number of carriers flowing through the high-field region to zero, quenching the avalanche [12].

As the discharge process is terminated, the switch is again open in the OFF condition and the circuit is in its initial configuration. The capacitance that is now charged at V_{bd} starts recharging to the bias voltage V with a time constant $\tau_r = C_D R_Q$, called the cell recovery time, and the device becomes ready to detect the arrival of a new photon [12].
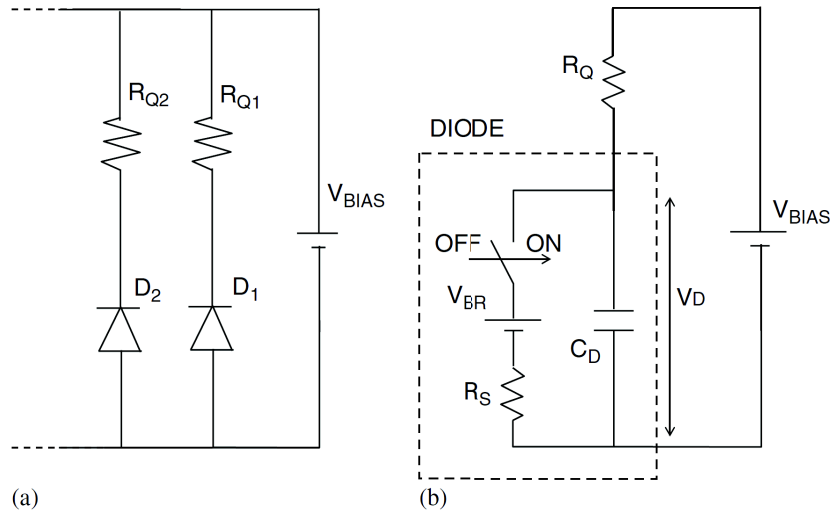
Figure 1.6: Equivalent circuits of a SiPM (a) and a single photodiode cell (b) [12].

Signal time development

The SiPM output signal time development is reported in Figure 1.7. Its response is intrinsically very fast due to the very thin depletion layer and the extremely short duration of the avalanche discharge development; the signal rise time

follows an exponential function with τ_D time constant and results to be less than 500 ps, independent from the applied bias voltage and the number of fired pixel. Therefore, good timing properties even for single photons can be expected [2].

The falling of the SiPM signal has an exponential development with time constant τ_r. The total time required at each pixel to recover from the discharge ranges between 20-250 ns accordingly to the cell size and the value of the quenching resistance, making the SiPM an optimal counting devices up to rates of few MHz [2]. After-pulses events can prolong the total recovery time, but this effect can be reduced only by operating at low gain or low temperature [3].
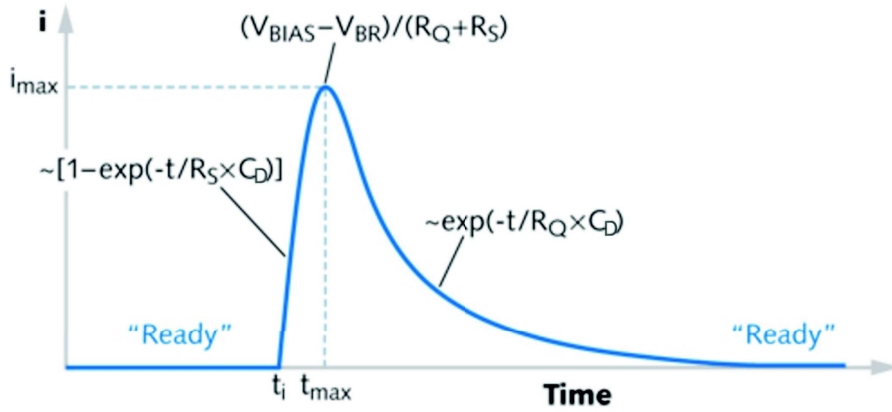
Figure 1.7: The time evolution of the current into a cell [13].

Timing

The SiPM response to a sharpe laser pulse is characterized by a Gaussian peak, which can be quantified through the FWHM, also called Single-Photon Time Resolution (SPTR). A typical SPTR is reported in Figure 1.8, with a FWHM of ≈ 100 ps for photons absorbed in the depletion region [14], [15]. Avalanche fluctuations are due to the mechanisms involved in the spreading of the avalanche over the device area; in particular, the main contribution is the lateral spreading by diffusion, which depends on the device geometry, while the vertical build-up is negligible. The closer the seed point is to the center of the junction area, the faster is the activation of the whole device and thus the rise of the avalanche current. The tail to the right can be explained by carriers created in field free regions which have to travel by diffusion taking several nanoseconds to reach the depletion region and trigger a breakdown. At low gain the lateral spreading of the avalanche in the entire depleted volume can be incomplete and can enhance the diffusion tail; operation at high overvoltage will instead improve the time resolution [3].

Figure 1.9 reports the new results for the SPTR of small sensors, which has reached the value of 60 ps.
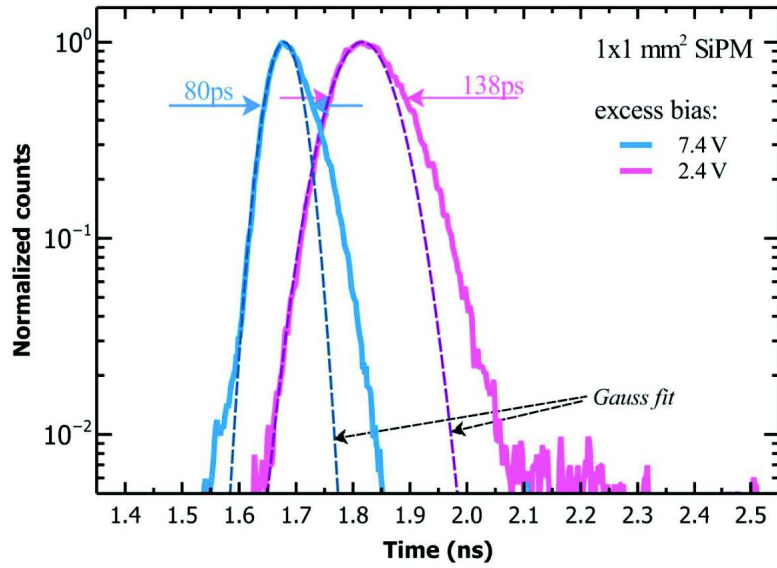
Figure 1.8: Single photon timing response of a 1x1 mm^2 SiPM by HAMAMATSU measured at three wavelengths (600 nm, 800 nm, and 1100 nm).
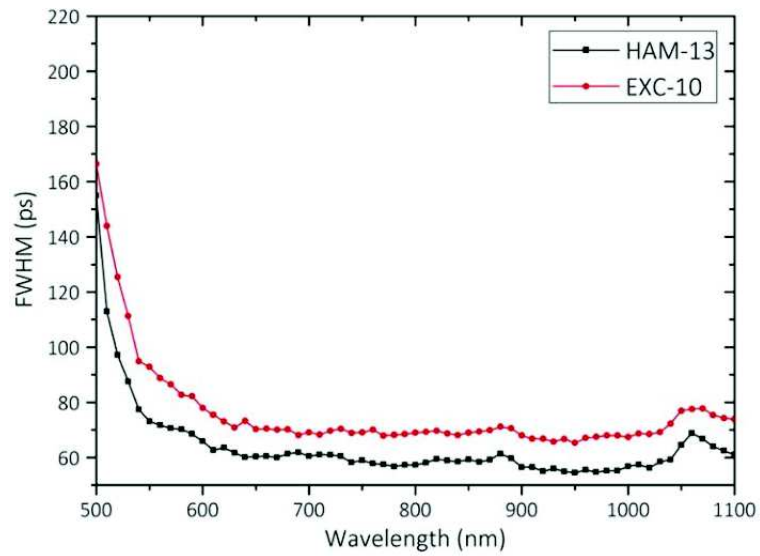
Figure 1.9: Single-Photon Time Resolution over the light excitation spectral range for the 1.3×1.3 mm^2 HAMAMATSU S13081-050CS and the 1×1 mm^2 Excelitas C3074011050C [16].

1.2 Photon Detection Efficiency

The Photon Detection Efficiency (PDE) is the probability that a SiPM produces an output signal in response to an incident photon [2], [3]. It is a function of the overvoltage ΔV, of the wavelength λ of the incident light and of the temperature T and can be factorized in three terms [17]:

$$PDE = G_F \cdot QE(\lambda) \cdot P_{trigger}(\lambda, \Delta V, T). \tag{1.2}$$

The geometrical fill-factor G_F is defined as the ratio between the sensitive area and the total device area. Each cell is in fact surrounded by a dead region due to the guard ring structure, the bias lines, the quenching resistor and the trenches preventing the optical cross-talk (discussed in Section 1.6), as shown in Figure 1.10. This parameter needs to be optimized depending on the application; for example when the application deals with low number of photons the best filling can be achieved with few big cells, while in case of many photons high number of small cells should be employed in order to avoid saturation effect. Currently, G_F ranges from 90% to 30% for 100 μm and 10 μm pitch cells, respectively (Figure 1.11).

(a) (b)
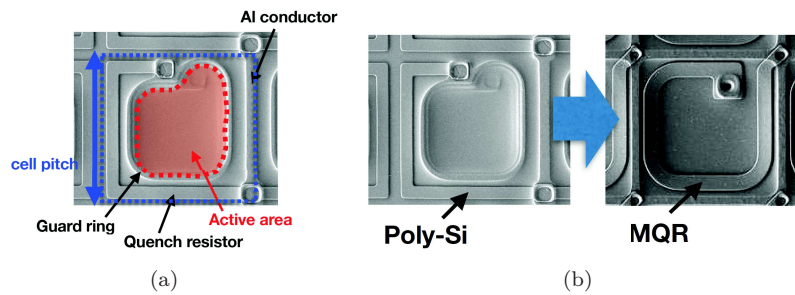
Figure 1.10: (a) SiPM active region. (b) Metal Quench Resistor improving the fill-factor on 25 μm cell.
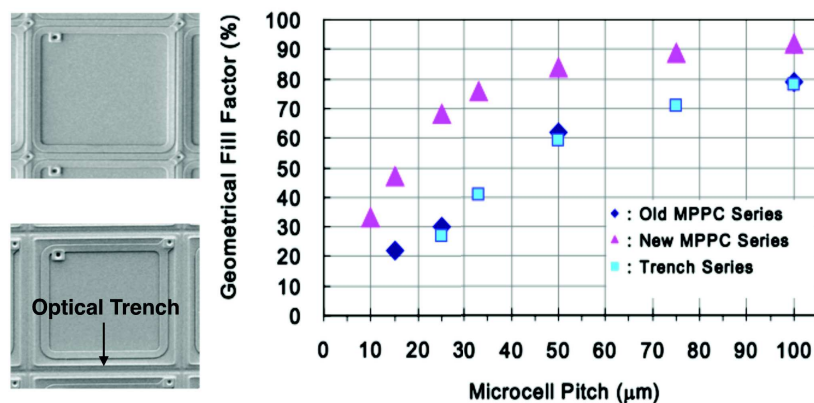
Figure 1.11: The geometrical fill-factor as a function of the cell size, with and without optical trenches, for Hamamatsu SiPM S10362 and S12571 series [18].

The quantum efficiency QE depends on the transmittance of the dielectric layer on top of the sensor, which can be maximized by using an anti-reflective coating, in addition to the probability for a photon that has passed the dielectric layer to generate an electron-hole pair in the active region. Like for other silicon-based photodetectors, the QE reaches values up to 80-90%, depending on the wavelength of the incident photon (Figure 1.12) [3].
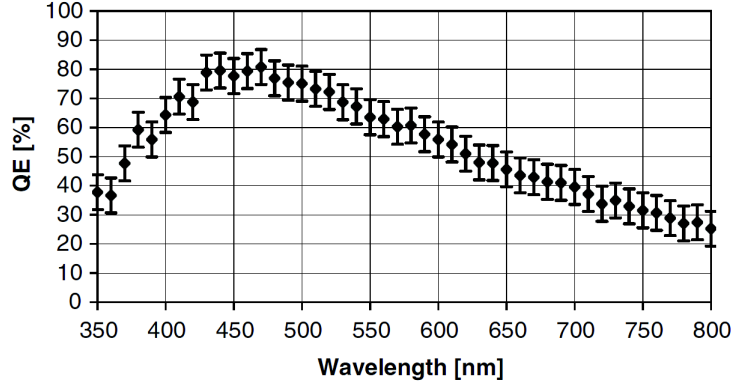
Figure 1.12: The quantum efficiency as a function of the wavelength of incident photon for 50 μm cell Hamamatsu SiPM [3].

The $P_{trigger}$ represents the probability for a carrier to trigger an avalanche when passing through a high-field region.When two carriers are created in the depletion region they start to travel in opposite direction, both contributing to the triggering probability:

$$P_{trigger} = P_e + P_h - P_e P_h, \qquad (1.3)$$

where P_e and P_h are the electron and hole breakdown initiation probabilities. These terms depend on the generation position, as shown in Figure 1.13, and increase when the electric field is increased and the temperature is reduced. The electron has about twice the chance to trigger an avalanche than holes (the electron impact ionization rate is about $5 \cdot 10^5$ V/cm), but this difference decreases with higher electric field. In practice, in a n^+-p-p^+ junction, when a pair is generated close to the n^+ layer the electron is collected at the electrode and only the hole passes the high-field region and contributes to the triggering probability. The situation is symmetrical if the generation occurs near the p^+ layer, where only the electrons could trigger the avalanche. In the central high-field region, both carriers contribute to a different extent to the triggering probability as a function of the interaction position [12], [19].

The p-type structure, where the n^+ layer thickness ranges from 0.1 to 1.5 μm and the depleted region goes from 3 to 10 μm, results to be optimal for green-red light detection, which has an absorption depth in silicon of about 1-3 μm. The blue-UV light, is totally absorbed in 500 nm of silicon, which is inside the n^+ layer in this p-type structure. The majority of carriers created in the non-depleted region recombine and do not produce an avalanche. To improve the blue-UV light sensitivity in this type of sensors the n^+ layer thickness is reduced. A better solution properly designed for blue-UV light detection is the n-type structure, based on the p^+-p-n^+ junction. The electrons generated close to the
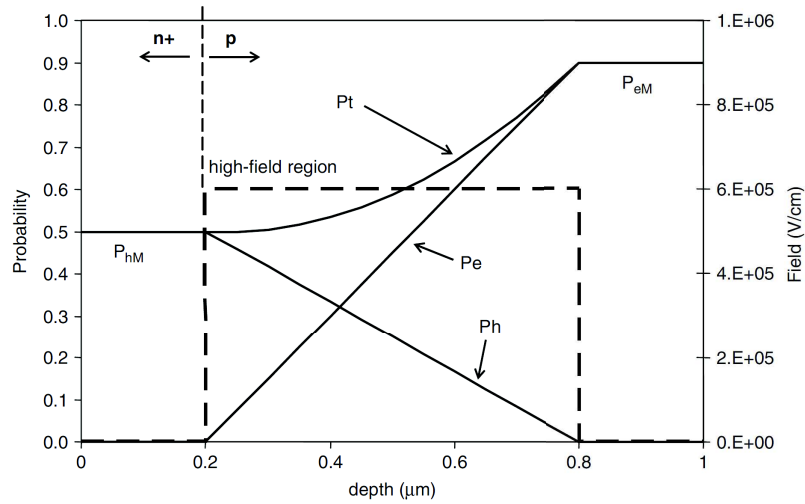
Figure 1.13: The triggering probability as a function of the photon generation position [12].

p^+ layer enter the high-field region and initiate the avalanche, while the holes move towards the electrode and do not contribute to triggering probability [17].

In Figure 1.14 the spectral dependence of the PDE is driven by the photon absorption length in Silicon and by the sensor technology, presenting a peak at 550-600 nm and at about 450 nm for p-type and n-type structure respectively.
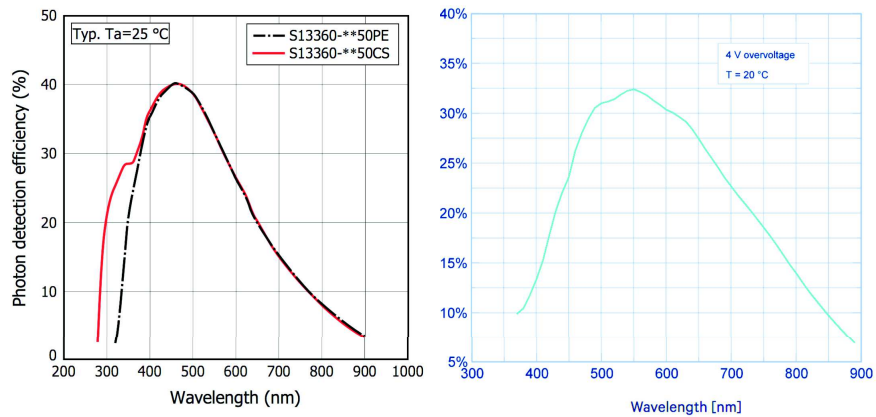
Figure 1.14: The PDE as a function of the wavelength: (left) HAMAMATSU S13360 50 μm pitch, at 3V of overvoltage and at 25°C and (right) First Sensor RBG SiPM 40 μm pitch, at 4V of overvoltage and at 20°C.

The dependence of the PDE on the overvoltage is shown in Figure 1.15: the triggering probability increases with the voltage and at same bias sensors with bigger cell pitch have an higher PDE thanks to higher gain and better fill-factor.
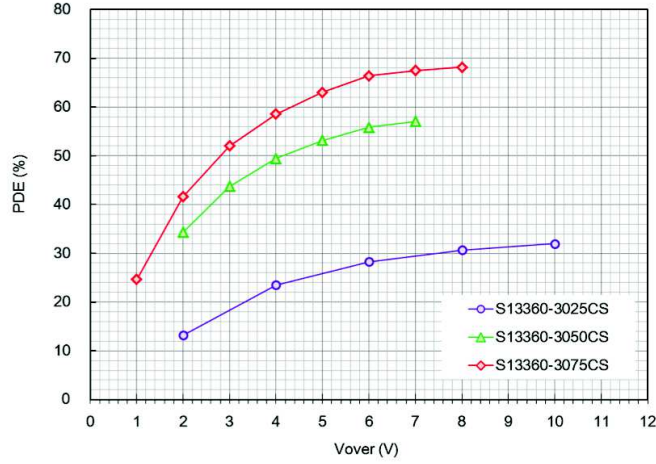
Figure 1.15: The PDE as a function of the overvoltage and of the gain for 25 μm, 50 μm and 75 μm cell size of S13360 3x3 mm^2 Hamamatsu SiPM.

1.3 Gain

The SiPM produces an electric signal when any of the cells goes to breakdown. The amplitude A_i of a single SiPM cell signal is proportional to the capacitance of the cell C times the overvoltage ΔV:

$$A_i \propto C_D \cdot \Delta V \propto C_D \cdot (V - V_{bd}), \tag{1.4}$$

where V is the operating bias voltage and V_{bd} is the breakdown voltage. As a result, the SiPM gain is equal to the charge stored in the pixel capacitance. Considering that the overvoltage is of the order of few volts and C_D is typically tens of fF, the gain is of the order of $10^6 - 10^7$ electrons. One pixel signal on 50 Ω load corresponds to a pulse amplitude of few mV and can be transmitted to the front end electronics over several meters distance without requiring a preamplifier near the sensor [2], [3].

Figure 1.16(a) shows that, at a given temperature, the single pixel gain increases linearly with the bias voltage, as expected from (1.4). The V_{bd}, determined from the intersection of the linear fits with horizontal axis, shows a linear increase with the temperature. For example, the Hamamatsu in Figure 1.16(b) have a dV_{bd}/dT of 60 mV/$^\circ$C [20]. It is in fact expected that in a silicon junction at higher temperature higher energy is required to ionize the electrons from the valence band to the minimum of the conduction band. As a consequence, the linear dependence of the gain to the breakdown voltage implies a proportionality between the gain and the temperature: an increase of the temperature leads to the decrease of the gain due to the drop of the avalanche current at steady voltage [21]. Figure 1.17(a) presents the linear function between the gain and the overvoltage at fixed temperature; a maximum gain variations of 1.7 %/$^\circ$C at constant overvoltage can be interpreted as the dependence of the cell capacitance C_D on the temperature. At the same overvoltage higher gain can be achieved by devices with bigger cell size due to their higher capacitance (Figure 1.17(b)) [20].
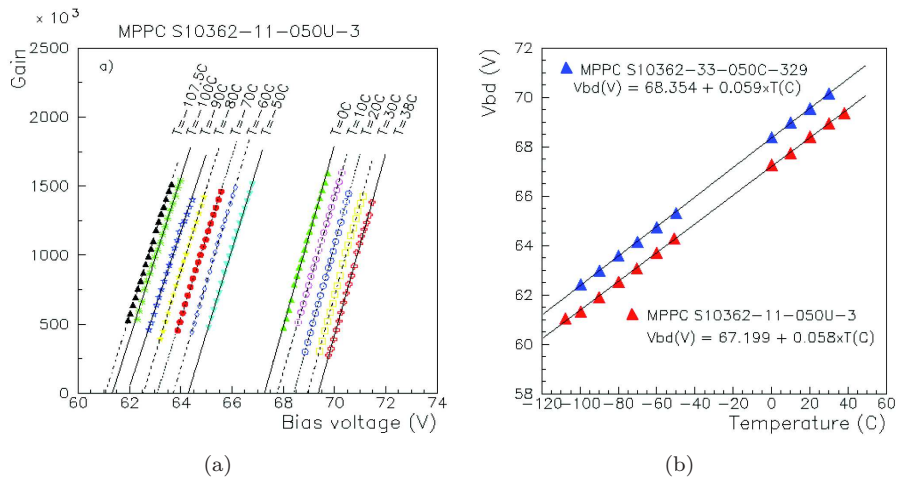
Figure 1.16: (a) The gain dependence with the bias voltage and (b) the breakdown voltage behavior as a function of the temperature for a 50 μm cell 1x1 mm^2 S10362 Hamamatsu SiPM [20].
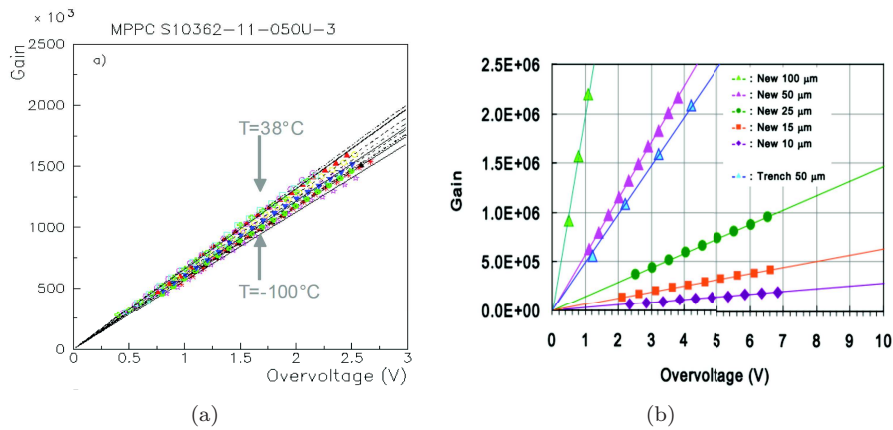
Figure 1.17: The gain dependence with the overvoltage at (a) different temperatures for 50 μm cell 1x1 mm^2 S10362 Hamamatsu [20] and (b) different cell size for S12571 Hamamatsu SiPM [18].

The strong effect of the gain drift due to temperature changes seriously limits the device performances. Any gain fluctuation causes undesired shifts in the distance between the detected photo-peaks, which may compromise the energy resolution of the system. Timing accuracy can also be affected by the excess time-walk generated by variations in the signals amplitude caused by gain drift [22].

One solution used to avoid these effects consists in the direct control of the sensor temperature through the Peltier cooling, which means to thermostat the sensor encapsulating it in vacuum. This technique is costly and in some application can be unreliable because it introduces a distance between the sensor

and the light source, which reduces the geometrical acceptance and worsens the device performance. The most straightforward way to compensate the temperature variations is to adjust the bias voltage of the detector accordingly in order to keep the gain at a constant value [23], [24], [25]. This stabilization technique requires a constant temperature monitoring either directly with thermistor pins positioned as close as possible to the sensor or analyzing the signal amplitudes. These procedures can be quite successful, however it should be noted that the detector performance are also impaired by the DCR and the stochastic effects featuring a significant temperature dependence.

1.4 Linearity and dynamic range

The SiPM output signal to a photon flux firing many cells may be naively expected to be proportional to the incident light intensity, since it results by the sum of the pulses of the single pixels A_i [3]:

$$A = \Sigma A_i. \tag{1.5}$$

However, as can be seen in the exemplary measurements reported in Figure 1.18, deviations from linearity have been seen to occur [26].
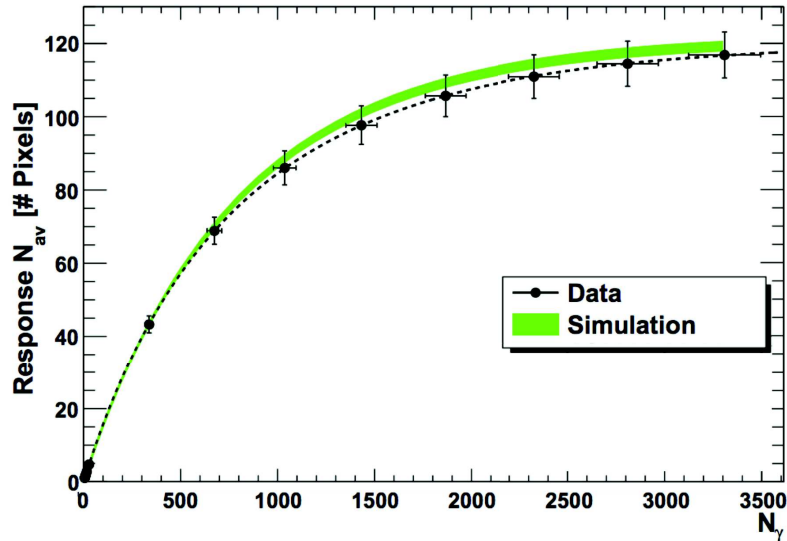
Figure 1.18: The simulated and measured number of fired cell as a function of the number of incoming photons (laser diode with 658 nm wavelength and 4 ns pulse width) for HAMAMATSU S10362-11-100C biased at 1V overvoltage [27].

The SiPM has a linear response until the number of incident photons per pixel is ≈ 1, then saturation effect occurs. The finite number of SiPM pixels determines its dynamic range, and it leads to a nonlinearity of its response when the number of produced photoelectrons approaches the total number of pixels. It is obvious that devices with a larger number of pixels are capable of a linear response in a wider range than devices with a smaller number of pixels [2].

The number of fired cells $N_{firedcells}$ is a function of the number of photons N_{ph} and of the total number of the SiPM cells N_{tot}. It is a random variable and its expected value can be determined considering the equivalent problem in mathematical statistics of distributing randomly n balls into m urns [28]. The expected value of the number N of urns containing one or more balls is:

$$N = m[1 - (1 - m^{-1})^n]. \tag{1.6}$$

In fact, m^{-1} represents the probability for a ball to be placed in a specific urn and $1 - m^{-1}$ is the probability for a ball not to be placed in that urn. Thus, the probability that none balls will be in that specific urn will be written as $(1 - m^{-1})^n$ and, finally, the complementary $1 - (1 - m^{-1})^n$ is the expression for the probability to have at least a ball in the urn. The distribution of N is gaussian when $m, n \to \infty$ and the ratio n/m is a finite value:

$$N = m[1 - e^{-n/m}]. \tag{1.7}$$

In the same way, $N_{firedcells}$ can be expressed as follow:

$$N_{firedcells} = N_{tot}\left(1 - e^{-\frac{N_{ph} \cdot PDE}{N_{tot}}}\right), \tag{1.8}$$

where the number of urns is substituted by the number of SiPM cells and the number of balls is replaced by the fraction of photons that can trigger an avalanche. The asymptotic formula is justified assuming a regime of high incident light intensity. Indeed the output signal is proportional to the number of fired cells as long as the number of photons in a pulse times the PDE is significant smaller than the number of cells [28].

This model is valid only if the duration of the light pulse is smaller than the pixel recovery time. When the mean time distance between two photons is of the same order of τ_r, the nonlinearity is strongly dependent on the width of the light pulse (Figure 1.19). A recovery time larger than the light pulse duration would eliminate this potential problem and increase the SiPM dynamic range [2].
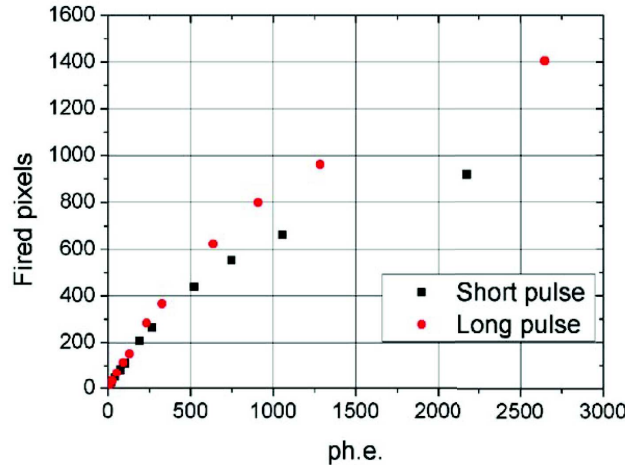
Figure 1.19: Nonlinear response to LED light pulses with different durations [2].

1.5   Dark Count Rate

The electronic noise of SiPM is negligibly small due to the very high gain; it corresponds to less than 10% of the single photoelectron signal. The main source of noise, which limits the single photon resolution, is the Dark Count Rate (DCR). This effect is due to breakdown avalanche triggered by any generation of free carriers in the depletion region. Results are spurious avalanches occurring randomly and independently from the illumination field. The main contribution is given by thermal generated free carriers and other minor processes are mediated by impurities and crystal defect acting like generation-recombination centers or related to the field-assisted generation (tunnelling) [2], [3].

At room temperature, a possible way to reduce DCR is to operate the SiPM at lower bias in order to reduce the active volume and the probability that a charge carrier develops an avalanche.

The DCR is also depending on the SiPM total active area; in fact, for the detection of very small light signals on large sensitive areas the DCR limits the performance at room temperatures. Thanks to the innovation of the last ten years, the DCR now reaches a value of about 40 kHz/mm^2 at about 2 V of overvoltage. In Figure 1.20 it is possible to see that the DCR for the Hamamatsu SiPM ranges from few MHz to about tens of kHz for the 6x6 mm^2 and the 1.3x1.3 mm^2, respectively.
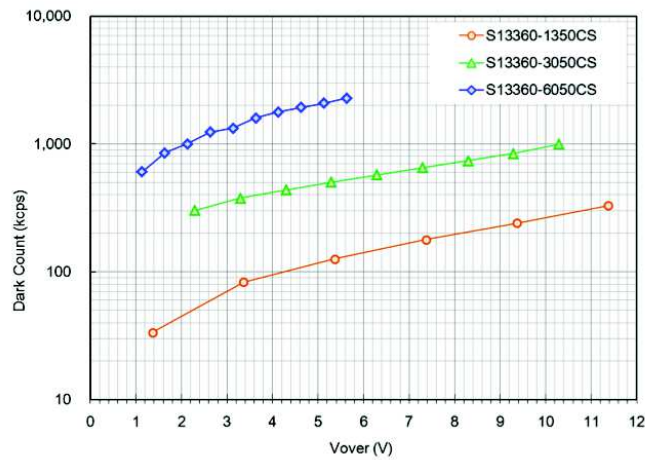
Figure 1.20: The DCR as a function of the overvoltage for different size sensors (6x6, 3x3 and 1.3x1.3 mm^2) of S13360 50 μm cell Hamamatsu.

Pulses due to thermally generated free carriers can be reduced by cooling, as reported in Figure 1.21. The DCR decreases with temperature from a few MHz/mm^2 (room temperature) to 50 Hz/mm^2-200 KHz/mm^2 (at 200 K), depending on the producers, with an exponential trend (a factor of 2 in reduction every 8°C). Below 200 K the DCR has a mild dependence with the temperature due to the minor processes of field-assisted generation and impurity-trapping, which can be reduced by decreasing the electric field and employing the purest silicon, respectively [20], [29]. Indeed, in order to reduce the DCR, besides

operating at low temperature and low bias voltage and employing small area sensors, the design and the sensor production technology play a crucial role.

(a)   (b)
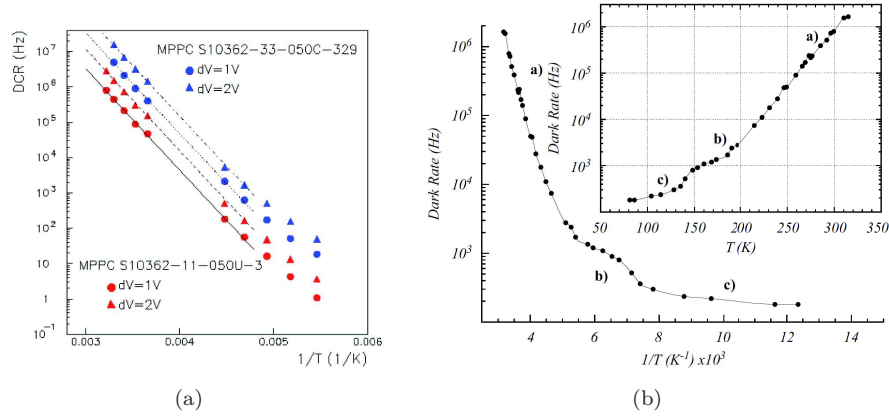
Figure 1.21: DCR as a function of inverse of temperature for (a) 1x1 mm^2 and 3x3 mm^2 50 μm S10362 Hamamatsu [20] and (b) 1x1 mm^2 FBK 40 μm cell [29].

1.6 Optical Cross-Talk

Already in 1955 it was demonstrated that a p-n junction which is reversely biased until breakdown has an emission spectrum in three energy regions: the region below the band gap energy, the near-band-edge region and the high-energy region, i.e., the visible wavelength range, where photons come from transitions of hot electrons within the conduction bands. Then it was measured that the efficiency for photon emission with energies higher that 1.14 eV, the band gap of silicon, is 2.9·10^{-5} per charge carrier crossing the junction [30]. Assuming a typical SiPM gain of 10^6, on average 30 visible photons are generated during a cell breakdown avalanche. Each of these photons can propagate and, depending on its energy and its generation position, has a certain probability to reach a neighboring not primarily fired cell and trigger an additional discharge, as sketched in Figure 1.22. This secondary pulse is produced simultaneously with the initial one and cannot be separated from the primary photon; as a result a double amplitude pulse is observed in the output signal [31].
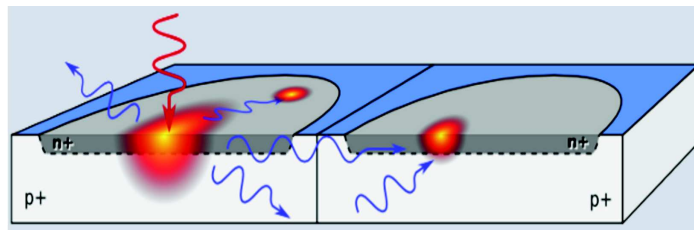
Figure 1.22: A picture of the Optical Cross-Talk process.

This phenomenon is called Optical Cross-Talk (OCT); it is a stochastic process which introduces an inter-pixel coupling and a correlated noise. The OCT leads to a non Poissonian behavior of the distribution number of fired pixel. Considering the DCR pulse height distribution of Figure 1.23(a) it is possible to infer that the average number of fired pixel is more than one, with a long non Poissonian tail indicating the probability of multi-pixel breakdown avalanches [17]. In Figure 1.23(b) the DCR is reported as a function of the discriminator threshold. The SiPM signal in dark conditions is discriminated at different voltages and for each value the number of signals above the threshold are counted for a fixed time interval. The result is a cumulative distribution of signal frequencies called Staircase due to its characteristic behavior: the DCR has a plateau and a subsequent drop each time the applied threshold exceeds the value of the signal amplitude corresponding to a finite number of photoelectrons. It can be observed that the OCT leads to a slower drop in the DCR with respect to that expected from simple random coincidences, as it increases the probability for a signal to have an higher amplitude [2].
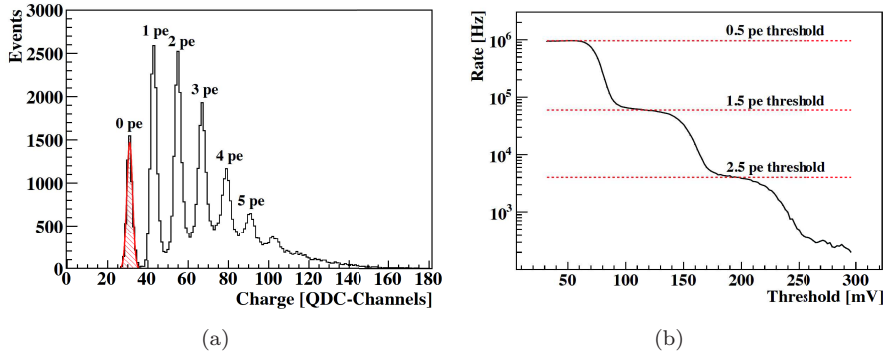
Figure 1.23: (a) The dark rate height distribution and (b) the DCR dependence on the threshold of a HAMAMATSU S10362-11-050C biased at 1.3V overvoltage [4].

In case of low DCR, the probability of two or more simultaneous thermal excitations can be considered negligible. The OCT can be estimated by comparing the event rate exceeding the threshold correspondent to 1.5 photoelectrons with the total amount of DCR (pulses above 0.5 photoelectrons threshold) [4]:

$$OCT = \frac{\nu_{1.5pe}}{\nu_{0.5pe}}. \tag{1.9}$$

More in general, it has been demonstrated that the experimental distribution of the DCR as a function of the threshold can be described by considering the OCT as a branching Poisson process [32], [37]. It means that one thermal or photon induced event produces a Poisson distributed random number of succeeding events, represented by the neighboring pixel triggering, until the branch extinction. In detail, if the primary event is a non random single event (Dark Count), the total number of events follow the Borel distribution, while, in case of Poisson distributed primary event, the statistics of the total number of event is governed by a Generalized Poisson distribution. When the OCT is low, the probability of more than one secondary event is negligible. Assuming that every primary event can produce only one chain of secondary events, the total

number of events belongs to a Geometric distribution or a Compound Poisson distribution if the primary event is respectively a single Dark Count or Poisson distributed photons. The four different cases are depicted in Figure 1.24, while an exhaustive demonstration will be available in Section 2.2 [32], [37].
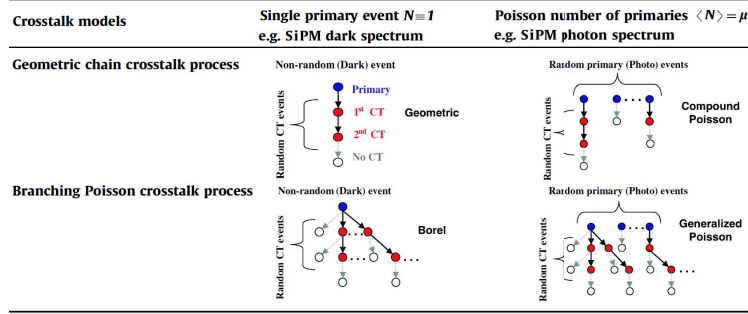
Figure 1.24: Schematic overview of the crosstalk process models [32].

Figure 1.25(a) shows that the OCT increases at higher bias voltage because more photons are produced during the avalanche and the effect is additionally enhanced by a higher triggering probability. Operation at relatively low bias again is advantageous, but can lead to a low PDE. Comparing devices with different cell size at the same gain (Figure 1.25(b)), it can be observed that the OCT increases also with reducing the cell dimension. This can be explained by the longer average distance that photons have to travel before reaching a neighbor pixel to be triggered [4].

(a)

(b)
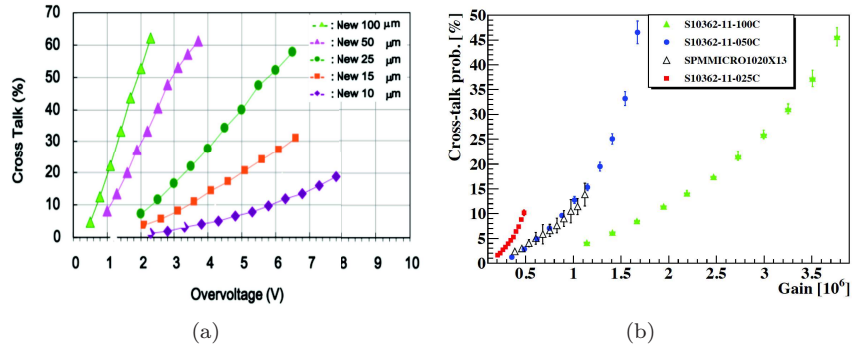
Figure 1.25: (a) OCT as a function of bias voltage for various cell size of S12571 Hamamatsu SiPM [18] and (b) OCT dependence on gain for different SiPMs [4].

The basic idea to reduce the OCT effect is that the SiPM pixels should be independent. At the beginning, pixel decoupling was realized with a dedicated design employing grooves between the cells which act as an optical isolation [33]. However, these grooves cause a larger dead area, with the effect of reducing the PDE. Recently, specially designed boundaries, deep trenches coated with reflective metal shown in Figure 1.26, has been introduced between pixels in order to reduce the OCT without affecting seriously the PDE. The incredibly

good results that have been achieved are shown in Figure 1.27: the OCT is reduced from the typical values of 10-20% of a few years ago to 1-2% thanks to the application of trench isolation technology.
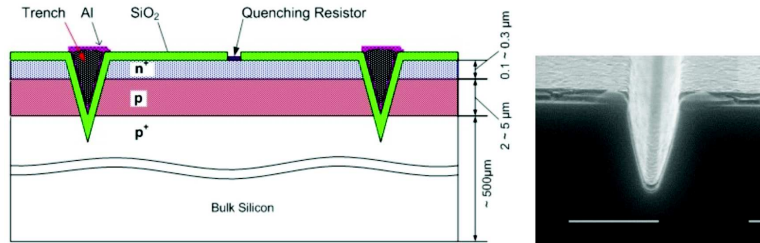
Figure 1.26: The implementation of optical trenches in SiPM design [34].
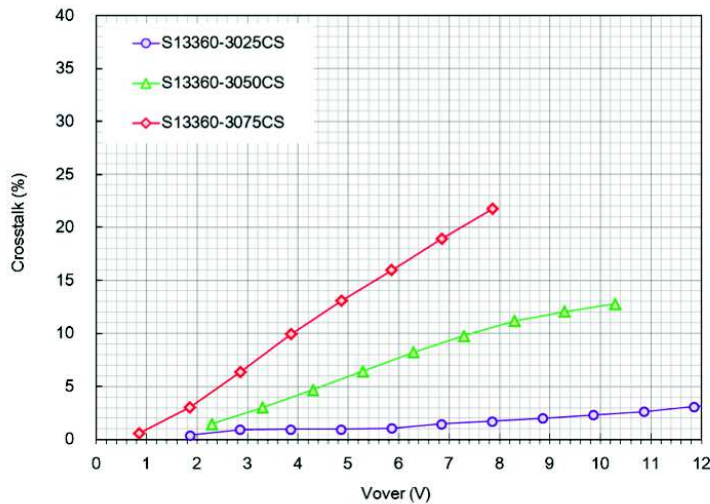
Figure 1.27: The reduction of the OCT thanks to the application of optical tranches in S13360 Hamamatsu.

1.7 After-Pulsing

After-pulses are generated when electrons produced in an avalanche are trapped by an impurity or a defect in the silicon lattice and released after an amount of time which can last from nanoseconds up to several microseconds, resulting in a delayed secondary pulse firing the same pixel [3]. The charge fraction carried by an After-pulse depends on the recovery state of the involved pixel. For an After-Pulse occurring with a time delay Δt with respect to the primary pulse in a pixel with a recovery time τ_r the signal amplitude is [4]:

$$AP(\Delta t) = 1 - e^{-\frac{\Delta t}{\tau_r}}. \tag{1.10}$$

Figure 1.28 shows that after-pulses with short time delay are generated with an

amplitude smaller than one photoelectron signal because the cells is not fully recharged, while a standard avalanche signal is triggered if $\Delta t \geqslant \tau_r$.
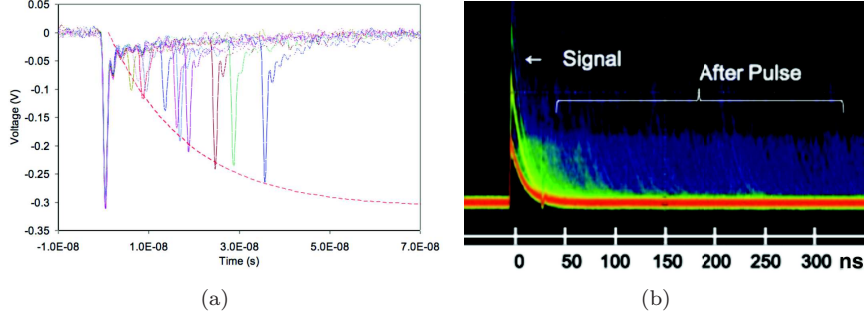
Figure 1.28: (a) Single cell signal: the after-pulse amplitude depends on the pixel recovery state [35]. (b) SiPM signal is followed by after-pulse events.

It is possible that some of the after-pulses are delayed OCT events in which a photon is emitted and absorbed in a non-depleted region. If the charge carriers are originated in the substrate of the same primary cell the signal amplitude will account for the cell recovery state, while if they are generated in the substrate of the neighboring cell the signal amplitude will correspond to a single photon. All these signals cannot be separated from primary photon-induced signals and thus deteriorate the photon-counting resolution and represent a critical issue in applications including correlation and coincidence analysis [36].

A typical distribution of the first pulse following a primary DCR pulse as a function of Δt is shown in Figure 1.29 [4]. The following pulse can be a Dark Count and, since DCR events are Poissonian distributed in time, the time interval distribution follows an exponential behavior:

$$n_{dcr}(\Delta t) = \frac{N_{dcr}}{\tau_{dcr}} e^{-\frac{\Delta t}{\tau_{dcr}}}, \tag{1.11}$$

where n_{dcr} represents the probability density for DCR events, N_{dcr} is the total number of DCR pulses and τ_{dcr} is the rate of pure dark count events. This result to be true only for long time intervals, while at low time intervals the experimental distribution shows a deviation from the thermal contribution that is due to after-pulse events. The experimental distribution can be fitted superposing to the DCR exponential another exponential describing the after-pulse contribution. It is constituted by two terms with different time constant, τ_{apf} and τ_{aps}, accounting for a fast and a slow after-pulse component:

$$n_{ap}(\Delta t) = \frac{N_{apf}}{\tau_{apf}} e^{-\frac{\Delta t}{\tau_{apf}}} + \frac{N_{aps}}{\tau_{aps}} e^{-\frac{\Delta t}{\tau_{aps}}}, \tag{1.12}$$

where n_{ap} indicates the probability density for after-pulse events, N_{apf} and N_{aps} correspond to the integrated number of fast and slow after-pulse, respectively. The after-pulse occurring probability is then given by:

$$P_{ap} = \frac{\int_o^\infty AP \cdot n_{ap} \quad \mathrm{d}\Delta t}{\int_o^\infty AP \cdot (n_{ap} + n_{dcr}) \quad \mathrm{d}\Delta t}, \tag{1.13}$$

accounting for the pulse amplitude dependence on the cell recovery state.
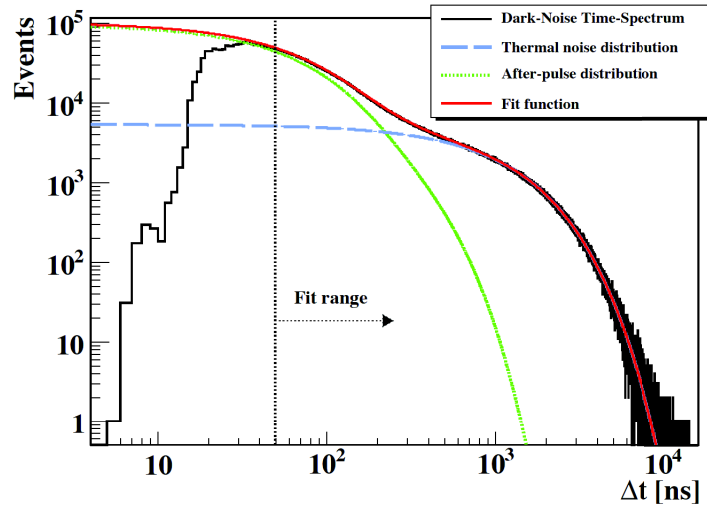
Figure 1.29: Pulses time difference distribution of Hamamatsu S10362-11-050C is well fitted by the superposition of two exponential curves for the thermal noise and the after-pulse time distribution. At small Δt values the pulse detecting efficiency is largely reduced due to the time needed for pixel recovery [4].

The after-pulse probability increases with the overvoltage, as can be seen in Figure 1.30 [4]. The reason for this increase is again due to the increase in gain, while the correspondent increasing of the avalanche trigger probability is responsible for the super-linear after-pulse probability rising.
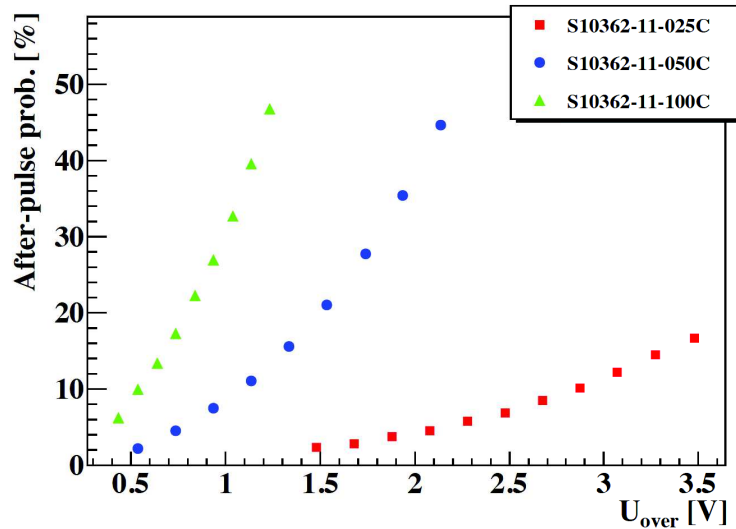
Figure 1.30: The after-pulse probability as a function of the overvoltage for S10362 Hamamatsu SiPMs of different cell size [4].

The trapped carrier lifetime becomes longer as the temperature decrease. A lower temperature can suppress the DCR and the OCT but, at the same time, it increases the after-pulse counts from trapped carriers. In fact, operating at low temperature elongate the delayed carrier release by a factor of 3 at every reduction of 25°C (Figure 1.31) [29]. In addition, after-pulse is essentially dependent on the sensor technology; producers are continuously improving the device material and the wafer process technology and in the last five years the after-pulse probability has been reduced from $\approx 25\%$ to $\approx 2\%$ (Figure 1.32.)
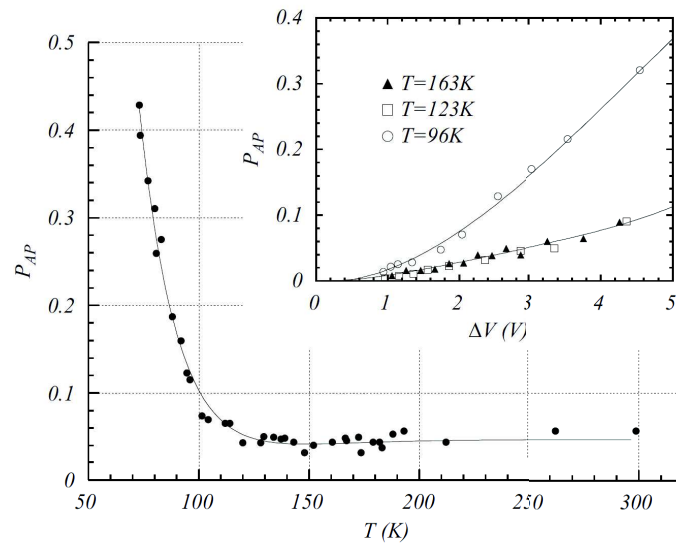
Figure 1.31: The after-pulse probability as a function of the temperature for the 1x1 mm^2 FBK 40 μm cell SiPM [29].
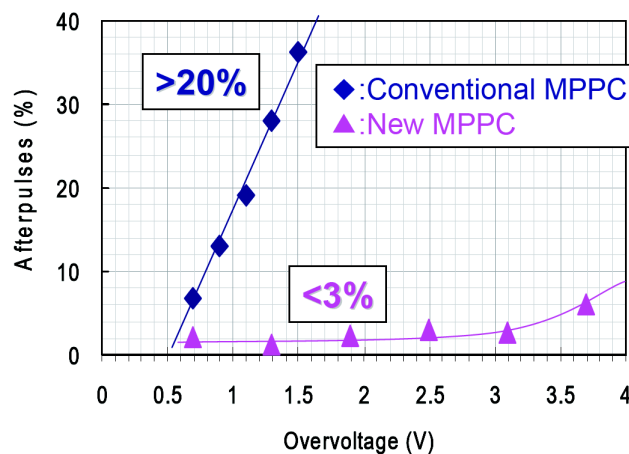
Figure 1.32: The after-pulse probability of the S13360 Hamamatsu SiPM [18].

1.8 Excess Noise Factor

Optical Cross-Talk and After-Pulses occur stochastically and introduce fluctuations in the number of pixel fired by a primary photon that contribute to broaden the peaks in the spectrum. As a result, they modify the probability distribution function of output signals (Figure 1.33) and cause the arising of not negligible multiplication noise, the Excess Noise Factor (ENF) [37], [38].
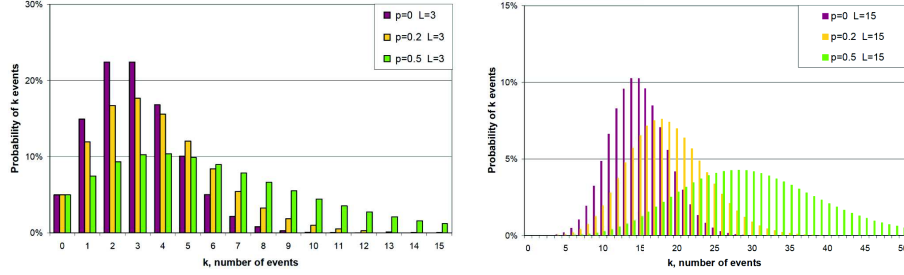
Figure 1.33: The Compound Poisson distribution with mean value $\mu = 3$ (left plot) and $\mu = 15$ (right plot) and probability of OCT and after-pulse detection $p = 0$ (Pure Poisson), 0.2 and 0.5 [37].

The ENF for amplification of a noisy signal is defined as the square of the degradation in signal to noise ratio (SNR) from input to output of the detector:

$$ENF = \left(\frac{SNR_{in}}{SNR_{out}} \right)^2, \tag{1.14}$$

where SNR is defined as the ratio between the mean and the square root of the variance. The input signal follows a Poisson distribution with mean vale μ while the output signal is described by a Compound Poisson distribution (as demonstrated in Section 2.2) with the parameter p accounting for the probability to detect OCT and after-pulse. The SNR results to be:

$$SNR_{in} = \sqrt{\mu} \qquad SNR_{out} = \sqrt{\frac{\mu}{1+p}}. \tag{1.15}$$

The ENF due to stochastic noise associated to OCT and after-pulse is:

$$ENF_{st} = 1 + p, \tag{1.16}$$

which means that it can not exceed the value of 2. Tacking into account the excess noise factor of photon detection, the total expression for ENF is:

$$ENF = \frac{1+p}{PDE}. \tag{1.17}$$

It can be measured from the single photoelectron charge distribution and calculated using [39], [40]:

$$ENF = 1 + \frac{\sigma^2}{G^2}, \tag{1.18}$$

where G is the SiPM gain, determined as the total charge released by the mean number of fired cell, and σ^2 is its variance. Currently, the value of Excess Noise Factor found in literature ranges from 1.01 to 1.5, as shown in Figure 1.34.
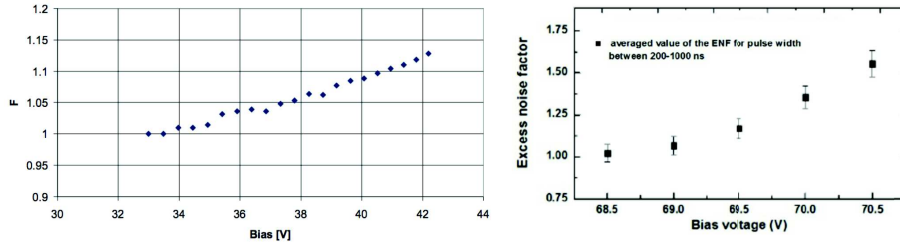
Figure 1.34: The ENF for CPTA/Photonique p-type 43 μm cell SiPM (on the left) and for S10362 50 μm cell Hamamatsu SiPM (on the right) [17].

1.9 Applications

The SiPM technology experienced a remarkable spread in the last ten years. A large number of producers start to invest increasing efforts in order to ensure a SiPMs mass production at high quality levels. As a consequence, this kind of device play a key role in the realization of a lot of new application in different fields.

The excellent timing properties of the SiPM can be useful for the Time Of Flight Positron Emission Tomography (TOF-PET), which will be described accurately in Chapter 4. In brief, the information of the time difference between the detection of two annihilation photons can be exploited to increase the quality and the efficiency of the image reconstruction. At this purpose the Coincidence Time Resolution (CRT) assumes high importance; it has been proved that a CRT value of about 100 ps can lead to an improvement of a factor 5 in the image signal to noise ratio (Figure 1.35) [41].
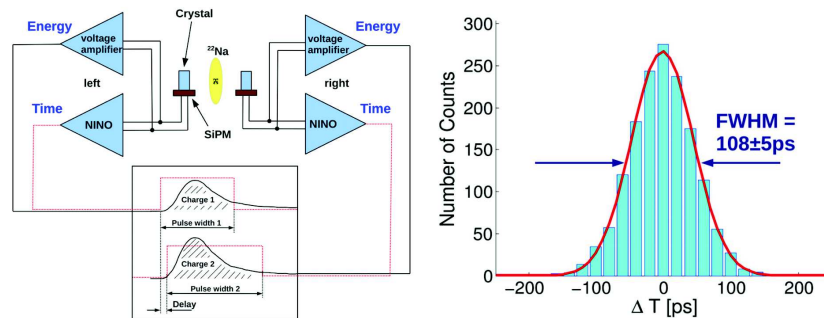
Figure 1.35: Coincidence Time Resolution of two $2 \times 2 \times 3 \text{mm}^3$ LYSO crystals coupled to two $3 \times 3 \text{ mm}^2$ Hamamatsu S10931-050P read with fast electronic [41].

Remaining in the field of medical imaging, SiPMs can also be employed in PET/MRI, as explained in detail in Chapter 4. In fact, thanks to their withstanding to the magnetic field, SiPMs can be adopted to build scanners that can incorporate both functional and anatomical information in order to obtained a better lesion detectability. Figure 1.36 shows that the behavior of the energy resolutions and the slopes of gain as a function of the bias voltage for three different size sensors are unaffected by a magnetic field of 7 T [42].
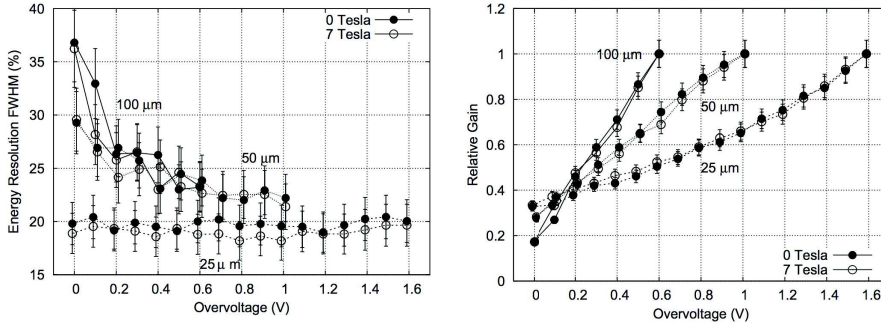
Figure 1.36: The energy resolution and the gain dependence with respect to the bias voltage for S10362-11-100P, S10362-11-050P and S10362-11-025P MPPC in absence and in presence of a 7 T magnetic field [42].

In addition, the fact that the SiPM DCR, OCT and gain are stable in presence of magnetic fields allows its operation in high energy collider detectors. For these applications, which require a huge number of channels, SiPM compactness, low bias voltage and small power consumption are desired features. The upgrade phase of CMS and LHCb, represent the first large scale application of SiPMs for high energy physics. In particular, the CMS Hybrid PhotoDiode used to read the scintillating tiles in the Hadronic Calorimeter will be replaced with SiPM. In fact, the Hybrid PhotoDiode resulted to be too sensitive to operate in the region of the return yoke, where the magnetic field could not be well known and the use of SiPMs will ensure to achieve a better energy resolution [43]. In LHCb the silicon strips of the Inner and the Outer Tracker are replaced with a huge number of small and fast Scintillating Fibers readout by SiPMs to guarantee an higher efficiency and a better spatial resolution with a low material budget [44]. The main problem for SiPMs operation in such environment is the radiation hardness. The device can undergo to a bulk damage due to non ionizing particles and to a surface damage due to ionizing energy loss. The first one has been tested with a neutron flux of $2 \cdot 10^{12}$ n/cm^2, mimicking the environmental LHC condition. As reported in Figure 1.37, the breakdown voltage and the quenching resistance remain unaffected, while the leakage current significantly increases, the PDE and the gain deteriorate, but SiPMs with high cell density and fast recovery time can operate adequately [43]. The second type of damage has been investigated using X-ray photons. After an irradiation of 3 kGy and 20MGy both the quenching resistor and the pixel recovery time increase with increasing radiation dose, together with the dark current, while inter-pixel cross talk and pixel capacitance showed no or little dependence [45].
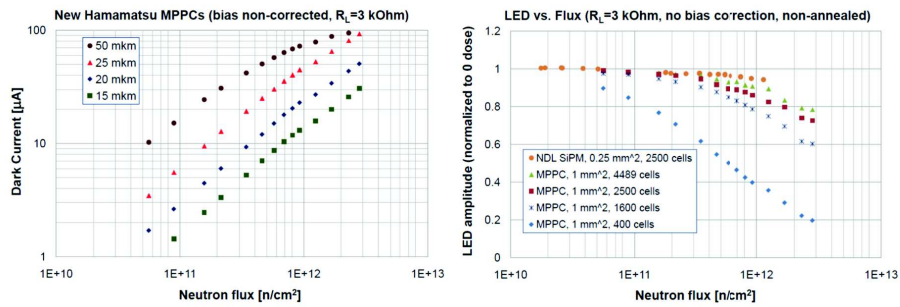
Figure 1.37: Effects of radiation damage on SiPM sensors from Hamamatsu as a function of neutron fluency on the PDE × gain and on the leakage current [43].

Another example of massive employment of SiPMs is represented by the Cherenkov Telescope Array (CTA), the next generation facility to observe atmospheric gamma ray and investigate the origin of cosmic rays, the black holes and the dark matter [46]. The CTA is constituted by tens of telescopes of three different dimensions, distributed in two sites to cover both hemispheres and arranged in a proper configuration to reach a large (8°) field of view and achieve unprecedented sensitivity, angular and energy resolution in the wide range of 20 GeV-100TeV (Figure 1.38). Due to the need of about 10,000 channels per telescope, SiPMs have the advantage to be cheap, to require a low operating voltage and have a low power consumption. In addition they feature a good tolerance to high illumination levels, a high detection efficiency and spatial resolution. However, considering that the telescope will be located in extreme environmental conditions, the spurious effects represent a challenge: a bias voltage feedback or the temperature control will be the adopted solution [47], [48].

Figure 1.38: Image of an artist's impression of the Cherenkov Telescope Array.

In addition, thanks to the single photon sensitivity and high detection efficiency, together with their compactness, SiPMs are employed in the field of:

- radiation protection, to develop personal gamma dosimeter for medical and industrial processes ([49], [50]);

- nuclear waste monitoring, to design devices able to detect traces of radiation in waste storage (Figure 1.39(a)) [51], or in vehicle loads entering or leaving industrial sites, scrap yards, steel plants, ports and terminals [52];

- homeland security, to discriminate with high efficiency neutrons from gammas and detect at boarders or at ports the illicit traffic of radioactive material to fabricate nuclear weapons (MODES FP7 project) [53];

- muon tomography, coupled to planes of scintillating material, to reconstruct a 3D image of cargo containers by measuring the deflection of muons when traversing high-Z materials to detect the presence of fissile elements (Figure 1.39(b)) or to probe the internal structure of volcanoes using almost horizontal muons to analyze the eruption dynamics (Figure 1.40).

(a) (b)
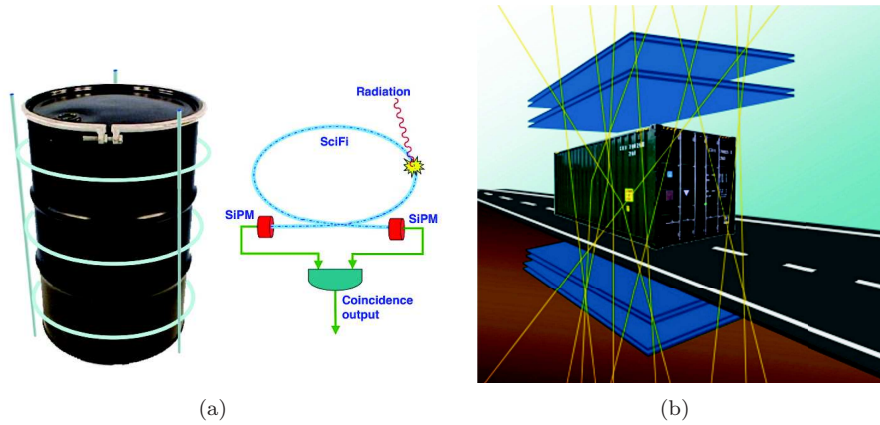
Figure 1.39: (a) INFN and SOGIN S.p.a. for a DMNR application: an annular detector, made out of a plastic scintillating fiber connected to SiPMs at both ends to reduce with the coincidence logic the random events effect. (b) MuonPortal [54] uses 8 position-sensitive X-Y planes to reconstruct, applying specific tracking algorithms, the tomographic image of the containers inside volume.
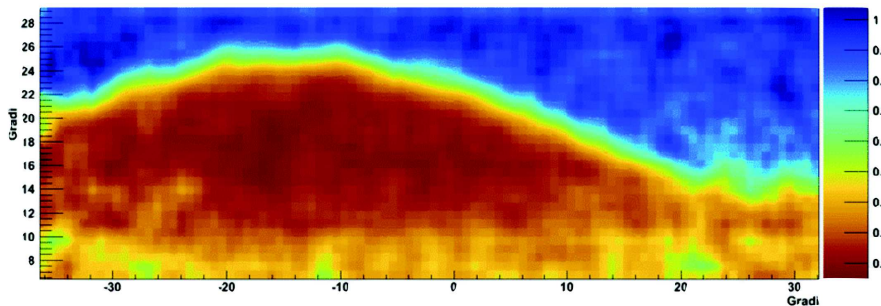
Figure 1.40: Preliminary results of the Vesuvio muon tomographic image with MURAY detector [55].

Chapter 2

SiPM standard characterization and Multi-Photon spectrum analysis

SiPM is a rapidly evolving technology and new generation of sensors are being continuously proposed by different producers. The development of a reliable and efficient SiPM characterization method is required to perform a quick assessment and comparison of their features and spurious effects.

In this chapter, a characterization procedure based on the analysis of the Multi-photon spectrum is proposed. The SiPM single photon sensitivity and their unprecedented photon number resolving capability open up the possibility to measure the SiPM properties which are of general interest for a multitude of potential applications.

In the method described here the SiPM under test is illuminated by an ultra-fast LED operated in pulse mode. The spectra are acquired by integrating the digitized SiPM output signal during a fixed time interval. A Multi-Gaussian Fit is implemented to fit all the peaks of the acquired spectrum. The calculation of the peaks distance and width allows to determine the sensor gain and resolving power, used to identify the optimal working point. An analysis of the peaks area with a model accounting for sensor related effects is crucial to disentangle the properties of the underlying photon source statistics and estimate the sensor Optical Cross Talk.

The setup is based on a flexible and modular system developed by Insubria University in collaboration with CAEN. It is fundamental for sensor characterization, as it allows measuring the main SiPM characteristics. In addition it constitutes a useful tool to implement experiments aimed to guide physics and engineering undergraduate and master students towards a comprehensive knowledge of the sensor technology and statistics analysis. Furthermore, it provides a platform for the proof of concept for the use of SiPMs in a variety of new applications in different fields [56].

2.1 Experimental setup

The setup consists of modular plug and play devices, USB connected to a computer and controlled by a Graphical User Interface (GUI) programmed in LabVIEW. It is a by-product of an FP6 funded project head by Insubria University (RAPSODI), in which a prototype of an easy-to-use and flexible tool for SiPM characterization was developed. In 2010 a joint development laboratory was established with CAEN to realize and commercialize the product as an educational kit [57]. The main component of the setup, shown in Figure 2.1, are:

- A two channel Power Supply and Amplification Unit (PSAU SP5600) integrating the sensors hosted in a replaceable holder. Each channel provides an independent biasing up to 120 V and a three-stage amplification, with a tunable gain up to 50 dB. The PSAU integrates a leading edge discriminator per channel and a circuit coincidence logic. An active temperature driven feedback controls the bias voltage allowing the gain stabilization with a granularity of 0.1°C.

- A two channel stand-alone Desktop Digitizer (DT5720A) with a sampling rate of 250 MS/s over a 12 bit dynamic range. A firmware enables the possibility to perform charge integration (DPP-CI). It can operate in self-trigger or can be triggered with an external signal.

- An ultra-fast LED driver (SP5601) emitting light pulses at 420 nm with FWHM of 14 nm. Pulses are characterized by an exponential time distribution of the emitted photons with a rising edge at sub-nanosecond level and a trailing edge with $\tau \approx 5$ ns. The driver is also providing a synchronization signal in TTL standard.

Figure 2.1: The PSAU, the digitizer and the LED of the CAEN educational kit.

The SiPM used to qualify the proposed methodology is the MPPC S10362-11-100C produced by Hamamatsu Photonics. It has an active area of 1x1mm^2, with 100 cells of 100 μm pitch. The other parameters provided by the manufacturer datasheet are reported in Table 2.1.

Number of Cells	100
Area	$1 \times 1\,mm^2$
Diode Dimension	$100\ \mu m\ \times\ 100\ \mu m$
Breakdown Voltage	69.6V
DCR	(600) kHz
OCT	10%
Gain	$(3.3) \times 10^6$
PDE $(\lambda = 440nm)$	35%

Table 2.1: Main characteristics of the S10362-11-100C at 70.3V and 25°C.

The block diagram of the experimental set-up is presented in Figure 2.2. The light pulses are conveyed by an optical fiber to the SiPM, which is housed in the holder and connected to the PSAU to receive the bias voltage and transmit the electric signal. The analog signal amplified and inverted by the PSAU is fed in the input of the digitizer, which is set to perform charge integration. The area of the digitized signal, measured integrating the SiPM output during a pre-defined time interval, is retained as a figure proportional to the total charge generated by the SiPM in response to the impinging photons. The integration time interval (gate) is adjusted to match the signal development and it is synchronized to the LED driver pulsing frequency. The main experimental working conditions are reported in Tab 2.2.
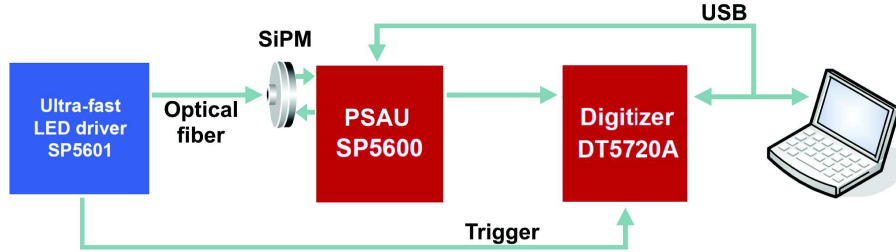
Figure 2.2: Schematic layout of the experimental setup.

PSAU gain	Gate width	Trigger frequency	Temperature
30 dB	300 ns	100 kHz	25.0 °C

Table 2.2: Acquisition parameters.

The plot on the left in Figure 2.3 shows a typical signal of the SiPM illuminated by a LED visualized at the oscilloscope: the well defined band of traces indicate an high resolution in the identification of the number of fired cells.

The plot on the right in Figure 2.3 displays an exemplary spectrum of the SiPM response to a statistics of light pulses in which every entry represents the digitized signal area, measured in ADC channels. Each peak in the spectrum corresponds to different number of cells fired at the same time. All peaks are well separated and the area underneath them (the probability for the corresponding

number of cells to be fired) is linked at first order to the LED light intensity statistics. The peak at 0 corresponds to no detected photons and is due to the stochastic fluctuations in the output signal in absence of any light stimulus.
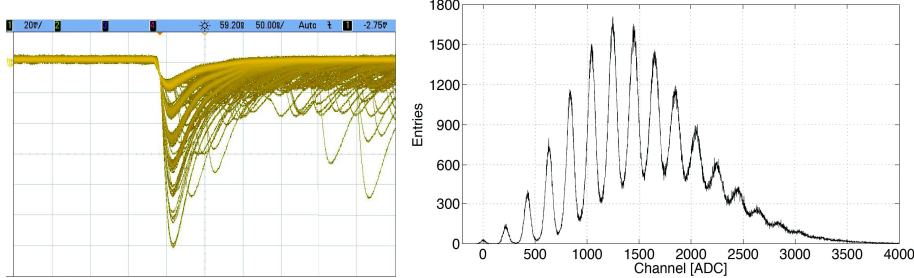
Figure 2.3: Exemplary SiPM output signal visualized at the scope (left plot) and a photoelectron spectrum (right plot), both obtained by probing a LED source with a S10362-11-100C biased at 70.3 V at 25°C.

2.2 Data analysis techniques

Multi-Gaussian fit

The recorded spectra can be seen as a superposition of Gaussians, each corresponding to a well defined number of fired cells.

The measurement of the distance between peaks (Δ_{pp}) and of the peak widths (σ_i) is fundamental for the sensor characterization. In fact, the Δ_{pp} is linked to the cell gain and, thanks to the high homogeneity of the SiPM response, is expected to be constant with respect to the number of fired cells. However, the system noise contributes in broadening the peaks and its effect can be measured by the width of the peak corresponding to 0 photoelectrons. The other peaks have widths exceeding the one at 0; the extra contributions are related to the fact that not all the cells were born exactly equal and, since fired cells are randomly distributed in the detector sensitive area, residual differences in the gain become evident broadening the peak. As a consequence, the peak width increases proportionally to the square root of the number of fired cells N and limits the maximum number of peaks that can be resolved.

The key point in the analysis for the reconstruction of the statistics of LED light is the estimation of the area underneath every peak, allowing the determination of the probability of the number of photons emitted per pulse.

A Multi-Gaussian Fit (MGF) procedure has been implemented in MATLAB and easily accessible thanks to a user-friendly GUI. The full spectrum is analyzed according to the following work flow:

- **Initialization**

  The robustness and efficiency of the fit procedure is guaranteed by having an educated guess of the initialization parameter values and by defining boundaries in the parameter variation space, a procedure increasingly important as the number of parameters grows. Initial values are provided with an iterative procedure. First the user is required to identify by pointing

and clicking on the spectrum the peak values and their position for three neighboring Gaussians, fitted to improve the estimate. Then initial values for every Gaussian are estimated by relying on the peak-to-peak distance from the previous step, presuming the 0 peak to be centered in the origin of the horizontal scale and assuming the standard deviation to grow as the squared root of the number of cells.

- **Fit**

  Spectra are fitted to a superposition of Gaussians with a non-linear χ^2 minimization algorithm presuming binomial errors in the content of every bin. The most robust convergence over a large number of tests and conditions have been empirically found bounding parameters to vary within 20% of the initial value for the peak position, 30% for the area and 50% for the standard deviation.

The outcome of the MGF procedure for the spectrum of Figure 2.3 taken as a reference is shown in Figure 2.4 and all the single Gaussian fit parameters are reported in Table 2.3. The probability associated to each peak is calculated normalizing the areas of each Gaussian to the total number of entries.
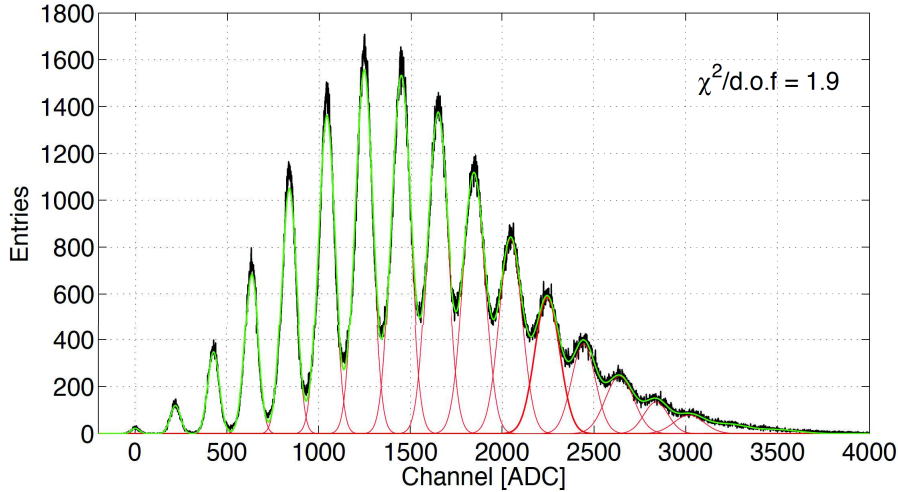
Figure 2.4: Outcome of the MGF procedure: individual Gaussians in red and their superposition in green. The $\chi^2/d.o.f. = 1.9$ indicates the good fit quality.

As expected, the peak-to-peak distance as a function of the number of fired cells is constant. Figure 2.5 illustrates the dependence of the squared peak widths to the peaks number. It is possible to infer that the linearity is guaranteed until a high number of cell has been fired. When the peaks start to be very broad and not clearly distinguishable it is obvious that the fit procedure assigns big errors to the estimated parameters. The outliers, the data points that are statistically inconsistent with the rest of the data, are identified with the robust Thompson Tau method and discarded [58]. The outlier interpolators method is based on autoregressive approximations, with coefficients estimated in an iterative loop along with the data-cleaning operation.

N	$PeakPosition(ADC)$	$PeakWidth(ADC)$	$Probability$
0	2.1 ± 0.9	21.7 ± 0.8	0.09 ± 0.01
1	220.1 ± 0.4	27.3 ± 0.3	0.56 ± 0.01
2	428.0 ± 0.3	31.5 ± 0.2	1.86 ± 0.02
3	633.6 ± 0.2	36.0 ± 0.2	4.17 ± 0.02
4	837.5 ± 0.2	40.5 ± 0.2	7.21 ± 0.04
5	1041.3 ± 0.2	44.7 ± 0.2	10.30 ± 0.04
6	1243.7 ± 0.2	48.2 ± 0.2	12.67 ± 0.05
7	1445.6 ± 0.2	51.9 ± 0.3	13.43 ± 0.06
8	1645.8 ± 0.3	54.8 ± 0.4	12.71 ± 0.07
9	1846.4 ± 0.4	59.5 ± 0.6	11.2 ± 0.1
10	2046.5 ± 0.6	62.0 ± 0.9	8.7 ± 0.1
11	2245 ± 1	66 ± 2	6.6 ± 0.2
12	2445 ± 1	68 ± 2	4.4 ± 0.2
13	2632 ± 2	65 ± 3	2.4 ± 0.1

Table 2.3: Peak position, width and probability of having N photo-electrons. The results are obtained with the MGF procedure for the reference spectrum.
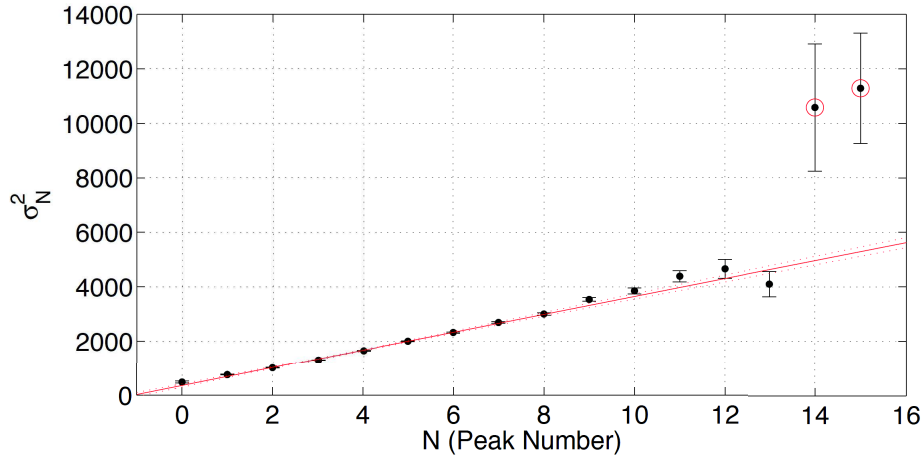
Figure 2.5: Peaks width squared as a function of the peak number. The dash lines represent the 95% C.L. for the fit, shown with the solid line. The circles indicate the outliers.

Working point optimization

The detector working conditions can be optimized to maximize the number of resolved peaks M. The main tunable parameter consists in the bias voltage.

In principle, increasing the peak-to-peak distance it should become easier to resolve more peaks. Since Δ_{pp} is proportional to the cell gain according to the relation:

$$G = \frac{\Delta_{pp} \cdot K}{q_e},$$

where q_e is the charge of the electron in Coulomb and K is a conversion factor that allows to transform the ADC channels into electric charge. K depends on the acquisition system parameters related to the charge integration:

$$K = \frac{V_{pp}}{R_{in}} \cdot \Delta_t \cdot \frac{1}{2^{N_{bit}}} \cdot \frac{1}{G_{PSAU}},$$

where V_{pp} is the digitizer dynamic range (2 V), R_{in} is the digitizer input impedance (50Ω), Δ_t represents the digitizer sampling time interval (4 ns), N_{bit} is the number of bits of the analog-to-digital converter (12) and G_{PSAU} is the PSAU gain defined by the user (30 dB). In fact, considering the Ohm law, the first term represents the maximum input current that the digitizer can accept. Then the second and the third term take into account the digitization and integration process which convert the electric signal into a digitized area, while the PSAU gain is considered in the last term.

The Multi-Photon spectrum can be acquired at different operating voltages and, measuring the mean peak-to-peak distance of every spectrum $\overline{\Delta_{pp}}$, the gain can be calculated from the above relation. From the result reported in Figure 2.6 it is possible to see that, as expected from the Equation (1.4), the gain grows linearly with the bias voltage. The linear fit parameters are $p_0 = (2.27 \pm 0.03) \cdot 10^6$ and $p_1 = (-1.58 \pm 0.02) \cdot 10^8$, and a $\chi^2/d.o.f. = 0.86$ confirms the good fit quality.
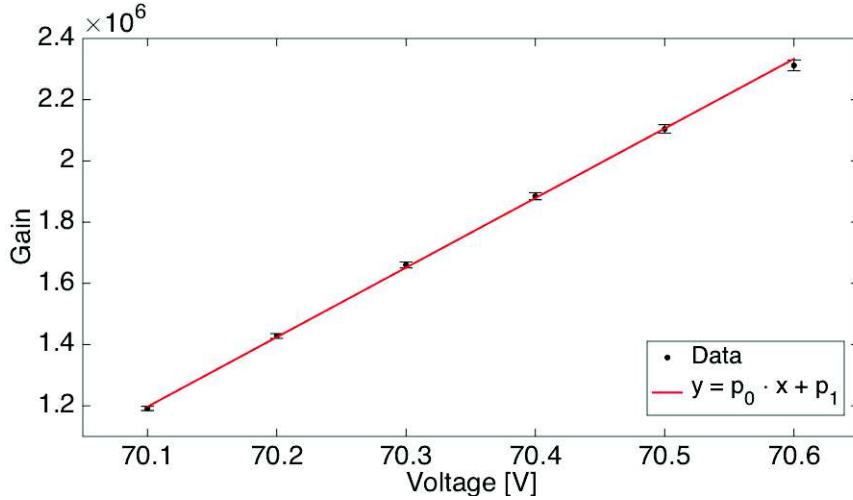
Figure 2.6: Gain as a function of the bias voltage for S10362-11-100C at 25°C.

In addition, it is possible to extrapolate the sensor breakdown voltage by using the slope and the intercept of the linear fit function, setting the gain to zero. The error on V_{bd} is calculated with the propagation of the fit parameter errors, taking into account their correlation matrix. The result is $V_{bd} = 69.57 \pm 0.01$, which is in agreement with the value provided by the manufacturer.

However, the increase of the bias voltage can introduce other competing effect broadening the peaks, which can grow faster than linear and worsen the expected resolution. These effects include the DCR, the OCT, the after-pulsing and are encompassed in the Excess Noise Factor. The resolving power R defined in Section 1.1 is a figure of merit that measures the capability to resolve the

detected photons, accounting for the ENF. R can be determined applying the Equation (1.1) and using the values obtained by the MGF procedure for spectra acquired at various bias voltage. The plot in Figure 2.7 shows the resolving power as a function of the bias voltage. The optimal bias voltage corresponds to the maximum R and is used as a working point.
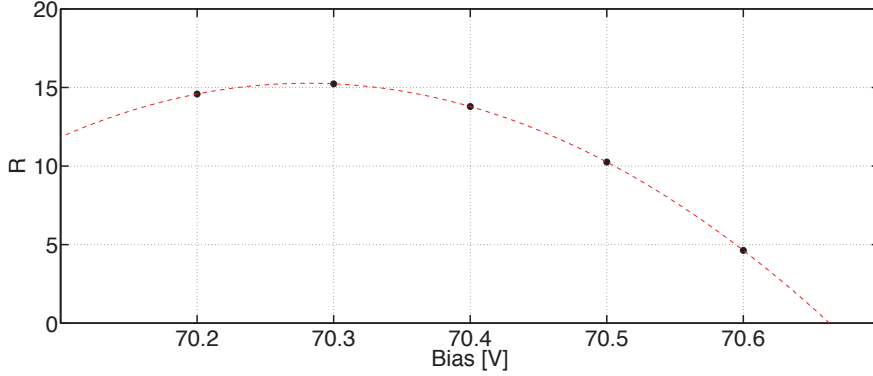
Figure 2.7: Resolving power versus bias voltage for S10362-11-100C at 25°C.

The DCR and OCT are essential for a complete SiPM characterization and they can be estimated trough the Staircase plot, reported in Figure 2.8. This plot is obtained by reporting the rate of the SiPM output signal exceeding a certain threshold in absence of light pulse by scanning on the threshold value. The measurement is performed counting he number of events during a deterministic period, using a leading edge discriminator to compare the signal amplitude to the threshold. The DCR is defined as the rate of pulses whose amplitude is above the value corresponding to 0.5 photoelectron and for the experimental setup is about 300 kHz. As the Staircase plot is a cumulative distribution, the DCR measurement includes also the OCT effect. In fact the OCT can be found measuring the rate of pulses exceeding the 1.5 photoelectron amplitude with respect to the DCR. For the sensor in use and under the experimental conditions described above the OCT results to be ≈10%.
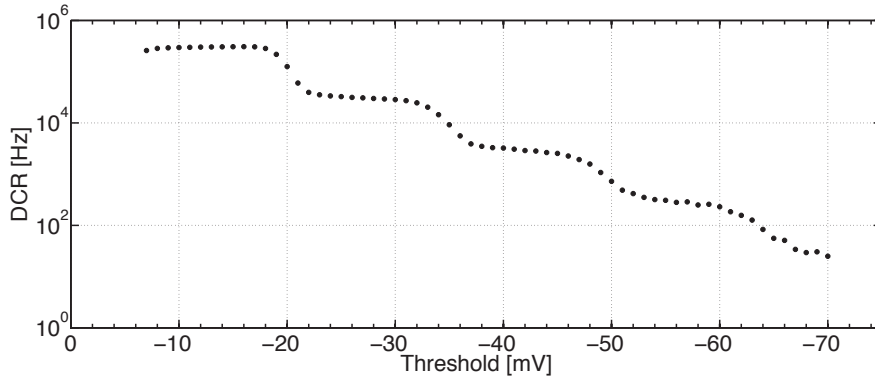
Figure 2.8: Measurement of DCR as a function of the signal threshold performed at 25°C with S10362-11-100C biased at 70.3 V.

In experiments dealing with a low number of photons the DCR contribution can compromise the spectrum quality and it has to be reduced as low as possible by reducing the integration time. However, in order to obtain a correct Multi-Photon spectrum acquisition, all the SiPM signal current should be integrated. As a result of this trade off, the gate length has been chosen to be equal to 300 ns, which results in a probability to integrate a noise event of about 9%.

Photon statistics

Spontaneous emission of the LED light results from random decays of excited atoms. Occurrences may be considered statistically independent, with a decay probability within a time interval Δt proportional to Δt itself. Being so, the statistics of the number of photons emitted within a finite time interval T is expected to be Poissonian, namely:

$$P_{n,\mathrm{ph}} = \frac{\lambda^n e^{-\lambda}}{n!},$$

where λ is the mean number of emitted photons.

The detection of the incoming photons has a stochastic nature as well, at the simplest possible order governed by the Photon Detection Probability (PDE) η, resulting in a Binomial probability to detect d photons out of n:

$$B_{d,n}(\eta) = \left(\begin{array}{c} n \\ d \end{array}\right) \eta^d (1-\eta)^{n-d} .$$

As a consequence, the distribution $P_{d,\mathrm{el}}$ of the number of detected photons is linked to the distribution $P_{n,\mathrm{ph}}$ of the number of generated photons by:

$$P_{d,\mathrm{el}} = \sum_{n=d}^{\infty} B_{d,n}(\eta) P_{n,\mathrm{ph}} . \tag{2.1}$$

However, the photon statistics is preserved and $P_{d,\mathrm{el}}$ is actually a Poisson distribution of mean value $\mu = \lambda\eta$ [59], [60]. In fact, multiplying and dividing by η^n each element in the series, Eq. 2.1 can be written as:

$$P_{d,el} = \sum_{n=d}^{\infty} B_{d,n}(\eta) P_{n,ph}(\lambda) = \sum_{n=d}^{\infty} \frac{(\lambda\eta)^n \eta^{d-n}(1-\eta)^{n-d} e^{-\lambda}}{d!(n-d)!}.$$

Hence, defining $n - d = z$:

$$P_{d,el} = \frac{(\lambda\eta)^d e^{-\lambda}}{d!} \cdot \sum_{z=0}^{\infty} \frac{(\lambda\eta)^z}{z!} \left(\frac{1-\eta}{\eta}\right)^z = \frac{e^{-\lambda}(\lambda\eta)^d}{d!} \cdot \sum_{z=0}^{\infty} \frac{(\lambda - \lambda\eta)^z}{z!}.$$

The series actually corresponds to the Taylor expansion of $e^{\lambda - \lambda\eta}$, so that:

$$P_{d,el} = \sum_{n=d}^{\infty} B_{d,n}(\eta) P_{n,ph}(\lambda) = \frac{e^{-\lambda\eta}(\lambda\eta)^d}{d!}$$

Detector effects (especially OCT and After-Pulses) can actually modify the original photo-electron probability density function, leading to significant deviations from a pure Poisson distribution. Following [59], [60], OCT can be accounted for by a parameter ϵ_{XT}, corresponding to the probability of an avalanche to trigger a secondary cell. The probability density function of the number of fired cells, the random discrete variable m, can be written at first order as:

$$P \otimes B = \sum_{k=0}^{floor(m/2)} B_{k,m-k}(\epsilon_{XT}) P_{m-k}(\mu),\tag{2.2}$$

where *floor* rounds $m/2$ to the nearest lower integer and $B_{k,m-k}(\epsilon_{XT})$ is the binomial probability for $m - k$ cells fired by a photon to generate k extra hit by OCT. $P \otimes B$ is characterized by a mean value and variance expressed as:

$$\bar{m}_{P \otimes B} = \mu(1 + \epsilon_{XT}) \qquad \sigma^2_{P \otimes B} = \mu(1 + \epsilon_{XT}).$$

In order to perform a more refined analysis, the probability density function of the total number of detected pulses can be calculated taking into account higher order effects [37]. The result is achieved by assuming that every primary event may produce a single infinite chain of secondary pulses with the same probability ϵ_{XT}. Neglecting the probability for an event to trigger more than one cell, the number of secondary hits, described by the random discrete variable k, follows a geometric distribution with parameter ϵ_{XT}:

$$G_k(\epsilon_{XT}) = \epsilon_{XT}{}^k (1 - \epsilon_{XT}) \qquad for \quad k = 0, 1, 2, 3....$$

The number of primary detected pulses is denoted by the random discrete variable d and belongs to a Poisson distribution with mean value μ. The total number of detected pulses m is a compound Poisson process given by:

$$m = \sum_{i=1}^{d} (1 + k_i).\tag{2.3}$$

The probability density function of m, which is fundamental to obtain the mean value and variance of the total fired cell number, is determined by applying the probability generating function definition and properties.

The generating function of a discrete random variable ϕ is defined as:

$$\tilde{\Phi}(s) = \sum_{i=0}^{\infty} P(\phi = i) \times s^i.$$

The probability distribution function, the mean and the variance of the random variable ϕ can be calculated as:

$$\Phi(\phi = m) = \frac{1}{m!} \times \left. \frac{\mathrm{d}^m \Phi}{\mathrm{d}s^m} \right|_0 \tag{2.4}$$

$$\bar{m}_{\Phi} = \Phi(1) \tag{2.5}$$

$$\sigma^2_{\Phi} = \Phi(1)'' + \Phi(1)' - [\Phi(1)']^2. \tag{2.6}$$

The random variable considered here, m, is defined as a sum of discrete random variables. Thus, its generating function is the composition of the pure Poisson distribution generating function:

$$\tilde{P}(s) = e^{\mu(s-1)}$$

and of the geometric distribution generating function:

$$\tilde{G}(s) = \sum_{i=1}^{\infty} \epsilon_{XT}{}^{i-1} \times (1 - \epsilon_{XT}) \times s^i = \frac{(1 - \epsilon_{XT})s}{1 - \epsilon_{XT}s}.$$

Finally, the analytical expression of the generating function for the total number of fired cells result to be:

$$\tilde{P} \circ \tilde{G} = \tilde{P}(\tilde{G}(s)) = e^{\mu(\tilde{G}(s)-1)} = e^{\mu\left(\frac{s-1}{1-\epsilon_{XT}s}\right)}.$$

Using the relation (2.4) it is possible to derive the probabilities to detect an arbitrary number of total pulses. For 0, 1 and 2 events the result is:

$$P \otimes G(0) = e^{-\mu},$$

$$P \otimes G(1) = e^{-\mu}\mu(1 - \epsilon_{XT}),$$

$$P \otimes G(2) = e^{-\mu}\left[\mu(1 - \epsilon_{XT})\epsilon_{XT} + \frac{\mu^2(1 - \epsilon_{XT})^2}{2}\right].$$

An analysis of these expressions lead to a compact and general formula which express the probability density function of m as a compound Poisson distribution:

$$P \otimes G = \frac{e^{-\mu} \sum_{i=0}^{m} B_{i,m}\mu^i(1 - \epsilon_{XT})^i\epsilon_{XT}{}^{m-i}}{m!}, \tag{2.7}$$

where

$$B_{i,m} = \begin{cases} 1 & \text{if } i = 0 \text{ and } m = 0 \\ 0 & \text{if } i = 0 \text{ and } m > 0 \\ \frac{m!(m-1)!}{i!(i-1)!(m-i)!} & \text{otherwise} \end{cases}$$

Applying the properties (2.5) and (2.6) at $\tilde{P} \circ \tilde{G}$, it is possible to obtain the mean value and the variance of the distribution of the total number of fired cells:

$$\bar{m}_{P \otimes G} = \frac{\mu}{1 - \epsilon_{XT}} \tag{2.8}$$

$$\sigma^2_{P \otimes G} = \frac{\mu(1 + \epsilon_{XT})}{(1 - \epsilon_{XT})^2}. \tag{2.9}$$

2.3 Results and discussion

The experimental distribution can initially be studied referring to the mean number of fired cells. A Model Independent estimate is provided by:

$$\mu_{MI} = \frac{\overline{ADC}}{\overline{\Delta_{pp}}}, \tag{2.10}$$

where

$$\overline{ADC} = \frac{\Sigma_i y_i ADC_i}{\Sigma_i y_i}$$

is the mean value of the experimental distribution (being y_i the number of events for the ith bin) and $\overline{\Delta_{pp}}$ is the mean peak-to-peak distance, defining the gauge to convert values in ADC channels to number of cells. The value of μ_{MI} can be compared to the expected average value estimated from the peak at 0 photoelectrons presuming a pure Poissonian behavior:

$$\mu_{ZP} = -ln(P(0)) \; = -ln\left(\frac{A_0}{A_{tot}}\right), \tag{2.11}$$

where $P(0)$ is the probability of having no fired cell, which is calculated by dividing the area of the 0-peak obtained with the MGF procedure (A_0) with the total number of acquired events (A_{tot}). Results for the reference spectrum are shown in Table 2.4: a statistically significant discrepancy can be observed.

μ_{MI}	7.81 ± 0.01
μ_{ZP}	7.08 ± 0.03

Table 2.4: Estimates of the mean number of fired cells by the average value of the reference experimental distribution and from the probability of having 0 photons, assuming an underlying Poisson distribution.

The question can be further investigated considering the full distribution and comparing the experimental probability density function with the assumed model distribution by a χ^2 test, where:

$$\chi^2 = \sum_{k=0}^{Npeaks-1} w_k \times (A_{obs,k} - A_{model,k})^2, \tag{2.12}$$

being $A_{obs,k}$ the number of events in the kth peak of the distribution determined with the MGF, $A_{model,k}$ the corresponding number estimated from the reference model and w_k the weights accounting for the uncertainties in the content of every bin. Presuming a Poisson distribution with mean value μ_{MI}, the returned value of the $\chi^2/d.o.f.$ is ≈ 300, confirming that the experimental distribution may not be adequately described by a pure Poisson model.

The spectra can be compared to the $P \otimes G$ distribution model of Equation 2.7, where the actual number of fired cells results from avalanches triggered by the incoming photons and by the optical cross-talk. The optimal values of the model

parameters, namely the cross-talk probability ϵ_{XT} and the mean value μ of the distribution of cells fired by photons, are determined by a grid search according to the following iterative procedure [61]:

- the $\chi^2/d.o.f.$ surface, henceforth referred to as Σ, is sliced with planes orthogonal to the ϵ_{XT} dimension, at differentvalues $\tilde{\epsilon}_{XT}$ taken with constant step;

- in each slice, the minimum of the $\Sigma(\tilde{\epsilon}_{XT}, \mu))$ curve is identified and the value $\mu_{min,0}$ corresponding to the minimum is determined;

- the $\Sigma(\epsilon_{XT}, \mu_{min,0})$ curve is scanned and the position ϵ_{XT}^* of the minimum is identified by a local parabolic fit, to overcome the limitations by the choice of the step in the grid;

- the procedure is repeated for $\Sigma(\epsilon_{XT}^*, \mu)$ vs μ, leading to the determination of the minimum in μ^*.

This method leads to estimate the optimal parameters μ^* and ϵ_{XT}^* by the minimization of the $\chi^2/d.o.f.$ surface for the two variables μ and ϵ_{XT} independently. The surface Σ and the $\Sigma(\epsilon_{XT}^*, \mu)$ and $\Sigma(\epsilon_{XT}, \mu^*)$ curves are shown in Fig. 2.9. Uncertainties are calculated assuming a parabolic shape of the $\chi^2/d.o.f.$ curves, leading to variances estimated by the inverse of the coefficient of the quadratic term [61], [62]. The results for the reference spectrum are $\mu^* = 7.06 \pm 0.02$ and $\epsilon_{XT}^* = 0.090 \pm 0.004$.

In order to account for the two-parameter correlation in the calculation of the uncertainties, it is worth to referring to the confidence region of the joint probability distribution [63], [64]. When the parameters are estimated minimizing the χ^2 distribution, confidence levels correspond to regions defined by iso-χ^2 curves. For two parameters, the region assumes an elliptic shape around the Σ minimum, χ_{min}^2. The Σ contour at the constant value of $\chi_{min}^2 + 1$ plays a crucial role due to its specific properties. In fact, the area enclosed by the ellipse corresponds to $\sim 38.5\%$ of the joint parameter probability distribution and its projections represent the $\sim 68.3\%$ of confidence interval for each parameter (σ_1 and σ_2). In addition, the correlation ρ among the parameters may be written as:

$$\rho = \frac{\sigma_1^2 - \sigma_2^2}{2\sigma_1\sigma_2} \tan 2\theta, \tag{2.13}$$

where θ represents the counter-clockwise rotation angle of the ellipse. The detailed demonstration is reported in Appendix A.

In this specific case, the χ_{min}^2 value is determined evaluating the $\chi^2/d.o.f.$ surface at the point of coordinates (μ^*, ϵ_{XT}^*) while the Σ contour at $\chi_{min}^2 + 1$ is shown in Figure2.10. The fit curve returns the value of the ellipse center (μ^0, ϵ_{XT}^0), while the projections of the ellipse on the μ and ϵ_{XT} axes are the uncertainties on the two values. The results for the reference spectrum are $\mu^0 = 7.06 \pm 0.05$ and $\epsilon_{XT}^0 = 0.09 \pm 0.01$. Comparing these values with (μ^*, ϵ_{XT}^*) it is possible to infer that the correlation does not affect the determination of the parameter central values while increases their standard deviation by a factor of about two. As a consequence, μ^0 and ϵ_{XT}^0 with their uncertainties are retained as the best estimate of the model parameter values. The angle returned by
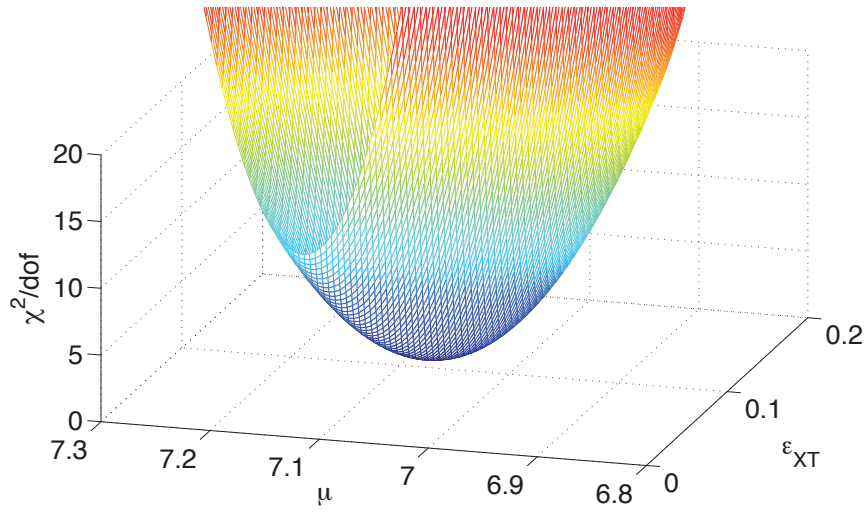
(a)
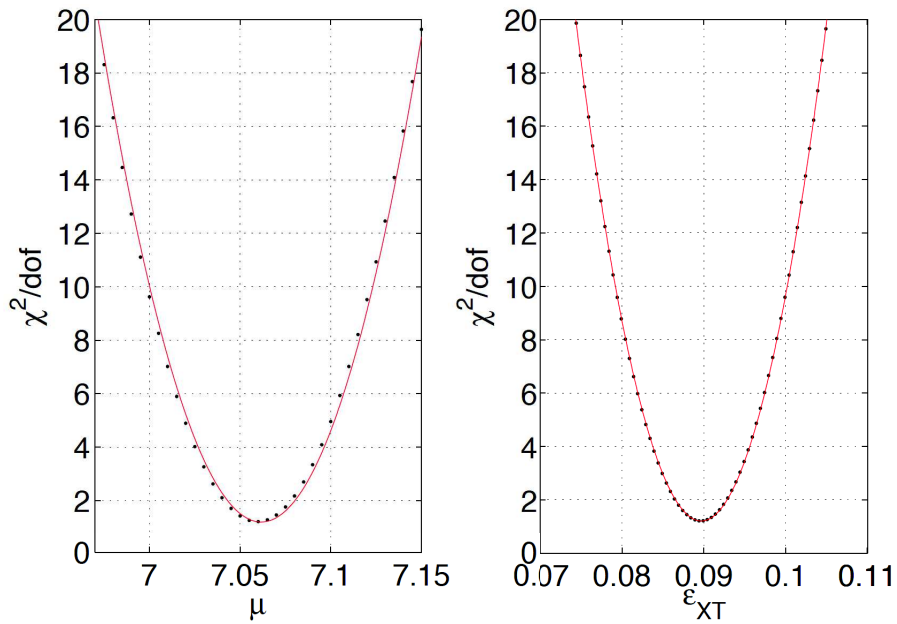
(b)

Figure 2.9: (a) $\chi^2/d.o.f.$ surface depending on μ and ϵ_{XT}. (b) The $\chi^2/d.o.f.$ (black points) nearby the minimum is fitted with a parabola (red line) in both planes at constant $\epsilon_{XT} = \epsilon_{XT}^*$ and $\mu = \mu^*$, respectively.

the ellipse fit is used to calculate the correlation ρ between the two parameters through the Equation (2.13). The result for the reference spectrum is $\rho = -0.8$.
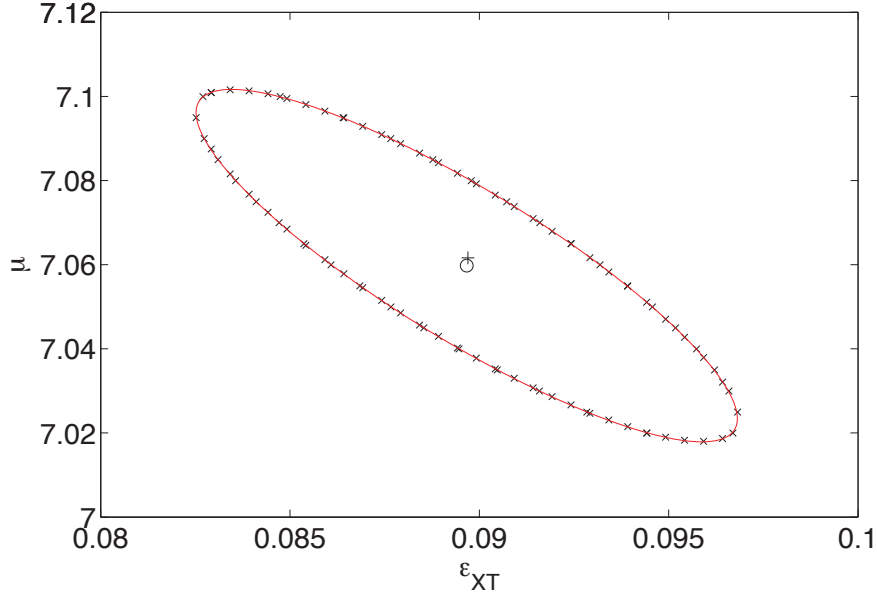
Figure 2.10: The black crosses are the $\chi^2/d.o.f.$ surface at the constant value of $\chi^2_{\min} + 1$, the fit curve is the red line, the center of the ellipse (μ^0, ϵ^0_{XT}) is represented with the black circle and the black cross identifies (μ^*, ϵ^*_{XT}).

Applying the relation (2.8) and exploiting the full covariance matrix, the value and the uncertainty of the mean of the $P \otimes G$ model can be obtained. For the reported spectra it results to be 7.76 ± 0.03. The result of the $P \otimes G$ probability function fit to the data distribution obtained with the MGF is displayed in Figure 2.11, showing an excellent agreement between data and model. The quality of the result is confirmed by the data reported in Table 2.5, where μ_{MI} and $\mu^0/(1 - \epsilon^0_{XT})$, the mean value of the $P \otimes G$ distribution are compared, showing a perfect consistency. In addition, the mean value of the distribution obtained by the ellipse fit is compared to the *Zero Peak*: as expected they are in agreement, because μ^0 relates to the pure Poisson model.

Mean Value of the Poissonian distribution	μ^0	μ_{ZP}
Reference spectrum	7.06 ± 0.05	7.08 ± 0.03
Mean Number of Fired Cells	μ_{MI}	$\mu^0/(1 - \epsilon^0_{XT})$
Reference spectrum	7.81 ± 0.01	7.76 ± 0.03

Table 2.5: The first row shows the comparison between the mean value of the Poisson distribution obtained by the peak at zero and the ellipse fit. In the second row is reported the mean number of fired cells estimated with the model independent method and the $P \otimes G$ model. Results from the reference spectrum.
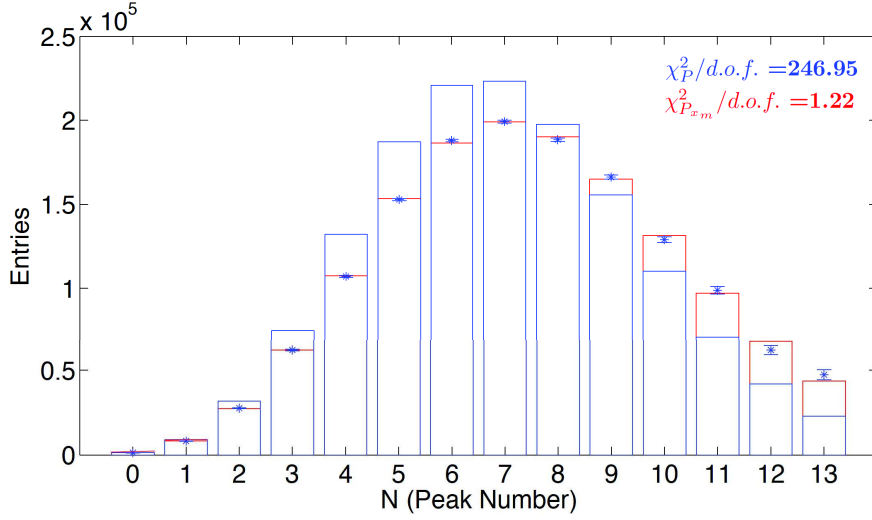
Figure 2.11: Data from the reference spectrum are compared to a simple Poisson model with mean value μ_{ZP} (blue) and to the $P \otimes G$ model (red), accounting for the optical cross-talk. The χ^2 value rule out the former at 99% C.L..

Data with other light intensities are used to assess the robustness of the approach and the validity of the model. The acquired spectrum are shown in Figures 2.12(a) and 2.13(a), while the outcome of the MGF compared to the pure Poisson model and the compound Poisson model is displayed in Figures 2.12(b) and 2.13(b). The results of the procedure are summarized in Table 2.6, confirming the validity of the compound Poisson model and the need to account for detector effects to have a proper understanding of the distribution.

Mean Value of the Poisson distribution	μ^0	μ_{ZP}
Low light	0.97 ± 0.01	0.985 ± 0.002
Medium light	1.82 ± 0.01	1.823 ± 0.004
Mean Number of Fired Cells	μ_{MI}	$\mu^0/(1 - \epsilon_{XT}^0)$
Low light	1.080 ± 0.002	1.08 ± 0.01
Medium light	1.994 ± 0.003	1.99 ± 0.01

Table 2.6: Comparison of the low and medium light spectra mean values estimated from the zero peak and the ellipse fit, together with a comparison of the mean number of fired cell estimated model independently and with $P \otimes G$ model.

A further cross-check of the correctness of the procedure is the comparison between the ϵ_{XT}^0 values obtained for the three light intensity spectra. As expected, they are in agreement: they result to be 0.09 ± 0.01 for the reference spectrum, 0.1 ± 0.01 and 0.09 ± 0.01 for the low and medium light intensity, respectively.

(a)

(b)
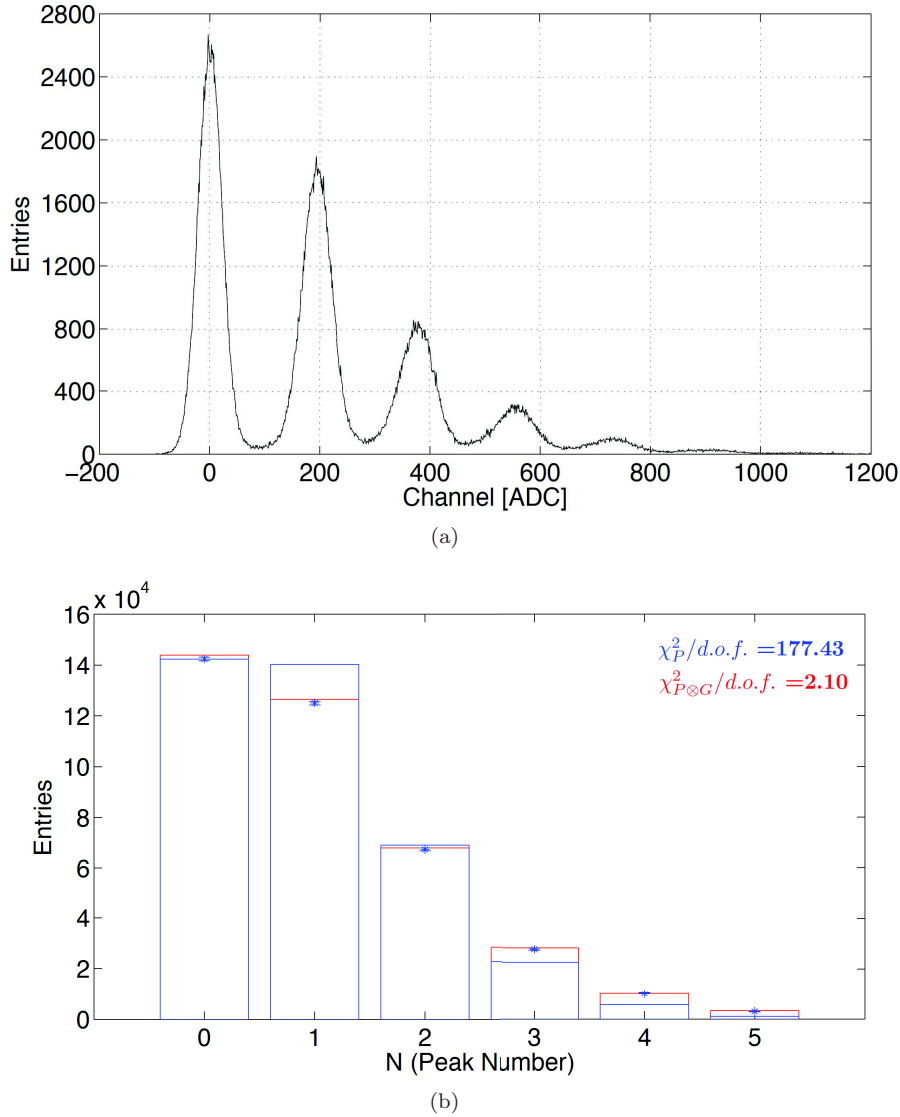
Figure 2.12: (a) Spectra acquired with a low LED intensity. (b) Comparison between data (blue points), pure Poisson model (blue) and compound Poisson model (red); the χ^2 indicate that the second one better describes data.

In conclusion, the standard characterization method described above, comprising the Staircase plot and the Multi-Gaussian fit of the Multi-Photon spectrum, allows to obtain the main information about the sensor, like the gain, the resolving power, the dark count rate and the optical cross-talk, with an easy data acquisition. The method, together with the interpretation of the Multi-Gaussian Fit analysis results in terms of Compound Poisson probability, can be used also to determine the statistics of the incoming light source, decoupling its effects from the sensor response. The limitation of the standard characterization procedure lies in the fact that the sensor should not present a high noise

(a)

(b)
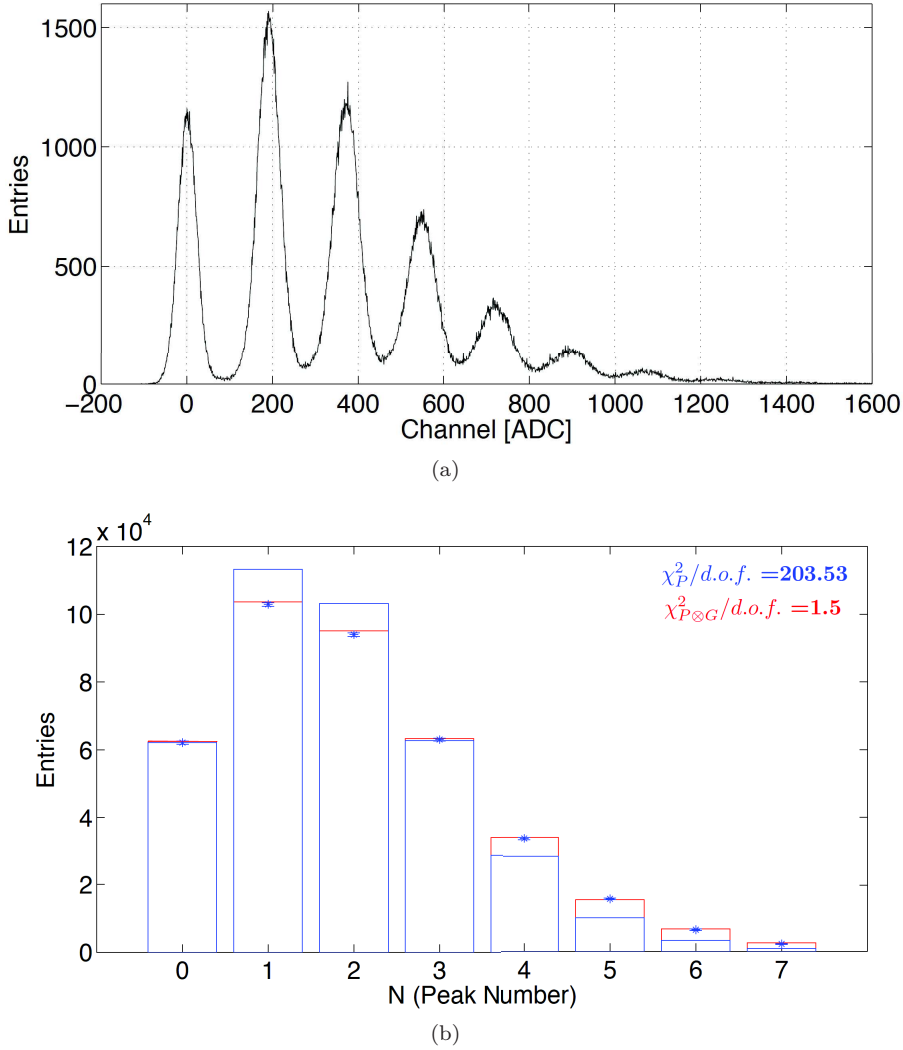
Figure 2.13: (a) Spectra acquired with a medium LED intensity. (b) Comparison between data (blue points), pure Poisson model (blue) and compound Poisson model (red); the χ^2 indicate that the second one better describes data.

component. Concerning the OCT, its effect consists in the modification of the peaks probability in the spectrum and it can be adequately accounted for till when the condition of the production of a single infinite secondary chain is valid. In practice, if the OCT probability is high enough, the chance of triggering two simultaneous avalanches in addition to the primary one should be considered and the Compound Poisson model has to be replaced by the Generalized Poisson model described in [32]. The DCR and the AP occurring during the event integration gate cause the mis-position of the event area in the spectrum, which is moved from the proximity of a peak to the valley between the peak itself and the consecutive one. As a consequence, in case of high DCR and/or AP, the Multi-Photon spectrum is ruined and the MGF outcome is no longer reliable.

Chapter 3

SiPM waveform analysis

The characterization procedure presented here is based on post-processing of SiPM waveforms, obtained by synchronously sample and record on the timescale of a few microseconds the response of a sensor to ultra-fast light pulses. The main goal is the determination from a single set of waveforms of a full picture of the sensor characteristics in terms of Gain, Breakdown Voltage, Dark Count Rate (DCR), Optical Cross-Talk (OCT) and After Pulse probability (AP). The use of a unique and consistent data set guarantees a fast and robust characterization (the acquisition lasts a couple of hours), stable against environmental condition changes, notably temperature.

The analysis technique has been implemented with a semi-automatic and flexible software developed with MATLAB®, suitable for sensors of various dimensions and produced by different vendors. It is extremely useful for both manufacturers and research laboratories as it constitutes an efficient characterization method that reduces testing time and provides meaningful data to compare devices fabricated with different technologies.

The procedure has been validated with a simulation able to reproduce the waveforms of the SiPM, taking into account the light source statistics and implementing all the stochastic effects related to the sensor photon detection. The robustness and the reliability of the characterization procedure have been assessed using simulated data with different settings, compatible with the typical values of various SiPMs.

The method has been used to characterize SiPMs from different companies and areas from 1x1 mm^2 up to 6x6 mm^2. In particular, it will be reported the comparison of large area sensors by three different producers. These sensors have been chosen as they are of great interest for the development of portable and cost effective gamma spectrometers and neutron detectors but their characteristics may be critical to measure. In fact, their high rate of Dark Counts is essentially spoiling the standard characterization method based on the staircase and the Multi-photon spectrum described in the previous Chapter.

3.1 Materials and methods

The experimental setup comprises the PSAU, the Digitizer and the LED source, part of the CAEN Educational Kit. The SiPM is housed in the PSAU and is illuminated by the LED via an optical fiber. The PSAU analog output is then sampled at 250 MS/s and digitized. A specific firmware enables the Digitizer to record and store the signal waveform during a pre-defined time window. The LED also provides the trigger to the Digitizer for a signal acquisition synchronous to the emitted light pulse [57]. The PSAU gain has been fixed at 32 dB and the measurements have been performed at a stable temperature of 25°C.

The data analysis technique requires a high statistics to provide results with reasonable errors: typically 100000 waveforms have been recorded for each different setting of each sensor under test. The procedure is based on a time acquisition window of 4 μs, with the LED trigger occurring 2 μs after the window opening, thus in the middle of the time acquisition. As a result, each data file is of the order of few gigabyte. In addition, in order to measure the Afterpulse probability, the mean number of photons emitted by the LED at each pulse has been set to five, as will be explained later in the Section.

A dedicated analysis software has been developed in MATLAB®to process the digitized waveforms to extract the key performance indicators of the sensors under test, as the DCR, the OCT, the AP, the Gain as a functions of the bias voltage and the breakdown voltage. The two techniques employed are the counting and the integration and their application modality will be described in detail later in this Section. The basic idea is to exploit the acquisition before the light pulse to determine the DCR and the OCT and use the second part of the time window to calculate the AP and to obtain off-line the Multi-photon spectrum. Since the data volume is of the order of Gb, the software analyzes the data event by event, i.e. considering a time window at a time.

The steps of the waveform analysis are described in detail in the following.

Waveform smoothing

A smoothing function is used to reduce noise fluctuations, which can cause errors in the pulses identification. The applied smoothing method consists in a moving average filter, that smooths data by replacing each data point with the average of the neighboring points in a defined data subset. This process is equivalent to lowpass filtering and can be mathematically described by the following equation:

$$y_s(i) = \frac{1}{2N+1}(y(i+N) + y(i+N-1) + ... + y(i-N)) \qquad (3.1)$$

where $y_s(i)$ is the smoothed value for the i-th data point, N is the number of neighboring data points on either side of $y_s(i)$, and $2N+1$ is the total number of points considered in the subset [65].

In spite of its simplicity, the moving average filter is optimal for reducing random noise while retaining a sharp step response. This makes it the premier and most common used filter in the time domain. In fact, since the noise is random, each of the point is just as noisy as its neighbor. Therefore, it is useless to give preferential treatment to any of the points by assigning a different weighting factor; as a result, the lowest noise is obtained when all the input samples are treated equally [66].

The smoothing outcome is shown in Figure 3.1, where a moving average filter with a subset of 6 points is applied to an exemplary simulated waveform event. It can be noticed that the noise fluctuations clearly decrease and, as a side effect, the peak amplitude is obviously reduced by the averaging procedure.
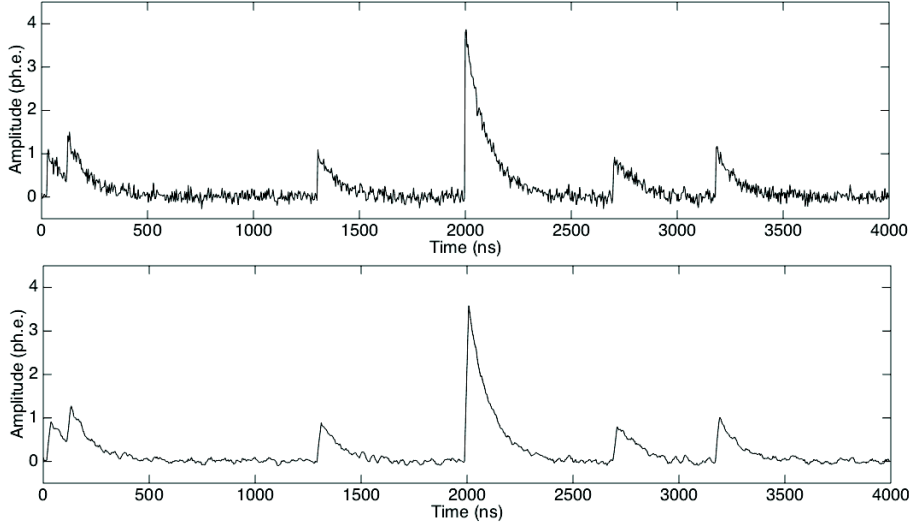
Figure 3.1: A waveform event is shown on the top plot and on the bottom plot a smoothing has been applied. Data refers to a simulation with a mean of 5 photons per signal pulse, 500 kHz of DCR and 10% of OCT and AP.

Waveform filtering

The core of the software analysis lies in a second filtering stage which is applied to the smoothed data in order to reduce the pulse time development and simplify the identification of pulse occurrences. The implemented filtering technique is based on zero-pole cancellation.

Originally, the zero-pole cancellation was a circuit used to get rid of the signal overshoot, as explained in Figure 3.2 [67]. In fact, when an exponentially decaying signal is processed by a CR differentiator, the circuit will no longer produce a strictly unipolar response but the signal will be characterized by a zero crossover. This undershoot recovers back to the baseline with the long time constant of the input signal. At count rates higher than the signal recovery time, a substantial fraction of the input pulses arrives during this period of time and will be superimposed on the undershoot. The measured pulse amplitude for these pile-up pulses will be significantly lower, deteriorating the energy resolution. The pole-zero cancellation describes a technique in which the network is modified by adding a resistance R_1 in parallel with a capacitor C to restore the simple exponential output without undershoot. The benefit of pole-zero cancellation is an improved peak shaping and a better resolution in the energy spectrum at high counting rates. The R_1 value is critical for the exact pole-zero adjustment and can be determined by the circuit analysis in terms of Laplace transformation [68].

The exponential input signal can be expressed as:

$$v_{in}(s) = \frac{v_0}{s + \frac{1}{\tau}},$$
(3.2)

where s is the Laplace variable, v_0 is the pulse amplitude and τ its decay constant. The response of the differentiator circuit to this pulse can be written as follows:

$$v_{out}(s) = \frac{1}{s + \frac{1}{CR_2}} \cdot \frac{v_0}{s + \frac{1}{\tau}}.$$
(3.3)

The presence of two poles in the denominator implies that it can not represent a simple exponential decay. The introduction of a resistance in the circuit corresponds to a zero in the Laplace transformation:

$$v_{out}(s) = \frac{s + \frac{1}{CR_1}}{s + \frac{1}{CR_1} + \frac{1}{CR_2}} \cdot \frac{v_0}{s + \frac{1}{\tau}}.$$
(3.4)

In order to use the zero to cancel a pole and ensure a simple exponential decay output, $CR_1 = \tau$:

$$v_{out}(s) = \frac{v_0}{s + \frac{1}{CR_1} + \frac{1}{CR_2}}.$$
(3.5)
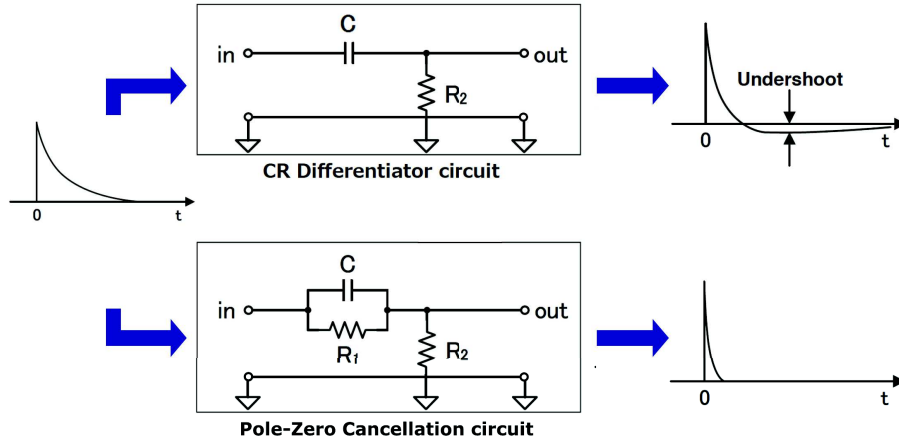
Figure 3.2: An exponential signal is applied to a CR circuit and the output pulse exhibits an undershoot. If a resistance is added in parallel to the capacitance, creating a zero-pole cancellation circuit, the output is a simple exponential decay.

As a result, the net effect of the zero-pole cancellation circuit is the changing of the exponential signal decay constant. This is the main reason that makes this type of filter suitable for the current analysis [68]. In this case the zero-pole cancellation is implemented offline by applying to every sampled point of the waveform the *zpk* MATLAB®function [69], a discrete transfer function in which the zeros, the poles and the gain can be defined by the user. This parameters are mainly related to the time decay constant of the signal, specific of each sensor.

The effect of this filter applied to simulated data is shown in Figure 3.3: the pulses are transformed into delta-like signals of a few nanosecond of duration and the input area information is preserved through a linear correspondence with the output pulse amplitude. In fact, is it possible to notice that the filter accentuates the pulse separation and in case of pile-up events it assigned them an amplitude taking into account their superposition. As a consequence, the filter simplifies the identification of the SiPM avalanches in the waveforms and reduces the pile-up by restoring the pulse correct amplitude.
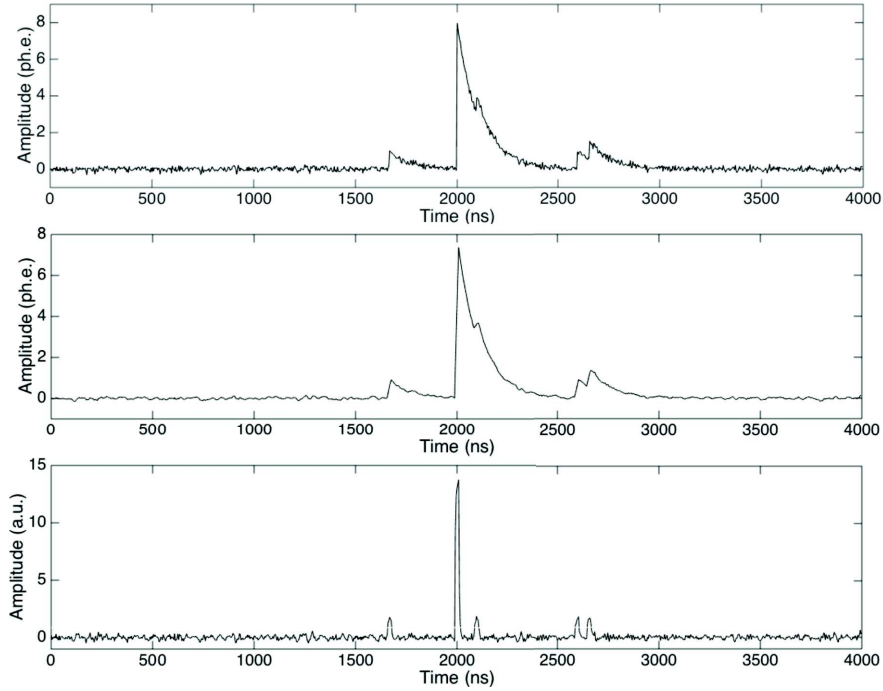
Figure 3.3: An example of the application of the zero-pole cancellation to a waveform event: the top plot is the raw acquired signal, the smoothed data is shown in the middle, while the effect of the *zpk* filter is illustrated in the bottom one. Data refers to a simulation with a mean of 5 photons per signal pulse, 500 kHz of DCR and 10% of OCT and 10% of AP.

Gate definitions

For every trigger, synchronous to the LED pulse, the waveform is recorded over a 4000 ns time window. The LED light pulse occurs at the centre of the waveform. All the relevant quantities are calculated referring to a set of specific time windows (gates) covering almost all the waveform duration.

The first gate, indicated as Δt_{dark}, starts at the the beginning of the digitization window and lasts for 1.8 μs, ending near the light pulse arrival. It is characterized by the presence of DCR pulses, which have a certain probability to produce OCT and AP discharges related both to the primary thermic pulses and to the secondary optical induced pulses. Informations retrieved within this

gate are used to measure the DCR and the OCT, and the technique developed to disentangle the various measurements is explained in the following.

Then, just after the Δt_{dark} gate and before the trigger, a second gate of about 100 ns, denoted as Δt_{pre}, is opened. This time interval is used to calculate the signal baseline if no pulses are present.

Due to the stochastic nature of the light source and of the detection mechanism, there is a probability to end up with a zero photon signal. A very small gate $\Delta t_{trigger}$ of 40 ns is set around the position of the trigger signal to determine if at least one photon emitted by the LED has been detected by the SiPM. Its duration is short enough to presume the occurring probability of a DCR or AP event to be negligible.

Together with the $\Delta t_{trigger}$ gate, the Δt_{signal} time window starts. This gate has a duration of the order of 3 times the signal decay constant, which is specific of each sensor. This gate is used to integrate the LED signal, allowing the offline reconstruction of the Multi-photon spectrum.

Finally, also the Δt_{ap} gate is synchronous with these last two time windows. It lasts for 1.8 μs and is used to measure the AP probability. In this region of the waveform it is possible to find the light signal, which can originate OCT pulses and AP pulses correspondent both to the signal itself or to its OCT pulses, in addition to the DCR contribution with its secondary effects. The detail method applied to obtain the AP from this waveform analysis is described later.

A pictorial explanation of the gate definitions is illustrated in Figure 3.4 for a typical simulated waveform.
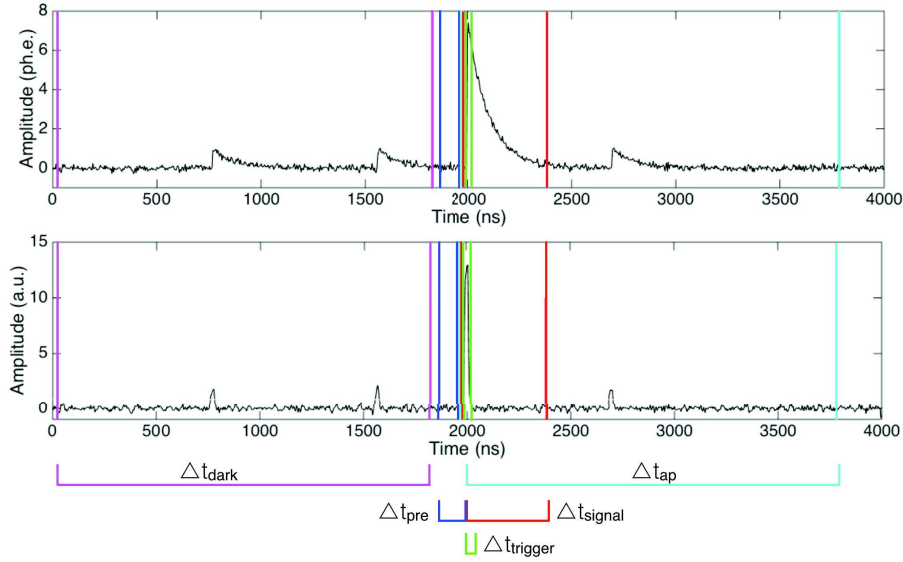
Figure 3.4: The colored lines corresponds to the different gate edges: Δt_{dark} gate in pink, the Δt_{pre} gate in blue, the $\Delta t_{trigger}$ gate in green, the Δt_{signal} in red and the Δt_{ap} in light blue.

DCR measurement

Dark Count Rate can be measured by counting the pulses in the Δt_{dark} gate shown in Figure 3.4.

A counting algorithm has been implemented to identify the pulses that after the smoothing and the zero-pole filtering have a consecutive number of data points exceeding a fixed threshold. The threshold is expressed in unit of baseline standard deviation σ_{th}. The distribution of the standard deviation of the filtered data in the Δt_{dark} gate is characterized by the presence of few peaks correspondent to standard deviation calculated in time intervals with zero pulses, one pulse and so on. The σ_{th} is determined by the mean value of the Gaussian fit of the first peak, as shown in Figure 3.5. The requirement of three consecutive data points above a threshold value correspondent to $5\sigma_{th}$ makes the counting algorithm robust, efficient in pulses identification and reduces to a negligible level the probability to confuse a mere baseline fluctuation with a pulse (algorithm purity).
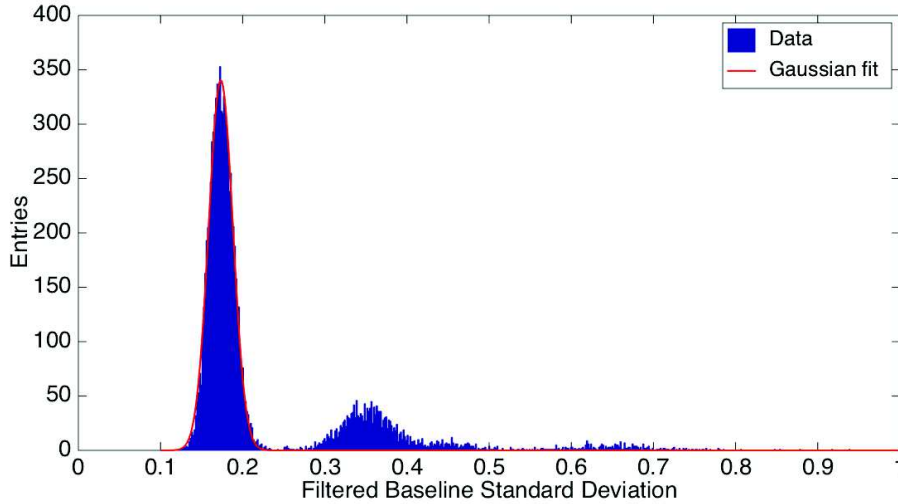
Figure 3.5: The distribution of the filtered baseline standard deviation in the Δt_{dark} gate. The first peak corresponds to events with no pulses and its Gaussian fit provides σ_{th} for the threshold calculation. The second peak is relative to one pulse events, the third one is due to AP with amplitude less than one photoelectron and events correspondent to two photons are in the last peak.

Considering the presence of AP in the Δt_{dark} gate, a simple counting of the number of pulses will lead to an overestimation of the sensor DCR proportional to the OCT and AP probabilities. The method developed to determine exactly the DCR is based on the assumption that the number n of the detected spurious avalanches follows a Poisson distribution (as demonstrated in Section 2.2):

$$P(k) = \frac{\mu^n}{n!} \cdot e^{-\mu}, \tag{3.6}$$

being μ the mean number of detected random pulses. The value of μ can be estimated also from the probability to record zero pulses, which is measured as the fraction of waveforms with no counts in the Δt_{dark} gate, n_0, with respect to the total number N of waveforms considered in the analysis:

$$P(0) = e^{-\mu} = \frac{n_0}{N}, \tag{3.7}$$

$$\mu = -\log\left(\frac{n_0}{N}\right). \tag{3.8}$$

As a result, the Dark Count Rate and its uncertainty can be measured as:

$$DCR = \frac{\mu}{\Delta t_{dark}} = \frac{-\log\left(\frac{n_0}{N}\right)}{\Delta t_{dark}}, \tag{3.9}$$

$$\sigma_{DCR} = \frac{1}{\Delta t_{dark}\sqrt{n_0}}, \tag{3.10}$$

where DCR results to be in Hz if Δt_{dark} is expressed in seconds. The advantage of this approach lies in its intrinsic immunity to afterpulsing contamination because the number of events without pulses is not modified by the presence of the AP associated to the DCR.

OCT measurement

The Optical Cross-Talk can be measured referring to the Δt_{dark} gate and analyzing the distribution of the recorded amplitudes corresponding to each pulse, identified with the counting algorithm above mentioned. The OCT probability and its uncertainty are estimated as:

$$\epsilon_{XT} = \frac{N_{>1.5pe}}{N_{>0.5pe}}, \tag{3.11}$$

$$\sigma_{\epsilon_{XT}} = \frac{\sigma_{N_{>1.5pe}}}{N_{>0.5pe}}, \tag{3.12}$$

where $N_{>1.5pe}$ is the number of pulses due to more than one photoelectrons and $N_{>0.5pe}$ is the total number of pulses. The approach is the same that is adopted to obtain the OCT from the staircase analysis.

In the current analysis, for each peak identified by the counting algorithm on the smoothed and filtered data in the Δt_{dark} gate, the correspondent amplitude in the smoothed data is find by taking the maximum height value of a certain number of points around the peak itself. The real pulse amplitude is then obtained by correcting for the baseline fluctuations that could increase or reduce the pulse height. The signal baseline is estimated at the signal rising edge.

However, in case of pile-up it will be more difficult to determine the exact amplitude of each peak. In addition, the probability for a superimposed pulse to be an AP is higher with respect to the probability to be a pure random event. If these pulses will be considered in the amplitude distribution, the total number of DCR events will be overestimated and, as a consequence, the OCT will be underestimated. In order to avoid this issue, the statistics is reduced

by discarding the pulses affected by the pile-up. A pulse can be considered for the OCT analysis if no other pulses occur within a following pre-defined time window. This gate is set to be long as the time development of a two photon pulse, guaranteeing not to count the majority of the AP growing on the tail of the associated DCR and OCT primary event. The effect of the veto application and of the real pulse amplitude estimation is shown in Figure 3.6.
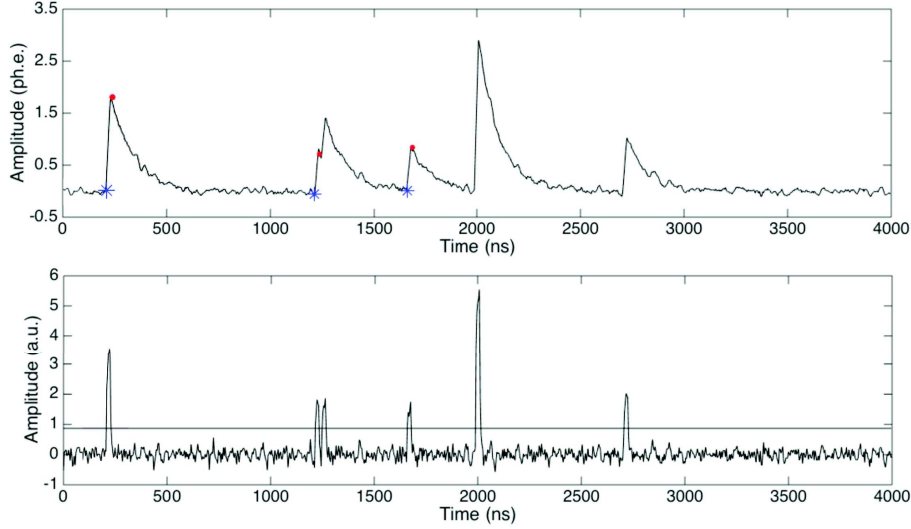
Figure 3.6: The first plot reports the smoothed waveform and the bottom one the filtered waveform. The horizontal black line is the threshold for the pulses identification. Red stars correspond the real pulse amplitudes, obtained by subtracting the pedestals represented with blue points. Pulses within the OCT veto are not taken into account for the OCT calculation.

After having analyzed all the waveform events, a distribution of the measured pulse amplitude is generated. As an exemplary illustration, the distribution of the measured pulse amplitude for the simulated waveform of reference is reported in Figure 3.7. The first and the second peak correspond to one and two photon pulses, respectively. It can be noticed that the peaks are not centered on 1 and 2 but the pulse amplitudes are slightly lower than expected because of the smoothing algorithm. The two peaks in the distribution are fitted with two gaussians to determine the mean values and the peaks distance. Then, the thresholds required in the OCT measurement to distinguish the amplitudes correspondent to one or two photoelectrons can be set at half of the two peaks distance. The OCT is finally calculated with the previous equation where $N_{>0.5pe}$ is the total number of entries of the distribution and $N_{>1.5pe}$ represent the sum of pulses whose amplitudes exceeds the threshold between the one and two photoelectrons.
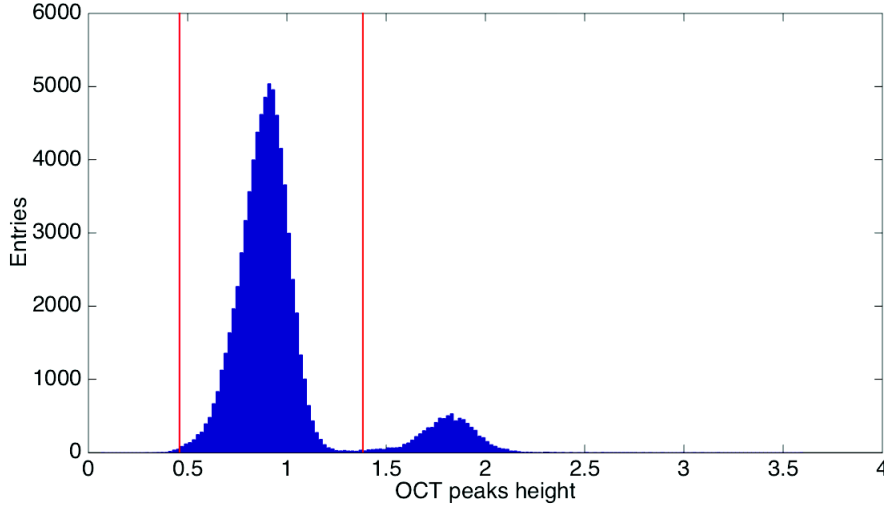
Figure 3.7: Histogram of the pulse heights in the DCR gate obtained with the reference simulation. Vertical red lines represent the thresholds to identify the one and two photoelectrons pulse amplitudes.

Offline Multi-photon spectrum

In Chapter 2 it has been explained that the Multi-photon spectrum is an important figure of merit in the SiPM characterization. Also in this analysis, based on the digitized waveforms, it is exploited to measure the sensor Gain, its dependence on the overvoltage and, as a consequence, the breakdown voltage. In addition, in the current analysis the Multi-photon spectrum is fundamental to estimate the mean number of photons emitted from the light source, which in turn is mandatory to calculate the sensor afterpulsing probability.

The Multi-photon spectrum is obtained offline by integrating each raw waveform event in a proper time window Δt_{signal} starting few nanoseconds before the trigger position and extended for three times the pulse decay constant to cover the pulse development. The histogram of the number of occurrences as a function of the area values returns the Multi-photon spectrum. The Δt_{signal} duration is sensor dependent and it is determined operationally measuring the trend of the peak-to-peak distance, supposed to increase till when the full charge is integrated. A special attention should be paid for the baseline calculation and at this purpose the Δt_{pre} gate has been introduced between the Δt_{dark} and the Δt_{signal} gates. If there are no pulses during this time interval, the mean value provides the baseline for the signal integration. In this way the correction for the baseline fluctuations can be implemented event by event. However, if a pulse of any kind occurs during the Δt_{pre} gate, the mean value would not be a proper estimate for the event baseline. To solve this problem, at the beginning of the analysis, the raw data in the Δt_{dark} gate of each waveform event are used to obtain the mean values distribution. Then, a Gaussian fit of the first peak, that corresponds to events with no pulses, allows to get the characteristics of the mean baseline. This value can be used to correct the events for which an event by event baseline determination is not possible. The result of the Multi-photon

spectrum reconstructed offline for simulated data reproducing the features of the sensors of interest is shown in Figure 3.8. It is clear that the spectrum has a significant gaussian shape underlying the individual peaks which is due to the DCR contamination. It affects the spectrum quality, resulting in a poor resolving power at peaks associated to higher photons number and possibly preventing the application of the Multi-Gaussian Fit described in Chapter 2 to infer exactly the areas underneath each peak.
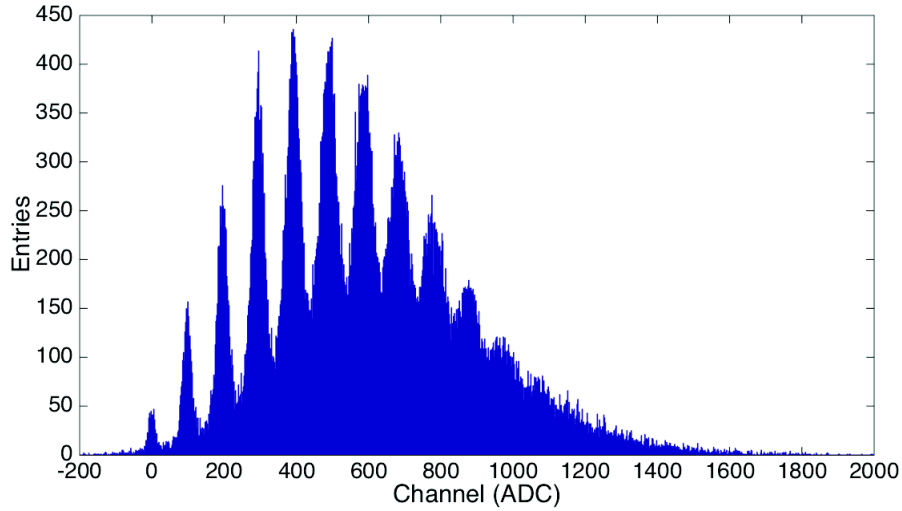
Figure 3.8: Multi-photon spectrum of simulated data with 500 kHz of DCR, 10% of AP and OCT and five mean number of emitted photons per light pulse. It has been obtained by integrating the raw waveforms in a Δt_{signal} gate of 400 ns.

To overcome this problem, pulses due to spurious avalanches and to the afterpulsing are identified and excluded from the analysis. In detail, it is required to have no pulses in the Δt_{pre} gate and it is imposed the occurrence of at most one pulse during the Δt_{signal} gate, located exactly in the $\Delta t_{trigger}$ gate to ensure that it represents the light emitted by the source. An example of acceptance and rejection criteria is reported in Figure 3.9.

The result of this procedure is shown in Figure 3.10; the Multi-photon spectrum appears to have less background contribution associated to DCR and AP and all peaks, also the ones correspondent to a high number of photons, are well resolved. Now it is possible to perform the Multi-Gaussian Fit and the result is reported in Figure 3.11. The sensor Gain can be calculated from the mean peak-to-peak distance. A scan of the Gain with respect to the sensor bias allows to assess its linearity and to calculate the breakdown voltage with an extrapolation of the bias at zero gain.

However, the MGF of this low background spectra can not provide neither an independent measurement of the sensor OCT nor the mean photon number emitted by the source. The motivation can be understand comparing the raw Multi-photon spectra with the one obtained applying the rejection criteria, as displayed in Figure 3.12. From this plot it can be inferred that the distribution modification can not be reduced to a scale factor, but depends on the peak
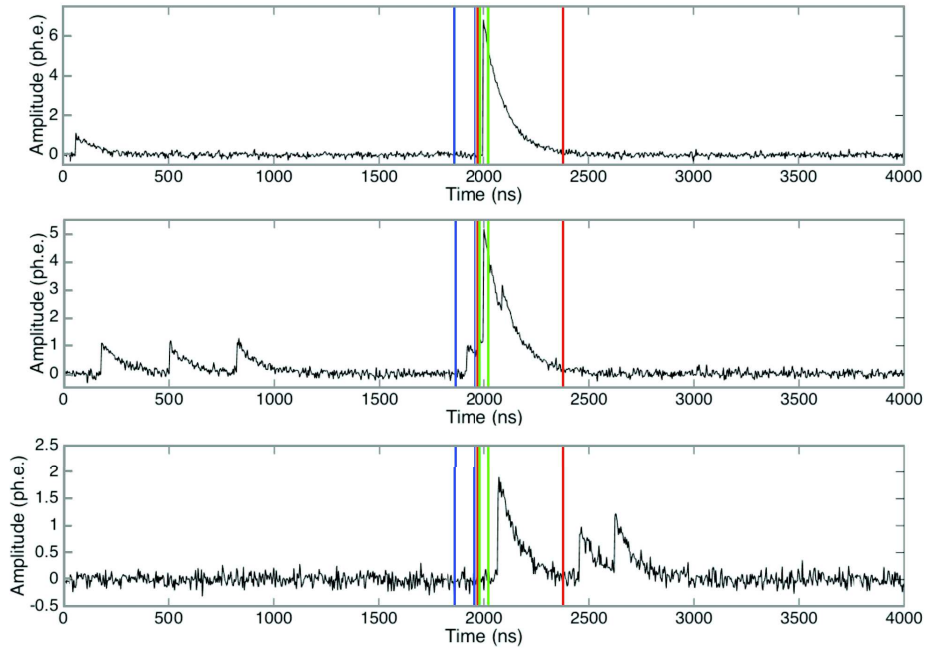
Figure 3.9: Examples from the reference simulation of accepted (first plot) and rejected (second and third plots) events in order to remove the DCR and AP contamination in the Multi-photon spectrum.
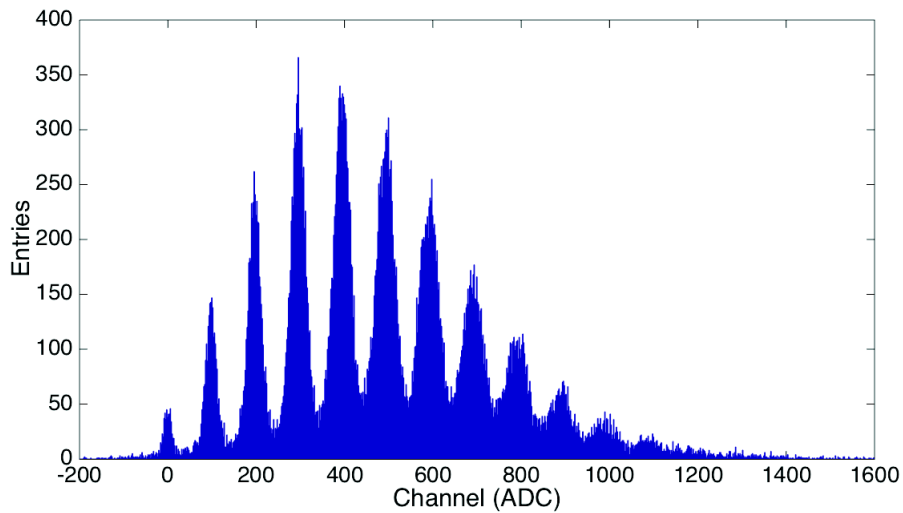
Figure 3.10: Multi-photon spectrum of simulated data with 500 kHz of DCR, 10% of AP and OCT and five mean number of emitted photons per light pulse. It has been obtained by integrating the raw waveforms in a Δt_{signal} gate of 400 ns and applying the rejection criteria described in the text.
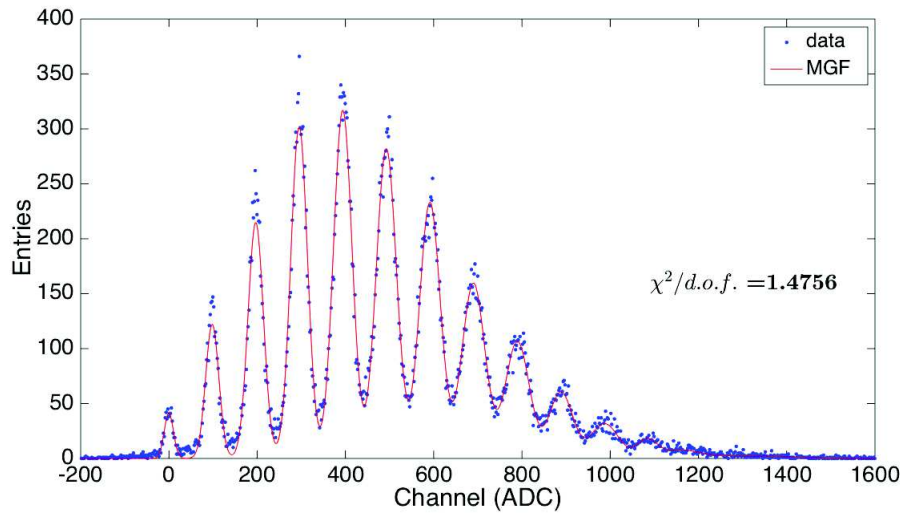
Figure 3.11: The red line represents the Multi-Gaussian fit to the Multi-photon spectrum of the reference simulation waveforms with the rejection of the DCR and AP contamination. The $\chi^2/d.o.f$ value indicates that the fit quality is good.

number. This effect is expected because the DCR is randomly distributed and affects in the same way each peak, while the AP probability depends on the number of photo-electrons in the pulse. In fact, a light pulse corresponding to an higher photon number has an higher probability to produce AP and, as a consequence, to be rejected. The net effect is a modification of the mean number of photoelectrons in the distribution.
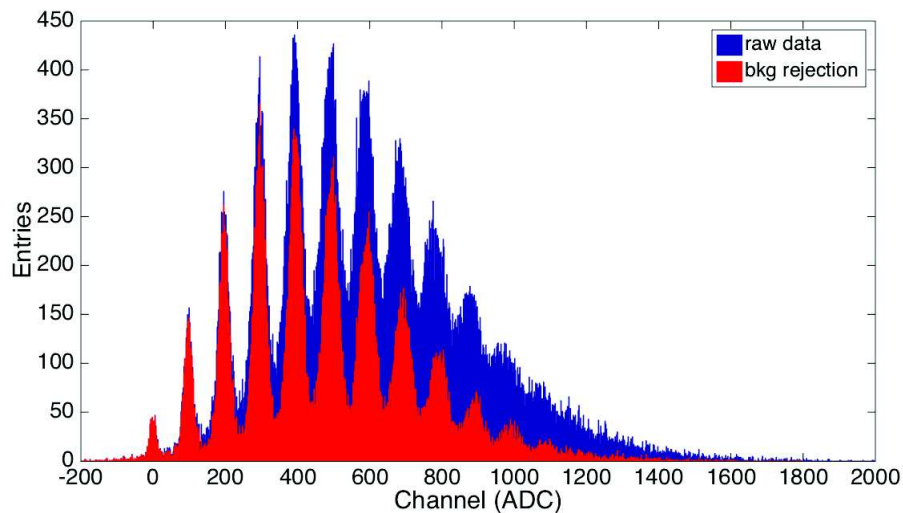
Figure 3.12: Superimposition of the reference simulation Multi-photon spectra with (red) and without (blue) the criteria to reject the background events.

In order to be more precise, the agreement of the distribution peak areas with the Compound Poisson model introduced in Chapter 2 can be investigated. Figure 3.13 shows the comparison between the areas estimated with the MGF and the Compound Poisson probability (Equation 2.7) calculated with the simulated OCT and the mean photon number determined from the zero-peak: the two data sets are clearly not consistent. As the OCT is the only possible contamination in the distribution and the validity of the Compound Poisson model has already been demonstrated, it is possible to conclude that the background rejection biases the statistical properties of the recorded photons distribution.
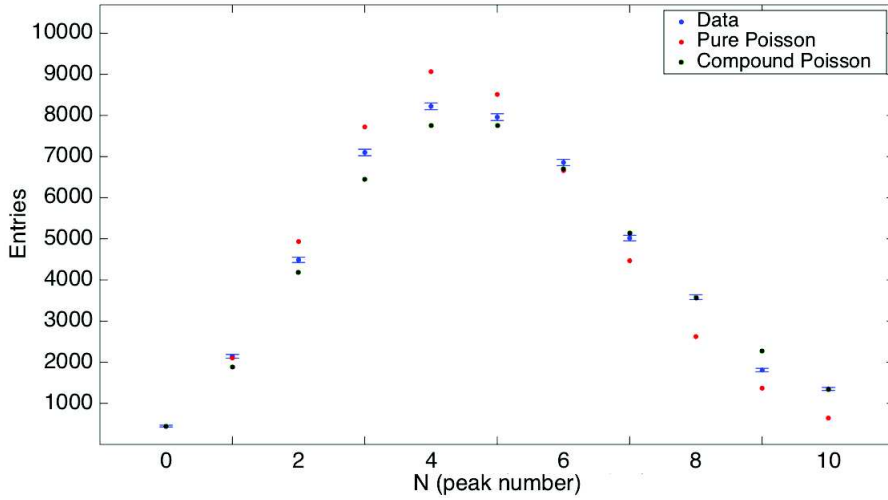
Figure 3.13: Data referring to the peak areas of the reference simulation distribution with background rejection are compared to the pure Poissonian distribution with the mean value estimated from the zero-peak and to its convolution with the geometrical distribution accounting for an OCT probability of 10%.

The problem can be solved by recovering the correct value of the zero peak area that has been modified. This can be achieved understanding the effect of the background rejection on the events with no emitted light pulses. In this case the main contribution is due to the DCR. In fact, if a random pulse occurs in the Δt_{pre} or in Δt_{signal} the event will not be accepted. Instead, if a DCR pulse takes place within the $\Delta t_{trigger}$ gate, the event is accepted but its area corresponds to one photon peak. In all cases an entry is subtracted from the zero-peak in the distribution. In order to evaluate the mean number of photoelectron exploiting the information included in the zero-peak area of the spectrum with background rejection, a correction accounting for this effect has to be applied. The probability to reject a zero photon event due to DCR is:

$$P_{DCR} = DCR \cdot (\Delta t_{pre} + \Delta t_{signal}), \tag{3.13}$$

and the total number of DCR event within that gate results to be:

$$N_{DCR} = N \cdot P_{DCR}, \tag{3.14}$$

where N represents the total number of waveform events considered. The number of DCR event that could occur in the $\Delta t_{trigger}$ gate when there is no pulse emitted by the light source is expressed as:

$$\tilde{N}_{DCR} = N_{DCR} \cdot P_0, \tag{3.15}$$

where P_0 represents the probability to detect zero photon in the light signal, measured by counting the fraction of empty $\Delta t_{trigger}$ gate. Thus, the area of the zero-peak A_0 should be corrected with this contribution and re-normalized taking into account the effects of the background rejection on the total number N of events considered:

$$\tilde{A}_0 = \frac{\tilde{N}}{N} \cdot \left(A_0 + \tilde{N}_{DCR} \right), \tag{3.16}$$

where $\tilde{N}$ is the number of accepted events. Using this information it is possible to determine correctly the pure Poissonian estimate of the mean number of photon M_{ZP} emitted by the light source, following Equation 2.11:

$$M_{ZP} = -log \left(\frac{\tilde{A}_0}{\sum_i (A_i)} \right), \tag{3.17}$$

$$\sigma_{M_{ZP}} = \sqrt{ \left(\frac{\sigma_{\tilde{A}_0}}{\tilde{A}_0} \right)^2 + \left(\frac{\sigma_{\sum_i (A_i)}}{\sum_i (A_i)} \right)^2 }, \tag{3.18}$$

where A_i indicates the i-th peak area measured with the MGF. Finally, applying Equation 2.8 and accounting for the OCT, the mean number M of fired cells can be obtained:

$$M = \frac{M_{ZP}}{1 - \epsilon_{XT}}, \tag{3.19}$$

and its uncertainty is calculated as:

$$\sigma_M = \sqrt{ \left(\frac{\sigma_{M_{ZP}}}{1 - \epsilon_{XT}} \right)^2 + \left(\frac{M_{ZP} \cdot \sigma_{\epsilon_{XT}}}{(1 - \epsilon_{XT})^2} \right)^2 }. \tag{3.20}$$

Afterpulsing measurement

The afterpulse measurement can be assessed by comparing the distribution of identified number of pulses in the Δt_{dark} gate before the light pulse and in the Δt_{ap} gate after the triggered signal. The two gates are set to the same value for the sake of simplicity and long enough to include the majority of AP. The afterpulse probability can be determined as the difference of the mean number of counts in the two gates, λ_{dark} and λ_{ap}, reduced by the probability to have a non zero signal pulse (1-P_0) and normalized to the mean number of fired cells M:

$$AP = \frac{\lambda_{ap} - \lambda_{dark} - (1 - P_0)}{M}. \tag{3.21}$$

Its uncertainty can be estimated as:

$$\sigma_{AP} = \sqrt{\left(\frac{\sigma_B}{M}\right)^2 + \left(\frac{B\sigma_M}{M^2}\right)^2}, \tag{3.22}$$

where $B = \lambda_{ap} - \lambda_{dark} - (1 - P_0)$ and $\sigma_B = \sqrt{\sigma_{\lambda_{ap}}^2 + \sigma_{\lambda_{dark}}^2 + \sigma_{P_0}^2}$.

This equation can be explained by considering the possible contributes to the pulse counting in the two gates. In the Δt_{dark} gate the pulses can be due to:

- single cell DCR,

- multiple cell dark counts, due to the DCR affected by OCT,

- afterpulses related to the single and multiple cell DCR.

As a result the mean number of identified pulses in the Δt_{dark} gate is expressed by the formula:

$$\lambda_{dark} = \mu + AP \cdot \mu + AP \cdot \epsilon_{XT} \cdot \mu, \tag{3.23}$$

where μ is the mean number of detected random pulses. Instead, the pulses in Δt_{ap} are due to:

- the light pulse, that could be affected by OCT,

- the afterpulses originated by the light pulse,

- the single and multiple cell DCR with its associated afterpulses, as occurring in the Δt_{dark} gate.

The mean number of identified pulses in Δt_{ap} is:

$$\lambda_{ap} = (1 - P_0) + AP \cdot M + \lambda_{dark}, \tag{3.24}$$

where the first term is the probability to have a non zero triggered signal, the second represents the afterpulse probability due to the mean number of fired cell (including the OCT) and the third term is the above defined mean number of pulses in the Δt_{dark} gate.

Operationally, the AP is estimated by applying Equation 3.21. The λ_i are obtained by identifying the pulses in the two gates with the counting algorithm described above, P_0 is calculated as the fraction of empty $\Delta t_{trigger}$ gates with respect to the total number of considered waveforms and M is measured with the Multi-photon spectrum and the OCT measurement.

In this case, a particular attention should be paid to the capability of the developed technique to distinguish pulses that occur very close to each other, i.e. the time resolution of the analysis counting algorithm. This can be studied by considering Figure 3.14 which represents the distribution of the time distances between the triggered light pulse and each of the following pulses. In the range of 40-800 ns the dominant component is due to the Afterpulsing effect, seen as a decreasing exponential distribution. When the afterpulse probability becomes negligible, the DCR contribute produces a flat distribution. It is also possible to

notice that the counting algorithm is not able to identify pulses at a distance from the light signal lower than 15 ns. In addition, from the smooth rising of the distribution it can be concluded that the efficiency in the discrimination of pulses with arrival time below 40 ns is quite low, clearly resulting in an underestimation of the mean number of detected pulse in both gates.
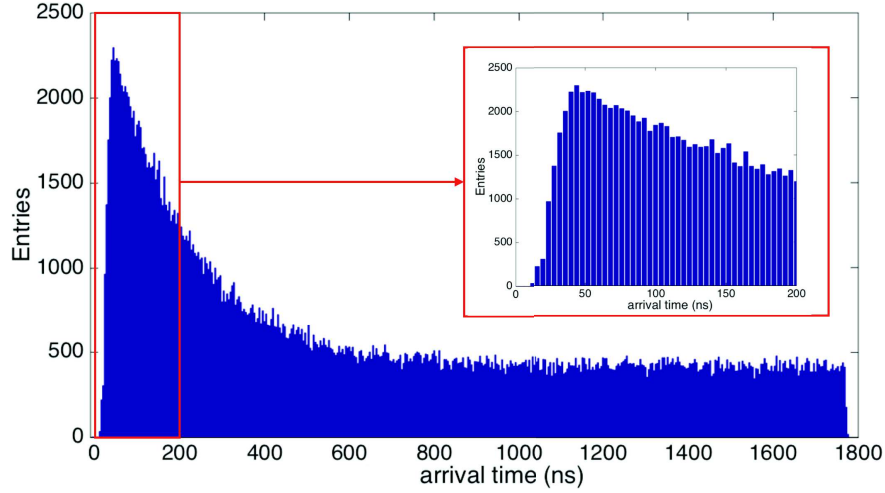
Figure 3.14: Arrival time distribution between the light signal and the following pulses in the Δt_{ap} gate. The zoom in the 0-200 ns region of the distribution shows the inefficiency in resolving pulses with a time distance lower than 40 ns.

This issue is overcome by considering the inter-arrival time distributions of the identified pulses in the two gates, shown in Figure 3.15. These distributions come from a complex interplay of DCR and AP contributions, whose description is out of the scope of this thesis. Heuristically, they can be adequately described by the superposition of two exponential functions. The number of pulses lost in each gate because of the counting inefficiency at small inter-time distances can be inferred by comparing the areas of the fit functions below 40 ns with the number of pulses identified with 40 ns inter-time. Then the mean number of events λ_{dark} and λ_{ap} are corrected for these factors and the AP can be calculated by applying the Equation (3.21).
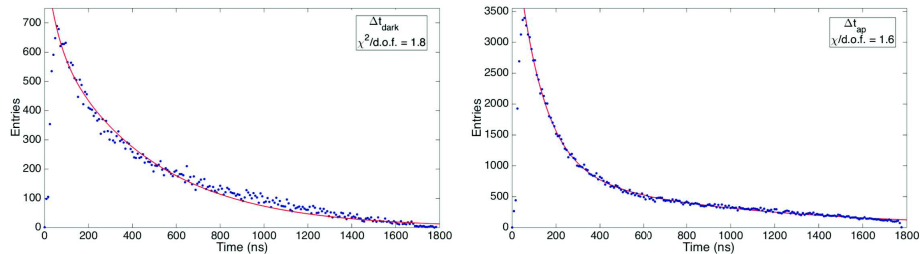
Figure 3.15: Inter-arrival time distributions in the Δt_{dark} and Δt_{ap}. The counting inefficiency below 40 ns is recovered using the area of the fit functions.

3.2 Analysis validation

Simulation

The analysis proposed has been qualified relying on a simulation developed to model the response of a SiPM to a LED light source. It consists of a simplified and fast simulation reproducing the waveforms recorded with a digitizer [70].

The first step is based on the geometrical description of the SiPM, with the possibility to select the sensor dimensions and the pixel pitch. Then, the number of photons impinging on the SiPM is generated event by event according to a Poisson distribution with a user defined mean value. The position of each photon inside the sensor is randomly chosen according to a uniform distribution. The number of fired cells is obtained assigning to each emitted photon a certain probability to be detected (the sensor PDE). In addition, a control ensures that if a cell has been hit more than once, the number of detected photons is not increased. Then, at each detected photon is associated an OCT probability, following the geometric distribution described in Section 2.2 and resulting in the possibility to create an infinite single chain of pulses. If the generation of an OCT event occurs, its position is limited to the neighboring cells of the primary pulse. Also in this case it is controlled if the selected cell has been already fired.

The second step of the simulation generates the waveform event by event by a over-imposition of pulses. Each pulse is obtained as a combination of two exponentials: one has a very short time constant to describe the signal rise time and the other accounts for the signal decay according to the sensor falling time. The mathematical expression for the signal time development is the following:

$$y(t) = A \cdot [e^{(-\frac{t}{\tau_{fall}})} - e^{(-\frac{t}{\tau_{rise}})}], \tag{3.25}$$

where A is the signal amplitude. A Gaussian spread in the signal amplitude has been considered to account for a cell to cell gain variation. Event by event, a time window is created and a signal with the amplitude determined by the number of fired cells is generated in correspondence of the trigger position.

Then the DCR contribution is added to the waveform. First, the number of spurious pulses in each event is obtained from a Poisson distribution with a mean value correspondent to the DCR chosen by the user. The time distance between two random pulses follows an exponential distribution with a time constant equals to the inverse of the DCR. This allows to have the number of pulses in each window randomly distributed in time.The DCR signal is considered to be generated by a photon, but the effect of the OCT is taken into account and can modify the pulse amplitude.

The last element introduced is the AP, associated to the light signal and to the DCR pulses, both including the OCT. For each fired cell the probability to have an afterpulse is evaluated, together with its position, which follows an exponential distribution with two time constant τ_{apf} and τ_{aps} for the fast and the slow afterpulse component, respectively. The amplitude of the AP depends on its time occurrence since it is related to the single cell recovery time, as explained in Chapter 1.

The last part comprehends the simulation of the digitization. The waveform is sampled and a white noise with a frequency below the sampling one is added in the form of a Gaussian spread on each waveform point.

The simulation parameters have been choosen in order to reproduce a waveform event very similar to the SiPM signal displayed at the oscilloscope. The robustness and the reliability of the analysis software is verified simulating different combinations of DCR, OCT, AP and mean number of emitted photons. The different settings are reported in Table 3.2.

Geometric parameters	
Sensor area	6×6 mm^2
Pixel pitch	50 μm
Physical parameters	
Mean emitted photons	8, 10
PDE	50%
DCR	0, 300, 500, 800 kHz
OCT	2, 5, 8, 10%
AP	0, 2, 5, 8, 10%
Signal parameters	
Signal rise constant	4 ns
Signal decay constant	100 ns
AP arrival constant	180 ns
Cell to cell gain variation	
Waveform parameters	
Events number	100000
Time window	4 μs
Time sampling	4 ns
Noise frequency	
Noise spread	

Table 3.1: Simulation parameter to reproduce the SiPM waveform events.

Method qualification

Pulse identification efficiency and purity

The first figure of merit used to qualify the analysis procedure is the pulse identification efficiency and purity. Comparing event by event the positions of the simulated pulses and the ones determined with the algorithm is possible to establish if there is a positive matching for each pulse. The pulse identification efficiency is defined as the fraction of matching pulses with respect to the total number of simulated ones. The purity refers instead to the capability to detect real pulses; in fact it can be calculated as the probability of having pulses correlated to simulated one normalized to the total number of identified pulses. This qualification has been performed for all the settings shown in Table 3.2, using all the pulses identified in the whole acquisition window and measuring an efficiency of about 93% and a purity of about 99%, respectively. In particular, the efficiency is about 95% if only the Δt_{dark} gate is considered, while it becomes

91% for the Δt_{ap} gate. This means that in general, in the Δt_{dark} gate is easier to identify the pulses because the mean number of events is lower. The AP, due to the fact that their distribution is concentrated near to the primary pulse, favor the pulse identification inefficiency. In addition, their contribute has a major impact in the Δt_{ap} gate, since it depends on the pulse amplitude. The fact that the purity is so high means that the threshold setting ensures a very low contamination of baseline fluctuations to the total number of detected pulses. In addition, its value is quite constant in all the gates of the acquisition windows, confirming the robustness of the method employed to choose the threshold.

Pulse decay time

A second validation check consists in the measurement of the simulated pulse decay time τ_{fall} from the reconstructed Multi-photon spectrum. In fact, the integral of a non normalized exponential decay function during an infinite time window is equal to:

$$\int_0^\infty A \cdot e^{(-t/\tau)} \mathrm{d}t = A \cdot \tau. \tag{3.26}$$

In the simulation and also in the measurements the integration gate can not be infinite, but it corresponds to 4τ, which represents the 98.2% of pulse time development. As a result, the distance between two consecutive peaks in the Multi-photon spectrum is expected to be exactly the 98.2% of the simulated τ_{fall} of 100 ns. The pulse area during Δt_{signal} gate is obtained by summing the pulse amplitudes of each sampling point and multiplying by the 4 ns of the sampling rate. The mean value of the peak to peak distances obtained from the MGF results to be 98.6 $\pm$ 0.2 ns, compatible with the expected value of 98.2 ns.

Pulse arrival time distribution

Another control is represented by the analysis of the arrival time distribution in the Δt_{ap}. In fact, as explained in the previous section and shown in Figure 3.14, it has an exponential decay component due to the afterpulsing effect plus a flat component caused by DCR contribution. The distribution obtained from the simulation is fitted with the following function:

$$y = a \cdot e^{-bx} + c, \tag{3.27}$$

and the resulting fit function is shown in Figure 3.16. The value of fit parameters are reported in Table 3.2. In particular, the time constant describing the arrival of AP event with respect to the light pulse is determined as $\tau = 1/b$, and results to be of 184.1 $\pm$ 2.2 ns, within a C.L. of about two standard deviation from the simulated value of 180 ns. The constant parameter indicates that there are 207 $\pm$ 3 mean number of pulses occurred in 4 ns, which can be translated in 517 $\pm$ 8 kHz considering that 100000 events have been considered. The result is in agreement with the simulated value od 500 kHz for the DCR.
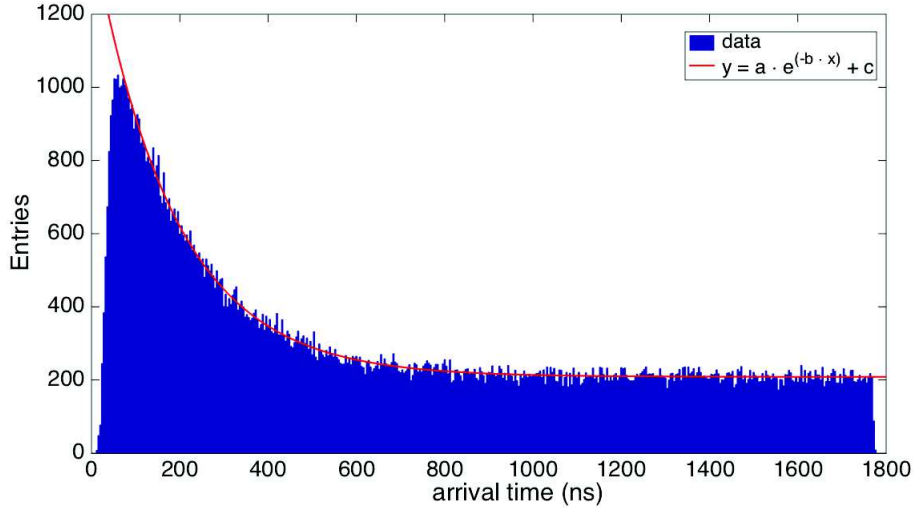
Figure 3.16: The arrival distribution Δt_{ap} fitted with a combination of an exponential and a constant functions to account for the AP and DCR contributions. The $\chi^2/d.o.f. = 0.97$ confirms the good fit quality.

Fit parameter	Result value
a	1220 ± 16
b	$(5.43 \pm 0.06) \cdot 10^{-3}$
c	207 ± 3

Table 3.2: Fit parameters and result values of the function fitting the distribution of the events arrival time in Δt_{ap}.

DCR, OCT, M and AP

The validation of the method to determine all the SiPM features is assessed by applying the analysis to the simulated waveform events with DCR values of 0 kHz, 300 kHz, 500 kHz and 800 kHz, generated keeping the AP and OCT contributions at 5%. In addition, for 500 kHz of DCR different combinations of AP and OCT have been generated: 10% of both AP and OCT probabilities, 0% AP with 10% OCT, 2% and 8% of AP combined with a 5% of OCT probability, and finally 2% and 8% of OCT combined with a 5% of AP probability.

Table 3.3 shows that the DCR resulting from the application of the characterization procedure on the simulated waveforms are consistent within one standard deviation with the simulated DCR values. In the case of 500 kHz the range of results refers to the values obtained with the various simulations with the same DCR but different combinations of OCT and AP.

The same test is performed for the OCT: Table 3.4 summarizes the analysis results compared to the simulated values. Also in this case the agreement between measured and generated OCT ensures the validity of the waveform analysis. As before, the ranges of values in the case of 5% and 10% are due to the availability of different simulations with the same OCT.

DCR	
Simulated value	Analysis result
0 kHz	0 ± 2 kHz
300 kHz	299 ± 2 kHz
500 kHz	$498\text{-}504 \pm 3$ kHz
800 kHz	799 ± 4 kHz

Table 3.3: Comparison between different simulated DCR and the results from the waveform analysis. The agreement is within one standard deviation.

OCT	
Simulated value	Analysis result
2%	$2.2 \pm 0.4\%$
5%	$5.0 - 5.4 \pm 0.4\%$
8%	$8.0 \pm 0.3\%$
10%	$9.9 - 10.0 \pm 0.3\%$

Table 3.4: Comparison between different simulated OCT and the results from the waveform analysis. The agreement is within one standard deviation.

A further check has been performed comparing between the simulated mean number of impinging (M_{ZP}) and detected (M) photons with the analysis results. Table 3.5 reports the simulated values of the mean number of impinging photons and the ones obtained applying Equation 3.17 to the Multi-photon spectrum, and a good agreement is observed.

M_{ZP}	
Simulated value	Analysis results
5	5.00 ± 0.04
4	3.97 ± 0.03

Table 3.5: The simulated number of impinging photons and the results from the waveform analysis are in agreement within one standard deviation.

Table 3.6 summarizes the results for the mean number of detected photons: the values obtained by correcting M for the OCT contribution, as in Equation 3.19, are consistent with the simulated ones.

M	
Simulated value	Analysis results
5.55	5.49 ± 0.05
5.26	5.29 ± 0.05
4.45	4.41 ± 0.04

Table 3.6: The simulated number of detected photons and the results from the waveform analysis are in agreement within one standard deviation.

In both cases the values refer to the reference simulation. These positive results confirm that the background rejection of the Multi-photon spectrum has been done adequately, ensure that the Multi-gaussian fit of the final spectrum describes well the peak areas and validate the application of the correction accounting for the background rejection on the zero-peak area.

The last simulation parameter that has to be controlled is the AP. In order to verify in detail the characterization procedure, each quantity appearing in Equation (3.21) has been controlled. Considering that P_0 can be expressed as $e^{-M_{ZP}}$, applying the Poisson statistics, the analysis results for both M_{ZP} and M have already been compared with the simulated values, with a positive outcome. The values calculated from the simulation input parameters and the results of the characterization procedure for the λ_{dark} and the λ_{ap} parameters, already corrected for the counting inefficiency below 40 ns of inter-arrival time, are reported in Table 3.7.

| AP | λ_{dark} | | λ_{ap} | |
	Simulated value	Analysis results	Simulated value	Analysis results
0%	0.900	0.895±0.003	1.893	1.889±0.006
2%	0.921	0.925±0.003	2.019	2.012±0.006
5%	0.953	0.948±0.003	2.209	2.200±0.006
8%	0.984	0.963±0.004	2.399	2.393±0.006
10%	1.011	0.993±0.005	2.560	2.579±0.008

Table 3.7: Comparison between the simulated values and the results from the application of the characterization procedure to the waveform data for the λ_{dark} and λ_{ap} parameters for different values of AP.

From their comparison it can be inferred that the analysis outcome is consistent to the expected value within two standard deviations, except for the λ_{dark} correspondent to the simulated AP of 8% and 10%. A "low level" analysis of the mean values of λ_{dark} for the 8% and 10% data set calculated using only the pure temporal information of the generated pulses before introducing the time development and the digitization process, result to be 0.963±0.003 and 0.995±0.003, respectively. This means that the problem lies in the data set and not in the analysis procedure.

The origin of the disagreement of the resulting values with respect to the expected ones can be explained by considering Figure 3.17, showing the temporal arrival of the afterpulse for the raw simulated data. The peak at 2000 ns with the exponential decay corresponds to the AP related to the signal pulses, while the flat component represents the AP of the DCR pulses, randomly distributed in time. However, it is possible to see that in the first region of the distribution some pulses are missing. This is due to the way the AP is implemented in the simulation: the AP can only follow a DCR pulses taking place in Δt_{dark}. In other words, the AP related to DCR occurring previous than Δt_{dark} could not be taken into account, resulting in a loss of AP events in the Δt_{dark} region of the distribution. This effect has clearly an impact on the mean number of events calculated in the Δt_{dark} gate at high value of simulated AP. In order to correct for this issue, the two simulations with high AP has been generated
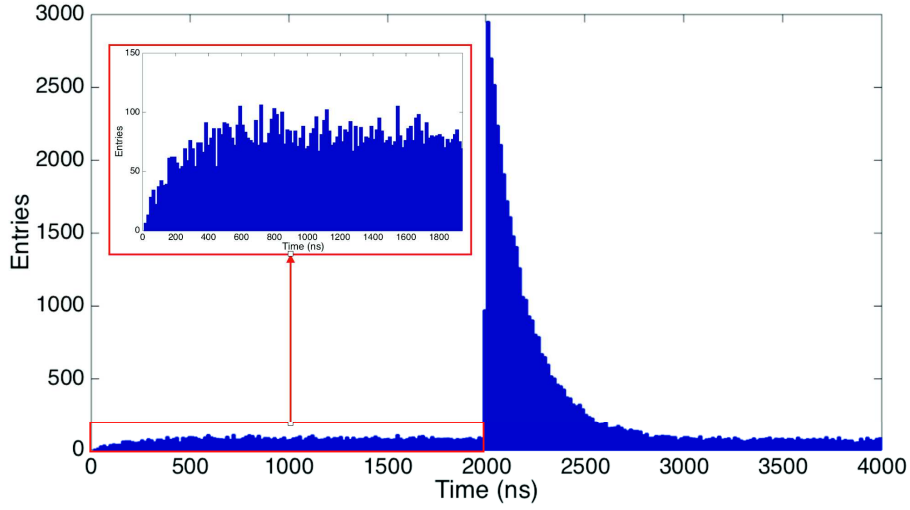
Figure 3.17: The simulated AP time position for the raw data, with a zoom on the Δt_{dark} region. The peak with exponential decay represents the AP correlated to the signal, while the flat contribution is due to the AP of the DCR pulses. A loss of events can be noticed in the first region of the time distribution.

with additional 2000 ns before the Δt_{dark} gate and the waveform analysis has been applied as usual. The measured λ_{dark} values result to be 0.971±0.005 and 1.003±0.005, for the data set with 8% and 10% of AP, respectively, and are in agreement with the expected simulated values. The result allows to affirm that the loss of information of AP related to pulses occurred in the 'past' with respect the acquisition window is the only reason of the underestimation of the λ_{dark}. Fortunately, this issue affects only the simulated data set, while the experimental ones are intrinsically immune to this effect.

Finally, coming back to a "high level" analysis, the AP can be calculated and the values are reported in Table 3.8 for the different data sets. The results obtained with the analysis procedure are in agreement with the simulated values in all cases. This confirms the validity of the characterization procedure for the AP determination and the reliability of the correction method for the inefficiency of the pulse identification with inter-arrival time below 40 ns.

AP	
Simulated value	Analysis results
0%	$0.02 \pm 0.07\%$
2%	$1.9 \pm 0.1\%$
5%	$4.9 \pm 0.2\%$
8%	$8.0 \pm 0.2\%$
10%	$10.6 \pm 0.3\%$

Table 3.8: Comparison between simulated AP values and the analysis results: the agreement is within two standard deviation.

3.3 Results and discussion

After the validation of the waveform analysis, real data are analyzed. The procedure is applied to characterize sensors of different area by various producers, namely: an Hamamatsu 1×1 mm² (S10362-11-050C), an Hamamatsu 1.3×1.3 mm² (S13360-1350CS), an Hamamatsu 2×2 mm² (S13360-2050VE), an Hamamatsu 6×6 mm² (S13083-050CS), a SensL 6×6 mm² (MicroSC 60035-X13) and an Excelitas 6×6 mm² (C30742-66).

The first three sensors can be characterized s well with the standard method since they have a low noise. As an examplary illustration, the behavior of the Gain, the DCR and the OCT as a function of the bias voltage for the Hamamatsu 1.3×1.3 mm² sensor obtained with the two characterization methods are reported. The results of the two analysis methods are compatible.

The results of the other two sensors will be summarized in Chapter 7, as they have been tested for the EasyPET application.

Figure 3.18 shows the Gain versus the bias voltage, calculated from the Multi-Photon spectrum by online and offline charge integration methods. The linear dependences are consistent and also the extrapolated value of the breakdown voltage is in agreement: it is 51.30 ± 0.05 V for the online spectrum and 51.26 ± 0.05 V for the offline spectrum.

The comparison between the DCR and the OCT determined with staircase analysis and the waveform post-processing analysis shown in Figures 3.19 and 3.20 confirms the validity of the characterization method. In addition, the latter allows the determination of the afterpulse probability, which is at the level of 0.5% with a very little dependence on the bias voltage.
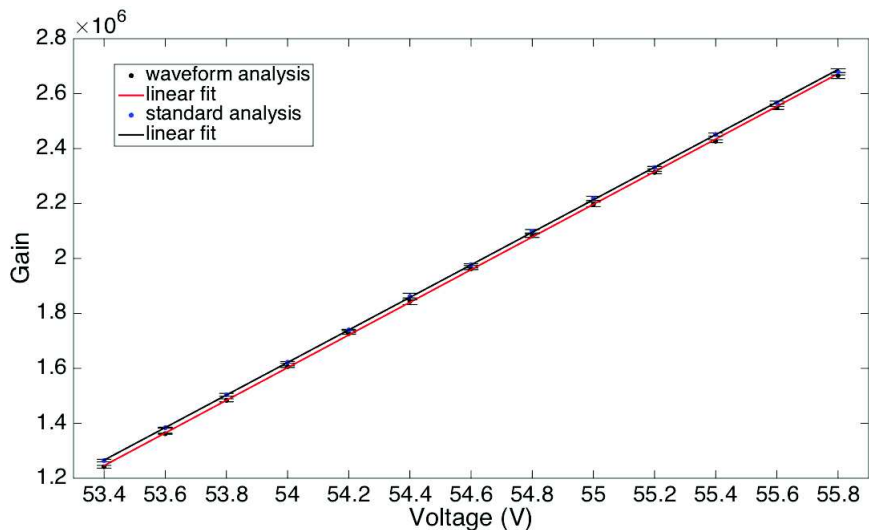
Figure 3.18: The Gain versus the bias voltage for the waveform analysis (blu points) and the standard analysis (black points) with the respective linear fit (black and red straight lines).
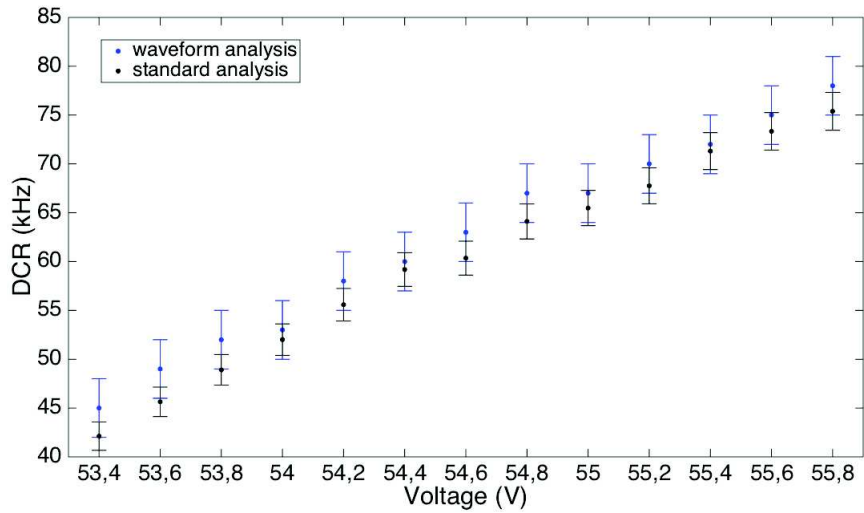
Figure 3.19: The DCR versus the bias voltage for the waveform analysis (blu points) and the standard analysis (black points).
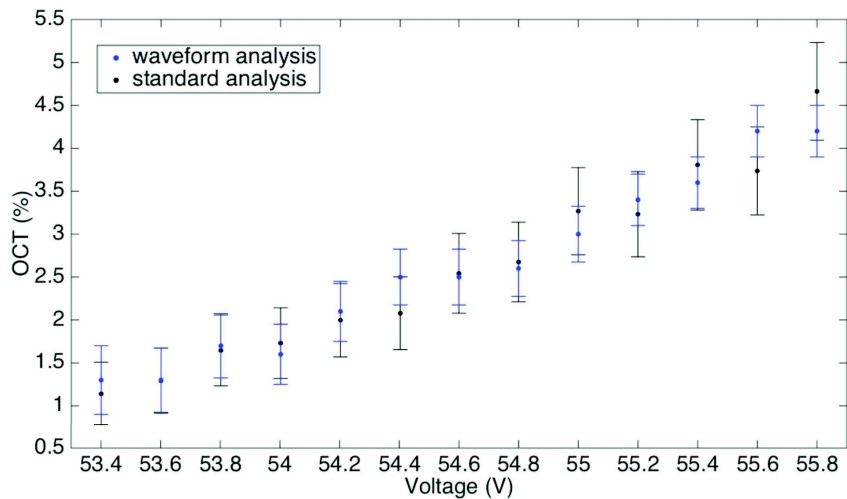
Figure 3.20: The OCT versus the bias voltage for the waveform analysis (blu points) and the standard analysis (black points).

The three sensors with the larger area can only be characterized through the waveform analysis. The information available on the data-sheets are incomplete: the characterization results can not be compared with a reference and can be used to predict all the sensor features. Figure 3.21 show some exemplary waveform events from the three sensors: it is clear that the DCR is very high and limits the application of the standard characterization method.

Figure 3.22 reports the Gain as a function of the Over-voltage. First, the peak-to peak distance has been determined from the Multi-Photon spectra

obtained integrating the signal with a gate of 320 ns for the Hamamatsu, of 500 ns for the SensL and 270 ns for the Excelitas. Then, by fitting the data points with three straight lines, the breakdown voltages result to be 52.2 ± 0.1 V for the Hamamatsu, 24.4 ± 0.1 V for the SensL and 95.5 ± 0.1 V for the Excelitas. The over-voltage can now be calculated and, applying the Equation (2.2), the Gain is determined. The sensor that features the higher gain in the SensL: at 3.5 V of over-voltage the SensL reaches a gain of $2.1 \cdot 10^6$, while the Hamamatsu has a gain of $1.6 \cdot 10^6$ and the Excelitas features a gain of $1.3 \cdot 10^6$.
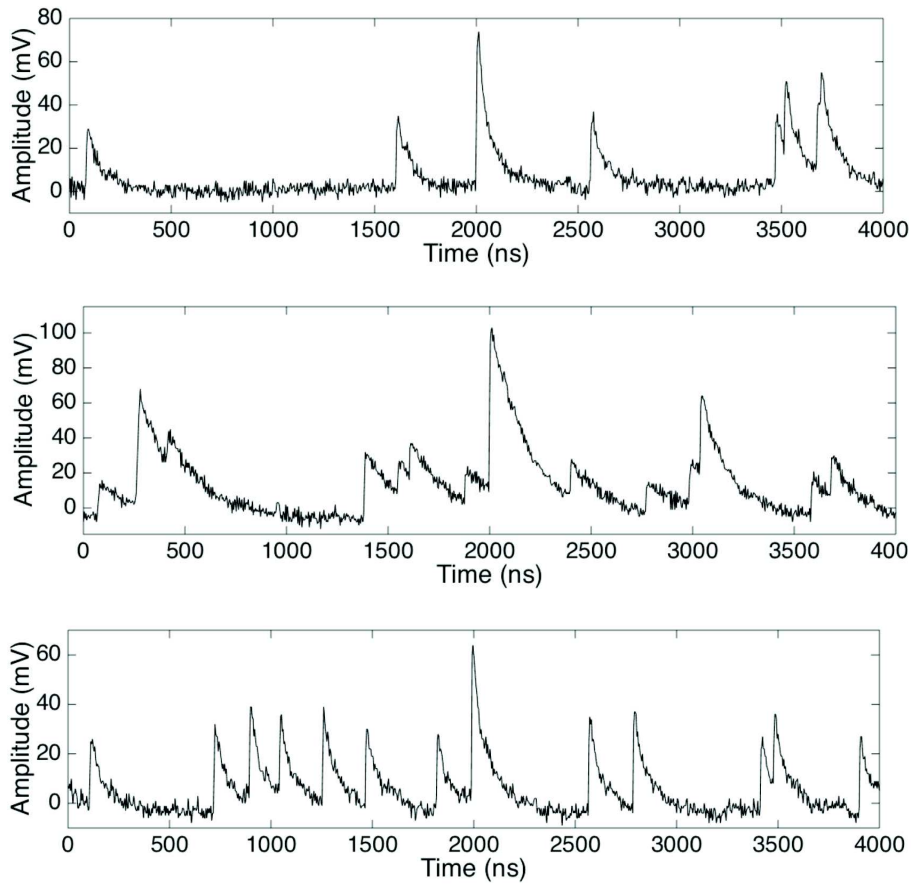
Figure 3.21: Exemplary waveforms from the S13083-050CS, the 60035-X13 and the C30742-66, respectively.

The DCR as a function of the over-voltage is shown in Figure 3.23 for the three sensors: the behavior is super-linear and the Excelitas features the highest DCR contribution, confirming the pictorial view in Figure 3.21. At 3.5 V of over-voltage the DCR featured by the Excelitas is 2.6 MHz, while it is 1.7 MHz for the SensL and 1.2 MHz for the Hamamatsu.

Figure 3.24 reports the dependence of the OCT with respect to the over-voltage. For all the three sensor the behavior is super linear, as expected from the theory. Also for this parameter the worst performance are shown by the

Excelitas, with a 11% of OCT at 3.5 V of over-voltage. At the same working point the Hamamatsu is characterized by an OCT of 6 % while the SensL has the best performance with 5% of OCT.

The same situation is depicted in Figure 3.25 for the afterpulse versus the over-voltage. The worst performance is attributed to the Excelitas, with an AP probability in the range 3.7-5.6 % for the interval of 2.3-4.6 V of over-voltage. The other two sensors have a very similar behavior, with a lower AP probability: it ranges from 1.2 to 2.5 % in the two over-voltage intervals considered.
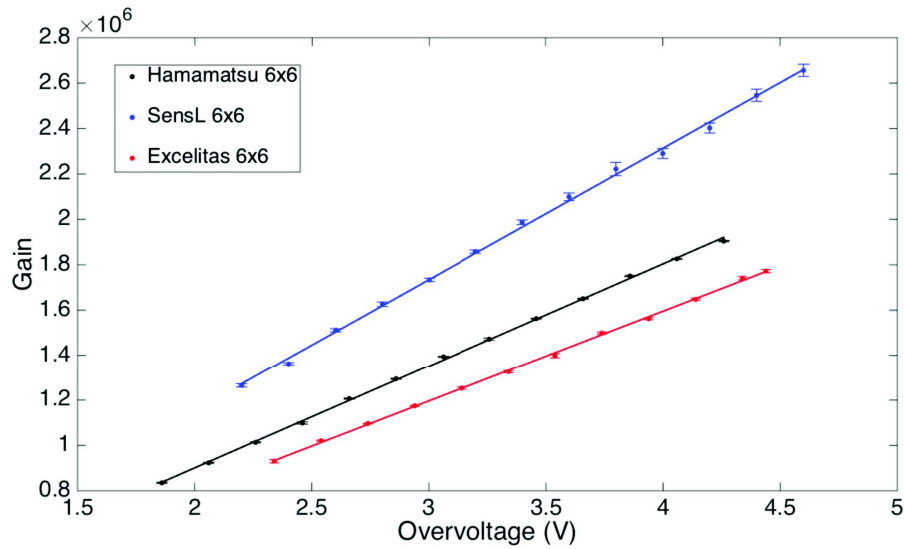
Figure 3.22: The points represent the three sensors gain as a function of the Overvoltage, while the straight line is the linear fit to the data.
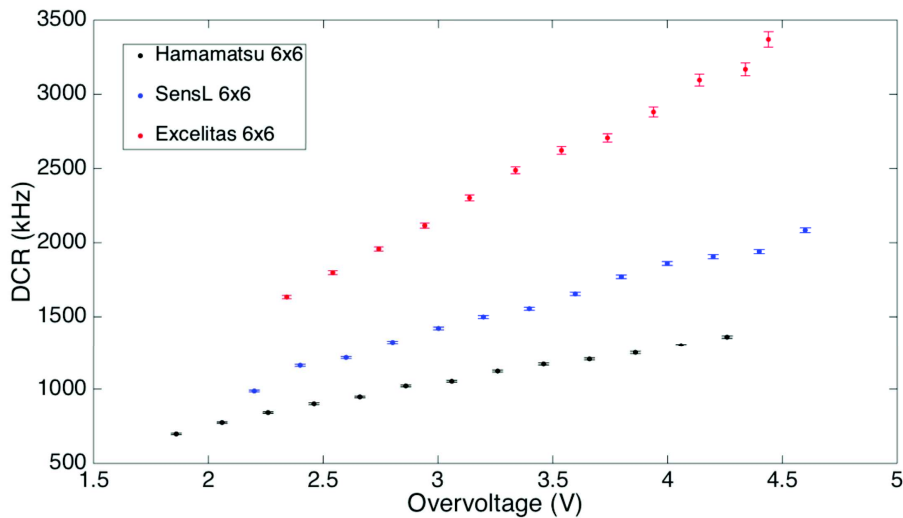
Figure 3.23: The three sensors DCR versus the Over-voltage.
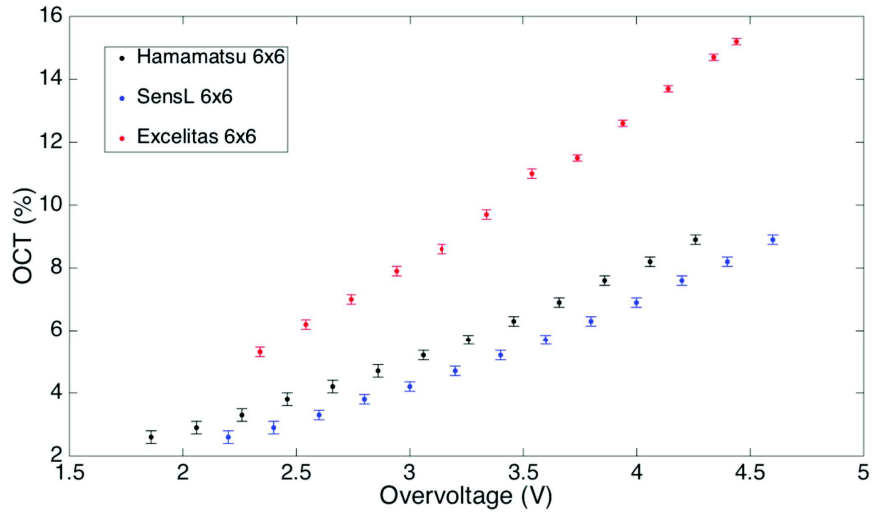
Figure 3.24: The three sensors OCT as a function of the Over-voltage.
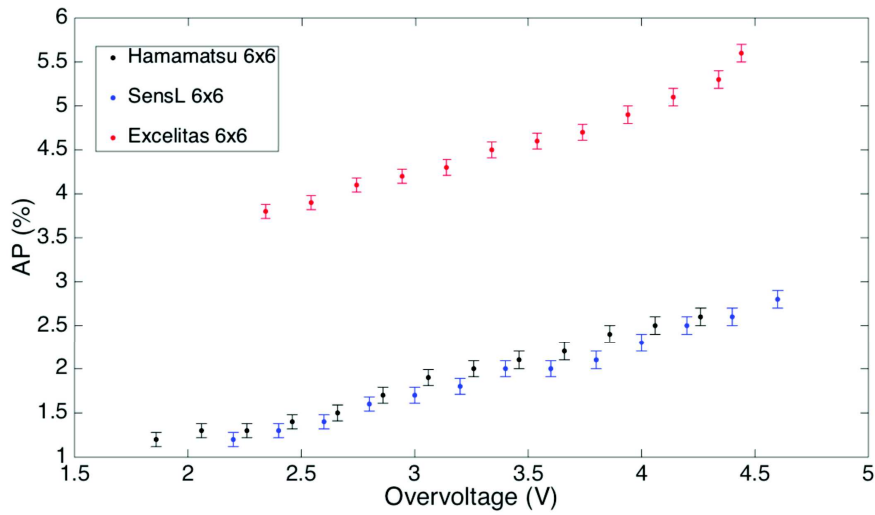
Figure 3.25: The three sensors AP versus the Over-voltage.

Chapter 4

Positron Emission Tomography

Nuclear medicine is the branch of radiology in which a compound containing a radioactive isotope is administered to a patient, distributes itself according to the physiologic status of the patient and is revealed by a radiation detector in order to reconstruct its spatial distribution inside the body. Nuclear medicine produces emission images, as opposed to transmission images of traditional radiology [71].

Nuclear medicine imaging is a form of functional imaging, providing complementary information with respect to the conventional radiology. In fact, rather than yielding anatomic and morphologic images, nuclear medicine allows to obtain information regarding the biologic, chemical, metabolic and molecular processes taking place in a living body.

Functional imaging constitutes a powerful and non invasive medical tool for prevention, diagnostic and therapy. It allows the characterization of the biochemical functionalities of organs and tissues, necessary to comprehend the physiologic mechanisms underneath the rising of a disease, avoiding the use of biopsy or surgery. In this way it permits the early identification of a disease, when there are no structural and morphological modification yet. Functional imaging is also able to establish the stage and the diffusion of a disease, evaluate the most appropriate therapy according to the specific patient physiology and to the molecular properties of the disease, monitor the treatment efficacy and determine eventual detrimental effect for the patient [72].

The traditional nuclear imaging refers to planar images; each point on the image is representative of the radioisotope activity along a line projected through the patient. Planar nuclear images are essentially two-dimensional maps of the real three-dimensional radioisotope distribution. This information superposition makes difficult to define the disease and distinguish adjacent structures in which the radioisotope can distributes.

Tomography technique consists in the acquisition of a series of planar images at different projection angles in order to provide an image of an individual slab of tissue, in absence of over- or underlying structures. Tomographic modalities are the Single Photon Emission Tomography (SPET) and the Positron Emission Tomography (PET).

PET is the most advanced nuclear imaging modality and has a great impact mainly in Oncology. Thanks to its spatial resolution and sensitivity it has a unique role in diagnostics of subtle pathologies and is a key research tool during studies on experimental animals. PET, notably when combined with morphological imaging through Computed Tomography (CT) or Magnetic Resonance Imaging (MRI), has a recognized diagnostic superiority over other imaging modalities. In the early days, high cost and complexity represented a limiting factor for PET technology spread, and few PET scanners were available only in specific centers. Nowadays, thanks to a continuous innovation and improvement of PET performances, a significant growth in number of installed systems/year and performed scans is occurring [73], [74], [75].

4.1 PET basic principle

The underlying principle of PET systems is the detection of high energy radiations emitted from a radioactive substance administered to a patient and the generation of images depicting its spatial distribution. The radioactive substance is a chemical marker containing radioisotopes of atoms existing in biologic molecules.

The marker constitutes a metabolically relevant compound; it distributes itself according to the physiological status of the patient, associating with molecules involved in specific biochemical or metabolic processes. As a consequence, it is possible to study the function of a particular organ or to evaluate the presence of a disease, revealed by the excessive concentration of the marker in specific locations of the body.

The radioisotope undergoes a β decay and emits a positron with a certain kinetic energy, which can range from zero to a maximum value depending on the radioisotope. The positron collides with the electrons of the surrounding tissue and loses most of it kinetic energy by causing matter ionization and excitation. When its kinetic energy is quite low, it interacts with an electron by annihilation. The entire mass of the electron-positron pair is converted into pure energy, called annihilation radiation: two 511 KeV photons are emitted in nearly opposite directions. The physics of positron interaction is sketched in Figure 4.1 [76], [67].
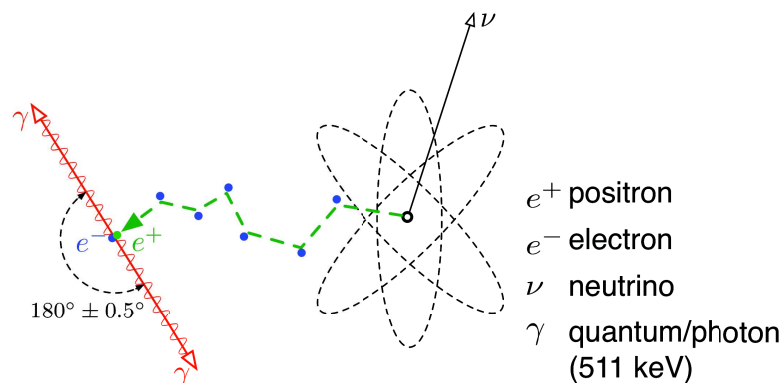
Figure 4.1: A schematic representation of radioisotope decay and positron annihilation with emission of two 511 keV γ.

In order to detect the two back to back photons in any direction, typical PET scanners are constituted by several rings of highly segmented detectors surrounding the patient, each composed of scintillator crystals coupled to photodetectors. They are equipped with dedicated circuitry that is capable of annihilation coincidence detection, i.e. the identification of the photon pairs emitted during annihilation. In fact, when two photons interacts with two detectors on the scanner within a coincidence time window it means that an annihilation event occurred along a straight line connecting the two detectors. PET circuitry implements a time coincidence logic and using the detector position allows to establish the trajectories of the emitted photons and the spatial origin of the emitted photons, defining the so-called Line Of Response (LOR). The information of the three-dimensional distribution of the marker is then reconstructed from the intersection of all the LORs. The final series of the tomographic emission images are computed from the projection data using iterative algorithms and filtering techniques. A scheme of the PET is shown in Figure 4.2 [71], [76].
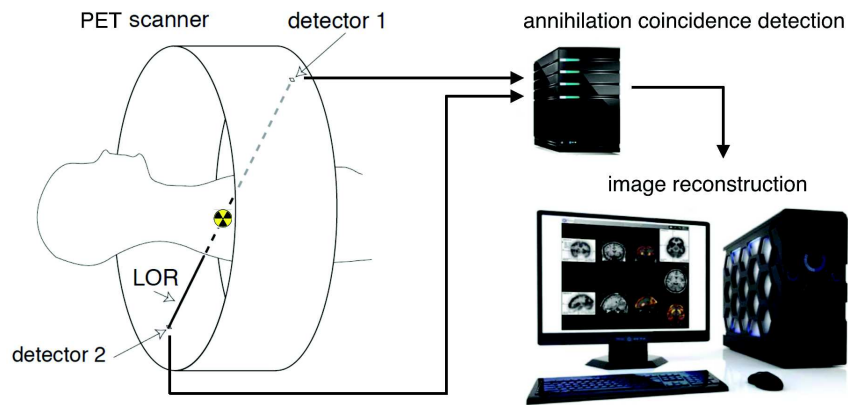
Figure 4.2: Radioisotope decay, annihilation photon detection, LOR identification and image reconstruction in PET.

4.2 Radioisotopes and diagnostic areas

The choice of the chemical marker is constrained by the short lifetime of the radioactive nucleus and its affinity to the metabolic process to be investigated. Many of the elements emitting positrons, like ^{11}C, ^{15}O and ^{18}F, are radioactive counterparts of natural elements that are quite physiologically relevant. This represents a big advantage because it means that they can be incorporated into a large number of chemical markers: fluorine is a good substitute for a hydroxyl group and can be used to create almost every radioactive substance.

Radioisotopes are produced by compact cyclotrons for medical use; hospitals are equipped with specific systems or are located in proximity to these radioisotopes production facility with a good distribution network [77]. The administered activity depends on the patient mass index and on the scan modality; for a typical PET examination, the activity is about 2.5-5 MBq/kg for a 3D and a 2D scan, respectively. Table 4.1 summarizes the chemical marker properties.

Nuclide	Half-life (min)	Application	Activity (MBq)
^{18}F	110	Oncology	400
^{11}C	20.4	Neurology	400
^{13}N	9.97	Cardiology	550
^{15}O	2	Cardiology, Neurology	2000
^{82}Rb	1.27	Cardiology	

Table 4.1: Main properties of the most used chemical markers in PET.

The most important chemical marker is ^{18}FDG, a glucose-analog with a quite long half-life, which allows to transport it through a reasonable distance from the cyclotron to the administration site. It is used mainly in Oncology; in fact, in 1931 it has been discovered by Otto Warburg that primary tumors and metastasis are characterized by high glucose metabolism. As a consequence, ^{18}FDG can be employed to differentiate malignant neoplasm from benign lesions, to stage malignant tumors and distinguish, after chemical or radioactive treatments, necrotic scar tissue from neoplasm recurrences. As it represents a non-specific marker of glucose metabolism, it is normally absorbed also by the brain, the heart, the spinal cord, the kidney and the muscular system; the correct interpretation of an ^{18}FDG image requires a deep knowledge of its distribution in normal conditions to identify regions of hyper-accumulation, as shown in Figure 4.3 [78].
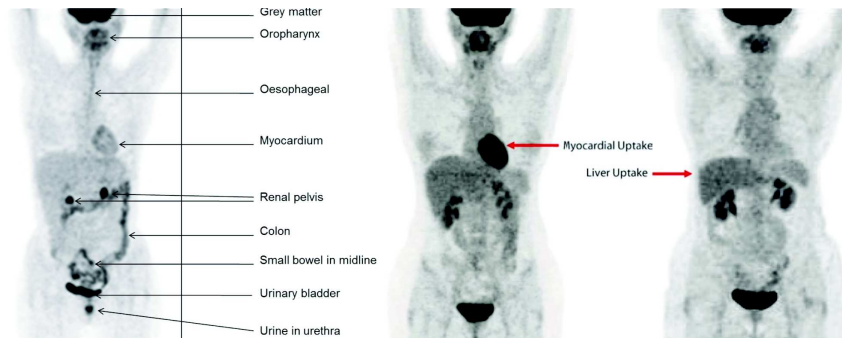
Figure 4.3: Normal distribution of ^{18}FDG (left) and cases of abnormal accumulation due to neoplasms (right) [79].

The ^{18}FDG is also applied in Cardiology to study cardiac metabolism, revealing cases of ischemia. The most suitable chemical markers for myocardium perfusion evaluation are ^{15}O, ^{82}Rb and ^{13}N, which have half-lives in the order of minutes. Usually, as can be seen in Figure 4.4, this study is associated with ^{18}FDG imaging in order to distinguish in hypo-perfused myocardium the necrotic areas from the viable areas that can be recovered through re-vascularization [80].

PET imaging in Neurology is useful to diagnose brain pathology trough the monitoring of the brain activity. Chemical markers with ^{15}O and ^{11}C allows to evaluate the flow of blood to different parts of the brain, but their short half-life make difficult this type of analysis. Since the brain is normally a rapid user of glucose, and since brain pathologies greatly decrease brain metabolism, the ^{18}FDG can be exploited to an early Alzheimer disease diagnosis and to differentiate Alzheimer disease from other dementing processes (Figure 4.5) [81].
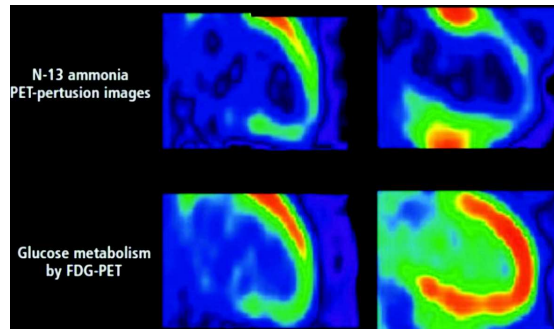
Figure 4.4: Comparison between myocardium perfusion with ^{13}N and glucose metabolism by ^{18}FDG: an image matching indicates an irreversible dysfunction, while with a mismatching normal functionalities can be recovered [80].
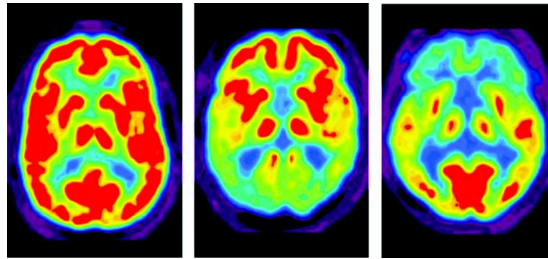
Figure 4.5: Normal brain activity (left) compared with Alzheimer (centre) and Frontal Lobe Disease (right) brain metabolism [81].

4.3 PET detectors

Interaction of radiations with solid state scintillation detectors is the basis of radiation detection in PET technology; the low intrinsic efficiencies of both gas and liquid scintillation detectors exclude their use in PET scanners. A variety of solid scintillation materials has been investigated to determine the most suitable for PET scanners. The choice is based on several characteristics, summarized in Table 4.2: the attenuation coefficient for 511 keV photons, the scintillation decay time, the light output per keV of photon energy and the energy resolution [71].

Annihilation photons interact with the scintillation material by either photo-electric absorption or Compton scattering. Since it is desirable to have short scan times and low activity, the detector must be characterized by the highest possible detection efficiency. A key issue is represented by the maximization of the linear attenuation coefficient μ, growing with the effective atomic number (Z_{eff}) and the material density [76].

The scintillation decay time arises when a photon interacts with an atom of the detector material, and the atom is excited to a higher energy level, which later decays to the ground state, emitting visible light. A short decay time of the scintillation light allows to minimize the coincidence time, which is relevant both for the maximization of the detector efficiency at high count rates and for the rejection of piled-up events.

The light yield of the detector obviously impacts on the energy resolution.

The intrinsic energy resolution depends on inhomogeneities in the crystal structure and on random fluctuations in the production of scintillation light. The energy resolutions at 511 keV of various detectors vary from 6% to 15% for integration time of the order of pulse formation. In PET imaging the integration time is lower in order to exclude noise signals, and the number of photoelectrons collected for a pulse is small, thus degrading the energy resolution to 10%-25%.

Property	NaI(Tl)	BGO	GSO(Ce)	LSO(Ce)	LYSO(Ce)
Z_{eff}	50	74	59	66	65
Density (gm/cm^3)	3.76	7.17	6.71	7.40	7.10
μ @ 511 keV (cm^{-1})	0.343	0.964	0.704	0.870	0.870
Decay time (ns)	230	300	56	40	41
Photon yield per keV	38	6	8-15	19-30	25-29
Light output (%)	100	15	20-40	50-80	65-75
Energy resolution (%)	7	15	9	10	12

Table 4.2: Physical properties of PET scintillator detectors

NaI(Tl) detectors provide good light output (40 photons per keV) and energy resolution at a low price. The NaI(Tl) crystal is hygroscopic and, therefore, hermetically sealed with aluminum foil. It is fragile and needs careful handling. The major drawback is its low density and low Z_{eff}, which make it not suitable for application in PET technology.

BGO detectors were used in most of the early PET systems because of its higher density and linear attenuation coefficient. Its longer decay time increases the dead time of the detector and limits the count rate that can be detected by the system, while the low light output results in poor energy resolution.

The overall characteristics of GSO detectors are quite good for application in PET technology. Even though it has lower density and effective atomic number than the BGO detector, its higher light output, its fast scintillation light and its better energy resolution has prompted some commercial manufacturers to use this detector in PET technology. Fabrication of GSO detectors requires great care, because the crystals are fragile, but can be cut into smaller crystals resulting in improved spatial resolution of the system.

The three characteristics of cerium-doped LSO and LYSO, namely high light output, high density, large linear attenuation coefficient and short scintillation decay time have made it an ideal detector for PET systems. A disadvantage of this detector is that it is slightly radioactive; [176]Lu, with an abundance of 2.6% and a half-life of 38 billions years, decays by emission of β^- rays and X-rays in the range 88-400 keV. However, the activity level is low, 40 Hz per mm^3, and it does not represent a problem for coincidence measurements; LSO and LYSO are the most common crystals used in modern PET imaging systems.

The light photons produced by scintillating crystals have to be converted into an electrical pulse by a photodetector. In the earlier designs of PET cameras, each crystal was glued to a single Photo-Multiplier Tube (PMT), and a large array of such detectors were arranged in multiple circular rings around the object of imaging. The larger the number of detectors and the better the spatial resolution of the system. However, the cost of using many PMT was high, and packaging of a large number of detectors with PMT became impractical.

The block detector was designed and used, in which small 6x8 or 8x8 crystal elements created by partially cutting a large block of detector material, were coupled to a reduced number of PMT, usually four. A schematic block detector is shown in Figure 4.6; the width of the crystal elements determined the spatial resolution of the imaging device. Typically, each block detector was about 3 cm deep and grooved into an array by making partial cuts through the crystal at varying depths, with the deepest cut at the edge of the block. The grooves between the elements were filled with an opaque reflective material that prevents optical spillover between elements [76].

Nowadays, SiPMs, thanks to their high gain, wide dynamic range and high PDE are good candidates for PET system. In addition, their low operating voltage and power consumption, compactness, robustness, flexibility and low cost solve all the problems related to the use of PMT. They are also employed in innovative TOF-PET, PET/CT and PET/MRI scanner, as explained in 4.9.
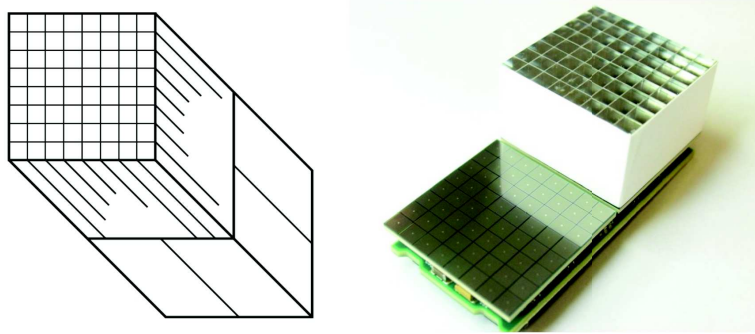
Figure 4.6: A schematic block detector with crystal segmented in 8x8 element read by 4 PMT (left) and 8x8 LYSO coupled to Hamamatsu S12642-0808PB 8x8 module detector of PETsys electronics [82].

Signals of each interaction from PMTs or SiPMs are amplified, shaped and processed separately from those of other interactions. In case of optical multiplexing, the relative amplitudes of signals from various detectors are used to determine the position of the photon interaction, identifying with an Anger logic which crystal has been hit [83] [84]. Then the signal is sent to energy discrimination circuit consisting of a discriminator with a lower level and an upper level setting or with a baseline and a window above the baseline. The energy released by the photon in the crystal is determined and only the events within a specific energy are accepted. This step is necessary to reject photons that have interacted with the patient and have lost part of their energy. Otherwise, also photons which have escaped from the patient without scattering can deposit only a part of their energy in the scintillation crystal. As a consequence, a narrow energy window ensures an accurate energy discrimination of photons from the sample, but reduces the detection efficiency (see 4.5).

The time signals of interactions accepted by the energy discriminator circuits are used for coincidence detection; a line in space connecting the two interactions, the LOR, is identified in real-time. The number of coincidences detected within each LOR is stored in the memory of the computer. Once the data acquisition is complete, computer assisted algorithms are used to produce transverse images of the radionuclide distribution in the patient (see 4.8).

If there are N detector elements in a ring, typically each detector is in coincidence with N/2 detector elements on the opposite side, creating N/2 projections for each detector element (Figure 4.7). These projections form for each detector an angle of acceptance in the trans-axial plane, and these angles of acceptance for all detectors in the ring form the trans-axial field of view (FOV). The larger the number of detectors in multi-coincidence with each detector, the larger the angle of acceptance and hence the larger trans-axial FOV for the PET system. The axial FOV is instead defined by the width and the number of rings.
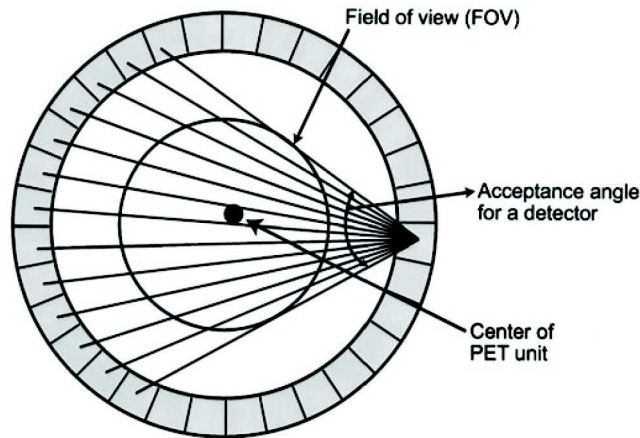
Figure 4.7: The transverse field of view is determined by the acceptance angles of individual detectors in a PET scanner [76].

4.4 Data acquisition

Each pair of detectors in coincidence in a PET scanner identifies a LOR, and data organization should preserve the spatial information carried by each LOR.

The first natural approach is the **list-mode organization**, in which data are stored as a list of detected events.

A second technique is to bin the acquired data into a 2D array, the **sinogram**. In fact, a line integral along the LOR can be identified by a radial position s (horizontal axis) and an orientation angle ϕ (vertical axis). PET acquisition mode is based on the process of transforming a continuous 2D distribution of the object in the (x,y) space into a discrete set of projections (line-integrals) in the (s,ϕ) domain through the Radon transform [85] [86]. In other words, when a coincidence event is detected, a count is added to the corresponding pixel in the sinogram, as shown in Figure 4.8 [87]. In a given projection, adjacent detector pairs constitute parallel LORs at different s and fixed orientation angle, representing an horizontal row in the (s,ϕ) space. The collection of projections at different angles forms the sinogram. This representation space takes its name from the fact that a single point source in the original image traces a sinusoidal path in the (s,ϕ) space. A sinogram for a general object can be seen as the superposition of all sinusoids corresponding to each point of activity in the object, as illustrated in Figure 4.9 [88].
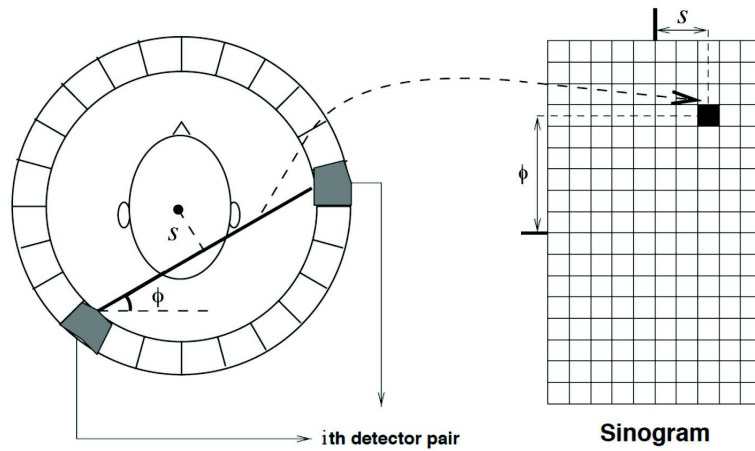
Figure 4.8: At each LOR corresponds a pixel in the sinogram [87].
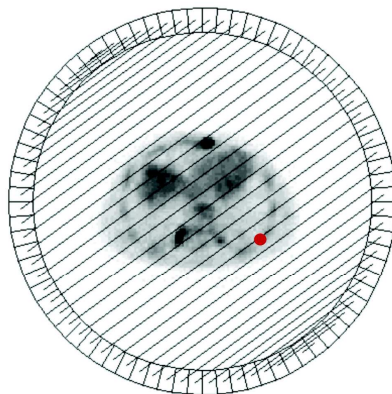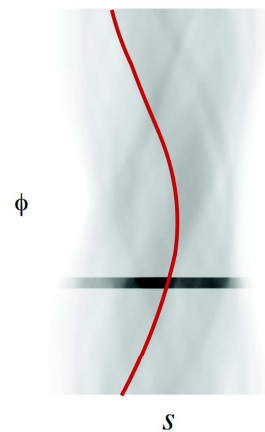
Figure 4.9: A projection corresponds to a row in the sinogram, while the collection of all projections for a point in the object is represented by a sinusoid [88].

The size of the sinogram grows with the number of independent detector elements. In 2D PET imaging projections are formed only acquiring LORs lying within a specified imaging plane. In 3D acquisition mode both the direct planes as well as the line-integral data lying on oblique imaging planes that cross the direct planes are considered. In this case measurements require more storage with data set sizes approximately 10^3 times larger than in 2D acquisition mode.

Sinograms are the most popular data format, but as more attributes for each PET event are recorded, list-mode data can become more practical for data storage without loss of information. For example, list mode acquisition of data is helpful in dynamic imaging, where the data are collected in multiple frames of sinogram to shows the changes in activity distribution in tissues over time [89].

4.5 Factors affecting the quality of acquired data

Ideally, PET data acquisition is based on the simultaneous detection of two 511 keV photons in two different detecting units. Actually, some photons can interact with the detector material by Compton scattering, depositing less energy; an energy acceptance window is necessary to avoid events loss. In addition, to account for the time of flight of the two annihilation photons, the crystal scintillation time and the processing electronics, events within a short coincidence time window have to be accepted. However, due to the introduction of these "loose" constraints on energy and time, some undesired effect, shown on Figure 4.10, can affect the data acquisition introducing background noise and artifacts in the final reconstructed image [87].
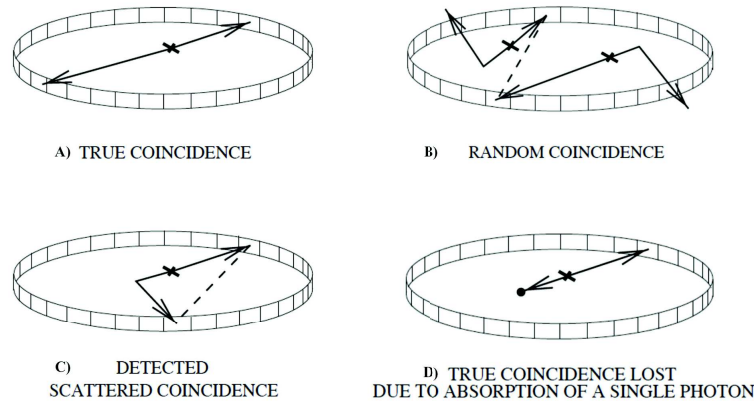
Figure 4.10: A true event and type of events altering the data acquisition.

Random coincidences

A random coincidence occurs when photons emitted from unrelated annihilations interact with two detectors within the coincidence time τ_c (Figure 4.10 B). The attribution of the LOR can be wrong and cause artifacts and loss of image contrast. The random coincidence rate R is strictly related to the single counting rates of each detector, S_1 and S_2, and to the coincidence time by the relation:

$$R = 2\tau_c S_1 S_2. \tag{4.1}$$

Therefore, a quadratic increase in random events will be observed by increasing the radioactivity in the FOV, whereas the true coincidence events will increase linearly with the administered activity. R can obviously be reduced without affecting the true counting rate by limiting the coincidence time window τ_c. However, there is a lower limit on τ_c accounting for the time walk of a true signal, dependent as well on the scintillator decay time. A typical τ_c of 12 ns is used for BGO-based PET systems, while it is reduced to 8 ns for GSO and NaI and to 6 ns for LSO-based systems [90].

Although individual random coincidences cannot be distinguished from true events, methods of correction are available. A possible solution is to store all coincidence events and also all the single events detected during the data

acquisition. Then the correction for randoms is performed by applying (1.1) and subtracting the random events from the total coincidences. This method is simple and efficient but requires a large memory and long processing times. A faster and more common technique of correcting for random events is to employ two coincidence circuits, one with the standard time window and another with a delayed time window. The counts in the standard time window include both the random plus true events, whereas the delayed time window contains only the randoms. For a given source, the random events in both time windows are the same within statistical variations. Thus, correction for random coincidences is made by subtracting the delayed window counts from the standard window counts [71], [76].

Scatter coincidences

Depending on photon energy and radioactivity distribution, a certain percentage of annihilation photons will interact while passing through the body tissue, being totally absorbed or deflected by a certain angle. In the latter case, the photons undergo Compton scattering and due to their high energy, most of them move in the forward direction without much energy loss. As a consequence, many of these scattered radiations may fall within the energy window and be detected because they occur in the coincidence time window (Figure 4.10 C). The result will be a misplacement of the coincidence events, increasing the image background and the blurring effect, which may lead to important quantification errors [71], [76].

Since both scattered and true coincidence rates vary linearly with the administered activity, the scatter to true events ratio does not depend on the activity. This ratio does not change with τ_c because scatter events arise from the same annihilation event and the two photons arrive at the detectors at the same time. Instead, the scatter contribution increases with the density and depth of the body tissue, the density of the detector material and the energy window width.

Ideally, the first and more practical way for scatter rejection should be the acquisition of only 511 keV events, excluding the majority of scattered photons. This cannot be achieved in practice, because PET scanners have limited energy resolution and a narrower energy window would also cause an high rejection of true events. In fact, PET systems with lower energy resolution use wider energy windows and are affected by a larger scatter component. BGO-based scanners (25% energy resolution) use a quite wide energy window (from 300-350 keV to 650 keV) and have a scatter component of 36%, while NaI- or GSO-based scanners (10-15% energy resolution, with energies accepted from 435 keV up to 590-665 keV) show only a 25% scatter contribution [90].

An effective way to reduce scattered events is shielding by means of lead septa, that are used in multi-ring PET scanners during 2D acquisition to significantly reduce the inter-plane scattered photons. From about 36% of 3D mode, the scatter component decreases to 15% in 2D acquisition with septa. Another method for scatter correction consists in measuring the counts just outside the field of view, where no true coincidence counts are expected. After subtracting the contribution of random counts, the scatter counts are obtained. Assuming that scattering is uniform throughout the FOV, the true coincidence counts is given subtracting the scatter component from the total counts across the FOV. Mathematic compensation for scattered events is also possible and is necessary when there is a large scatter background that can degrade PET images.

Some methods consist of simply estimating the scatter component by fitting or convolving the starting images with a priori defined de-blurring filters. Others that are more rigorous and computationally intensive are based on Monte Carlo simulation and the Klein-Nishina formula [90].

Attenuation

PET images can be also degraded by photon attenuation due to interactions occurring in the body (Figure 4.10 D). If μ is the linear attenuation coefficient of 511 keV photons in the tissue and d_1, d_2 are the tissue thickness traversed by two photons, the probability of a coincidence detection is given by:

$$P = e^{-\mu d_1} e^{-\mu d_1} = e^{-\mu(d_1 + d_2)} = e^{-\mu D}, \tag{4.2}$$

where D is the total thickness of the body along the projection line. Therefore, for objects with uniform μ, a very simple analytic correction can be made by knowing the thickness along all angular directions, but this model can be applied to only a few clinical situations, such as brain imaging [76], [90].

When photons travel through different organs or tissues with different attenuation coefficients, as is the case for the thorax or abdomen, the contributions from all of the different tissues must be considered. The above relation becomes:

$$P = e^{-\Sigma_{i=0}^{n} \mu_i D_i}, \tag{4.3}$$

where μ_i and D_i are the linear attenuation coefficient and thickness of *ith* organ or tissue, and n is the number of organs or tissues the photon travels through. Photon attenuation causes non-uniformities in the images, because of the loss of relatively more coincidence events from the central tissues than the peripheral ones and also because of the different organs that the two photons may traverse along the LOR. Therefore, on emitters characterized by a non constant attenuation coefficient distribution, corrections for photons attenuation must be implemented. Considering that the probability P is independent of the location of positron annihilation and depends only on the total thickness of the tissue, this allows to use the transmission method to estimate attenuation correction factors. In fact, also the attenuation of an external radiation passing through the body is expressed by Equation (4.3) [76], [90].

The most used transmission source is ^{68}Ge, a β^+ emitter with an half-life of 270 days, which is rotated around the scanner, exposing all detector pairs to radiation uniformly. Two scans are required; data of a blank scan without the patient (I_0) and data of a transmission scan with the patient positioned in the scanner (I). Correction factors are calculated for each detector pair as:

$$\frac{I_0}{I} = e^{\Sigma_i \mu_i D_i} \tag{4.4}$$

These factors are then applied to all individual LOR counts for the data obtained in the patients emission study. This means that the transmission scan must be taken at each bed position of the emission study; in fact, the ^{68}Ge source is configured as a rod parallel to the scanner axis and revolves around the patient. Usually, in order to reduce imaging time and the misalignment of transmission and emission scans due to patient movement, the attenuation map is acquired during the PET scan. Disadvantages related to the increase of patient dose and of statistical noise in the image can not be avoided [76], [90].

Dead Time

When a photon interacts within the detector and it is absorbed in the crystal, a light output is produced and the photodetector convert it into an electrical pulse. The energy and the spatial position of the photon are determined and finally the coincidence processing occurs. The total time required to complete these steps defines the system dead time τ_{dead}. During this time, the detection system is unable to process new events, which will be lost. When working at high counting rates this loss represents a serious problem [76], [90].

It is obvious that the dead-time loss can be reduced by using detectors with shorter scintillation decay time and faster electronics components in the PET scanners. Also the use of as-small-as-possible independent detection units reduces the dead time loss by lowering the number of dead units for each detected event. This solution requires, however, a more complex and expensive detection system architecture. Various techniques such as the use of buffers, in which overlapping events are held off during the dead time and the use of pile-up rejection circuits are implemented in order to reduce the dead time. Dead time correction is made by empirical measurement of observed count rates as a function of increasing concentrations of activity. From these data, the dead time is calculated and an analytical correction is applied to compensate for the dead-time loss. Obviously, when a too-high counting rate is reached, this approach is no longer feasible.

4.6 Evaluation of physical performance

Spatial resolution

The spatial resolution of a PET scanner is a measure of its ability to faithfully reproduce the image of an object, clearly depicting the variations in the object radioactivity distribution. It is defined as the minimum distance between two small point sources that can be distinguished by a scanner. Several effects contribute to determine the spatial resolution of the PET image, some intrinsically related to the β^+ annihilation and some depending on the detection system.

The dominant factor degrading the spatial resolution is usually the **intrinsic resolution** of the scintillation detectors. Figure 4.11(a) illustrates the origin and magnitude of this effect, which is due to detectors solid angle coverage and the fact that the position of interaction within the crystal width d can not be determined. A β^+ point source moving between two detectors on opposite side of the PET emits isotropically back-to-back pairs of annihilation photons. The coincidence rate measured by the detector pair is zero when the source is below the bottom edge of the detectors, increases roughly linearly to a maximum when the source is halfway between the top and bottom edges, then decreases roughly linearly to zero when the source is at the top edge of the detectors. Thus, the response function for this LOR is a triangle whose FWHM is $d/2$. For multi-detector PET scanners, the intrinsic resolution is $d/2$ on the scanner axis at mid-position between the detectors and by d at the face of either detector. Thus it is best at the FOV center and deteriorates toward the FOV edge [76], [91].

The use of **block detectors** in order to reduce the number of electronics channels introduces a further loss in spatial resolution. Statistical fluctuations in detectors signals, scatter within the crystal and imperfections in decoding scheme cause errors in event localization. The magnitude of the block effect is

complex to be analyzed, but was empirically observed to be ≈ 2.2 mm FWHM with BGO detector modules of 6-8 mm in cross-section. The value is tied to the width of the detector element and it is reasonable to quantify this contribution as a Gaussian function of width $d/3$ FWHM. In addition, it can be minimized by using better light output scintillators such as LSO and LYSO [76], [91].
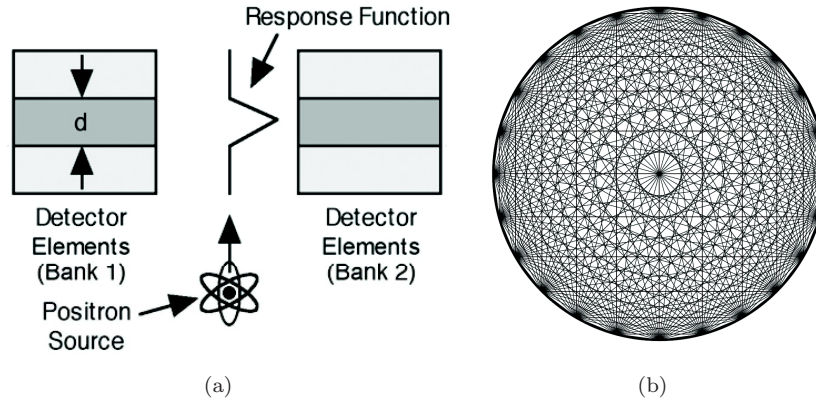
Figure 4.11: (a) Coincidence response function between two PET detector. (b) Sampling error due to non-uniform LOR distribution in the FOV [91].

Another effect to be considered is the **sampling error**, which is connected to the distribution of the LORs in all the FOV. Looking at Figure 4.11(b) it is clear that the sampling is not uniform: some pixels in the FOV have a large number of LORs going through them, as the exact centre, and some are transected by very few lines of response. The effect is especially pronounced near the center of the scanner, where LORs are spaced uniformly, creating a degradation multiplication factor that has been empirically observed to be 1.25 [76], [91].

The **positron** is ejected from the nucleus with a certain **kinetic energy**, it travels along some distance in the tissue before it thermalizes and captures an electron, forming positronium, which decays emitting two 511 keV photons. Since positrons are emitted with a spectrum of energy, their range is essentially an effective range (defined as the shortest distance from the emitting nucleus to the positron annihilation) having a non-Gaussian distribution, with a sharp central cusp and broad tails. Since coincidence detection is related to the location of β^+ annihilation and not of β^+ emission, there is some blurring which increases with positron energy and decreases with the tissue density. Table 4.3 lists the spatial resolution degradation for radioisotopes used in PET [76], [91].

Another factor of concern is the **annihilation photons non-collinearity**; their emission angle is not exactly $180°$. The positronium has non-zero kinetic energy when it decays, so although the annihilation photons are emitted back-to-back in the positronium rest frame, they are slightly acollinear in the PET frame, with a mean deviation of $0.25°$. Thus, the observed LOR does not intersect the point of annihilation, but is somehow displaced from it, as illustrated in Figure 4.12(a). This uncertainty causes a Gaussian blurring that is proportional to the radius R of the tomograph detector ring with a constant of 0.0044. Therefore, this effect is much more evident as the detector ring diameter increases [76], [91].

Nuclide	E_{mean} (MeV)	E_{max} (MeV)	R_{mean} (mm)	R_{max} (mm)
^{18}F	0.25	0.64	0.54	2.4
^{11}C	0.39	0.96	0.92	4.1
^{13}N	0.49	1.22	1.49	5.1
^{15}O	0.74	1.72	2.48	7.3
^{82}Rb	1.52	3.35	6.14	14.1

Table 4.3: Contribution to spatial resolution due to positron range for PET radioisotopes: mean and maximum β^+ emission energy and range in water.

The 511 keV photons penetrate some distance into the crystal before they interact. As shown in Figure 4.12(b), if they are not normally incident on the detector ring, they can be detected in a crystal different from the one that they impinge upon. As a result, they are assigned to the "wrong" crystal and the identified LOR is misplaced from the real annihilation line, resulting in an image blurring. The effect is asymmetric and occurs only in the radial direction; for this reason is called radial elongation or **parallax error**. In addition, the penetration increases as the point source moves radially in off-centre positions of the FOV and decreases with larger tomograph ring and thicker crystals. Its contribution to the spatial resolution depends on the detector material and for BGO, LSO and LYSO is described by a Gaussian whose FWHM in mm is $12.5r/\sqrt{r^2 + R^2}$, with r the source radial position and R the PET ring radius [76], [91].

(a)　　　　　　　　　　　(b)
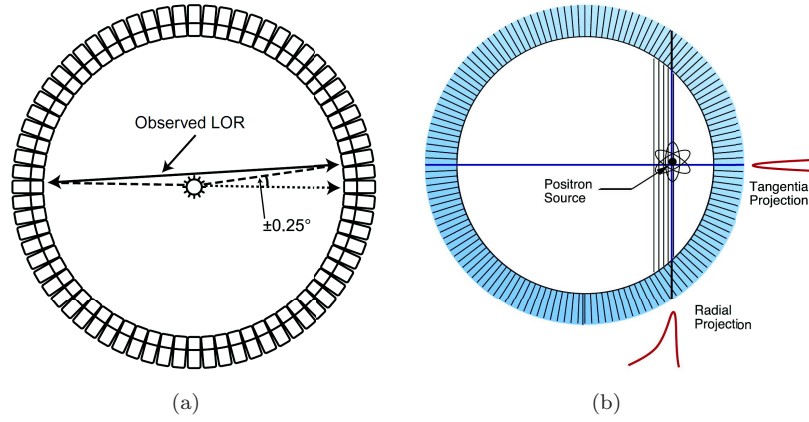
Figure 4.12: (a) Due to non-collinearity of 511 keV annihilation photons the detected LOR is slightly deviated from the original annihilation line [76]. (b) Obliquely incident photons emitted from off-centre sources penetrate some distance before interact causing an asymmetric spread in the radial projection [91].

The overall spatial resolution of a PET scanner is given by [91]:

$$FWHM = 1.25\sqrt{\left(\frac{d}{2}\right)^2 + \left(\frac{d}{3}\right)^2 + (R_{mean})^2 + (0.0044R)^2 + \left(\frac{12.5r}{\sqrt{r^2 + R^2}}\right)^2}.$$

$$(4.5)$$

This equation holds for a point source when there are a large number of counts in the image. In clinical imaging a further statistical noise contribution comes from the finite number of detected events, depending also on the extension of radiation distribution. The reconstructed spatial resolution is also affected by the reconstruction algorithm used, as will be explained in 4.8.

The fundamental limitation to the spatial resolution is due to the irreducible contributions related to the intrinsic property of positron; the positron range and the non-collinearity. The best value of 1.83 mm FWHM can be achieved using the ^{18}FDG and a detector with the minimum radius of 40 cm.

Several methods can be implemented to improve the spatial resolution [91]:

- Concerning the detector, it would be obvious to decrease the crystal width and avoid optical multiplexing to eliminate the decoding error. The drawback is the increased number of detectors, electronics channel and construction complexity which imply a cost increasing.

- The implementation of an hardware-driven method to determine the depth of interaction (DOI) of a photon in a crystal provides an improvement in the spatial resolution. PET scanner with the ability to measure the DOI can correct for the parallax error. Many approaches are possible and in general the drawback is complexity and/or cost [92].

Discrete DOI encoding involves the recoding of DOI using multiple discrete layers of crystal blocks (Figure 4.13). The most direct method consists in dividing the crystal along its length and interspace photosensors to read the light output from each crystal block. The large numbers of photosensors required is not cost effective. DOI information can be also obtained using stacked, optically coupled, crystals with different scintillation decay times. The analysis of photosensor pulse shapes determine the interaction position. This encoding method, offering cost advantages, is applied to several commercialized PET scanner. For example, the brain-dedicated HRRT scanner by Siemens uses LSO and LYSO crystals with 40 ns and 53 ns decay times [93]. The relative offset method provides another mean to obtain DOI information using two crystal layers shifted by half a crystal pitch in both the horizontal and vertical directions and a single readout of Position-sensitive PMT or multi-channel PMT, providing the centroid of light distribution, which is also shifted between crystal layers [94].

Continuous DOI encoding within scintillation crystals offers another way for DOI encoding (Figure 4.14). This method does not require multiple layers of crystals, and thus, is cheaper in terms of crystal costs. The most popular methods involves the signal readout of scintillation light from both ends of a discrete crystal; the interaction position is estimated from the ratio of the signals obtained from both ends [95]. Solid-state photo-sensors are commonly used for the crystal surfaces directed toward the object. The light dispersion in a monolithic crystal also provides DOI information in a continuous manner. Manufacturing costs are lower than the approaches that use discrete crystals but the statistical estimation algorithm is needed to improve the DOI spatial resolution performances. Quasi-monolithic crystal arrays use a combination of monolithic crystals in the trans-axial direction and discrete crystals in the axial direction, improving positional accuracy and DOI estimations [96].

An additional benefit coming from the incorporation of the DOI measurement consists in the addition of the number of LOR. If the DOI is implemented with
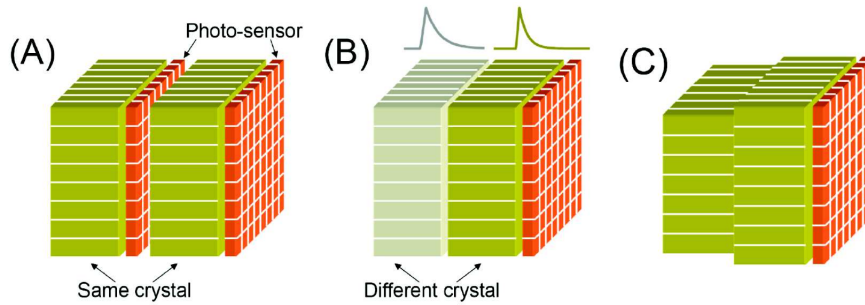
Figure 4.13: Discrete DOI encoding: light readout from each crystal layer (A), pulse shape discrimination using crystals with different decay times (B) and relative offset method (C) [92].
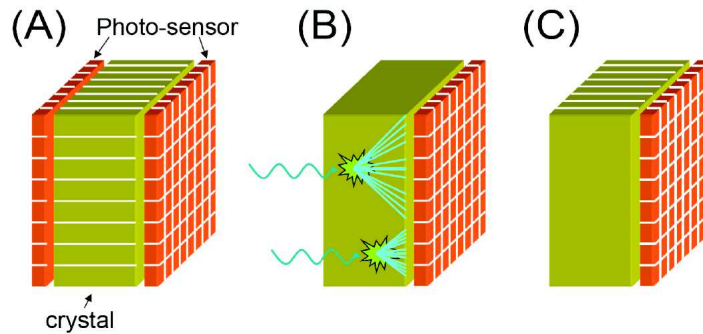
Figure 4.14: Continuous DOI encoding: dual-end light readout (A), monolithic crystal (B) and quasi-monolithic crystal array (C) [92].

the continuous encoding method, PET scanners can have lines of response that are spaced arbitrarily closely together, eliminating the sampling error [91].

As a result, a system which do not use light sharing to decode crystals and measures the depth of interaction, has a spatial resolution depending only on the positron range, acollinearity and detector width. Applying the conditions described above to minimize the first two contributions and using a detector width of 3 mm, that represents a reasonable compromise between spatial resolution and practical manufacturing considerations, the best spatial resolution that PET systems can achieve is 2.36 mm FWHM. Currently PET scanners quote a spatial resolution in the range of 3-4 mm FWHM, which constitutes a good result.

Sensitivity

The sensitivity of a PET scanner is defined as the number of counts per unit of time detected by the device for each unit of activity emitted by a source and is normally expressed in cps/μCi or cps/MBq. The principal elements influencing the sensitivity are the detection efficiency, the energy window settings, the dead time of the system and the geometric efficiency [90].

The **detection efficiency** of a scintillator crystal depends on its scintillation decay time, density, atomic number, and thickness (see 4.3).

The effect of the **energy window** setting and of the **dead time** on detection efficiency has been discussed in 4.5.

The **geometric efficiency** of a PET scanner is defined by the solid angle projected by the radioactive source towards the detector, i.e. the active area of the tomograph seen by annihilation events. The geometric factor depends on the distance between the source and the detector, the diameter of the ring and the number of detectors in the ring. Increasing the distance between the detector and the source reduces the solid angle and thus decreases the geometric efficiency and vice versa. Increasing the diameter of the ring decreases the solid angle subtended by the source at the detector, thus reducing the geometric efficiency and in turn the sensitivity [90].

The sensitivity of a point source positioned in a single PET ring centre is:

$$S = \frac{G \cdot \epsilon^2 \cdot e^{-\mu t} \cdot 3.7 \cdot 10^4}{4\pi r^2}(cps/\mu Ci), \tag{4.6}$$

where G is the detector area seen by the point source, ϵ represents the crystal detection efficiency, μ is the linear attenuation coefficient for 511 keV photons in the scintillating material, t is the thickness of the crystal, r is the radius of the detector ring and the numerical factor converts the Bq to μCi.

For an extended source in the center of a single ring, it has been shown that the geometric efficiency is approximated by $w/2r$, where w is the detector axial width and r is the ring radius. Thus the sensitivity of a scanner is higher in the center of the axial FOV and gradually decreases toward the periphery. In typical PET scanners there are multiple rings and each detector can be put in coincidence with the half of the detectors on the opposite side in the same ring as well as with the detectors in other rings. Thus the sensitivity of multi-ring scanners will increase with the dimension of the axial FOV [76].

The sensitivity of a PET scanner increases as the square of ϵ, thus results to be very important to maximize scintillating crystal detection efficiency. This is why LSO and LYSO detectors are preferred to other crystals. There is also a trade-off between sensitivity and resolution; smaller crystals enable better resolution but reduce the individual crystal solid angle coverage and the number of measured events in each detectors, which lead to noise data.

The sensitivity is determined by acquiring data in all projections for a given duration of time from a volume of activity and dividing the total counts by the acquisition counting time and by the activity concentration. Manufacturers normally use this unit as a specification for the PET scanners.

Noise Equivalent Count Rate

Data noise is the random variation in pixel counts across the image and is given by the relative uncertainty of the counts N in the pixel, $1/\sqrt{N}$. It can be reduced by increasing the total counts in the image, which means either imaging for a longer period or injecting more radioisotope or improving the detection efficiency of the scanner. The first solution may be uncomfortable to the patient and an improvement of the detection efficiency may be limited by the imaging device design [90]. There are also obvious limitations in the patient administered dose; moreover, a high activity implies random coincidence counts and dead time loss.

The noise component for a PET data-set is characterized by a parameter called the noise equivalent count rate (NECR) which is given by:

$$NECR = \frac{T^2}{T + S + R},$$

(4.7)

where T, R, and S are the true, random, and scatter coincidence count rates, respectively. Scatter and random events are measured according to methods described previously and the true events are determined by subtracting scatter and random events from the total events [76].

The NECR serves also as a good parameter to compare the performances of different PET scanners. The best data acquisition condition is reached when acquisitions are performed positioning an activity concentration in the FOV region corresponding to the NECR maximum.

Scatter Fraction

The scatter fraction is another parameter that is often used to compare the performances of different PET scanners. It is defined as:

$$SF = \frac{C_s}{C_{tot}},$$

(4.8)

where C_s and C_{tot} are the scattered and total count rates, assessed with a low radioactivity source to assume negligible random events contribution. The lower the SF value, the better the performance of a scanner and better the quality of images. A narrower energy window, possible for system with good energy resolution, results in a lower scatter fraction [76], [90].

4.7   PET design

2D and 3D mode

In 2D data acquisitions, coincidences are detected and recorded within each detector ring (direct plane) or two adjacent rings (cross planes), as shown in Figure 4.15. To shield out-of-plane coincidence photons that are emitted obliquely, annular septa composed of lead or tungsten are used to separate the rings. In this way the scatter fraction is greatly reduced; in fact, it is likely that the new trajectory of a scattered photon is prevented by the septa to reach the detector. Furthermore, photons from activity outside the FOV are prevented to cause counts in the detectors. However, many valid photon pairs are also absorbed by the septa. In the newer systems, a ring difference up to 5 rings can be used to improve sensitivity without a significant loss in spatial resolution. A large increase in sensitivity can be obtained by collecting all possible LORs by removing the septa [76], [90].

This approach, called 3D acquisition mode (Figure 4.15), produces important changes in the physical performance of the PET scanner that require special 3D reconstruction algorithms. In 3D mode, the sensitivity is approximately 5 times higher than in 2D mode. However, this gain is associated with an increase of the true coincidence, together with an increase in random coincidences, which can result in loss of events due to dead time. Thus, 3D mode requires less activity

to be administered to the patient. Furthermore, the scatter fraction is larger than 2D mode and the number of interactions from activity outside the FOV is increased. This data acquisition modality is useful in low-scatter studies, such as pediatric and brain scans. In other cases, to fully take advantage of the 3D mode, high energy resolution, fast electronics and scintillation crystals, high computing power for acquisition and post-processing are required [76], [90].
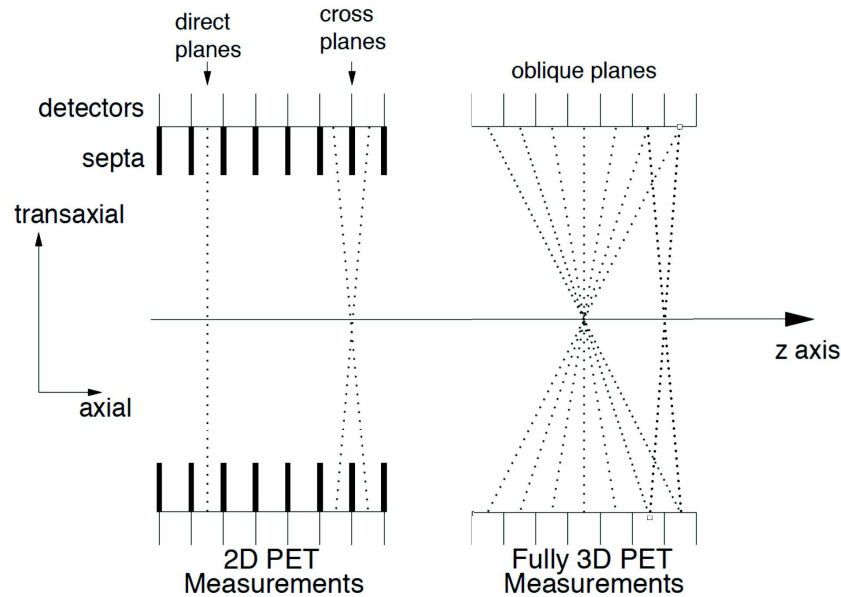
Figure 4.15: Comparison between 2D and 3D acquisition mode; removing septa sensitivity improvement can be seen for sources placed in the FOV centre.

Scanner geometries

PET scanner configurations are illustrated in Figure 4.16, together with the detection surface structures. The most common PET geometry is a solid ring with full angular coverage, where scintillation detectors cover a full 360° around the volume to be imaged [97]. The advantages offered by this particular configuration are the optimal system sensitivity, which is necessary to obtain high counting statistics and to achieve the desired resolution, and the reduction of image artifacts due to tracer, organ or patient motion. The full ring geometry is realized in a circular or hexagonal form with either the use of block detectors, which requires Anger logic to localize the scintillation element, or the use of curved crystals placed side by side [98].

Improvements in the scanner technical performance are always associated with higher cost. However, manufacturers have developed systems with partial ring rotating geometry, permitting scaling of the cost and performance to satisfy the needs for different PET clinical applications [99]. Partial Ring are obtained with two opposed curved matrices of crystal blocks with a reciprocal 15° angular shift to increase the transverse FOV during the detector rotation.This configurations are used when the open PET geometry is preferable, because it

allows easier patient access. In breast dedicated PET this geometry enables
PET-guided biopsies to be performed on suspicious breast tissues. However,
despite these advantages, its use has been limited because it is characterized by
lower overall sensitivity with respect to full-ring systems and it is prone to serious
reconstruction artifacts due to limited angular sampling. Detectors rotation,
which allows to obtain complete data and prevent these artifacts, requires the
technically challenging implementation of rotating detectors, implying further
calibrations and additional variables to be considered.
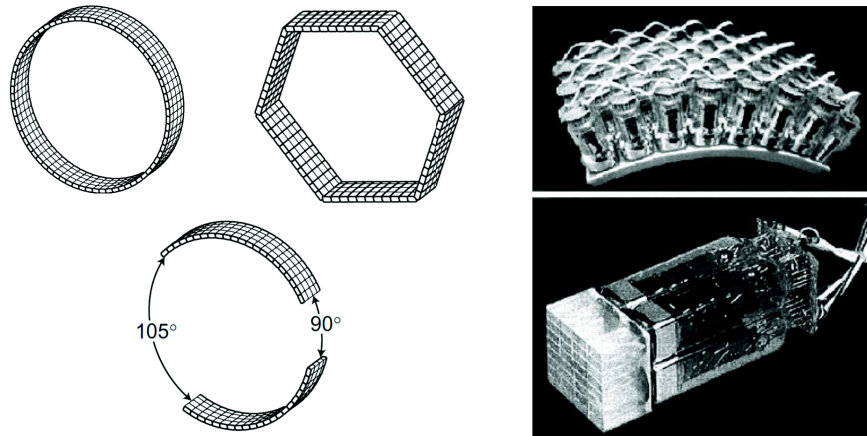
Figure 4.16: Full-ring and partial-ring PET geometries (left) [76]. Block detectors
(top right) and curved crystal (bottom right) [90].

Whole-body scanners

The main requirements for oncologic whole-body PET imaging are short scan
times, good lesion detectability and accurate radioactivity quantification. Until
2003, one of the PET scanners main limitations preventing practical whole-body
imaging was the short axial FOV of the scanner, which required excessively
long scan times. The implementation of ≈ 20 cm axial FOV PET system
with a computer-controlled bed, used to move the patient through the scanner,
allows whole-body studies [100]. GSO- and LSO-based scanners, with their fast
scintillation time and coincidence electronics, can acquire at high coincidence
counting rates with good signal-to-noise ratio; they introduce the 3D acquisition,
markedly increasing the scanner sensitivity. The effective axial FOV is less
than the real FOV because it is necessary to overlap adjacent bed positions to
avoid image artifacts due to poor counting statistics. The effect is even larger
for 3D acquisition mode, where the increase in system sensitivity produces a
sensitivity profile with a maximum in the center of the FOV and a rapid decrease
on planes near the edge; multi-bed acquisitions are needed to maintain a uniform
counting profile. Another important parameter that strongly affects total scan
time is the acquisition of the attenuation-correction scan. In addition to the
techniques already explained, a further reduction in transmission acquisition
time is achieved by the use of segmentation procedure to low-counting statistics

acquisitions. Using this approach, based on knowledge of a priori μ values, transmission scan times can be reduced from 10-15 min to 1-2 min without losing accuracy or precision on attenuation values estimation. Finally, performing attenuation-corrected whole-body studies require 30 min or less [101].

Application-specific systems

When PET was not generally available for clinical use, the few available PET were used for various clinical purposes and for research studies. Whole-body PET scans for cancer detection were the most frequently performed studies and allowed to scan any specific part of the body. However, as the number of conducted PET studies is increasing due to the wide recognition of PET usefulness, small and large PET scanners designed for specific applications or organs are catching on as new diagnostic tools to maximize PET performance. Some example are reported in Figure 4.17 [92].

Figure 4.17: Brain PET system by Philips (top left), PEM scanner (top right) and transformable PET allowing two bore configurations (bottom) [92].

Brain-dedicated PET scanners are designed to provide detailed information of small brain structures, assess regional brain activity and improved quantitative accuracy. They have smaller ring diameters (40-50 cm) and crystal sizes (2-4 mm) than whole-body PET scanners to increase spatial resolution, sensitivity, and image quality. Despite these advantages, the clinical uses of brain-dedicated PET scanners have been limited primarily due to their marginal cost-effectiveness. However, the its potential remains open because molecular brain imaging agents are a topic of active research, particularly for the early accurate diagnosis of neurodegenerative disorders [102].

Breast-dedicated PET systems have received a lot of attention because breast cancer is the most common cancer in woman, and its incidence continues to increase. Whole-body PET examinations are limited for the detection of small breast masses, and their spatial resolutions is not enough because breasts are placed at the periphery of the FOV. Accordingly, the sensitivity for PET scanner in the detection of breast masses smaller than 1 cm is less than 60%. Positron emission mammography (PEM) systems consist of two parallel detectors providing slice data parallel to detectors (limited-angle tomography). The breasts are compressed by the detector head to spread out breast tissues; this open geometry allows detector distance to be adjusted for scanning breasts of different sizes and for performing needle biopsies during the exam [103]. Limited angular coverage causes image blurring along the axis perpendicular to the detector plane and broad background noise, which reduces image contrast [104]. Widening the angular coverage by rotating the planar detectors or utilizing a full ring or rectangular camera geometry provides the most direct ways of obtaining isotropic resolution in all three dimensions and high geometrical detection efficiency [105].

In parallel with approaches targeting the use of organ-specific PET scanners, efforts are also being made to create a transformable PET system; a group at the University of Texas have developed a PET that can adaptively change ring geometry to suit the dimensions of the object imaged. Therefore, this system can have two ring geometries, namely, a diameter of 83 cm and an axial FOV of 13 cm for whole-body imaging or a diameter of 54 cm and axial FOV of 21 cm for brain/breast imaging, optimizing PET images for specific applications [106].

There is also a need to increase the PET ring diameters; radiation therapy planning procedures require an imaging system with a sufficiently large bore to provide flexibility with respect to patient position. A PET system with 85 cm bore (the standard one is 70 cm) has been designed by Philips.

4.8   Image Reconstruction

Measured data are indirect measurements (line integrals) of an unknown activity distribution in the patient. Image reconstruction performs an unfolding of the acquired data to provide transverse images from which vertical long axis (coronal) and horizontal long axis (sagittal) images are formed [76], [89].

In fact, a way to represent the imaging system is the following relationship:

$$p = Hi + n, \tag{4.9}$$

where p is the set of observations (projections), H is the known system model, i is the unknown image and n is the error in the data. The goal of reconstruction is to use p to find the image i, modeling the observed data either as deterministic or stochastic variables [107].

A common approach for dealing with PET data is to assume that the data is deterministic, containing no statistical noise. Therefore, n is a deterministic number and the exact solution for the image can be found. This is the approach of analytic reconstruction methods, which use the inverse of the discrete Radon transform to find a fast and direct mathematical solution for the image [85] [86]. This deterministic assumption is advantageous because it simplifies the reconstruction but, disregarding the noise structure in the observations, it can lead to images with reduced resolution and artifacts.

In reality, the data values are intrinsically stochastic due to several physical factors affecting data in PET imaging. Consequently, the n is more accurately representative of random noise making it impossible to find the exact solution for the original image. Therefore, statistical reconstruction exploits estimation techniques, which lead iteratively to approximated solution of the image.

Analytic reconstruction

A foundational relationship that allows conceptually analytic image reconstruction is the central-section theorem, whose principle is illustrated in Figure 4.18. It states that the Fourier transform of a one-dimensional projection ($\mathcal{F}_1\{p(s,\phi)\}= P(v_s,\phi)$) is equivalent to a section at the same angle passing through the center of the two-dimensional Fourier transform of the object ($\mathcal{F}_2\{f(x,y)\}= F(v_x,v_y)$) [108]. As a result, knowing the projections $p(s,\phi)$ at all angles is possible to find all the values of $F(v_x,v_y)$ and to obtain the reconstructed image $f(x,y)$ by applying the inverse of the two-dimensional Fourier transform.
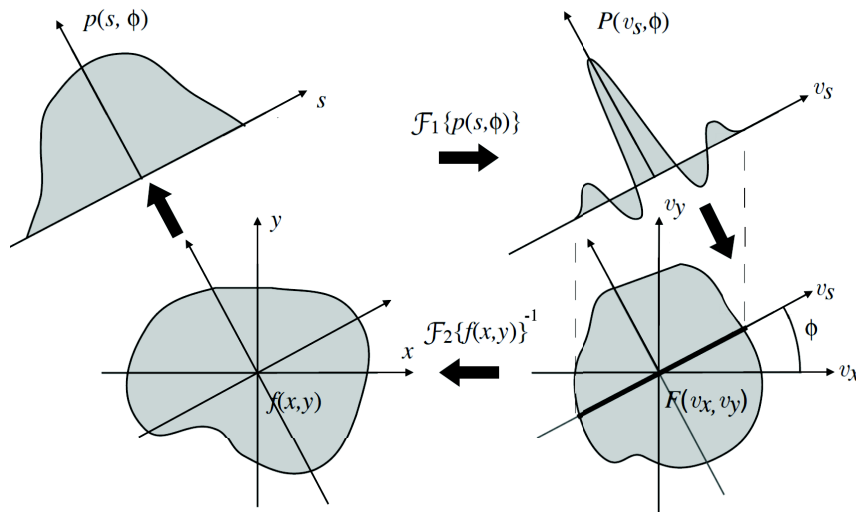
Figure 4.18: Pictorial illustration of the central-section theorem: the one-dimensional Fourier transform of a projection at angle ϕ is equivalent to the section at the same angle of two-dimensional Fourier transform of the object [107].

The simplest analytic method is the back-projection, which is the inverse of the projection process that generates the data. Conceptually, back-projection can be described as placing a value of a pixel sinogram back to the image array along the correspondent LOR. Since the knowledge of where the values came from was lost in the projection step, a constant value is assigned to all image elements along the LOR. The process is repeated adding the counts of all the collected projections, i.e., for all detector pairs in the PET scanner, resulting in a back-projected image of the original object. The result does not correspond to the original image due to the oversampling in the center of the Fourier transform that causes "star pattern" artifacts [76], [107].

One possibility to minimize this effect is to apply a cone filter $v = \sqrt{v_x^2 + v_y^2}$ to the two-dimensional Fourier transform of back-projected image (BPF). This filter accentuates values at the edge and diminishes values at the center of the Fourier space, in order to have equal contributions throughout all the FOV.

The other solution is accomplished by interchanging the order of the filter and of the back-projection, obtaining the filtered-back-projection (FBP) reconstruction method. The projection data in each profile are subjected to the one-dimensional Fourier transformation, then a ramp filter is applied (a section of the rotationally symmetric two-dimensional cone filter) and the inverse Fourier transformation is performed. Filtered projection data are then back-projected to produce an image that is more representative of the original object. The advantage of FBP is that the image can be efficiently calculated with a much smaller reconstruction matrix than BPF for the same level of accuracy; this is the main reason for the popularity of the FBP algorithm [107].

Iterative reconstruction

Iterative methods offer a more accurate reconstruction over the analytical approach because they account for the noise structure in data and they use a more realistic model of the system. These improvements come at the cost of added complexity, resulting in mathematical problems that can be solved only with iterative approximations of the unknown image. Advances in computational speed and faster algorithms allow them to receive growing clinical interest [109].
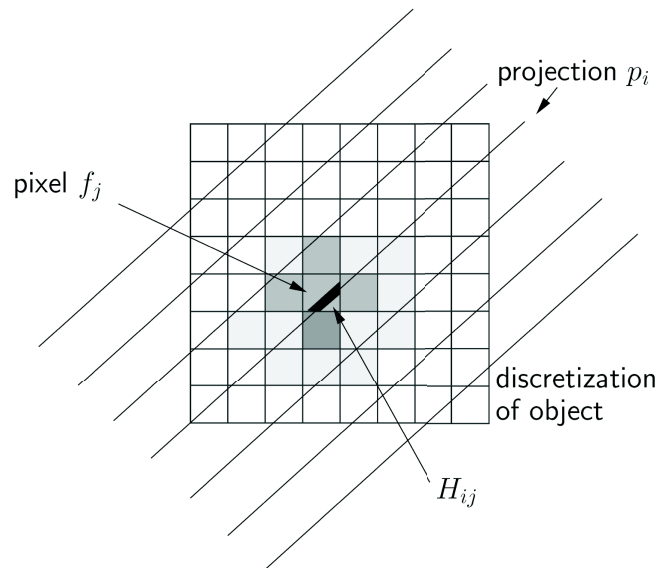
Figure 4.19: Illustration of a single element of the system model H_{ij} [107].

All iterative methods contain five basic components. The first one is the **initial estimate** of an image, usually consisting in a discretization of the image domain into N distinct pixels. The second basic element is a **system model** that relates the image to the data; it allows to compute the estimated projections that are compared with the measured ones. The unfolding of the estimated

image into a set of projections is considered as the forward projection, as opposed to the back-projection. The projection p_i of the estimated image is calculated as the weighted sum of the activities in all pixels f_j along the LOR i [107]:

$$p_i = \Sigma_{j=1}^{N} H_{ij} f_j, \tag{4.10}$$

where H_{ij} characterizes the imaging system and represents the probability that an emission from pixel j is detected in projection i. H_{ij} is equal to the fraction of activity in the pixel j out of the total activity along the LOR i, as shown in Figure 4.19. Most clinical methods use spatially invariant system models with responses simplified for computationally efficiency, while in emerging research spatially variant system models provide an improved resolution. The third component of all iterative methods is a **data model**, which describes the statistical relationship between the value of the measurements and their expected values. It is derived from the basic understanding of the acquisition process, which is the Poisson distribution of detected photons. Although this model is appropriate for a conceptual view of PET imaging, once the corrections for randoms, scatter, and attenuation are applied, the data are no longer Poissonian. Other models have been proposed for improving model accuracy and for practical computational reasons. The fourth element concerns the adoption of a **governing principle** that defines the "best" image. The most common principle is the Maximum Likelihood approach, in which it has to be maximized the probability that the estimated projections come from the original image. In practice, after having calculate the difference between the estimated and measured projections, corrections are made on the system model elements to improve the estimated image Likelihood, and a new iteration is performed. The process continues until a reasonable agreement between the two sets of projections is achieved. Maximum likelihood estimators are advantageous because they offer an unbiased minimum variance estimates when the number of iterations increases towards infinity. In reality, too many iterations can easily lead to noise amplification. For this reason, it is important to establish e convergence criterion to determine the number of iterations needed to obtain the best image quality. The final component is an **algorithm** that finds the best image estimate. Numerous algorithms have been developed, which differ in the order and in the type of error corrections to be applied to the estimated projections [107].

The most widely used iterative algorithm in PET is Maximum Likelihood Expectation Maximization (MLEM), which is based on an image update using a multiplicative factor assessed as the ratio between the original acquired projections and the newly estimated ones [110]. The low frequency components of the image appear within the first few iterations, then more and more high frequency definition is resolved in the image. Advantages of this iterative method are very low noise amplification, while the main disadvantage is the large number of iterations (20-50) required to converge to an optimal solution. Since each iteration consists in a forward and in a back-projection, this method demands long processing times, hampering its applicability in clinical routine.

To overcome the problem of slow convergence rate, the Ordered-Subsets Expectation Maximization (OSEM) algorithm has been introduced [111]. It is a modified version of MLEM in which projections are grouped into subsets uniformly distributed around the volume to be imaged. If there are n subsets of projections, then the image after a single iteration of OSEM is similar to that

obtained by n iterations of MLEM, accelerating convergence. The speed increase comes at the expense of slightly more image variance and an optimization of subsets and iterations number is required.

Iterative reconstruction methods do not produce artifacts observed with FBP methods, as shown in Figure 4.20. MEML and OSEM provide high-quality images and are the most widely used method for PET image reconstruction [76].
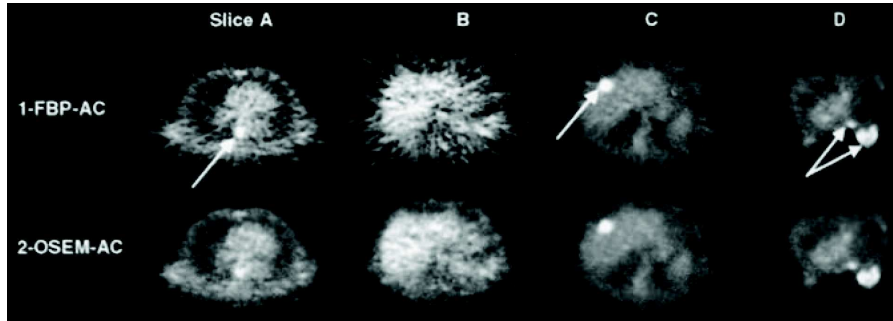
Figure 4.20: The FBP compared to the OSEM for lungs, normal liver, liver with tumor and breast: FBP reconstructed images are noisier than OSEM ones [76].

3D reconstruction

Reconstruction of images for 3D acquisition is complicated by the huge amount of data. In a scanner with N rings, a full 3D acquisition would generate N direct and $N(N-1)$ oblique sinograms, for a total of N^2, compared to $2N-1$ of 2D acquisition. Additional difficulties are due to the incomplete sampling of 3D volumes, related to the finite axial extent of the scanner. As a result, the scanner is more sensitive to activity in the center of the axial FOV than at the edge. On the positive side, 3D data contains redundancies because from an analytic point of view only a single slice of data is required to reconstruct an image [76].

The 3D Re-Projection (3DRP) algorithm is used to restore spatial invariance; an initial estimate is formed by reconstructing an image applying FBP to the direct planes and is then forward-projected to estimate the unsampled regions. The 3DRP has been now substituted by new efficient and practical solutions [112].

A method of 3D reconstruction is based on the rebinning algorithms; mathematic procedures rearrange acquired data into a set of 2D equivalent projections. They have the advantage that rebinned sinogram can be efficiently reconstructed with either analytic or iterative 2D reconstruction methods. In addition rebinning can significantly reduce the size of the data. The disadvantages is a penalty in terms of a spatially-varying distortion and/or amplification of the statistical noise. The simplest method is the Single-Slice Rebinning (SSRB) [113], where oblique sinograms are averaged by assigning axially tilted LORs to transaxial planes intersecting them in their axial midpoints. This method works well along the central axis of the scanner, but steadily becomes worse with increasing radial distance. The Fourier rebinning (FORE) [114] is a more accurate method which is performed by applying the 2D Fourier method to resort each oblique sinogram into transverse sinograms in the frequency domain. It slightly amplifies statistical noise compared to SSRB, but results in significantly less axial distortion.

4.9 Innovative systems

TOF PET

The two 511 keV photons hit PET detectors at different times if they have not been generated in the exact center of the ring. Time Of Flight PET uses the time-of-flight difference t to better determine the distance of annihilation position from the centre of the FOV, $x = ct/2$, where c is the speed of light (Figure 4.21). Accordingly, in ideal conditions, image reconstruction algorithm should be no more needed. The limitation is the capability in measuring the time difference, i.e. the time resolution Δt, which gives an uncertainty in the annihilation localization $\Delta x = c\Delta t/2$. The timing resolutions of currently available clinical PET detectors based on fast LSO and LYSO crystals and on SiPMs as photodetectors, are of the order of 100 ps FWHM, which gives a positional uncertainty of $\approx$ 15 mm. This result is not good enough to provide clinically relevant PET images based on positional information alone, [115], [116].
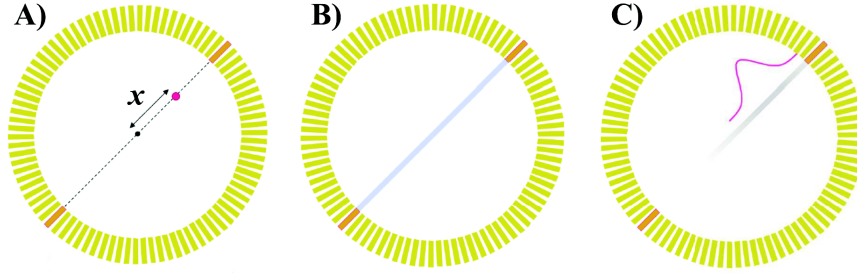
Figure 4.21: The annihilation is at distance x from the FOV centre (A) and in non-TOF PET a flat probability is assigned to the LOR (B), while in TOF a Gaussian probability is assigned to the LOR (C) [92].

However, TOF information can be used to reduce background in back-projection based reconstruction images, as reported in Figure 4.22. This is because in non-TOF PET each event is back-projected with a flat probability along the LOR, while in TOF PET events can be confined assuming a Gaussian probability centered in x with a FWHM of Δx. In conventional PET all volume elements along the LOR contribute to the noise of each image pixel; $n_{non-TOF} = D/d$, where D is the emission source diameter and d the image pixel size. Instead, in TOF PET only the volume element within the annihilation location contribute to the noise, $n_{TOF} = \Delta x/d$. As a result, the improvement in the NECR achieved by incorporating TOF information is described by [115]:

$$NECR_{TOF} = \frac{D}{\Delta x} NECR_{non-TOF}. \qquad (4.11)$$

Thanks to this signal to noise enhancements, the TOF PET iterative reconstruction converges faster to the true image and provides images of better quality, as can be observed in Figure 4.23. This means a reduction either in the scan times or in the radioisotope doses administered, both important advantages from the practical and ethical viewpoints. This would be especially beneficial in large patients, because the improvements are proportional to patient size [117].
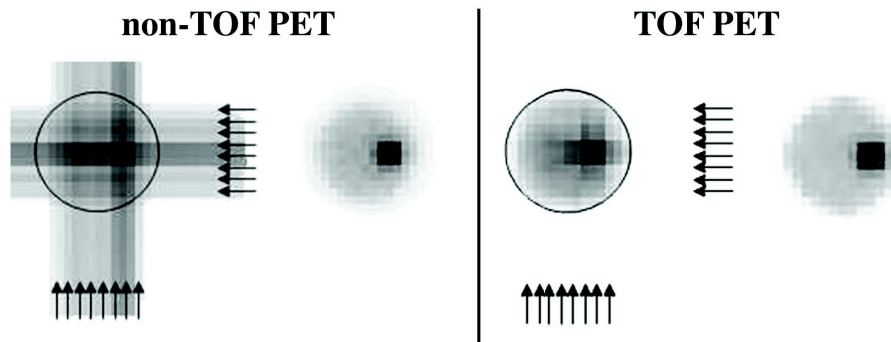
Figure 4.22: The back-projections and the image obtained with iterative method for conventional (left) and TOF PET (right) [115].
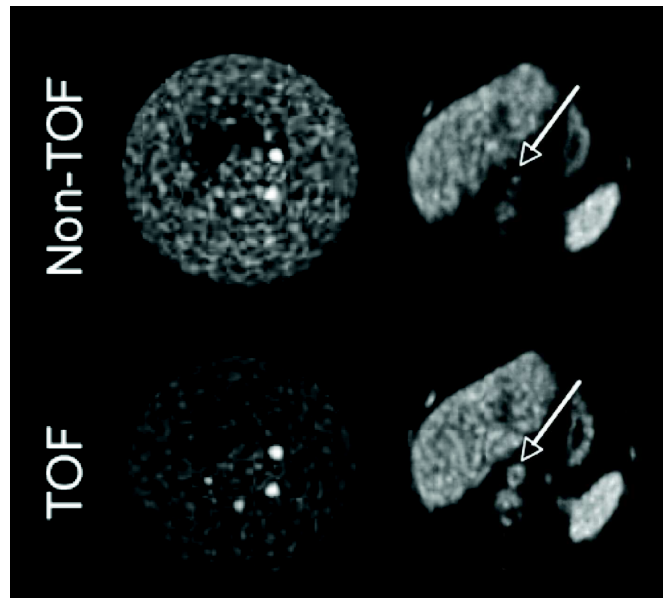
Figure 4.23: Benefit of TOF PET in the image quality assessed with phantom with 2 cold and 4 hot spheres (left) and better lesion detection performance on heavy patient with FDG studies [92].

PET/CT

An important new perspective in the field of nuclear imaging was created by the introduction of combined PET/CT, which is the major responsible for the widely expansion of PET in diagnostic oncologic applications. Now multi-modality represents the state of the art for medical imaging technique. Today all newly purchased and installed PET scanners are PET/CT devices. CT is a transmission technique that provides tomographic images detecting an intense x-ray beam passing through the patient. The attenuation of the x-ray beam reflects the density of the body tissue, giving structural information of different organs [76].

The advantages provided by the ability to combine accurate functional PET information with high-resolution morphological CT information can be appreciated in Figure 4.24 [118]. Compared to two stand-alone machines, the PET/CT scanner reduces examination times, provides greater flexibility, better image quality and quantitative accuracy, improving diagnostic confidence and convenience for the patient. In fact, CT transmission data can be used to derive a precise μ attenuation map to correct the PET emission images, obviating the need for a separate long transmission scan in the dedicated PET system. In general, CT scans permits to anatomically localize lesions found with PET exam. Combined PET/CT scanning is very useful in equivocal clinical situations; a very small tumor can be well detected by PET but missed by CT, while a large tumor with minimal functional deviations may be seen on a CT image, but not on a PET. All the improvements in the image quality and detection capability come at the cost, however, of a higher dose to the patient [119].
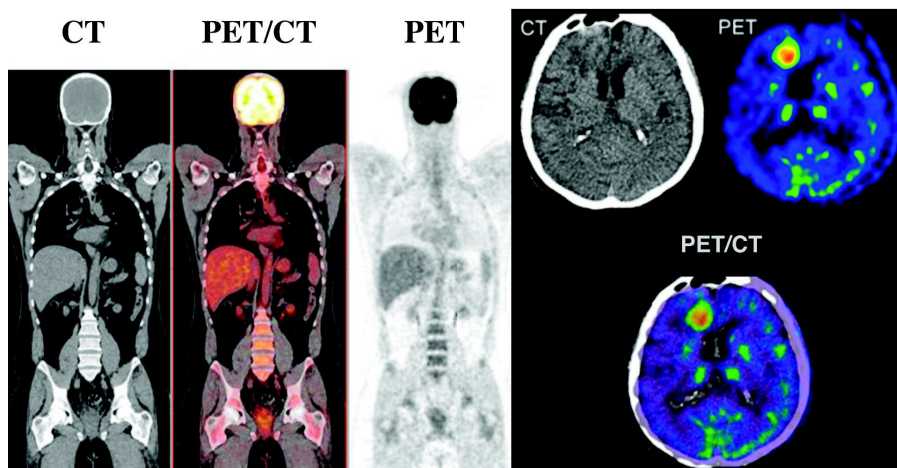
Figure 4.24: CT, PET and PET/CT images of whole body and brain [118].

When the first attempts were made to fuse PET and CT images, several problems were encountered as the two studies were performed on different scanners, and bed profiles and, consequently, organ positions could be significantly different [120]. To circumvent the problems of positional variations, integrated PET/CT scanners were engineered. PET and CT can be acquired sequentially during the same scan ensuring same bed profile, no patient repositioning and very little time between the two studies. All major medical device producers have developed an integrated PET/CT system, and in Figure 4.25 a device from Philips is shown. In all these scanners, PET and CT units are mounted on a common support and they use a common imaging table which axially translates the patient. The CT unit is placed in the front and the PET unit at the back, with the centers of the scan fields separated by a fixed distance. Because of this displacement, the actual scan field is limited by the maximum distance given by the travel range of the table minus the displacement distance.

Also in this operational conditions some issues remain. The CT scan should be performed without injecting contrast agent, which is necessary in oncologic imaging, but can affect attenuation correction map. The contrast agent can

Figure 4.25: The PET/CT integrated scanner by Philips.

be easily confused with bone tissue because of the high Z value, resulting in overestimation of radioisotope concentration. In addition, CT is acquired in breath-holding conditions to reduce movements artifacts, which is not feasible in PET acquisition. This represent a permanent obstacles to good image co-registration and correct μ map estimation. A good solution is to allow respiration during the CT scan, thus reducing errors in μ maps, but reducing the quality of anatomic information near the anterior chest wall [121].

PET/CT whole-body scanning and in brain-dedicated studies has been highly successful in detecting various oncologic conditions and neurologic diseases, while the application of PET/CT in cardiac imaging has faced difficulty because of the motion of the heart.

PET/MRI

Magnetic Resonance Imaging (MRI) provides unsurpassed soft-tissue contrast and does not require the use of ionizing radiation. MRI exploits the nuclear magnetic resonance of protons that, when placed in magnetic fields, absorb and reemit some radio frequencies. Because of different types of tissue have different local magnetic features, MRI images show high sensitivity to anatomic variations, high contrast and a spatial resolution at the millimeter level [71]. Therefore, it is expected that combined PET/MRI scanners represent the future for biomedical imaging, and that these scanners will either supplement or compete with PET/CT for specific clinical applications [122]. Figure 4.26 illustrates the power of this multi-modality system [123]. However, the implementation of MR-compatible PET systems is technically challenging; the basic issue is the mutual interference between the two modalities. The magnetic field can induce currents in PET conductive materials, which distort the effective applied field, or PET electronics can interact with MRI radio frequency. In addition, PMT, that is conventionally used in PET scanners, can not operate in magnetic field [122], [124].

In Philips system a PMT-based TOF PET scanner and a MRI system are co-planar: they sequentially operates in the same room, separated by a face-to-face distance of few meters and a bed placed in between is used to present patients to the scanners (Figure 4.27). This approach is accomplished with a
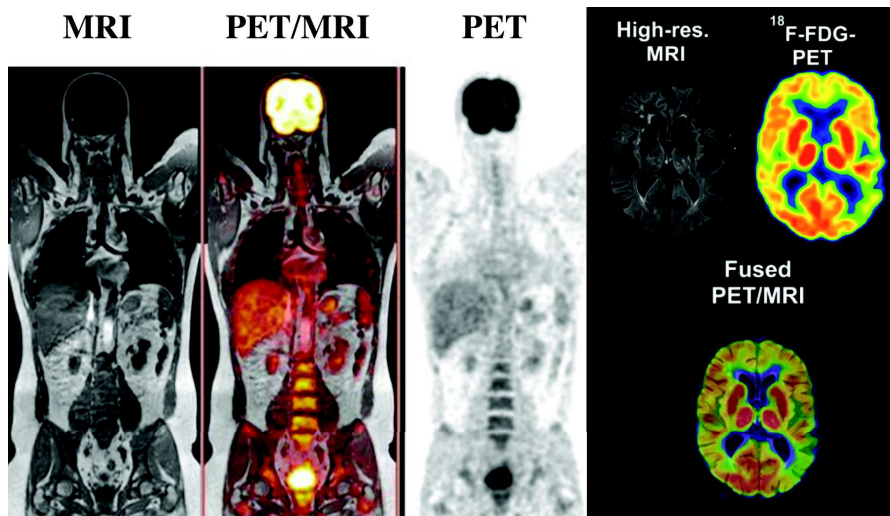
Figure 4.26: MRI, PET and PET/MRI images of whole body and brain [123].

self-shielded MRI machine, which reduces the magnetic field in the PET gantry and, in addition, shielding materials are used to protect individual PMT [92].

The optimal configuration is the full integrated PET/MRI system (Figure 4.27), which does not require the patient transfer, allowing an easy superposition of the images due to their simultaneous acquisition. PMT-based PET scanners have limited performance because long optical fibers are needed to transfer the light signals from the scintillation crystals inside the MR scanner to environments isolated from magnetic fields. A significant light loss occurs during this optical transfer, leading to a degradation of time and energy resolutions [125], [126].
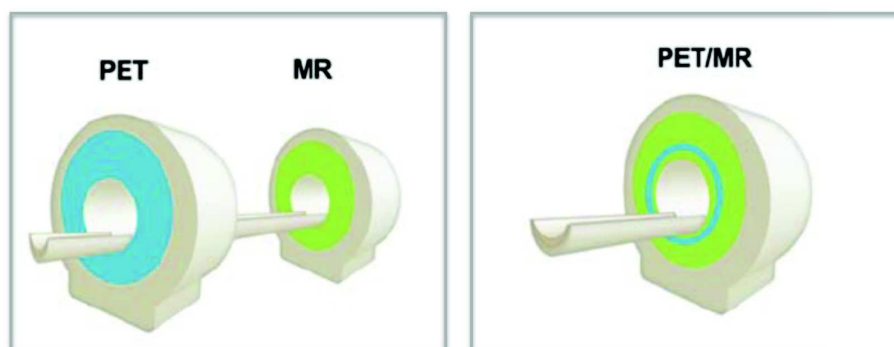
Figure 4.27: The co-planar and the integrated configurations for PET/MRI.

SiPMs represent the best alternative for PET/MR scanners thanks to their withstanding to magnetic fields, high gain and PDE and compactness. In addition, they also exhibit good timing resolution, resulting promising for TOF capable fully integrated PET/MRI scanners. General Electrics has produced a whole body TOF PET/MR integrated systems exploiting this technology [127].

Chapter 5

Small-Animal PET

Small-animal PET imaging refers to studies on animals such as rats and mice using a small, high resolution PET scanner designed specifically for this purpose.

The demand for small-animal PET is driven by the importance of animal model-based research, due to the fact that mouse and rat host a large number of human diseases. With animal models widely used in the basic and preclinical sciences, finding ways to conduct animal experiments more accurately and efficiently becomes a key factor in the success of research. As a consequence, there has been a considerable increase in the need to adopt non-invasive clinical imaging techniques in preclinical research studies. Before the development of small-animal PET, preclinical data could be obtained only through sacrificing and dissecting the tissues of a large number of animals. Since its introduction in the mid 1990s, small-animal PET has been used extensively in modern biomedical research because it offers the possibility to study biochemical processes in vivo and in a non-invasive manner [128], [129].

The main advantage of in vivo imaging is that it provides a bridge from preclinical research to human clinical application, enabling similar and sometimes identical experiments to be carried out across species. In fact, small-animal PET can provide a quantitative measure of the dynamic radiopharmaceutical distribution, enabling the same animal to be studied in a single scan and multiple times over the course of the evaluation [130].

These longitudinal studies allow analyzing physiologic processes and molecular abnormalities at the origin of a disease, characterizing the disease progression, evaluating therapeutic response and developing novel treatment strategies. As a result, small-animal PET represents a key research tool in understanding the disease dynamics. In fact, 70-80% of small-animal PET scanners is concentrated in academic or government research laboratories. Often mice are the experimental model of choice, due to many factors, including fast breeding cycle and decreased housing and maintenance costs. The great advantage offered by mice is the relatively high genetic homology with humans and highly developed methodology for genetic manipulation. In some disciplines, primarily in neuroscience, rats are more favorable as animal models; the larger brain size means better identification of structures in images that have limited resolution [129].

Pharmaceutical companies can also benefit from small-animal PET. For example, before a new drug is tried on patients, there must be extensive data from animal studies on dose, route of administration, bio-distribution, excretion,

together with effectiveness for a clinical indication and toxicity. Preclinical data should be approved (by the Food and Drug Administration for the USA and by the European Medicines Agency for the Europe) before moving on to human clinical studies. In vivo pharmacokinetic and pharmacodynamic studies allow faster screening of investigational compounds and earlier decisions about a compound suitability, thus potentially accelerating and simplifying the new drug development cycle. In addition, thanks to the reduction in the number and cost of laboratory animals used in experiments, there is the potential to reduce drug development costs. Small-animal PET gives also a fundamental contribution to the development of new radio-tracers, mainly for cancer diagnosis, which needs to be previously validated in animals imaging [129].

5.1 Small-animal PET scanners

The physical dimensions of the organs of small animals are of the order of millimeters; the linear dimensions of the brain in mice and rats are, respectively, nearly 15 times and 6 times smaller than in human subjects. The weights of a typical mouse and rat are about 25 g and 300 g: compared with an average-sized adult of 75 kg, mouse and rat are scaled down by a factor of 3000 and 250 in weight, respectively. It follows that a clinical PET scanner is not suitable for studies on mice and rats and a dedicated machine for animals is required to identify the critical organs or target areas. The small animal PET is only seemingly considered as a miniaturized human PET, because the need to achieve a much higher resolution and at the same time a good sensitivity represents a hard task. In fact, to distinguish the same level of structural detail of clinical images, small-animal PET scanners should provide a spatial resolution at the sub-millimeter level for mice and at the millimeter level for rats [129], [131].

Because of the small size of the imaging subjects, a small-animal PET system has a detector gantry that is only a fraction the size of a human PET scanner. For example, typical small-animal PET systems have a detector ring diameter of approximately 150 mm, as compared with approximately 800 mm for clinical PET systems. Reducing the distance between the detectors, the effect of the 511 keV photons non collinearity on the system resolution can be reduced [129].

The primary advancement factor that leads to a very high spatial resolution of recent scintillator based small-animal PET scanners is the use of scintillator crystals with a reduced cross-section facing the imaging FOV and a long side aligned with the radial direction. A drawback of this configuration is the higher probability that the detected photons are not from the head-on interaction but from the side, oblique projections by penetrating the neighboring crystals. This parallax error represents the main factor degrading the spatial resolution of small diameter PET systems with an uncertainty increasing with the distance of the positron source to the center of the field of view. The parallax error can be mitigated and non-uniformity in the spatial resolution can be restored through the use of a few short crystals to replace each single long crystal or by measurement of the depth of interaction within the crystal. Both approaches increase the complexity and the cost of small-animal PET scanners [130], [131].

In fact, even if the reduced size of the gantry offers the advantage of raw material and detector cost saving, the use of thin crystals and the ability to expand the detector rings in the axial direction increase the number of detector

channels. Preclinical PET systems have about 20,000-30,000 scintillation crystals, similar to that used for human PET and, as a consequence, their price ranges between $400,000-$1,200,000, depending on the small-animal PET configuration.

Concerning the sensitivity, the smaller detector ring is advantageous also because it improves the geometric detection efficiency of the system. However, there is a tradeoff between sensitivity and resolution; on one hand smaller crystals enable better resolution, but on the other hand the solid angle covered by a single small area detector element is lower, thus decreasing the sensitivity. This means that there are fewer detected events in each individual crystal, which leads to noisy data and loss of image contrast [129].

The importance of maximizing the system sensitivity and the total number of detected events can be understood considering the image quality. At high spatial resolution a precise image reconstruction is possible only through an increase in the number of detected coincidence events or through the development of reconstruction algorithms that are less sensitive to the noise. Accounting for the relative organ size differences across species, it is possible to calculate a set of scale factors to determine which is the radio-tracer dose needed in a rat or mouse to achieve a signal-to-noise ratio similar to those of human PET studies [132].

The sensitivity plays an important role in receptor binding probes stdies, where low numbers of receptors are present and low occupancy rates are needed to avoid pharmacological effects, thus a low injectable mass of the tracer is required. Depending on the specific activity and the radiochemical yield, this can lead to rather low radioactivity concentrations in the injectable volume and thus a high sensitivity is needed [130].

Mice and rats are much smaller than humans; for this reason, the amount of scattered events and the magnitude of attenuation are both much less in small-animal PET than in human PET. By simple calculation, the fractions of photons transmitted through polyethylene phantom cylinder diameters of 25, 50, and 203 mm length representing mouse, rat, and human are 79%, 62%, and 14%, respectively. The typical values of scatter fractions are 8% and 17% for mouse and rat phantoms, respectively, while scatter is a dominant factor with scatter fractions of up to 36% in human PET [129], [130]. When only qualitative results are required, scatter and attenuation corrections may be skipped in small-animal PET studies. When quantitative animal PET is required, a transmission or CT scan is included in the data acquisition protocol, and attenuation and scatter corrections are enabled in the image generation protocol. Attenuation and scatter correction are also required when, in order to increase the throughput of small animal imaging facilities and also to optimize utilization of a radiochemical synthesis batch, multiple subjects are imaged at the same time [133].

5.2 Review of commercial pre-clinical systems

The first small-animal PET scanners were developed about 25 years ago. Since then, both the technology and the number of small-animal PET have experienced an extraordinary growth. On the technology development side, small-animal PET has been an active research topic since its emergence. This continued endeavor has established the knowledge base for small-animal PET technology. Several small-animal PET systems developed in laboratories have become commercial products. Currently, there are hundreds small-animal PET installed systems.

Among the commercial small-animal PET manufacturers, Siemens Preclinical Imaging has a wider selection of models and owns more than 50% of the world market share of small-animal PET scanners. The globalization of the economy and science has also triggered the proliferation of small-animal PET in emerging development countries such as South Korea, Taiwan, and China [129].

Figure 5.1 shows some of the major commercially available preclinical systems manufactured since 2000 and Table 5.1 reports their main design specifications. The majority of small-animal PET systems are based on small individual scintillators of LSO, LYSO or GSO coupled to photomultipliers. An exception is the LabPET, which uses semiconductor avalanche photodiode [134]. The ALBIRA scanner is made of larger monolithic scintillators coupled to SiPM arrays, capable of 3D interaction point determination [135]. Other systems measure the DOI thanks to the use of different scintillating crystals. In particular, ClearPET is a very flexible system which allows different rotating partial detector configuration and two adjustable ring diameter to image not only mice and rats, but also monkeys and rabbits [136]. Most systems can also offer a combination with a small-animal CT scanner for co-registration of the anatomic image with the PET data. Among these, PerkinElmer developed a very particular solution with a compact size system which breaks away from a conventional ring-based scanner by surrounding the animal with four head panel detectors [137].

In order to compare the performances of different system designs, a standard procedure for preclinical PET system testing was established by the National Electrical Manufacturers Association (NEMA). The NU 4-2008 was published in 2008 and various vendors could provide clear small-animal PET scanners specifications [138]. In Table 5.2 are summarized the main performance measurements obtained following the NEMA method for the major preclinical systems [139] in terms of spatial resolution, sensitivity and scatter fraction.

The spatial resolution and the sensitivity are measured using a ^{22}Na point source of activity confined to no more than 0.3 mm in all directions and embedded in an acrylic cube of 10 mm extent on all sides. The **spatial resolution** is related to the FWHM of the point source response function, obtained by summing all one-dimensional profiles in x,y and z directions from the reconstructed image [138]. The value reported in Table 5.2 refers to an effective FWHM with the source at 5 mm radial position, defined as a geometric mean:

$$\sqrt{\left(\frac{FWHM_{rad,0} + FWHM_{rad,1/4}}{2}\right)\left(\frac{FWHM_{tan,0} + FWHM_{tan,1/4}}{2}\right)}, \quad (5.1)$$

where $FWHM_{rad,0}$ and $FWHM_{rad,1/4}$ are the FWHM radial resolutions at the axial center and 1/4-offset axial position, respectively, and $FWHM_{tan,0}$ and $FWHM_{tan,1/4}$ are the corresponding tangential resolutions. Generally, the spatial resolution is better off-axis because of the more oblique LOR used in the center with respect to 1/4 axial position. The current resolution limit of commercial small-animal PET systems is slightly more than 1 mm. Therefore, the resolution capability of preclinical PET is close to what is needed for rat imaging but not yet fully optimal for mouse imaging. For every system, the spatial resolution exceeds the crystal size, mainly due to signal multiplexing and light sharing at the detector level. The only exception is the LabPET; thanks to its unique acquisition architecture individual signal readout is implemented [139].

Figure 5.1: Preclinical PET systems commercially available: (a) microPET, (b) ClearPET, (c) LabPET, (d) Albira and (e) Genisys.

Manufacturer	Model	Detector design	Crystal type	Ring diameter (mm)	Axial FOV (mm)	Crystal size(mm^3)	Additional features
Siemens	microPET P4/R4	block, 8x8 PSPMT	LSO	261/148	78	2.2x2.2x10	
Siemens	microPET Focus 220/120	block, 12x12 PSPMT	LSO	258/147	76	1.51x1.51x10	
Siemens	Inveon	block, 20x20 PSPMT	LSO	161	127	1.51x1.51x10	
Philips	Mosaic HP	pixelated Anger logic PMT	LYSO	197	119	2x2x10	
Raytest GmbH	ClearPET	block, 8x8 PSPMT	LYSO LuYAP	135-225	110	2x2x10 2x2x10	Rotating ring, DOI
Sedecal	Argus	block, 13x13 PSPMT	LYSO GSO	118	48	1.45x1.45x7 1.45x1.45x8	DOI
Sedecal	VrPET	block, 30x30 PSPMT	LYSO	140	45.6	1.4x1.4x12	Partial and rotating ring
Gamma Medica	LabPET 8/12	2 crystal per APD	LYSO LGSO	162	75/112.5	2x2x11.9 2.2x2.2x13.3	Individual readout
Mediso	NanoPET	12 modules per ring, PSPMT	LYSO	181	94.8	1.12x1.12.13	PET/CT
Bruker	ALBIRA	12x12 SiPM	LYSO monolithic	111	148	50x50x10	DOI
PerkinElmer	Genisys 8	4-head panel	BGO	50*	94	1.8x1.8x7	PET/CT benchtop

* Corresponds to the opening of the PET scanner, not to the ring diameter.

Table 5.1: Design specification of commercial preclinical PET scanners.

Model	Effective FWHM (mm)	Resolution/ crystal size	Energy window (keV)	Peak detection efficiency (%)	Mouse scatter fraction (%)	Rat scatter fraction (%)
microPET P4/R4	2.24/2.20	1.02/1.00	350-650	1.19/2.06	5.2/9.3	16.7/22.2
microPET 220/120	1.78/1.74	1.18/1.15	350-650	2.28/3.42	5.6/7.2	20.3/19.3
Inveon	1.64	1.08	350-625	6.72	7.8	17.2
Mosaic HP	2.34	1.17	385-665	2.83	5.4	12.7
ClearPET	2.02	1.01	250-650	3.03	31.0	
Argus	1.66	1.14	250-700	4.32	21.0	34.4
VrPET	1.61	1.15	100-700	2.22	11.5	23.3
LabPET 8/12	1.64	0.82	250-650	2.36/5.4	15.6/16.0	29.5/29.3
NanoPET	1.6	1.43	250-750	7.7		
ALBIRA	1.55*		350-650	2		
Genisys 8	1.4*	0.8	150-650	14		

* Spatial resolution measured in the central FOV.

Table 5.2: Performances of commercial preclinical PET scanners.

The **sensitivity** is measured positioning the source in the trans-axial centre, moving the source along the axial direction and recording the event rate. The latter is then corrected for random events and normalized to the source activity [138]. The largest factor affecting the detection efficiency is the solid angle coverage of the detector ring. In fact, scanners with longer axial FOVs and smaller bore diameters exhibit the highest sensitivity. The Inveon scanner with the rather long axial FOV of 127 mm (161 mm ring diameter) has a reported sensitivity of 6.72%, whereas the Genisys scanner with the smaller opening of 50 mm combined with a 94 mm axial FOV exhibits an even higher sensitivity of 14% [130], [139].

In order to measure the NECR and the Scatter Fraction a line source filled with ^{18}F is inserted along the length of a high-density polyethylene cylinders, representing a mouse phantom (70 mm long, 25 mm diameter) and a rat phantom (150 mm long, 50 mm diameter) [138]. The high activity source is positioned in the FOV centre and the counting rate measurements allow to find the NECR. As time lapses, the source decays and when the ratio between the random events and the true events is less than 1%, the scatter fraction can be measured [139].

Figures 5.2(a) and 5.2(b) show the **NECR** counting rate versus activity curves for the systems being qualified for the mouse and rat phantoms, respectively. The general shape of the curves is similar for all systems, with an extended linear range below the peak NECR value. The peak NECR value and activity level at which it occurs represent a complex interplay between system design factors. When the microPET R4 is compared with the microPET Focus 120, its improved sensitivity results in significantly higher NECR values at lower activity levels than for the microPET R4. The effects of an extended axial FOV can be seen by comparing the LabPET 8 with the LabPET 12: the NECR peak is higher for longer axial FOV. The effects of system ring diameter can be seen by considering the microPET P4 and microPET R4 results for the rat phantom. The peak NECR for the two systems is similar; however, the activity at which peak NECR occurs is larger by nearly a factor of 2 for the higher ring diameter system. The Inveon system had the highest values of peak NECR for the mouse and rat phantoms; a key reason is the minimal block dead time due to the processing electronics, which allow minimal pulse shaping before digitization with 100 MHz analog-to-digital converters and a timing window of only 3.4 ns [139].
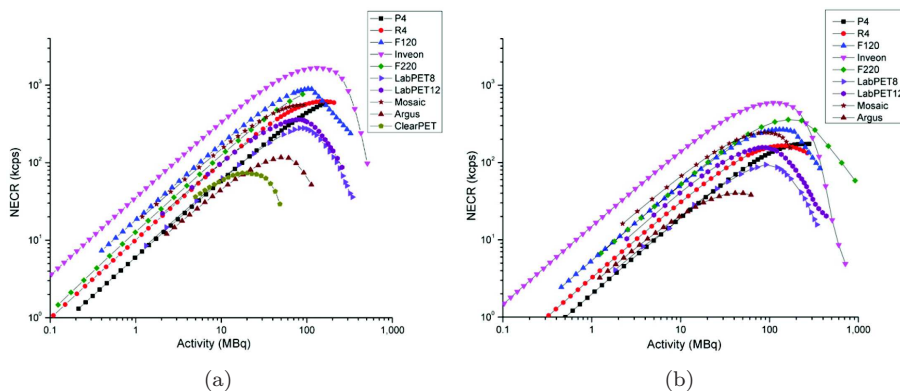
Figure 5.2: NECR vs. activity for (a) mouse and (b) rat phantoms.

As expected, the **scatter fraction** is generally lower for larger-ring systems and for narrower energy windows. The exception is the VrPET system, which uses an energy window of 100-700 keV but has a scatter fraction lower than that of any system with a 250- to 750-keV window. The most likely reason is that the VrPET is a partial-ring system and thus has less scatter from gantry materials. The scatter fraction is lowest for systems that use conventional single-layer block detector designs, such as the Siemens family of systems, or the pixelated Anger logic approach of the Mosaic HP, while the highest observed scatter fractions are for the 2 dual-layer ClearPET system and the monolithic detector of Argus. This can be related to several factors: event mispositioning in the block, high levels of gantry scatter events, the effect of scintillators with lower photofractions and the smallest ring diameters, which affect the amount of gantry scatter. The LabPET systems, with their individual crystal readout design, have scatter fractions between these two extremes [139].

5.3 Animal specific factors

Several animal specific factors affect preclinical imaging measurements. Overall, the biological variability, which is about 15-20% even considering the same strains of animals with the same sex and age, exceeds all the scanner related factors. Therefore, great care should be taken to optimize all factors that could lead to large standard deviations in small-animal PET imaging research such as anesthesia, temperature, diet, injectable volumes and others [130].

Rats and mice are not as cooperative as humans. A large number of small-animal PET imaging studies are performed under general anesthesia to render the subjects motionless. The most common anesthesia method is the use of an inhalant mixture of isoflurane and oxygen gases. By constantly adapting the isoflurane level it is possible to achieve quite long anesthesia periods up to several hours without adverse complications. Another method well suited for short imaging protocols is the use of injectable anesthetics such as ketamine or xylazine. The use of anesthesia and of the carrier agent can induce a perturbation of the animal physiology and can alter the outcome of a study: the lowest possible dose of anesthetic should be used to minimize these side effects [140].

The most important factor when putting an animal under anesthesia is temperature control. Because of their small bodies, the physiologic conditions of mice and rats are more susceptible to environmental changes. During anesthesia their internal body temperature quickly equilibrates to the temperature of the surface they are placed upon. Therefore the animals become hypothermic and can easily die within minutes. Almost every metabolic process is altered by temperature changes, including enzymatic activity, blood flow and muscle activity. Since it is important to ensure that the animal remains in a fully recoverable physical state through several imaging sessions and the goal is usually to measure normal metabolism, a heating source (light bulb, air flow, or pad) is used to maintain the animals body temperature at all stages of the experiment. In addition vital signs must be monitored to verify the animals homeostasis throughout the whole imaging procedure [141].

The posture of the animals inside the scanner can affect the image results and position consistency must be ensured during a longitudinal study. Several different imaging chambers offer the possibility of some fixation devices such

as tooth bars or ear plugs: they allow holding the animals in specific positions determined by the investigators, guaranteeing the reliability and reproducibility of PET data. Figure 5.3 shows an imaging chamber used to help restrain the animal while providing anesthesia and oxygen gas during image acquisition [129].
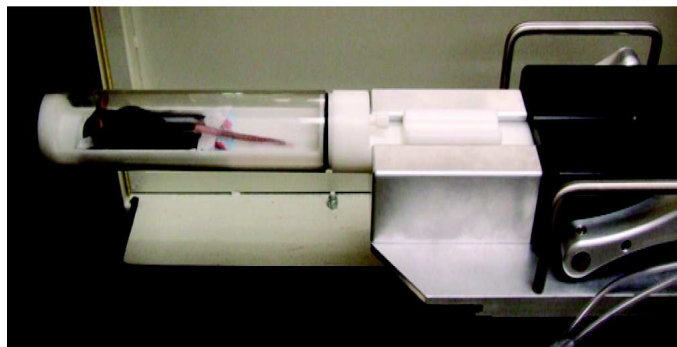
Figure 5.3: A tube designed to facilitate anesthesia and positioning consistency.

The housing conditions for animals can have a significant impact upon physiology and imaging results. Since animals spend nearly all of their time in the vivarium, the bedding amount, type, cage changing frequency, light/dark cycle, room temperature and humidity are the primary factors that influence the biology under investigation. In the last years, caging system has been shifting to individually ventilated cages, where animals are protected by use of air filters that defends them from all micro-organisms. These cages allow for multiple health status and mouse types to be housed adjacent to each other [142].

In addition, measurements can be dependent on the fasting state of the animals. The duration of the fast and the type of food can alter factors such as glucose level, which in turn can alter PET metabolic signals [143].

Animal monitoring and supportive care aims to maintain the animal physiological status as near to normal as possible and to minimize animal pain and distress. Monitoring of vital signs and potential signs of pain should be done throughout the whole animal handling procedure. It can either be performed visually, by watching the respiration, the color of mucous membrane and skin or manually, by testing the jaw tone, feeling the heart rate, respiration rate and body temperature. In most preclinical scanners visual and/or manual monitoring is not possible due to the small bore sizes and restricted space inside the scanners. Another possibility is using electronic monitoring systems, which is a very helpful and reliable tool, especially during imaging scans [130].

The tracer mass injected into a small animal must be sufficiently low that the natural physiologic state of the animal is not affected. The rule of thumb is that the tracer mass will cause a maximal receptor occupancy of 1%. Another constraint is that the total injection volume should be less than 10% of the animal blood volume, which is 30 and 2.5 mL, respectively, for rats and mice. For example, it was estimated that the maximal injected radioactivity of ^{11}C-labeled raclopride should be 5.2 MBq in rats and 0.3 MBq in mice [129].

In addition, the administration itself has to be performed reliably. Highly trained personnel are required in order to deliver all the radioactivity reproducibly from the syringe into the blood stream. If one is only interested in a static

image post injection, then this error is not dramatic, but for a dynamic study where one is interested in the kinetics of the radio-tracer, a paravenous injection severely confounds the results. Development of automatic injection systems, near infrared light, image processing techniques, computer controlled motors and a pressure feedback system was used to insert the needle and to validate the proper location within the tail vein [130].

5.4 Small-animal PET applications

Small animal imaging can be applied to study any organ or tissue whose physical dimensions are consistent with the spatial resolution of the PET scanner.

Oncology is the primary application of small-animal PET; longitudinal studies allow tissue characterization, disease modeling, staging and therapy control. As in human PET, ^{18}F is the most used tracer in monitoring glucose metabolism. There exist many other targeted mechanisms, such as tumor cell proliferation, gene expression, tumor angiogenesis, tumor hypoxia and tumor apoptosis. New drugs can also be radio-labelled to investigate pharmacokinetics and probe their mode of action and efficacy. Figure 5.4 shows a small-animal PET study for evaluating a new agent for cancer diagnosis and treatment. The FDG image was acquired as a reference to evaluate the agent as a diagnostic and therapy follow-up tracer. The same mouse was then injected with a ^{124}I-labeled derivative of pyropheophorbide-a, a bifunctional diagnostic and therapy agent. Because of the ^{124}I long half-life (4.2 d), a longitudinal study has been possible; tumor uptake relative to the rest of the body increased over time, indicating that the agent has promising potential as both therapeutic and tumor-monitoring agent [144].
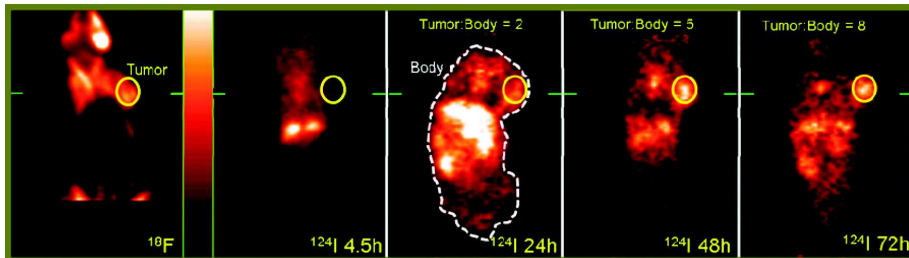
Figure 5.4: FDG image on left and ^{124}I-labeled agent image at 4.5, 24, 48, and 72 h after injection. Concentration ratios in tumor (solid-line circle) to that in animal body (dashed outline in middle image) indicate that agent has desired properties to be used in therapeutic and monitoring applications.

Small-animal PET has been validated for a reliable and serial investigation of **cardiac physiology**. Imaging techniques to minimize wall motion effects such as electrocardiogram-gated data acquisitions and the corresponding image analysis approaches developed for human PET cardiology can be applied on small animals. Figure 5.5 shows an example of small-animal PET imaging with FDG of the cardiac functions of a normal rat and a rat with myocardial infarction. The electrocardiogram gating eliminates the image blurring due to cardiac motion and higher image contrast and definition are achieved [145].
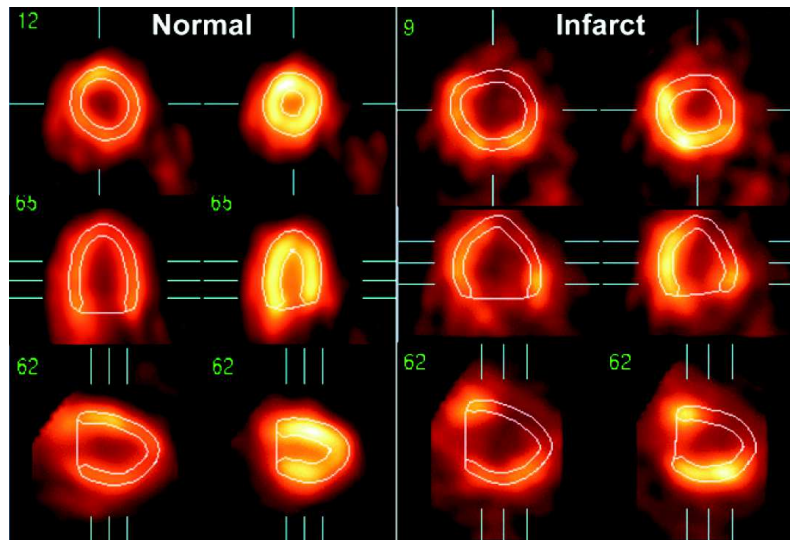
Figure 5.5: Electrocardiogram-gated FDG study in normal and infarcted rat.

Small-animal PET is an established diagnostic procedure also in **neurology**, applied to monitor neurotransmitter function in vivo over time and to find the correlations between radio-tracer distribution and behavioral parameters. Over the years, a wide selection of PET radio-tracers has been developed for brain imaging, such as $H_2{}^{15}O$ for measuring cerebral blood flow, ^{18}F for measuring glucose metabolism and ^{11}C compound for imaging b-amyloid deposition. Using these tracers, small-animal PET has many applications for studying the patho-physiology, pharmacology, drug mechanisms and brain tumors. Figure 5.6 is an example of a small-animal PET application in neuropharmacology. The study was to quantify how P-glycoprotein and its blockade with cyclosporin A affect rat brain uptake of ^{11}C-compound. Two regions of interest on the left and right hippocampi are imaged after injection within time intervals for kinetic modeling. From the total-brain images of the control and cyclosporin A-treated rats it is clear that when the efflux of the P-glycoprotein was blocked with cyclosporin A, the rat brain uptake of ^{11}C-compound increased significantly [146].
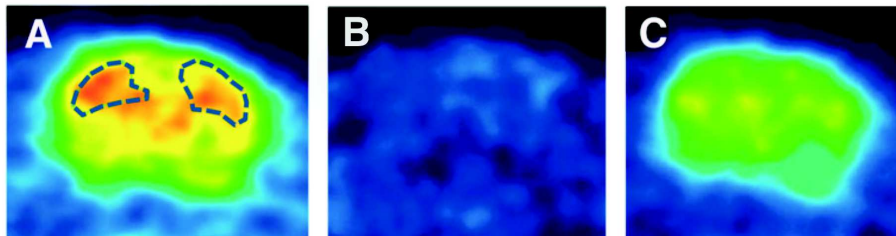
Figure 5.6: ^{11}C rat brain image: regions of interest on left and right hippocampi (A) and total uptake in control (B) and in cyclosporin A-treated rats (C).

5.5 Cutting-edge developments

Although small-animal PET has established its position in molecular imaging, many exciting new technologic developments are bringing the methodology to the next level [129], [130].

In standard small-animal PET setup the subject rodent lies on an animal bed within a fixed gantry. Any motion would cause displacement of detected events and therefore undermine image quality. Forced immobilization or anesthesia are the only available means to minimize animal movement, although it is well known that they can lead to unusual physiologic responses in the animal that may affect the experimental results. Recently, two revolutionary better alternatives have just emerged that are capable of imaging conscious animals. The first is enabled by a miniaturized small-animal PET scanner that a rat can wear (Figure 5.7(a)). Weighing only 250 g, the detector ring and front-end electronics of the scanner are fitted to the head of a rat and attached to an animal mobility system that allows the rat to move freely around a 40x40 cm^2 behavioral chamber while PET images are acquired [147]. The second involves a small-animal PET detector system that surrounds a chamber and a precise and continuous tracking system that determine the position of the rodents head over time during an imaging session. For image reconstruction, the tracking information is used to align the detected PET events to form a coherent animal body volume. These new techniques allow assessing brain function and behavior in response to a wide variety of interventions in freely moving, non-anesthetized rodents [148].

<center>(a)   (b)</center>
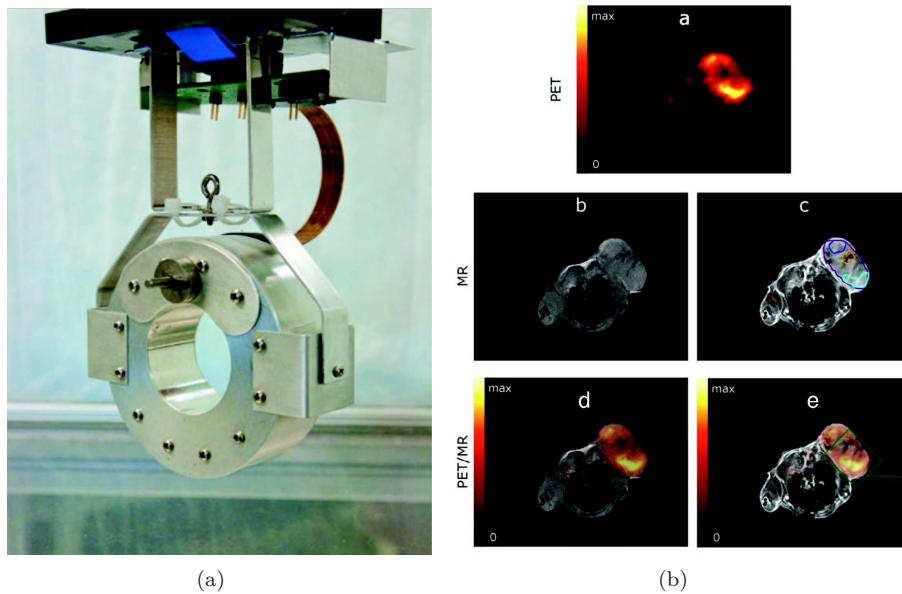
Figure 5.7: (a) RatCAP, a miniaturized wearable PET for conscious rodent brain imaging. (b) PET (A), pre (B) and post (C) contrast MRI and fused PET/MRI (D,E) images. In tumor areas a low uptake of the marker in PET images corresponds to shallow uptake of MR contrast media, indicative of necrosis.

As with human PET imaging, there are ongoing efforts to integrate small animal PET with complementary imaging modalities. The integration of PET and CT has demonstrated the strength of the fusion of anatomic and functional imaging. Using the same strategy, the integration of PET with MRI is the latest breakthrough in multimodality imaging developments [149], [150], [151]. Compared with CT, MRI has three critical advantages: superior soft-tissue contrast, simultaneous imaging with small-animal PET and freedom from ionizing radiation. These advantages make integrated small-animal PET/MRI an enabling technology for creating a new field in molecular imaging and opening new insights into the organization of the brain and its changes in disease [129]. For example, integrated small-animal PET/MRI may be used to assess cell replacement approaches for treatment of various neurologic disorders. First, the stem cells are labeled with MRI contrast-enhancing agents, then the migration of the transplanted cells can be imaged in the morphologic context of MRI, and their viability and function can be imaged in the functional context of PET [152]. Encouraging results in the field of oncology have already been achieved using PET/MRI animal scanner. As an example, Figure 5.7(b) reports the PET/MRI imaging results for a mouse bearing a colon tumor [153]. Regions of interest in the MR images show an increased contrast enhancement in those areas of the tumor have high ^{18}F uptake and a slow contrast in those tumor areas having low ^{18}F uptake, identifying necrotic areas in the core of the tumor. This discrimination can be identified only by interpreting the MR contrast time-signal curves; the PET images alone would not have disclosed such information.

Future efforts in small animal PET imaging technology will continue to push the limits of both spatial resolution and detection sensitivity. Overcoming the sensitivity limitation of very high spatial resolution in small animal PET will require novel detector designs and advanced image reconstruction algorithms with a reduced sensitivity to the noise in the raw data collected by these systems. The ultimate utility of small animal and human PET imaging will depend on the availability of molecular imaging agents that target specific biological processes. Most PET tracers available today measure receptor expression or enzyme activity, but these are not typically the underlying processes that lead to disease. Therefore, one of the important future directions for PET imaging is targeting gene expression. Early efforts in this area include imaging of reporter genes in which genes that express uniquely identified proteins or enzymes are incorporated into regulatory regions of genes of interest. A PET tracer specific to the reporter proteins is then used to examine the expression of the reporter over time. The long range goal is to identify approaches that enable the assessment of gene expression without the need to transfect cells with reporter genes [132].

Chapter 6

EasyPET: the principle and the concept demonstrator

Preclinical PET systems are used to study human diseases and validate new drugs and therapeutics through the study of animal models, as well as to develop new radio-pharmaceuticals. Despite the high sensitivity and diagnostic power of PET imaging, there are two strong limiting factors to the adoption of preclinical PET technology: high complexity and cost. In fact, preclinical PET scanner are unbearable for most research institutions and universities.

The EasyPET described here is an innovative concept protected under a patent filed by Aveiro University (WO201/147130), which can be exploited to achieve a simple and affordable preclinical PET system. The EasyPET, original in its operating principle and image acquisition method, is based on a single pair of detectors and a rotating mechanism with two degrees of freedom, reproducing the functionalities of an entire PET ring.

A first device has been realized by Aveiro University to assess the easyPET concept and optimize the system electronic circuit for coincidence counting and image acquisition. Using these indications, a second device was developed as a demonstrator of the EasyPET concept by the collaboration of the research group of Insubria University and of Aveiro University.

In this chapter the detailed qualification of this 2D imaging device, in terms of signal quality, energy resolution, spatial resolution and image contrast will be presented. Starting from the characterization, all the potential and the strength of the EasyPET concept emerged, as its intrinsic immunity to parallax errors and the possibility to accept coincidence events from Compton scattered events, which results in a good and uniform spatial resolution. In addition, some issues related to the electronic readout have been identified, with an impact on the signal quality and spectrum energy resolution which affects the possibility to lower the energy threshold and to measure the system sensitivity.

The EasyPET outreach activity through the demonstrator allowed to found new partners participating in the project. In particular, a great achievement is the collaboration with Nuclear Instrument and Caen S.p.a., leading to the EasyPET licensing to Caen S.p.a. and the prototype commercialization as a product for the educational market addressed to high level teaching laboratories.

6.1 The EasyPET operating principle

The easyPET concept is based on a single pair of collinear detectors that move together and execute two types of independent movements, around two rotation axes in order to provide the 2D image reconstruction of the position of positron emitting sources. The operating principle is sketched in Figure 6.1.
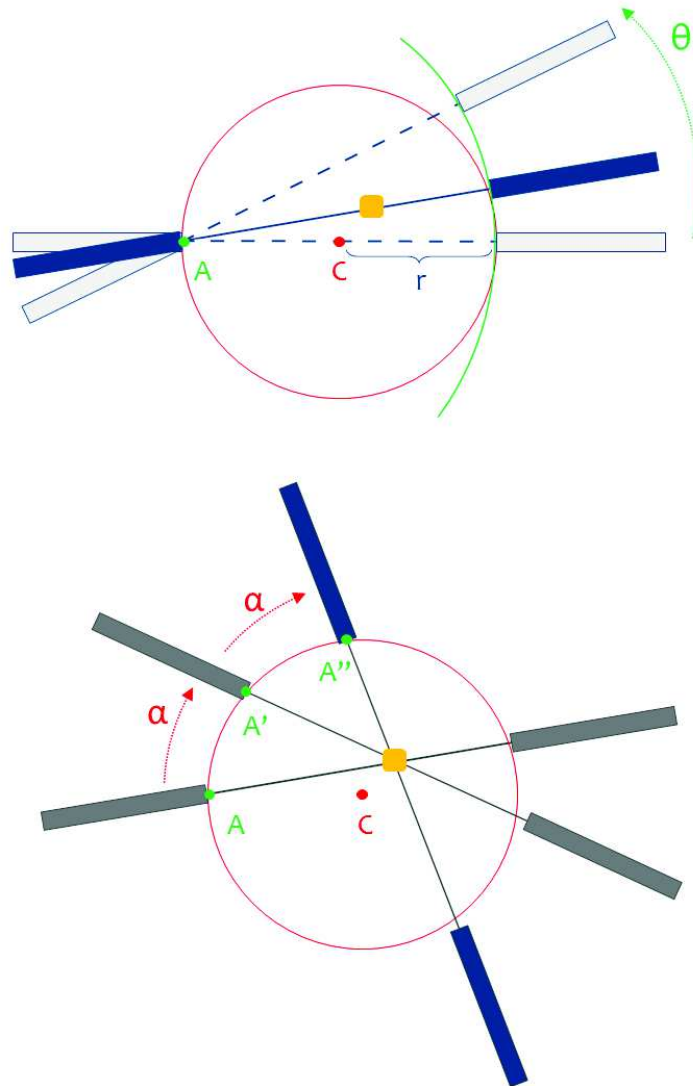
Figure 6.1: The EasyPET principle of operation. The square represents the β^+ source placed in an off-centre position. The letter C indicates the rotation centre, coincident with the system center. The letters A, A' and A" identify the scan centers within the same acquisition, corresponding to the centre of the detector surface. The solid lines are LORs determined during each scan.

The detectors are mounted on a structure at distance $2r$ with respect to the system centre, C, which corresponds also to the one of the two rotation axes. Presuming the detectors to execute only the rotation around C, a positron source located in the centre of the FOV would induce, for every azimuthal detectors position, the simultaneous detection of the isotropically distributed back-to-back photons resulting by the positron annihilation. However, for every off-centre position, coincidence detection would occur for a unique angle, preventing the reconstruction of the source position. This problem is overcome in the easyPET concept by introducing a second degree of freedom and modifying the scan movement as follows:

- the detector pair performs a scan of range θ moving along an arc of circumference with the axis located on the front face centre of one detector, e.g. position A in the top picture of Figure 6.1;

- the θ scan axis is then moved in a sequence of positions A', A" and so on (shown in the bottom picture of Figure 6.1), by a rotation of the system of an angle α along the circumference centered in C;

- in each position a new θ scan is repeated, until a whole rotation of the system around the centre is completed.

During each θ scanning movement, a positron source, irrespective of its location inside the FOV, will induce a coincidence detection at the α dependent azimuthal angle, determining a LOR. As a result, after the complete system rotation, the provided series of LORs allows the image reconstruction and the identification of the source position.

This novel concept represents a breakthrough in terms of reduction of the system complexity and cost, by reducing the number of detectors required for the acquisition of a PET image. Moreover, the present invention is bound to be robust against image aberration effects due to non-collinear photon emission, scatter radiation and parallax error, since the crystal pair is always kept aligned and collinear during the imaging. The original implementation of the acquisition method based on two degrees of freedom ensures a uniform spatial resolution without the need to measure the DOI. In fact, existing systems with a partial ring of detectors rotating only around their central axis suffer from a degradation of the spatial resolution in peripheral regions of the FOV due to the parallax error. As a consequence, they have to implement methods of correction through DOI determination, enhancing the cost and the complexity of the scanner.

However, sensitivity may be expected to be an issue, because of the reduced geometrical acceptance given by the use of only two detectors. This limitation could be partially compensated with the possibility to accept events with a low energy threshold. In fact, standard apparatus have to discard photons from Compton scattering events using hard energy cut at about 350 keV. In order to obtain as much as possible true coincidences, they have to sacrifice the overall sensitivity [139]. On the other hand, the EasyPET concept, with the detector pair kept collinear during acquisition, is intrinsically immune to scatter radiation and allows accepting Compton scattering events without image degradation effects. As a result, the energy threshold could be in principle decreased to the level at which the random coincidence event rate is negligible.

A thorough investigation is worth to analyze the net balance of advantages and disadvantages of the EasyPET concept with respect to the standard approaches.

6.2 The EasyPET design layout

The schematic layout of the components required to implement the EasyPET concept is shown in Figure 6.2. The two types of movement around two different axes are implemented using two stepper motors.

The bottom motor has a fixed axis centered at half distance between the detectors pair. It defines the center of the FOV and the centre of the system. It supports and performs a complete rotation, in predefined steps of amplitude α, of a second motor (top motor). The top motor is moved along a circumference of radius equal to the distance between the two axes, r. The top motor supports through its axis a U-shaped printed circuit board, where a pair of aligned and collinear detector modules is mounted. The frontal face of one detector is positioned along the top motor axis, allowing the U board to perform a symmetric scan of range θ with respect to the center C for each position of the bottom motor. This scanning movement is alternated clockwise and counterclockwise in order to minimize the acquisition time.

The diameter of the field of view is defined by the amplitude of θ, the range of the top motor scan. In this way, EasyPET can identify a β^+ source placed anywhere within the free cylindrical region between the pair of detectors. Each detector is composed of a scintillator crystal optically coupled to a Silicon Photomultiplier; the detector unit provides a signal when a photon interacts in the crystal and its scintillation light is detected by the SiPM.
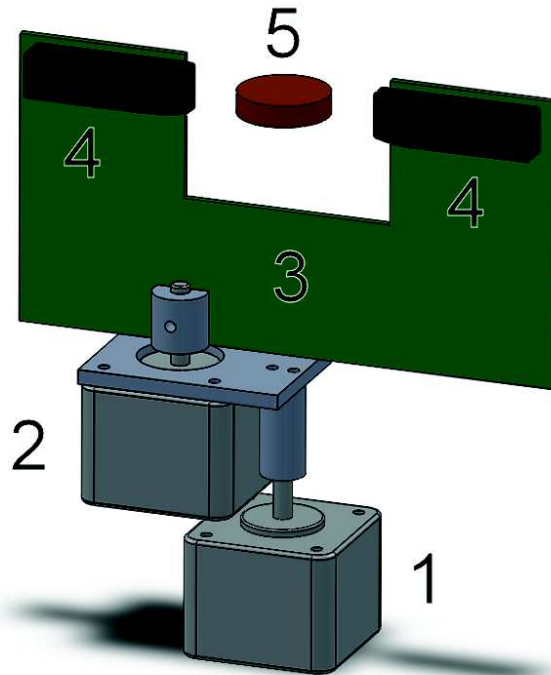
Figure 6.2: The EasyPET component layout: 1 - bottom motor, 2 - top motor, 3 - Printed Circuit Board, 4 - pair of detector modules, 5 - radioactive source.

The block diagram of the electronic circuit is sketched in Figure 6.3. It is composed by a power supply that polarizes both SiPMs with the same bias voltage and by a fast readout system that allows to detect coincidence events from the two detectors. It consists of amplification and discrimination circuits applied on individual detector signals and of a coincidence logic between the two discriminator outputs. If the amplified signals from each detector exceed a fixed threshold and occur within a specific time validation window, they are considered as a coincidence event. For each scanning position, the number of coincidences occurring during a predefined time window is recorded. A controller unit, which is responsible for the stepper motors movements, is also used to acquire and communicate to the computer the angular position of the motor axes and the number of coincidences in each system position to accumulate the lines of response and reconstruct in real-time the image of the source distribution.
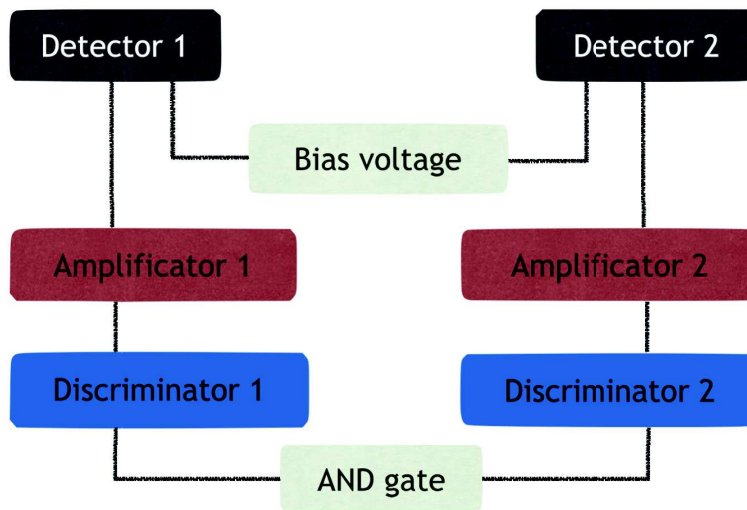
Figure 6.3: The EasyPET electronic circuit scheme.

6.3 The image reconstruction algorithm

The data are recorded with the list mode organization: event by event the angular position of both motors and the number of coincidence counts are saved. The online image reconstruction is performed using a back-projection algorithm. The basic idea consists in the discretization of the FOV in order to create a correspondence between the line of response and the pixels of the image.

A matrix of 10×10 cm^2, enough to mapping the maximum possible FOV, is created. The matrix is made out of pixels of a dimension that can be chosen in the range 0.5-2 mm, reproducing the desired image granularity. Then, event by event, the angular position of the motors is converted in Cartesian coordinates to determine the position of the crystals front face in the matrix. The LOR is the straight line connecting the two crystal front face positions. In order to establish which elements of the matrix correspond to the LOR, the following algorithm is applied. The procedure is schematized in Figure 6.4.

As a first step, the projection of the LOR on the x axis of the matrix is divided in many elements as the matrix size, obtaining the vector $\tilde{x}$. Then the vector of the projection of the LOR on the y axis, $\tilde{y}$, is obtained by applying the straight line transformation:

$$\tilde{y} = m\tilde{x} + q, \tag{6.1}$$

where m and q are determined by the two crystal front face positions. As a result, the element step is different on the two axes but the number of elements is the same. The correspondence between the elements of the $\tilde{x}$ and $\tilde{y}$ axes and the elements of the x and y axes is determined with a proportion and a rounding up to the higher entire element value. The net effect is the association of multiple elements of $\tilde{x}$-$\tilde{y}$ to the same element in x-y. As an example, the vectors on x and y determined in Figure 6.4 are:

$x = [6{-}7{-}7{-}8{-}8{-}9{-}9{-}10{-}10{-}11{-}11{-}12{-}12{-}13{-}13{-}14{-}14{-}15{-}15{-}16]$

$y = [8{-}8{-}9{-}9{-}9{-}9{-}10{-}10{-}10{-}10{-}10{-}11{-}11{-}11{-}11{-}12{-}12{-}12{-}12{-}13]$

As a final step, the matrix elements corresponding to the LOR are identified by the set of coordinates $(x_i;\ y_i)$. These pixels are filled with the number of coincidence counts recorded for that specific motors position. In practice, only the elements of the matrix crossed by a certain portion of the LOR are taken into account for the reconstruction of the image. The fact that the number of coincidences is assigned to each selected element means that each point of the line has the same probability to be the emission source. This represents a fundamental assumption of non TOF-PET devices.
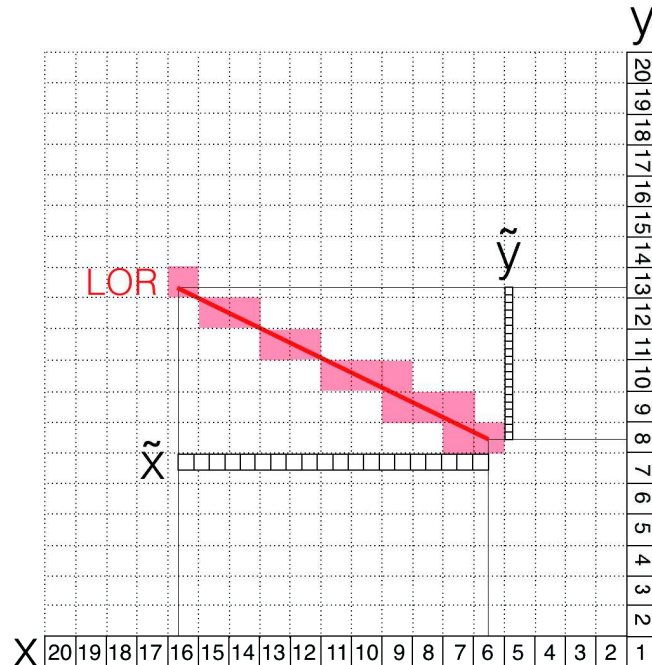
Figure 6.4: The image reconstruction algorithm.

6.4 The EasyPET proof-of-concept module

The first device, shown in Figure 6.5, has been developed by Aveiro University as a proof of concept of the EasyPET operating principle.
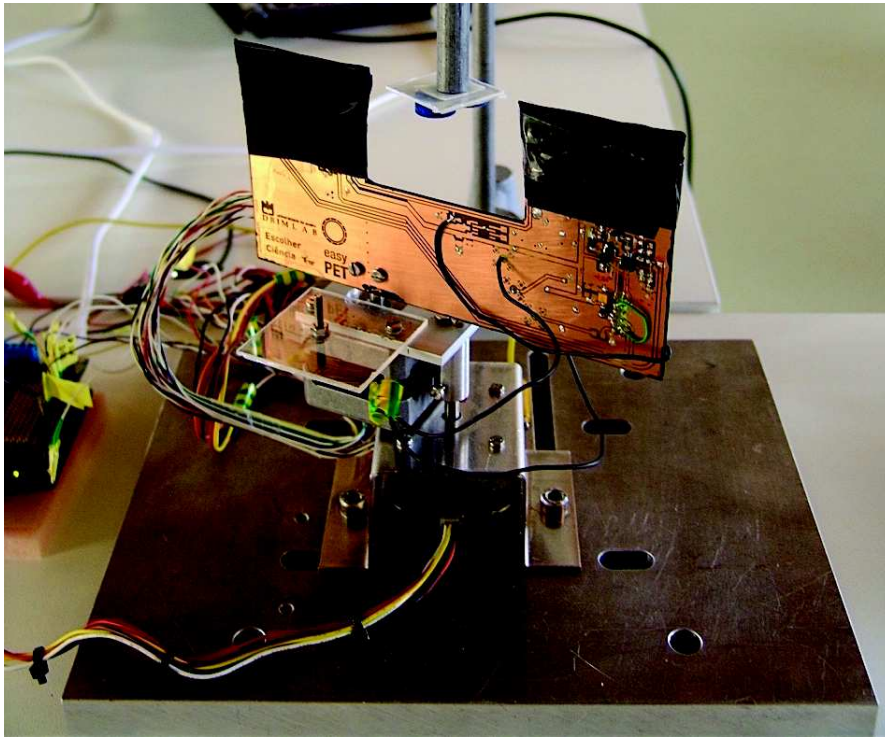
Figure 6.5: The EasyPET proof of concept.

The detecting unit is composed by a LYSO scintillating crystals with dimensions of $2{\times}2{\times}30$ mm^3 produced by Kinheng Crystal (China) [154] and wrapped with an aluminum foil to optimize the light collection by reflecting the light back into the crystal. The only face not covered by the aluminum foil is the one that is coupled with an optical grease to the SiPM. The light detector is a $1{\times}1$ mm^2 MPPC produced by HAMAMATSU Photonics (Japan). A small board is used to house the Surface Mount Technology (SMT) SiPMs. It is also equipped with adjustable pins for the sensor positioning on the PCB. The whole detecting unit is covered with black tape in order to protect it from the ambient light. The LYSO crystal and the SiPM are shown in Figure 6.6(a), while their features are reported in Table 6.1. The crystal front faces are at a distance of 5.77 cm.

The PCB integrates the detector power supply circuit and the front-end electronics, including a signal amplifier and a discriminator for each detector and a time coincidence logic. In this first version some components were still analog because their values had to be properly set; for example, the coincidence time was fixed to 240 ns because the length of the discriminator output could not be adjustable.

(a)   (b)
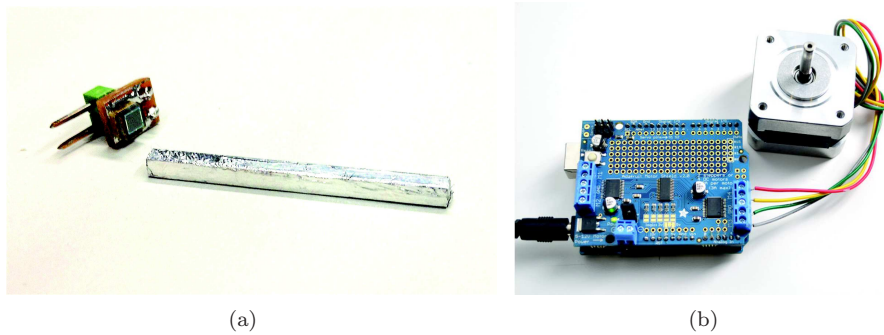
Figure 6.6: (a) LYSO crystals $2\times2\times30$ mm^3 by Kinheng Crystal and 1×1 mm^2 MPPC (S10362-11-050P) produced by HAMAMATSU Photonics. (b) Arduino UNO controller connected to the stepper motor Y129 produced by Astrosyn.

Crystal		SiPM	
Density (g/cm^3)	7.18	Area (mm^2)	1×1
Decay Time (ns)	40	Pixel size (μm)	50
Light Yield (ph./MeV)	32000	Peak wavelength (nm)	440
Peak emission (nm)	420	PDE (%)	40
Radiation length (cm)	1.15	DCR (KHz)	100
Reflective index	1.82	Gain (10^5)	7.5

Table 6.1: Datasheet features provided by the crystal and the SiPM producers.

The PCB is attached to two bipolar stepper motors produced by Astrosyn (type Y129) [155], that perform respectively the scan and the rotation. Each motor has a step angle of 1.8° with an accuracy of 5%, a mass of 0.22 Kg and a rotor inertia of 28 g/cm^2. The bottom motor rotates of 360°, while the top motor can scan a range of 180°. As a result, the FOV covered by the device is of 44 mm.

The two motors are steered by the Arduino UNO micro-controller based module [156] (Figure 6.6(b)) equipped with Adafruit motor shield [157], USB interfaced to a computer. This motor shield allows to alternate between single and double coil activation at a time to get twice the resolution in the motor step, resulting in a granularity of 0.9°. The Arduino UNO, in addition to the stepper motor movements, is also responsible for the communication of all the parameters from the control system on the computer to the electronic circuit, to the counting of coincidence events and to the transmission of the acquired data to the computer.

All these elements are fixed on a massive metal base to provide stability during the image acquisition against the torque generated by the motors movement.

6.5 The EasyPET demonstrator

Starting from the proof-of-concept module, the EasyPET demonstrator, a more advanced device was designed and engineered (Figure 6.7).
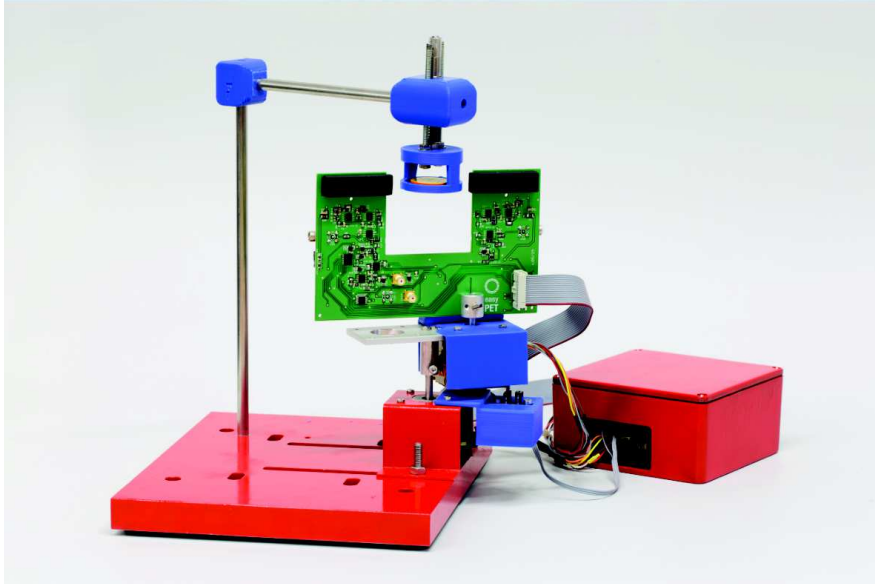
Figure 6.7: The EasyPET demonstrator prototype.

The main components have been inherited from the proof-of-concept module and only few modifications have been introduced with the aim to improve the quality of the signals and allow a fully qualification of the system.

The first involves the U-shaped PCB: the electronic circuit has been optimized for the coincidence counting, saturating the SiPM signal at adequately high energies (about 350 keV for the voltage range permitted by the power supply). As already explained in the operating principle section, the possibility for the EasyPET to maximize the sensitivity is to accept coincidence events of energy lower than 511 keV; events in which one or both the annihilation photons have interacted through Compton scattering in the crystals can be considered as true coincidences thanks to the crystal alignment. The signals saturation can guarantee an higher efficiency on the detection of low energy photons, as long as the random coincidence rate is kept to a negligible level. The technique of saturation reduces the energy dependent time walk and allow to decrease the coincidence time window. In this demonstrator the length of the discriminator signals can be modified in order to reduce the coincidence time window. The final produced PCB is shown in Figure 6.8.

The detecting unit has been improved embedding a light-tight case to avoid noise counts due to the ambient light. It is characterized by a housing for the crystals and the board with the SiPMs to facilitate their positioning and alignment, with a reproducible procedure. The case, shown in Figure 6.9, has been made with a 3D printer with a precision of 300 μm, and the impact of this accuracy is addressed later.
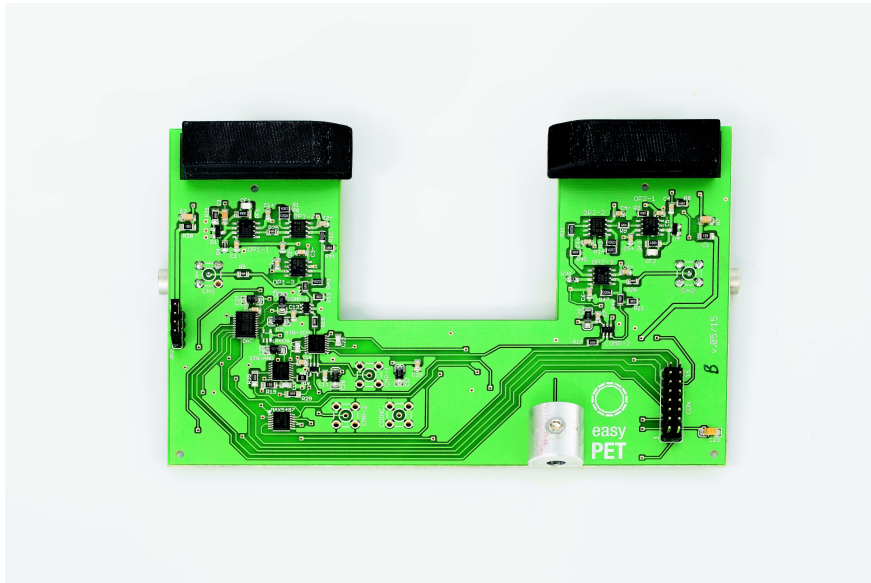
Figure 6.8: The EasyPET U-shaped PCB.
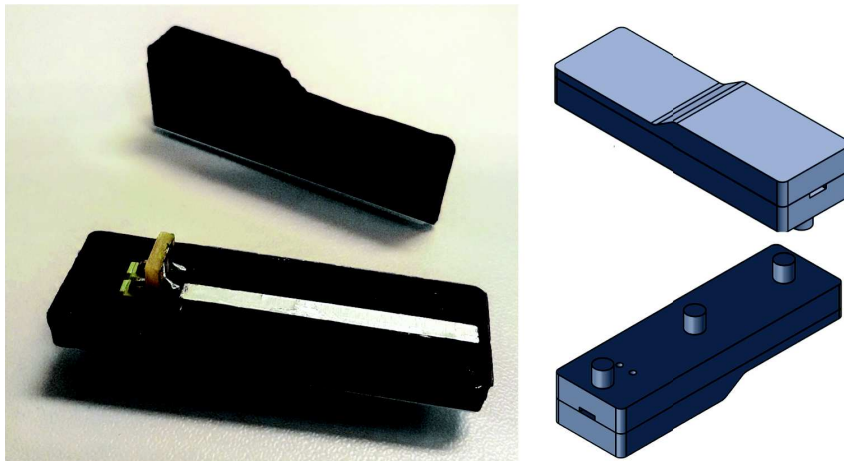
Figure 6.9: The EasyPET light-tight case with the housing for the scintillating crystal and the SiPM sensor.

Other minor changes have been introduced to make the device more user-friendly and appealing.

Five *lemo* connectors have been added to the PCB to easily probe the main stages of the electronic circuit: one per channel after the amplification stage, to visualize the analog output of the amplified SiPM signals, two to check the digital discriminator outputs and one to control the coincidence logic signal.

The issue od the cable routing has been considered due to the fact that a high number of cables that should move together with the motor and the PCB is required. A flat cable has been used replacing the multiplicity of single

cables to transport the input and output signals between the PCB and Arduino UNO (Figure 6.10). This kind of cable is very useful because it keeps all the wires together during the PCB rotation and, thanks to its flexibility, it does not compromises the movement fluidity. Another advantage is represented by the easiness and fastness of its plugging. For the connections between the top motor and Arduino UNO a ribbon cable containing all the wires has been chosen on order to minimize the motor vibrations and reduce the torque caused by the rigidity of the cables. A different solution has been adopted for the bottom motor, which is fixed: a more rigid cable encloses the wires that go to Arduino.

Some mechanical parts covering the motors have been created with a 3D printer, as shown in Figure 6.10. Their functionality is related to the application of some position sensors for the motors that are required for their relative correct alignment and as a reference in the acquisition starting and ending. The bottom motor position sensor is an optical sensor composed of an infrared light emitter and receptor placed on the bottom motor. This sensor is activated when the light emission is interrupted, and this is achieved when the pin on the support of the top motor passes through the space between the emitter and the receptor. This sensor is used to mark the starting and the ending position of the bottom motor (0° and 360°). The top motor position sensor is a mechanical end-stop placed on one side of the top motor and it is used to align the two motors. The sensor is activated when the board pushes it with its movement. By doing so, the orthogonality between the position of the PCB with respect to the bottom motor when it is in the starting/ending position can be determined exactly.
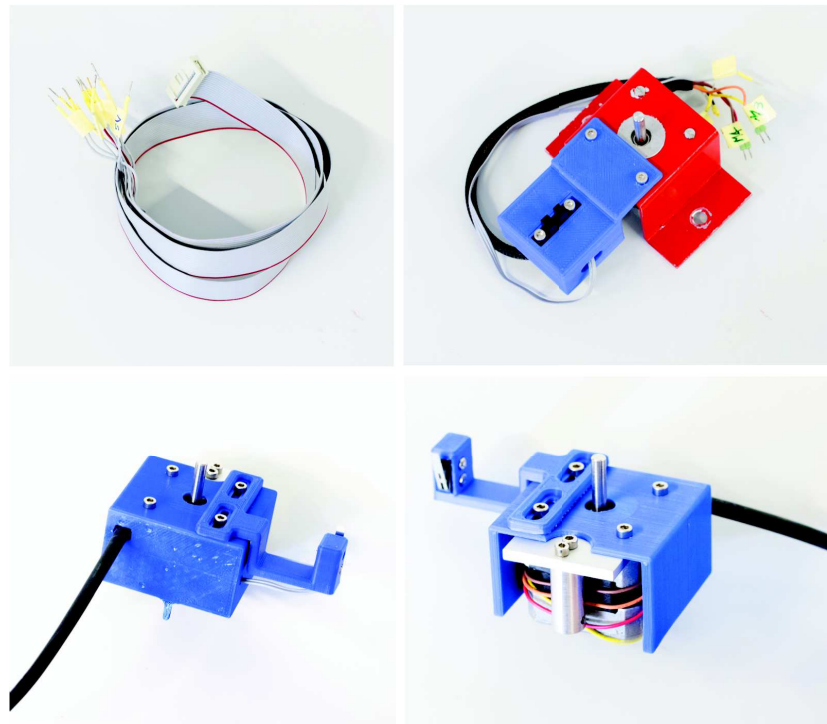
Figure 6.10: The EasyPET bottom and top motors, with the different cables used and the 3D printed mechanical parts to implement position sensors.

The massive base supporting the system integrates the source holder (Figure 6.11). It is constituted of a 3D printed plastic receptacle and a metallic arm to allow the horizontal and vertical adjustment of the source position. The metallic arm is long enough to place the source between the two detectors, exactly in the centre of the FOV, considering the x and y coordinates. The z coordinate can be adjusted with a screw placed on the receptacle to find the optimal position, the one that maximizes the coincidence count.

Finally, a box has been used to enclose the Arduino UNO with the openings for the wires connecting the motors and the board and for the usb cable to communicate with the computer (Figure 6.11). The box can protect the microcontroller module and prevent the accidental removal of the wires.
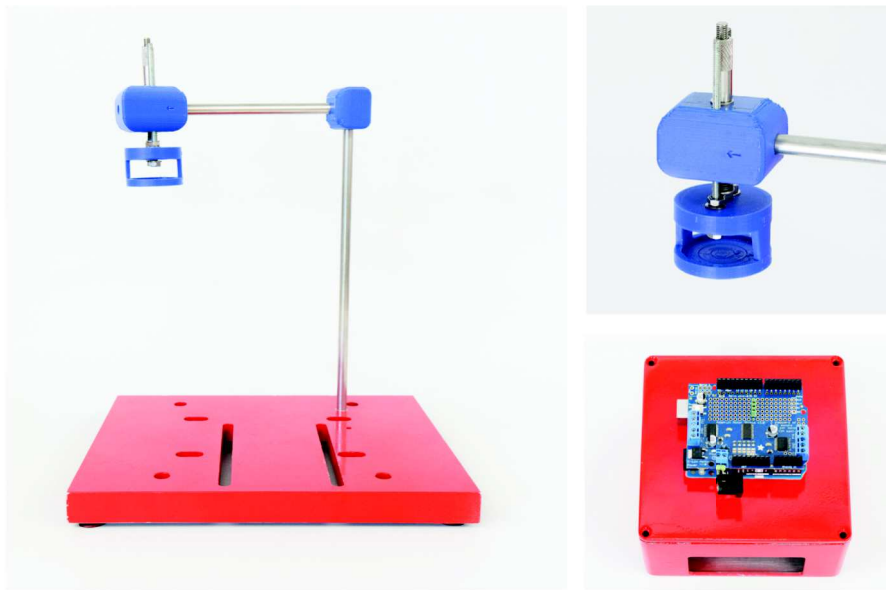
Figure 6.11: The EasyPET base, source holder structure and Arduino UNO box.

6.6 Control software

The EasyPET is controlled through a MATLAB® Graphic User Interface (GUI) which allows setting the acquisition parameters, performing the acquisition, visualizing the reconstructed image in real time during acquisition and recording the data for the offline analysis. In addition the calibration and the spatial resolution measurement can be performed through the control software. The main panel of the GUI is shown in Figure 6.12.

The "Connection" section allows to select the PC communication port for Arduino UNO between the active ports auto-detected by the control software. The "Connect" and "Disconnect" buttons allow, respectively, to open and to close the communication with the Arduino UNO module. The closing of the communication ensures the turning off of the SiPMs bias voltage in the case the sensor is still biased. The disconnection occurs also when the control software window is closed.
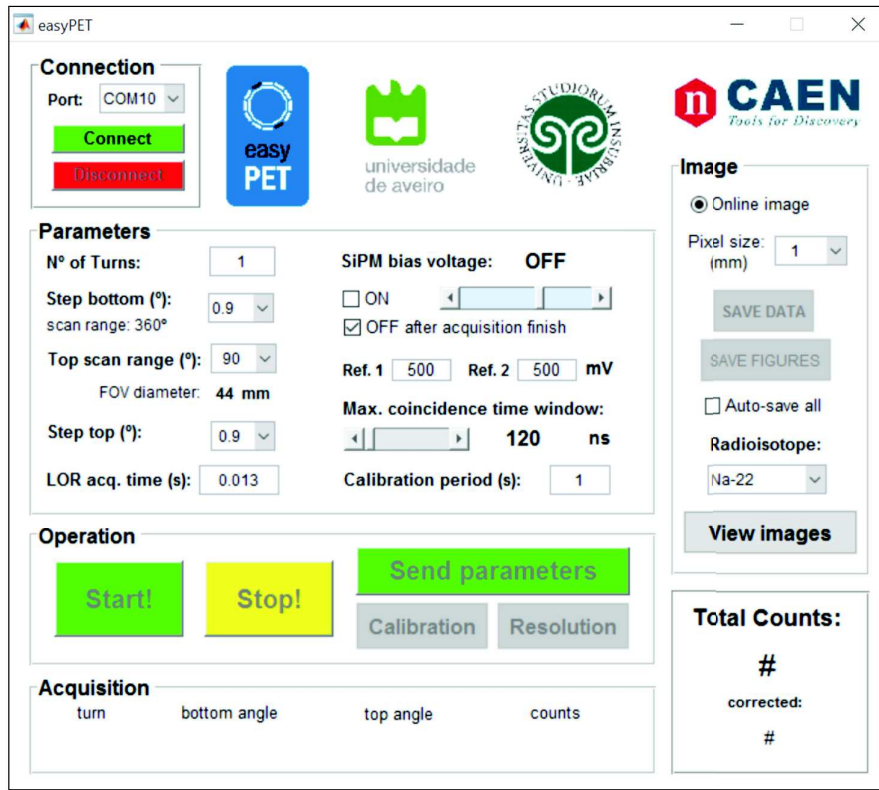
Figure 6.12: The EasyPET control software in MATLAB®.

In the "Parameters" section the acquisition parameters can be set:

- "N° of Turns": the number of complete rotations performed by the bottom motor during the acquisition.

- "Step bottom": the angle for the bottom motor step (from 0.9° to 180°).

- "Top scan range": the θ scanning range of the top motor performed for each position of the bottom motor (from 0.9° to 90°, corresponding to a FOV from 1.5 mm to 44 mm).

- "Step top": the α angle for the top motor step (from 0.9° to 90°, depending on scanning range).

- "LOR acquisition time": the acquisition time for each step of the two motor positions. The minimum possible value depends on the setting of the real time image pixel size, being higher for smaller pixel sizes.

- "SiPM bias voltage": two checkboxes allow to turn on or off the supply voltage for both the SiPMs and to turn it off only after finishing the acquisition. A slider permits to adjust the value of the bias voltage within a range of 4 V in steps of about 16 mV.

- "Ref1" and "Ref2": the reference voltage for the two discriminators above which signals are considered as valid events (from 0 mV to 2,5 V).

- "Coincidence time window": the width of the time window within which two events of the two detectors are considered as a coincidence and counted. A slider allows adjusting the value from 120 ns to 1.4 μs.

- "Calibration period": time of coincidence counting in calibration mode.

The "Image" section allows to activate the real-time image reconstruction with the back-projection during the acquisition, to choose the pixel size of the online image and to save the final image and the acquired data in list mode for further analysis. In addition it is possible to select the radioactive source in use for the imaging in order to correct the number of counts during the acquisition for the radioactive half-life decay time.

In the "Operation" section there is the sequence of command to operate the EasyPET. First, the "Send parameters" should be pressed to communicate the selected acquisition and imaging parameters to Arduino and to move the system to its initial position, in order to start a new acquisition. Then the "Calibration" should be performed to determine the correct source vertical alignment with the crystals. For this operation mode the system moves in order to have the two detectors aligned to the centre of the FOV, where is placed the source, and continuously counts the coincidences during successive calibration periods defined in "Parameters" section. The updating number of coincidences, together with the maximum number of counts/period since the beginning of the calibration are shown in the box on the bottom right of the GUI. At this point the spatial resolution measurement or the image acquisition can be performed. In the first case, pushing the "Resolution" button some additional parameters have to be set, as the distance of the source from the FOV centre, the scanning range of the top motor and the time acquisition of the coincidence counts for each motors position. The detail of this measurement will be explained in the following section. In the second case, the "Start" button allows to start the image acquisition and the "Acquisition" box allows to visualize the status of the easyPET acquisition, showing the current position of the system and the coincidence counts. Now, the box on the right shows both the total number of counts and the value corrected for the radioisotope in use for all the positions scanned from the beginning of the acquisition. The image acquisition stops when the bottom motor has completed the number of complete turns selected above and the pin of the top motor passes through the optical sensor position on the bottom motor. Otherwise, the "Stop" stops the current operation (image acquisition, calibration or resolution measurement) at any time and make the system to return to the initial position.

6.7 EasyPET demonstrator performance

Signal quality

The first feature that can be analyzed is the quality of the analog signals produced by the SiPMs and amplified with the electronic circuit. When the SiPMs are not biased, the signals show an electronic noise band of about 200 mV peak-to-peak, on both channels, as can be seen in Figure 6.13. In addition there is a random positive ripple of even 300 mV with a mean frequency of 10 kHz on both channels and a deterministic negative ripple of 200 mV at 4 kHz, especially on the second channel. Both present a superimposed electronic noise of about

50 mV peak-to-peak with a frequency of 300 kHz. When the SiPMs are biased and an event occurs, the signal is characterized by a severe undershoot up to 400 mV and the baseline is restored only after 12 μs (Figure 6.13).
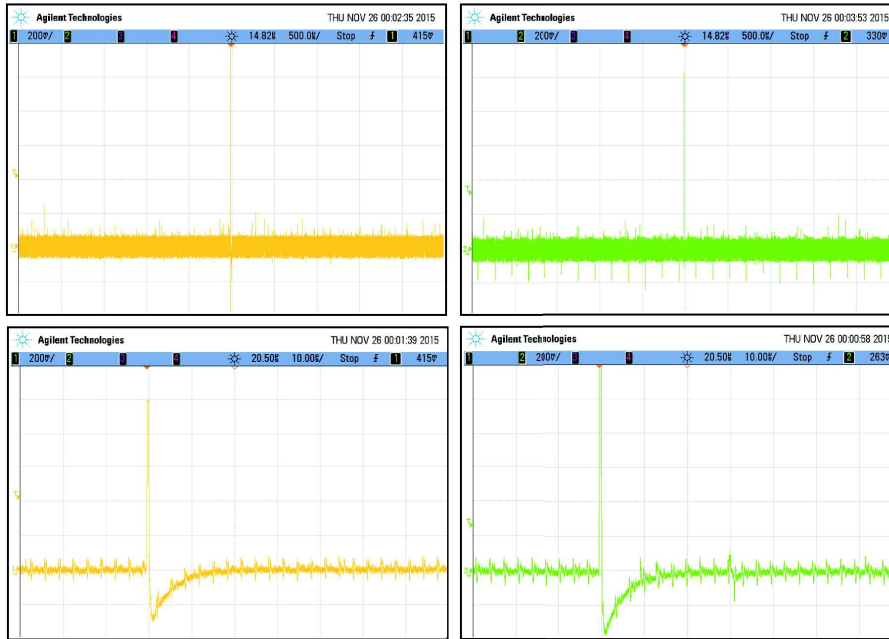
Figure 6.13: The SiPMs amplified signals of both channels with an electronic noise band, various ripples and an undershoot.

Considering Figure 6.14, which shows the coincidence signals generated by the positron annihilation, it can be seen that the overshoot appears mainly in case of signal saturation. In fact, also at medium and low SiPMs bias, the electronic readout has been designed to saturate the signals at 1.6 V and make the coincidence counting measurement easier. This effect is enhanced as the SiPMs bias is increased. It can also be noticed that the time decay of the two channels are perfectly equal and the signals time duration is of about 600 ns.

The main goals of the EasyPET demonstrator consist in the coincidence detection counting and in the online image reconstruction and they can be successfully fulfilled even with these signals. It is true that the energy acceptance threshold can not be set as low as possible due to the electronic noise and the demonstrator can not achieve its best performance. In the following paragraph it will be analyzed in detail the effect of the signal quality on the system performance. However, in these conditions optimized for the counting, it is impossible to detect the single photoelectrons characterizing the SiPMs signals in condition of no illumination. Consequently, the SiPMs figures of merit can not be analyzed and the spectrometric studies can not be performed. In particular, the energy spectrum of the radioactive sources can not be interpreted in terms of photoelectrons in order to study the efficiency of the system response. As a result, the strategy of signal saturation makes difficult to fully qualify and characterize the system.
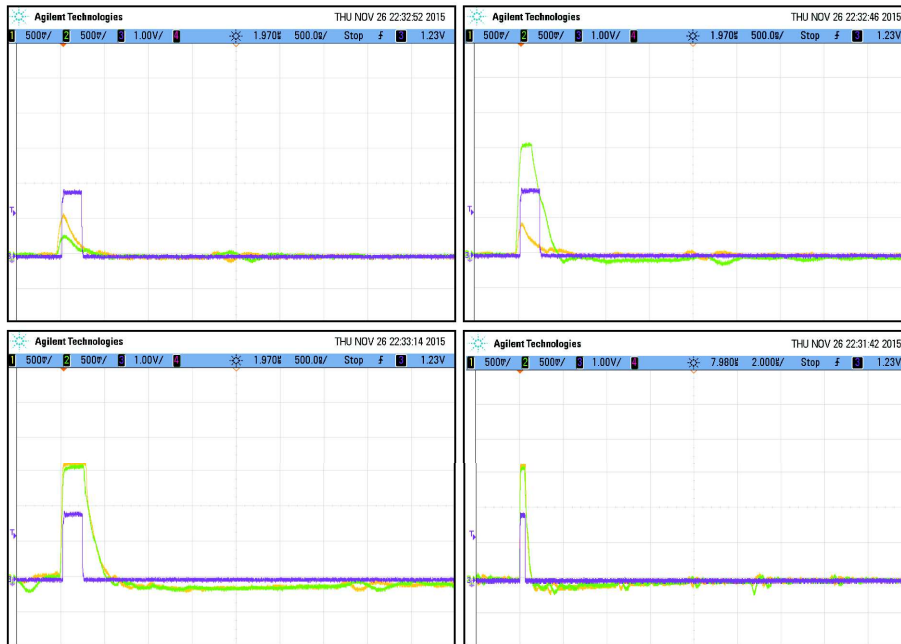
Figure 6.14: Events are triggered by the coincidence gate of 120 ns (violet signal). The two channels analog signals saturates at 1.6 V most of the times and the undershoot follows. Both have a constant decay time of about 180 ns.

Single channels and coincidence counting

The counting rate of the single channel in condition of no illumination has been measured as a function of the discriminator threshold expressed in mV and in Figure 6.15 is reported for three different bias voltages. It can be inferred that below the threshold of 200 mV the single counting rate is dominated by the electronic noise and the SiPM DCR, as expected. Above 200 mV the rate is due to the self-activity of the LYSO crystal. The ^{176}Lu is a β emitter decaying to an excited state which emits photons with energies of 307 keV, 202 keV, and 88 keV, resulting in 39 cps/g. Considering the dimension and the density of the crystal in use the expected rate due to self-emission is 36 Hz and the measured rate at 400 mV is compatible with this value for all the three voltages. Increasing the threshold the single counting rate decreases to about 5 Hz for the low voltage due to the shape of the energy spectrum of the LYSO self-activity. The single counting rate remains quite constant for higher bias voltages due to the higher SiPM gain and the consequent signal saturation.

In the same condition, the counting rate of the coincidence of the two channels can be measured in order to estimate the contribution of the random coincidence to the true coincidence events. For all the three voltages the coincidence dark rate is below 0.1 Hz for discriminator thresholds above the electronic noise at 200 mV. This result ensures a good quality of the coincidence events rate, with a negligible noise contamination.
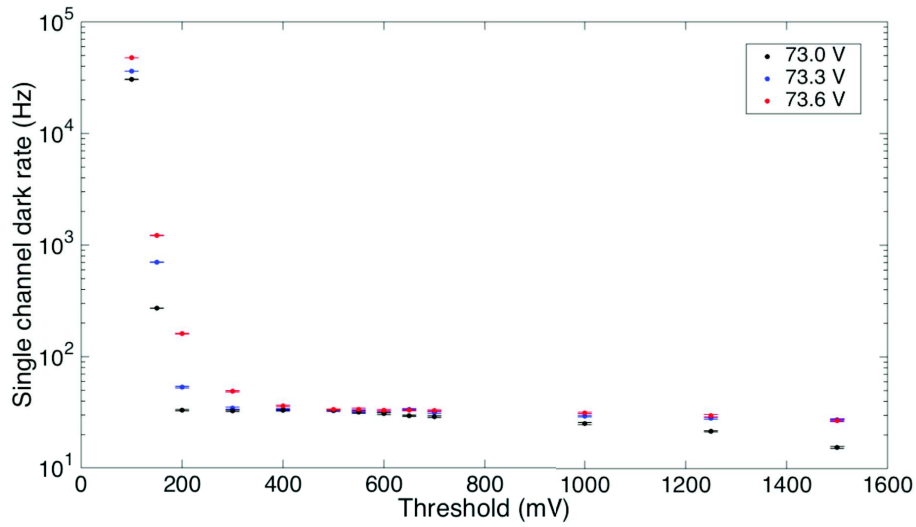
Figure 6.15: The single channel rate in dark condition as a function of the discriminator threshold for three different SiPM bias voltages.

The single channel rate is then measured positioning a non point-like 10μCi ^{22}Na in the centre of the FOV. The vertical alignment between the two detectors and the source is determined by using the "Calibration" operation mode and changing the z position of the source holder through the micro-metric screw till a maximum in the coincidence rate is reached. Figure 6.16 reports the single channel rate as a function of the threshold for the same bias voltages, subtracting the background represented by the single channel dark rate.
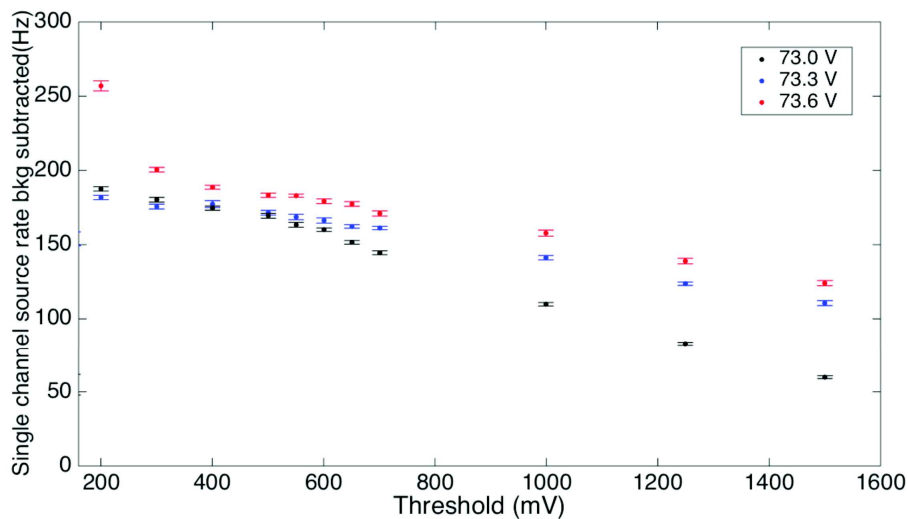
Figure 6.16: The single channel rate in presence of a radioactive source, background subtracted, as a function of the threshold for three different bias voltages.

Figure 6.17 shows the coincidence count rate versus the discriminator threshold for three bias voltages. The values have been measured with the same conditions of the previous counting measurement. Both for the single and the coincidence counting rate the behavior at different bias is the same: the results are more similar for the two higher voltages due to the signals saturation, while for the 73.0 V bias the rates are always lower. In order to understand in detail the behavior of both rates as a function of the threshold, it is necessary to convert the mV value in energy to interpret the results on the basis of the source energy spectra.
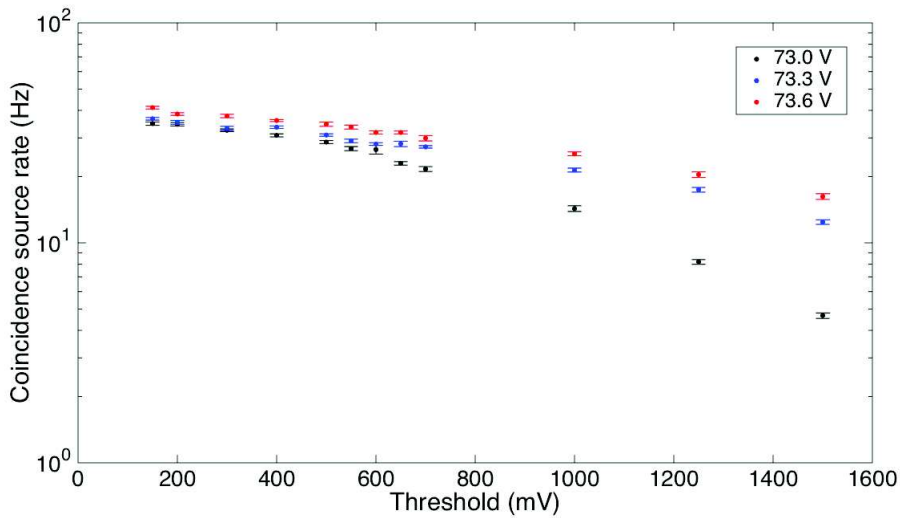
Figure 6.17: The coincidence rate in presence of a radioactive source, background subtracted, as a function of the threshold for three different bias voltages.

For this purpose, spectra of various radioactive sources have been acquired biasing the SiPMs at 73 V in order to avoid the signal saturation and to asses higher energies. The spectra are obtained by feeding the analog signal from one channel (before discrimination) into the DT5720A Digitizer (described in Chapter 2) with the firmware performing the charge integration. The signal have to be attenuated in order to match the ± 1 V input range of the digitizer. The results for the ^{133}Ba, ^{57}Co and ^{22}Na sources are shown in Figure 6.18. It can be seen that the lowest energy that can be detected is the line at 81 keV of ^{133}Ba, while the 32 keV peak can not be identified due to the electronic noise. A Gaussian fit of the peaks in the spectra is performed to determine the ADC channel corresponding to the various peaks and the FWHM to evaluate the energy resolutions. Figure 6.18(d) shows the peaks position in ADC channel as a function of the correspondent energy. The red linear fit represents the energy-channel calibration: a $\chi^2/d.o.f.$ of 0.3 indicates that the errors on the peaks positions are considerable. This is due to the low energy resolution which spreads the peaks: a FWHM of $(30 \pm 1)\%$ has been measured at the 511 keV. The poor energy resolution can be caused by the not optimal signal quality which degrades the measurement of the digitized area.
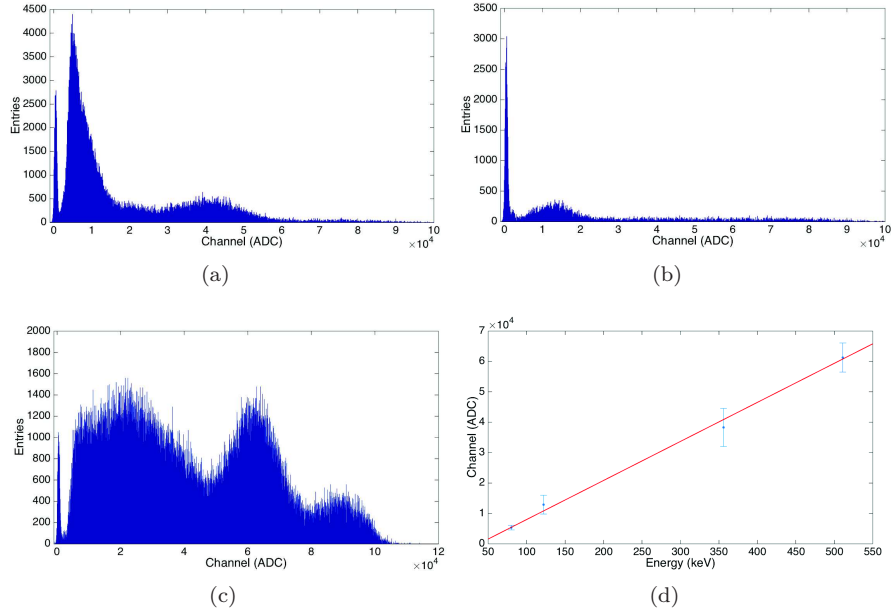
Figure 6.18: (a) ^{133}Ba, (b) ^{57}Co and (c) ^{22}Na spectra. (d) ADC channel-energy calibration: error bars are the data points while the red line is the linear fit.

In Figure 6.19 the number of entries as a function of the energy is reported for the spectrum of the ^{22}Na acquired by using the coincidence output to trigger the digitizer. The threshold set for the discriminators is 150 mV and it can be inferred that the noise will be removed by applying a cut at 80 keV, which can be achieved by setting 200 mV as a discrimination value. Considering the correspondence between the threshold in mV and the energy cut in the coincidence energy spectrum, the trend of the plot in Figure 6.17 is made clear. The ratio of the sum of the number of coincidence events with energy higher than 450 keV (which represents the 30% of the total) and above 80 keV is 35%, which is consistent with the ratio of the coincidence rate between 1200 mV and 200 mV in the case of the non saturated signals from the 70.3 V biased SiPMs.

Comparing the spectra from the single channel and the coincidence it can be noticed that, as expected, the contribution of non-coincidence events with an energy higher than the Compton peak is reduced to a negligible level. In addition, the peak-to-total ratio is increased because the geometrical selection of only the back-to-back photons performed by the detectors alignment enhances the probability to detect coincidences of photons releasing all their energy with respect to photons undergoing to Compton scattering events.

In order to precisely measure the effect of the difference in the geometrical acceptance between the single channel and the coincidence on the number of selected events, a 3D simulation has been implemented. The source is simulated to be a disk of 3 mm diameter and thick 2.5 mm, positioned in the centre of the FOV. The decay origins are randomly distributed in the disk and the direction of the emitted photon pairs is determined by randomly choosing an azimuthal and a polar angle. Their trajectories are then propagated till the rear surface of
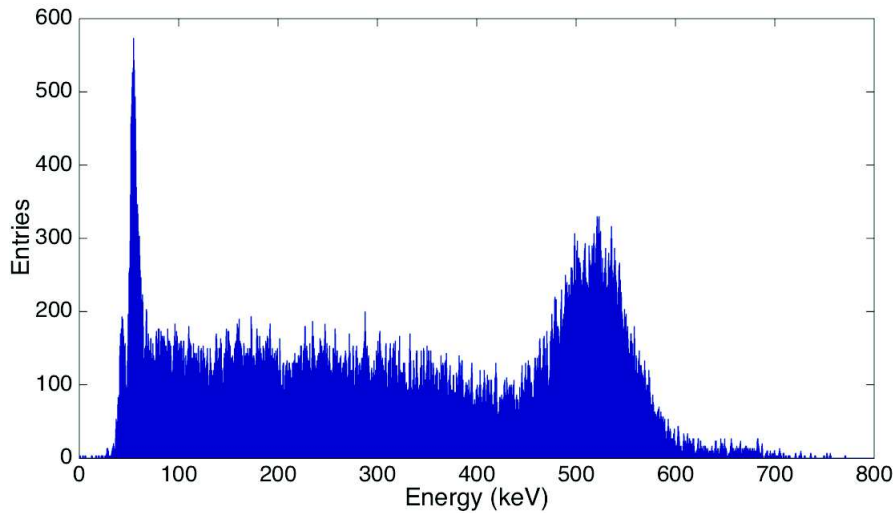
Figure 6.19: Coincidence ^{22}Na spectrum.

the crystals and if they cross the crystal they are considered to be detected. A graphical representation of the geometric simulation is illustrated in Figure 6.20. Although this represents a rough model in which both the minimum distance that a photon should travel inside the crystal to interact and the energy spectrum of the emitted photons are not taken into account, it shows a good agreement with the results of the single and coincidence count rates (Figures 6.16 and 6.17).

The simulated detecting probability for the single channel, calculated as the ratio between the events detected in the single arm and the emitted photon pairs, is 0.056%. Considering that the activity of the source in use for the counting measurement is of 370 kBq with an uncertainty of 20%, as measured by the producer, the geometrical acceptance of the single channel reduces the detectable number of photons to 207 ± 42 in one second. This value is in agreement with the acquired single counting rate measurements at the lowest threshold: despite of the huge uncertainty it indicates that the main effect in decreasing the statistics of the detected events is the geometrical acceptance.

The coincidence geometrical acceptance, determined as the number of events detected in both detectors and normalized to the number of emitted photons, result to select the 0.01% of the generated events. The experimental value is expected to be in the range of 37 ± 7 photons per second, which is consistent with the measured coincidence rate at the lowest threshold.

These results confirm a reduction of a factor five between the rate of each single channel and their coincidence, which is mainly due to the different geometrical acceptance of the two measurements. The cause of this effect lies in the use of an extended source; with a point-like source distribution no difference will be observed in the geometrical acceptances. Further analysis on the photons interaction length in the crystal and on the energy threshold will be reported in the next Chapter.

(a)

(b)

(c)
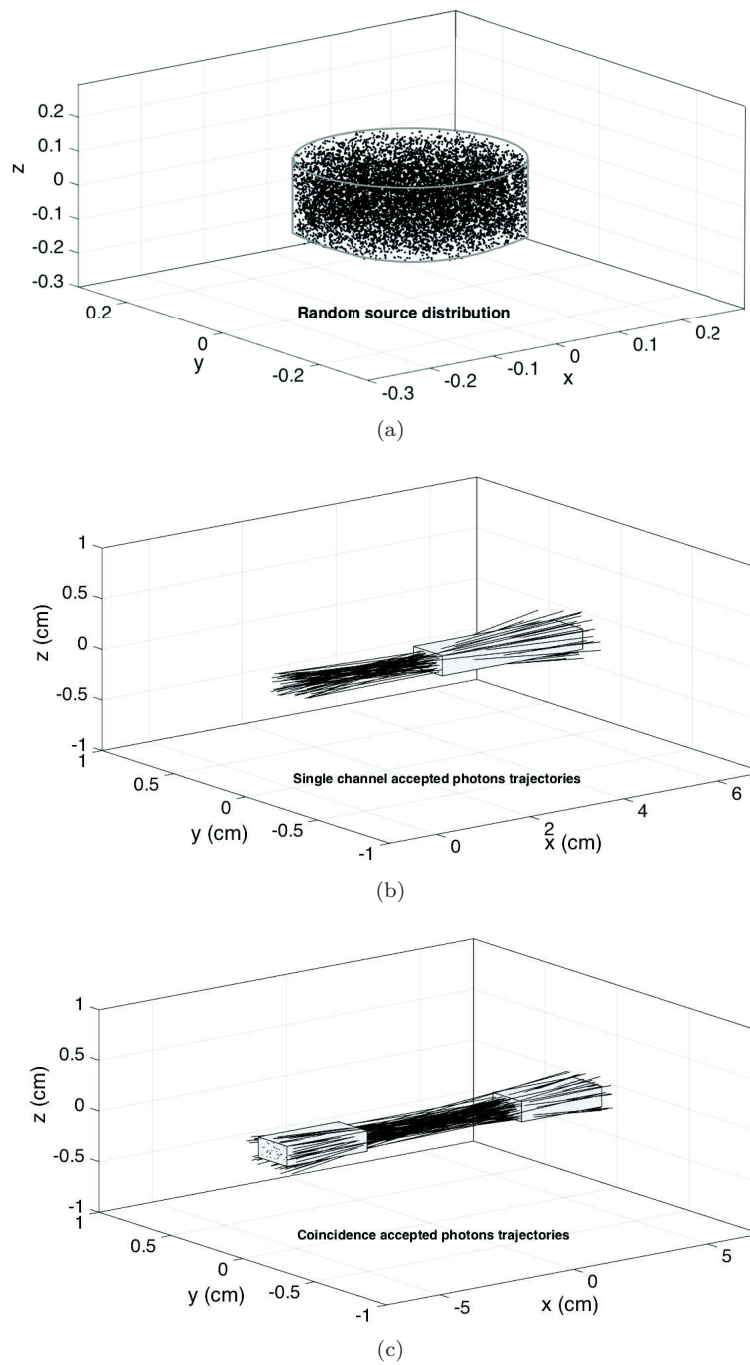
Figure 6.20: Exemplary images of the geometrical simulation showing (a) the random distribution of emission positions in the cylindrical source with 3 mm diameter and 2.5 mm height and the trajectories of photons accepted by a (a) single crystal and (b) in coincidence.

Spatial resolution

The spatial resolution can be defined as the smallest distinguishable detail level of an image. The NEMA procedure states that the spatial resolution is measured from the FWHM of a point-like source response function, obtained by the projections of the reconstructed image in the x,y and z directions [138].

The procedure proposed here to determine the spatial resolution is based on the coincidence events counting and can be accomplished with an extended radioactive source. In fact, the source in use is a 3 μCi ^{22}Na radioactive solution deposited into a 6 mm diameter well in a plastic disk 3 mm thick. The well is filled with an epoxy sealing the radioactive material inside the source [158]. When the source is positioned vertically its activity distribution results to have a sharp edge on one side and a smoothed edge on the other one, as shown in the scheme of Figure 6.21. The properties of the response function of a sharp edge is exploited in order to measure the system spatial resolution without the need to describe exactly the source activity distribution.
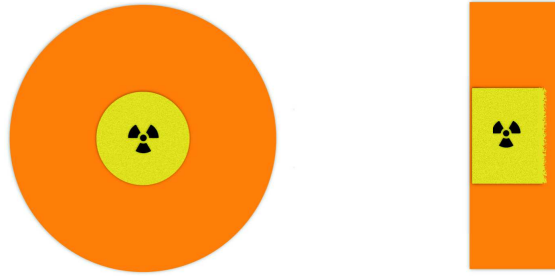
Figure 6.21: The top and side view of the ^{22}Na source scheme (not to scale): the radioactive liquid (yellow) is encapsulated into a plastic enclosure (orange) with a sharp edge on the left and a smoothed edge on the right.

The measurement can be performed using the dedicated operation mode programmed in the EasyPET control software, and its setup is sketched in Figure 6.22. The ^{22}Na source is positioned vertically in the centre of the FOV. The EasyPET performs a θ scan around the source and for each position the number of coincident events is recorded. The granularity of the scan is fixed at 0.9°, the lowest achievable with the EasyPET. Instead, the range of the scan, θ, together with the acquisition time at each position, can be set with the GUI, as their optimal values depend on the source distribution and activity.

With the source in use, the EasyPET response function is obtained by counting the coincidence events for 30 s in each scanning position, covering a θ of 45°. at different source-detectors distances. At each scanning position i it can be calculated the distance between the source and the line connecting the front faces of the crystals, D, with the following formula:

$$D_i = r \cdot \tan \theta_i, \tag{6.2}$$

where r is half the distance between the two detectors and θ_i is the angular position of the top motor at each step.

In Figure 6.23 is reported the number of coincidence counts as a function of the distance D. An asymmetry can be noted in the distribution: the lefthand
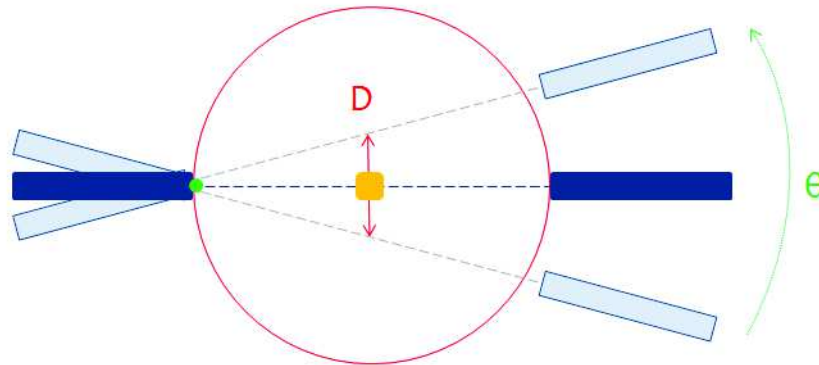
Figure 6.22: The EasyPET setup for position resolution measurement.

side of the peak has a Gaussian behavior and represents the EasyPET response function to the sharp edge of the source activity distribution, while the righthand one has a wider spread, corresponding to the smoothed edge of the sealed radioactive liquid.
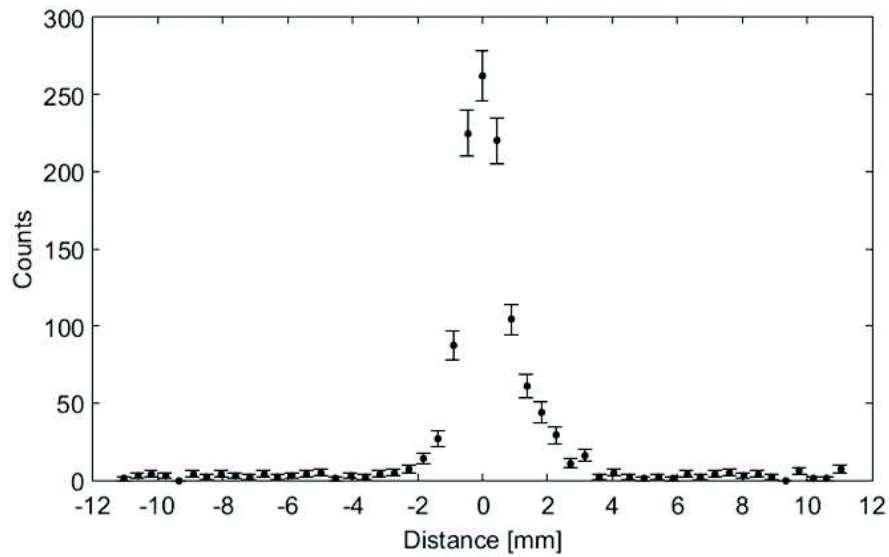
Figure 6.23: The EasyPET coincidence counts measured using a 3 μCi ^{22}Na source as a function of the distance D.

The EasyPET spatial resolution can be determined by considering that a sharp edge activity distribution, described with a Step function, is convoluted with a Gaussian function representing the spread induced by the detecting system to produce the edge imaging. Consequently, the derivative of the measured edge

response function results to be the Gaussian describing the detecting system, whose FWHM represents its spatial resolution.

Figure 6.24 reports the gradient applied to the data points of Figure 6.23. The first peak corresponds to the derivative of the edge response function and can be fitted with a Gaussian function, shown in red. The results of the fit parameter values are reported in Table 6.2. The spatial resolution estimated from the fit parameters is 1.0 ± 0.1 mm FWHM.
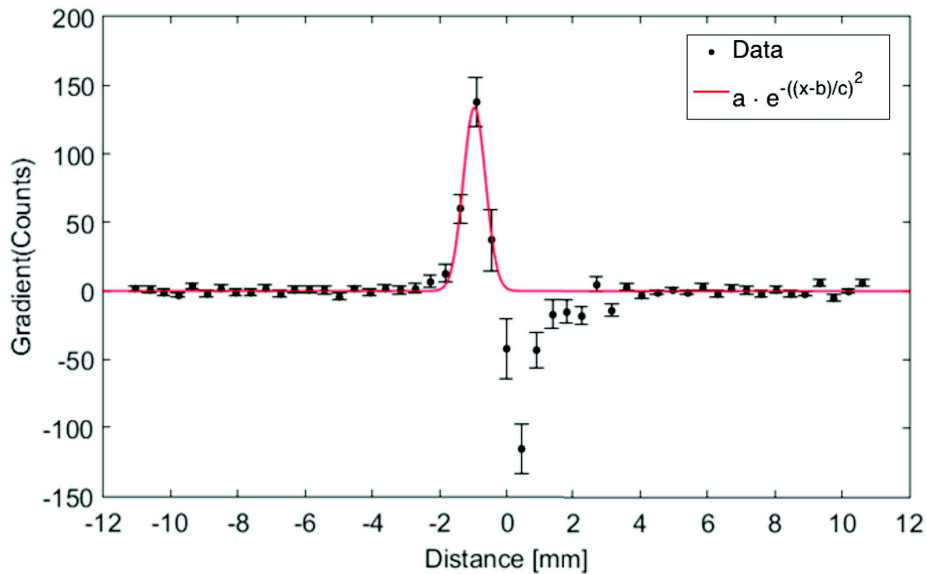
Figure 6.24: The EasyPET gradient of the counts measured using a 5 μCi ^{22}Na source as a function of the distance D.

Fit parameter	Result value
a	134 ± 19
b	-0.97 ± 0.07
c	0.58 ± 0.08

Table 6.2: Fit parameters and result values of the Gaussian function to the gradient of the number of coincidence counts as a function of the distance D.

The EasyPET spatial resolution is dominated by the crystal width and by the angular step of the scan and result to be better than commercial preclinical scanner. This result is expected since the EasyPET is based on a single crystal pair readout. Instead, the majority of small animal PET, in order to reduce the system complexity, employ optical multiplexing and light sharing and degrade the spatial resolution [139]. The EasyPET spatial resolution is sufficient to distinguish the same level of structural details of human PET for rat imaging, while it is not yet optimal for mice, where a 0.4 mm FWHM is desirable [129].

As described in Section 6.1, the EasyPET spatial resolution is expected to be uniform over the full FOV. In fact, irrespective of the source position, the detection of a coincidence will occur only when the source lies on the line connecting the two detectors. The described spatial resolution measurement does not depend on the source position and the result holds in the whole FOV. In addition, a test has been performed by imaging the same ^{22}Na source with an activity of 3 μCi and a diameter of 6 mm for the same amount of time in two different regions of the FOV, one in the centre and one in the periphery. The source is defined as the set of data exceeding five times the background standard deviation. An elliptic fit is applied to the corresponding contour of data to evaluate the dimension of the reconstructed source. The length of the axes of the two ellipses are compatible: 6.6 mm and 7 mm for the source in the centre and 6.8 mm and 7.2 mm for the source in the off-centre position. The result confirms that the spatial resolution is uniform in all the FOV. Figures 6.25 and 6.26 show the reconstructed image and the elliptic fit when the source is positioned in the centre and in the peripheral region of the FOV, respectively.
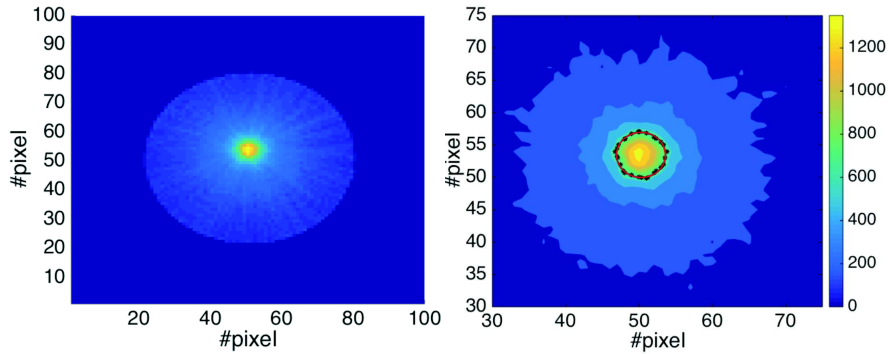
Figure 6.25: Image of the source placed in the centre of the FOV (left). A zoomed contour plot: the black stars represents the data points, 5 times higher than the background. The red line corresponds to the elliptic fit (right).
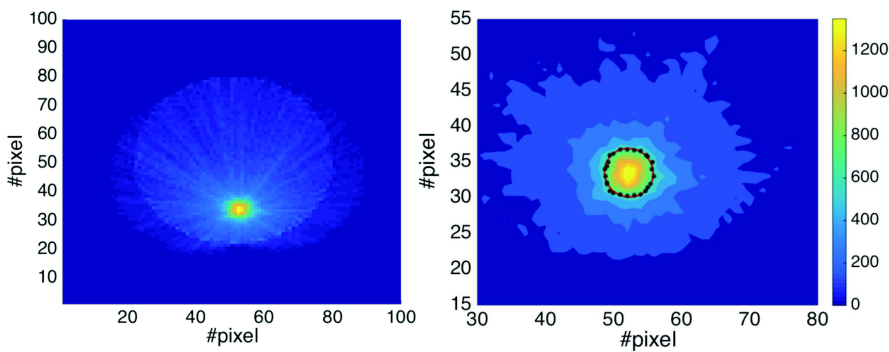
Figure 6.26: Image of the source placed in a peripheral region of the FOV(left). A zoomed contour plot: the black stars represents the data points, 5 times higher than the background. The red line corresponds to the elliptic fit (right).

An exemplary illustration of the EasyPET capability in terms of spatial resolution is depicted in Figure 6.27, representing the back-projected image of a PMMA phantom consisting of two wells filled with ^{18}FDG, with a diameter of 5 mm and 2 mm and separated by a thickness of 1 mm. In the reconstructed image the two source distributions are clearly distinguishable, confirming the measured spatial resolution of 1.0 mm.
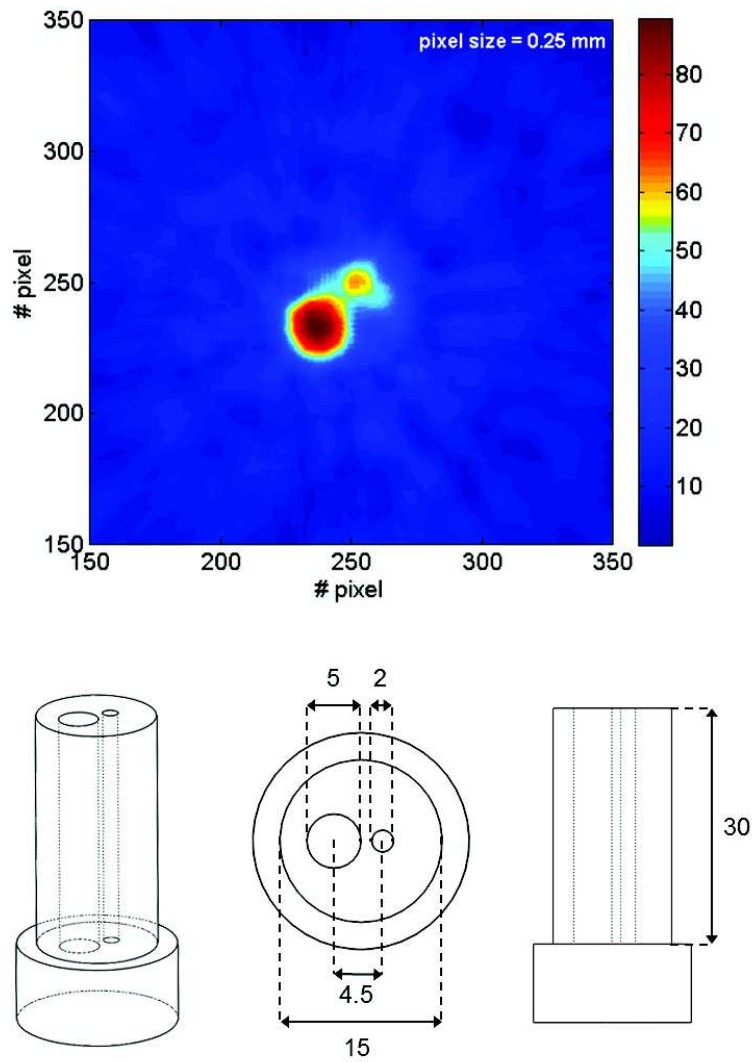
Figure 6.27: Image of two wells in a PMMA phantom filled with ^{18}FDG obtained acquiring a total number of 6150 events in 24 minutes (top). The schematic layout of the phantom with all the dimensions in mm (bottom).

Image contrast

The reconstructed image quality can be characterized in terms of contrast, which arises from the relative variations of count densities between adjacent areas in the image of a source. Contrast gives a measure of the detectability of an abnormality relative to normal tissue and is expressed as:

$$C = \frac{I_{max} - I_{min}}{I_{min}}, \tag{6.3}$$

where I_{max} and I_{min} represents the count densities recorded in the abnormal and normal tissues, respectively. For a given image, a minimum number of counts are needed for a reasonable image contrast. Even with adequate spatial resolution of the scanner, lack of sufficient counts may give rise to poor contrast due to the high noise level, and the lesions may be missed. The number of count densities depends on the administered dosage of the radiopharmaceutical, uptake by the tissue, length of scanning and the detection efficiency of the scanner.

The EasyPET image contrast has been measured by acquiring an image of a 9.8 μCi of ^{22}Na for about 167 minutes, collecting a total number of counts of about $6.6 \cdot 10^6$ (Figure 6.28). The above equation has been applied, determining I_{max} and I_{min} from the counts in the source and background regions and considering the image pixel size. Then the contrast C has to be divided by the source activity (346.1 kBq) and the total acquisition time, in order to be independent from these contributes. As a result, a value of 60 $C/(\text{kBq} \cdot \text{s})$ has been obtained, indicating a good disease detecting capability.
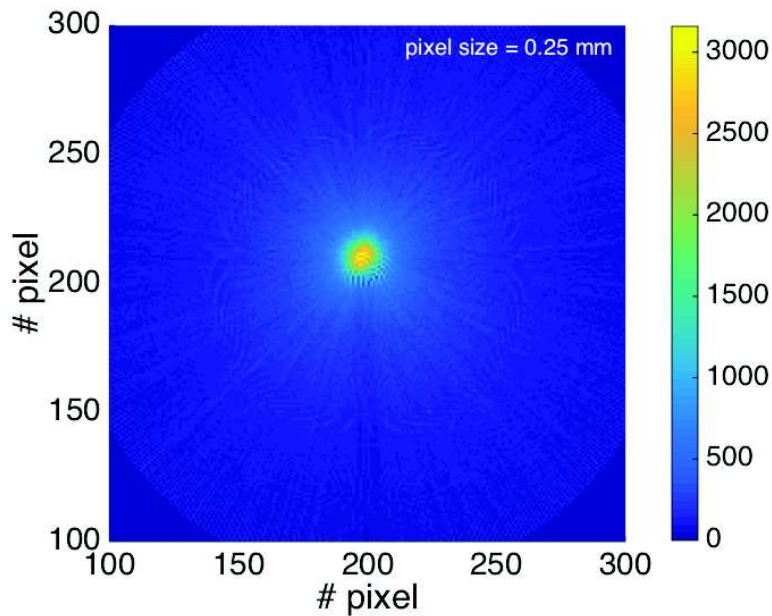
Figure 6.28: Reconstructed distribution of a ^{22}Na source with an activity of 9.8 μCi imaged with a single LOR time acquisition of 0.5 s, bottom step 0.9°, top range 45° and top step 0.9°, for a total acquisition time of 167 minutes.

Chapter 7

Qualification of new SiPMs for the EasyPET

The signal quality of the demonstrator does not allow to analyze the performance of the detecting unit: i.e. it is not possible to perform an energy calibration of the discriminator thresholds, to establish the lowest possible energy threshold and to evaluate the coincidence detection efficiency of the system as a function of the energy window.

In this Chapter a dedicated experimental set-up has been realized to gather this information and study the critical aspects of the EasyPET demonstrator, with an emphasis on the system sensitivity. In particular, the importance of the alignment between the sensor and the crystal in the light collection optimization is analyzed, together with the impact of the geometrical coupling between the sensor and the crystal (the ratio of their areas), and the effect of the sensor performances. The figures of merit that will be considered are related to the spectrometric properties of the detecting unit: the minimum detectable energy, the energy resolution, the peak-to-total ratio of the energy spectrum and the system linearity. Finally, a crucial role is played by the coincidence detection efficiency, which will be determined by using a source collimator to simplify the model behind the data analysis.

The assessment of the detecting unit performance requires a dedicated electronic readout, improved with respect to the demonstrator circuit scheme. In particular, two branches will be implemented, one optimized for spectroscopy measurements and one dedicated to the imaging measurement. In this way it will be possible to achieve better quality signals with a very low electrical noise, which allows to analyze the impact of the performances of various sensors.

The information resulting by this investigation will lead to an improved version of the EasyPET, that will be described and commissioned in Chapter 8. The optimized system will represent a prototype of the final commercial product dedicated to the educational market.

7.1 Experimental set-up

The mechanics of the dedicated experimental set-up has been designed and assembled with the aim to define a reliable and reproducible procedure to align all the components involved in the measurements. The analysis of the coincidence efficiency requires the use of two detecting units, that have to be perfectly collinear and aligned also to the radioactive source.

The set-up, shown in Figure 7.1 is composed of a massive metal plate on which two metallic holders are arranged, covered by a black insulating tape, to house the SiPMs. Each sensor holder is connected to a micro-metric control used to adjust its position in the three spatial directions. The scintillating crystals are housed in two black plastic holders drilled for all their length and fixed to the metal plate at the same distance from the sensor holders. The crystals are collinear and their front faces result to be 5 cm apart, to mimic the geometry of the EasyPET. Their position is kept fixed by using a plastic screw to avoid the aluminum coating foil to be damaged. In the volume between the two crystals there is the possibility to place a collimated ^{22}Na radioactive source. The collimator has a one millimeter diameter emission hole and results, thanks to its design, to be aligned in height with both the scintillating crystal front faces. A block of wood is fixed to the metal plate to correctly align the collimator to the crystals also in the horizontal coordinates, to guarantee the reproducibility of the procedure of the collimated source removal and replacement.
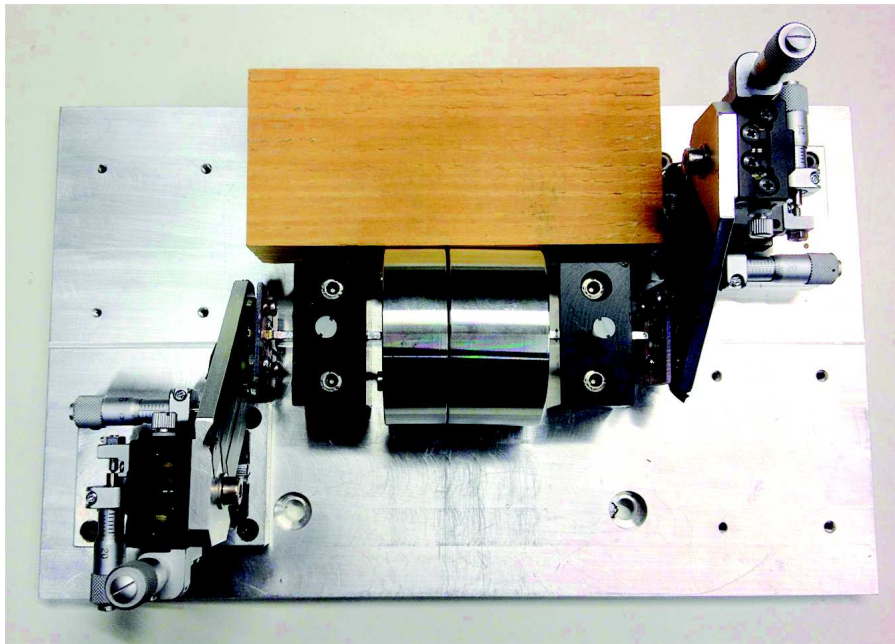
Figure 7.1: The experimental set-up used to test the performances of the various sensors. They are housed on two holders whose positions can be adjusted in the three directions through micro-metric screws. The crystals are kept fixed and aligned thanks to two black plastic holders. When the use of the source collimator is required, its emission hole is mechanically aligned to the crystal.

The **collimator** has been realized in order to reduce the unknown source geometry to a well defined distribution and the advantages will be explained in the section dedicated to the coincidence detection efficiency. The choice of the collimator material is a trade off between the machining, the cost and the boundary conditions. In fact for the emission hole realization a long and thin drill is required, together with a good attenuation capability for the other directions, that has to be obtained occupying only the volume between the scintillating crystals. The adopted material is the stainless steel composed of 74% iron, 18% chromium, 8% nickel and a percentage of carbon lower than 1%. The characteristics of these elements are reported in Table 7.1.

Element	511 keV attenuation coefficient	Density	μ
Fe	$0.084 cm^2/g$	$7.86 g/cm^3$	$0.66 cm^-1$
Cr	$0.083 cm^2/g$	$7.20 g/cm^3$	$0.59 cm^-1$
Ni	$0.087 cm^2/g$	$8.90 g/cm^3$	$0.77 cm^{-1}$

Table 7.1: Total attenuation coefficient at 511 keV, density and linear attenuation coefficient of iron, chromium and nickel.

The collimator consists in a cylindrical block divided into two parts providing a housing for the radioactive source in the centre. The emitted photons have to cross a thickness of 2 cm of material and their probability to be stopped is about the 80%. In addition, considering coincidence measurements, the probability to count a pair of annihilation photons that has not been attenuated by the collimator is less than 4%. Taking into account also the geometry selection on the events and the fact that oblique photons travel a greater distance in the material, the contamination of non-collimated events results to be negligible.

A 1 mm diameter hole has been drilled for the whole length of the cylinder, as can be seen in Figure 7.2. The dimension of the hole is chosen in order to have, once the collimator is position in the set-up, the coincidence emission cone of the radioactive source fully contained in the solid angle defined by the crystal surface. In fact, as depicted in Figure 7.3, the source is positioned in the centre of the collimator and the semi-aperture of the coincidence emission cone is determined by the straight line connecting the centre of the source and a corner of the hole. Quantitatively, being the centre of the source at a distance of 21.5 mm to the face of the collimator and 0.5 mm the radius of the emission hole, the half of the divergence of the cone results to be:

$$\theta_e = atan\Big(\frac{0.5}{21.5}\Big) = 1.33°.$$
(7.1)

Propagating the coincidence emission cone to the crystal surface it can be calculated that the maximum displacement y_D from the centre of the crystal face is:

$$y_D = tan(1.33°) \cdot 25mm = 0.58mm,$$
(7.2)

where 25 mm is the distance between the source centre and the crystal face. As a consequence, being y_D smaller than the half of the crystal face edge, the coincidence radiation emitted by the collimator can be retained to totally impinge on the crystal surface.

Figure 7.2: The stainless steel collimator with 1 mm emission hole.
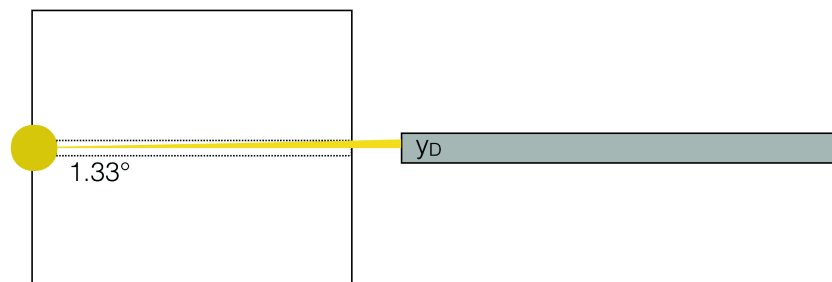
Figure 7.3: A scheme of the collimator emission hole projected onto the crystal.

The full setup is placed inside a black box to avoid direct light on the sensors. The electronic readout circuit is positioned outside the black box in order to prevent temperature changes in the box. Cables are used to bring the power supply from the electronic circuit to the sensors and to carry the output signals from the SiPMs to the readout circuit.

The block diagram of the **electronic scheme** is sketched in Figure 7.4. It has been designed to achieve a double purpose: the SiPM output signal is split and one branch is directly fed into the digitizer to be integrated, while the other provides the trigger after a 32 dB amplification and a leading edge discrimination. This electronic scheme allows to perform spectroscopy measurements and to characterize the SiPM in dark conditions, which in turns permits to evaluate the system response in terms of energy and of number of collected photons. At the same time, the events will be counted for the coincidence detection measurements using the trigger signal: the amplification reduces the rise time difference of the signals corresponding to different energies and eliminates the time walk uncertainty. The digitizer and the amplification unit used are contained in the SiPM Educational Kit, described in Chapter 2. The two channels of the PSAU have been verified to be equalized on the base of the peak-to peak distances of the Multi-Photon spectra acquired by using the same sensor on both channels.
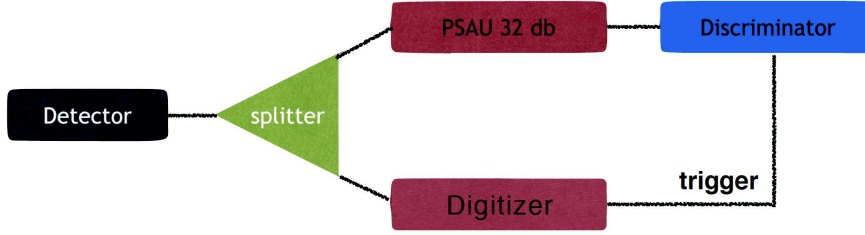
Figure 7.4: The layout of the SiPM readout of the experimental set-up.

The scintillating **crystals** in use are the same of the EasyPET demonstrator (LYSO bars by Kinheng of $2\times2\times30$ mm^3 coated with the white reflector of BaSO$_4$ and wrapped in aluminum). The tested **sensors** have different dimensions in order to evaluate the effect of the geometrical coupling in the light collection efficiency. In fact, the first one is the SiPM by Hamamatsu used in the EasyPET demonstrator, which has only 1×1 mm^2 area, not matching the crystal cross area. In addition it is from an old series of sensors (S10362-11-050P), which feature a high noise. For these reasons, two additional sensors were also tested with the experimental set-up: an Hamamatsu sensor with area of 1.3×1.3 mm^2 (S13360-1350CS) and another Hamamatsu sensor with area of 2×2 mm^2 (S13360-2050VE), both belonging to the latest generation. Table 7.4 summarizes the main characteristics of the considered sensors as reported in the data-sheets.

Parameter	S10362-11-050P	S13360-1350CS	S13360-2050VE
Number of pixels	400	667	1584
Area	$1 \times 1 mm^2$	$1.3 \times 1.3 mm^2$	$2 \times 2 mm^2$
Pixel pitch	$50\mu m$	$50\mu m$	$50\mu m$
V_{bd}	$\cdot$	$\cdot$	$52.07V$
V_{op}	$V_{bd} + 3V$	$V_{bd} + 3V$	$V_{bd} + 3V$
DCR	$100kHz$	$90kHz$	$300kHz$
OCT	$\cdot$	3%	$\cdot$
Gain	7.5×10^5	1.7×10^6	1.7×10^6
PDE @ 440 nm	35%	40%	40%

Table 7.2: The main characteristics extracted from the data-sheets of the three sensors under test: Hamamatsu 1×1 mm^2 S10362-11-050P, Hamamatsu 1.3×1.3 mm^2 S13360-1350CS and Hamamatsu 2×2 mm^2 S13360-2050VE.

The S13360-2050VE matches perfectly the crystal surface but it is affected by higher noise contribution with respect to the other sensors. The S13360-1350CS instead has a very small noise and its area is in between the one of the other two SiPMs. The following analysis will highlight which sensor constitutes the best compromise for the EasyPET prototype in terms of light collection and coincidence detection efficiency.

7.2 SiPMs characterization

The characterization of the sensors under test has been performed according to the waveform analysis protocol previously outlined in Chapter 3. The SiPM signal is amplified by 32 dB, digitized at 250 Ms/s and recorded for a time window of 4 μs. For all the three sensors and at each bias voltage an acquisition time of about 10 minutes allows to record $\sim 10^5$ waveform events. The acquisition is synchronous to the LED pulse and the sensor response, a pulse following a Poisson statistic with a mean number of 5 photons, is centered with respect to the acquisition window.

Figure 7.5 displays typical events for the three sensors. It is evident that the 1.3$\times$1.3 mm^2 sensor appears to be minimally contaminated by spurious effects.
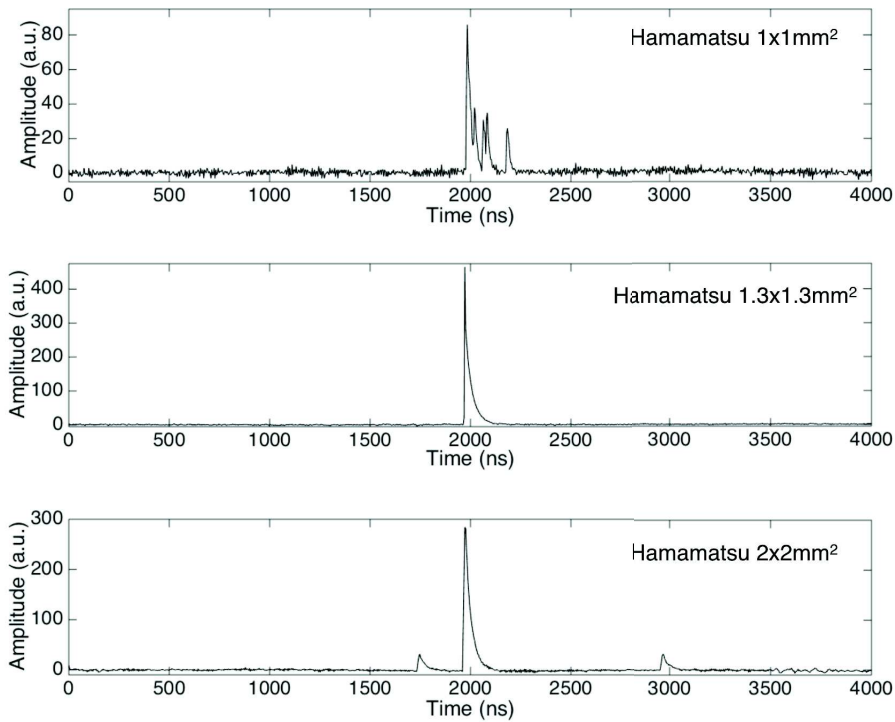
Figure 7.5: Exemplary waveform events by the three sensors under test.

This is confirmed by the Multi-Photon spectra of the three sensors, shown in Figure 7.6, obtained by integrating the waveform events around the signal pulse. Qualitatively, it can be seen that the stochastic terms have an impact on the quality of the spectrum in terms of the spread of the peaks and of the underlying background component.
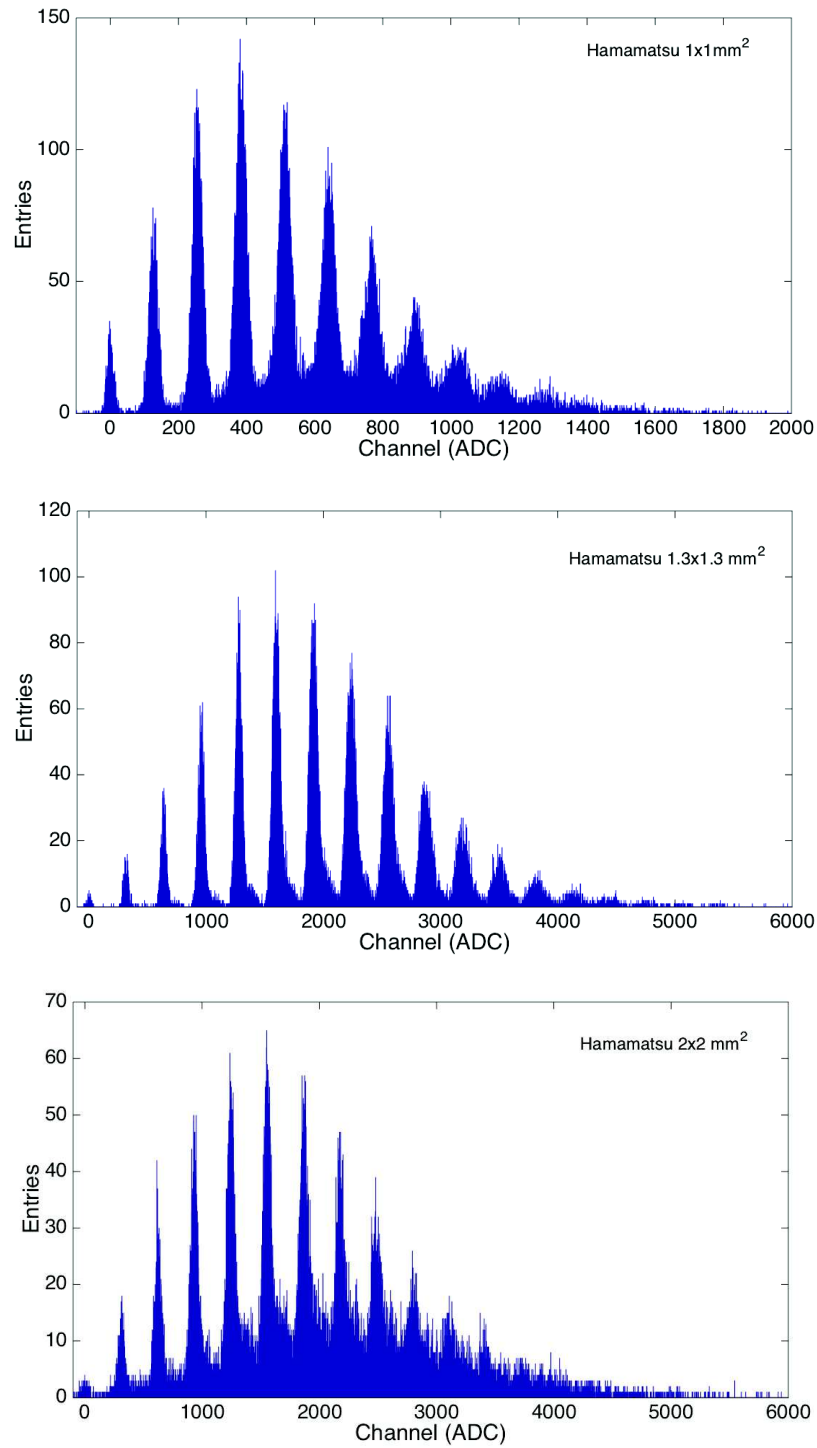
Figure 7.6: The Multi-Photon spectra obtained by integrating the waveform of the digitized pulses for 100 ns, 224 ns and 160 ns for the 1×1 mm^2, the 1.3×1.3 mm^2 and the 2×2 mm^2, respectively.

From the Multi-Photon spectra the Gain of the sensors can be assessed at each bias voltage and by a linear fit the breakdown voltage can be extrapolated. The data points in Figure 7.7 represent the Gain of the three sensors as a function of the Over-voltage and the superimposed dashed lines correspond to the straight line fits. Looking at the line trends and considering that the Gain depends on the pixel capacitance, it can be inferred that the producer has used the same capacitance in the three cases but an higher gain is reached in the new generation sensors. The resulting values of the breakdown voltages for the three sensors are reported in Table 7.3, together with the adopted working point conditions in terms of bias voltages and Gain.
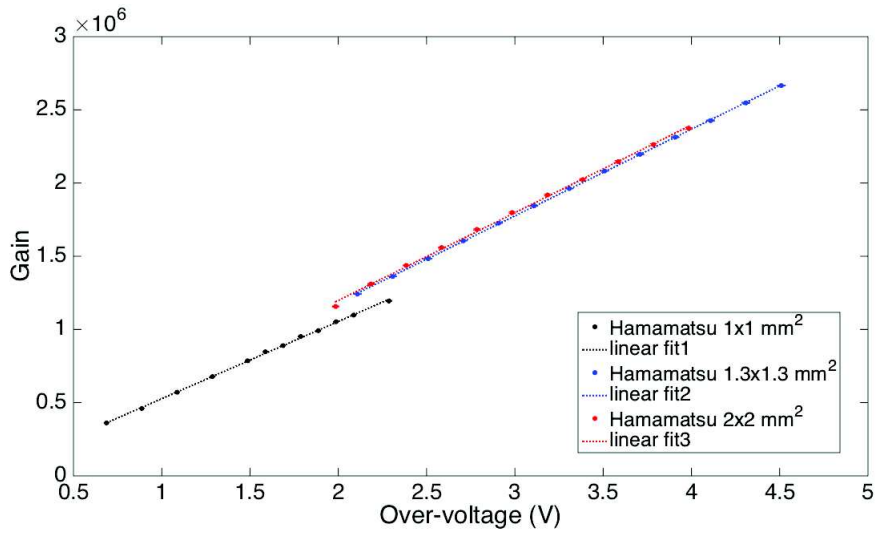
Figure 7.7: The gain versus the Over-voltage for the three sensors. The points represent the data and the dotted lines are the linear fit functions.

Measurement	S10362-11-050P	S13360-1350CS	S13360-2050VE
$V_{bd}(V)$	71.81 ± 0.01	51.29 ± 0.01	52.12 ± 0.04
$V_{op}(V)$	73.3	54.6	55.1
Gain	$8.37 \cdot 10^5 \pm 2 \cdot 10^3$	$1.96 \cdot 10^6 \pm 2 \cdot 10^3$	$1.80 \cdot 10^6 \pm 4 \cdot 10^3$

Table 7.3: The measured breakdown voltages, working point bias voltages and Gain for the three sensors under test.

The method described in Chapter 3, essentially based on the pulse identification and counting in the two regions of the acquisition window, before and after the signal pulse allows to measure the DCR, the OCT and the AP of the three sensors. The results reported in Figures 7.8, 7.9 and 7.10 confirm the qualitative assessment of the Multi-Photon spectra. The 2×2 mm^2 has higher DCR due to the higher active area, while the 1×1 mm^2, considering the DCR per unit area, is the sensor with the major noise contribution.
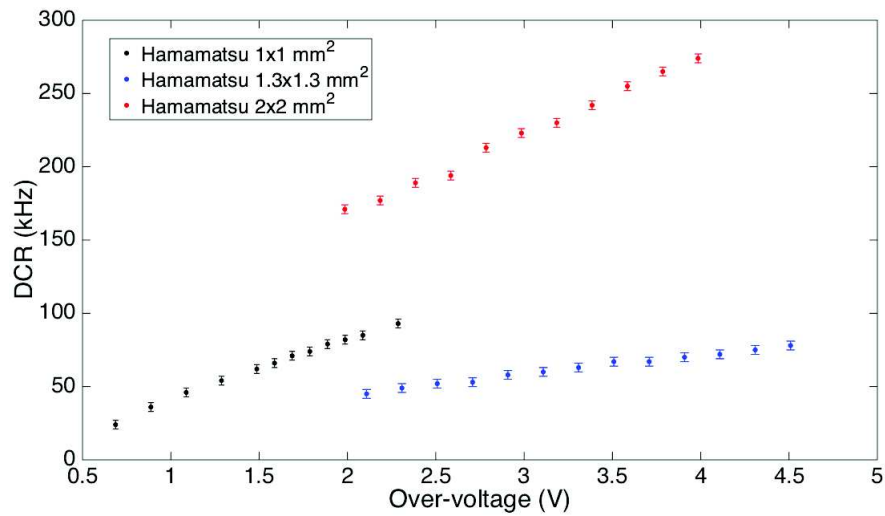
Figure 7.8: The DCR as a function of the Over-voltage for the three sensors.

Also for the OCT the worse performance correspond to the smaller area sensor, due to its old technology. The best features in terms of both DCR and OCT are instead attributed to the 1.3×1.3 mm^2.
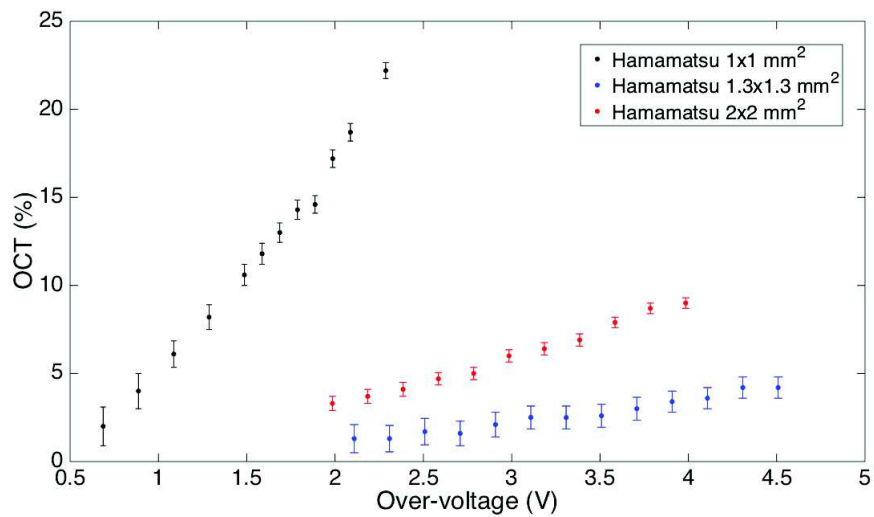
Figure 7.9: The OCT dependence to the Over-voltage for the three sensors.

Concerning the AP, it is clear that the newly developed sensors have a really low AP effect, less than the 3%, while the old one has a tremendously huge AP probability, growing almost exponentially with the Over-voltage.
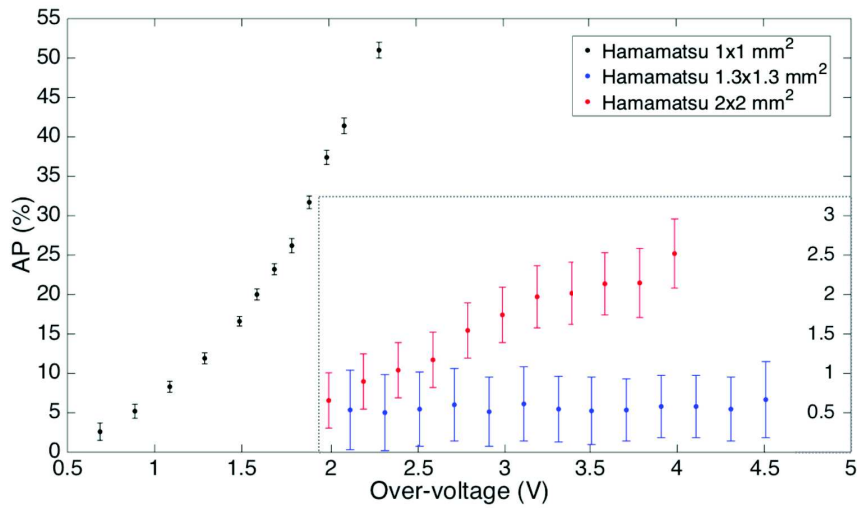
Figure 7.10: The AP versus the Over-voltage for the three sensors. Two scales have been used as the data sets have very different values.

As a consequence, it can be concluded that the new sensors feature better performance in terms of Gain and spurious effect with respect to the SiPM originally in use in the EasyPET demonstrator. It is not trivial to choose which one is the optimal choice for the new EasyPET prototype among the 1.3×1.3 mm^2 and the 2×2 mm^2 without a full qualification of the whole detecting unit.

7.3 Crystal-sensor alignment

The determination of the optimal alignment between the sensor and the crystal plays a crucial role in order to evaluate the overall performance. The figure of merit for the alignment measurement is based on the ADC value corresponding to the 511 keV photo-peak of the ^{22}Na spectrum. In fact, when the sensor and the crystal are aligned the light collected is at maximum and also the integral of the signal pulse corresponds to an higher ADC channel. This represents only a relative measurement, but at this phase the goal is to find the best operative conditions for each sensor at the working bias voltage.

The procedure starts with the pair of sensors fixed to the holders of the set-up in Figure 7.1 and biased at the operating voltage. Each sensor is aligned with respect to its crystal, independently from the other sensor, one coordinate at a time, by acquiring and analyzing the sodium spectra with the single detecting unit. The 10 μCi source of ^{22}Na is housed in the half part of the collimator to be at the right height and in contact to the front face of the crystal of the considered detecting unit. In the reference system adopted the height is the z coordinate, while the y is longitudinally directed as the crystal length and the x coordinate is perpendicular to the axis where are lying the crystals and the source (Figure 7.11).

The first step consists in the optical coupling between the sensor considered and the correspondent crystal by putting some optical grease between them.

Figure 7.11: The system coordinates.

As the crystals are already fixed in the correct positions, the y coordinate is determined by placing the sensor almost in contact to the crystal.

Then the x position is determined by changing the offset between the sensor and the crystal at steps of 200 μm with the micro-metric screw, acquiring the spectrum at each position and determining the channel corresponding to the 511 keV peak through a Gaussian fit. The higher value of the ADC channel is retained to be correlated to the best x alignment.

Finally, having fixed the sensor in the correct positions for the y and the x coordinates, the z is determined through a scan of the sensor position along the system height. Figure 7.12 shows the response of the three tested sensors in terms of the photo-peak position as a function of the z of the sensor. The optimal z position of the sensors corresponds to the maximum of the curve.

This measurement can also be exploited to establish the tolerance required in the alignment between the sensor and the crystal. For the smaller area sensor the alignment is not such a critical issue: the position of the peak has a plateau in the centre and starts to decrease significantly only when the displacement between the crystal and the sensor is of 0.4 mm. For this reason, the fact that the detecting unit case of the EasyPET demonstrator has been realized with a 3D printer featuring a precision of 0.3 mm is considered to be adequate. Instead, a relative mis-alignment of 0.4 mm will cause a 9% decrease of the peak position for the 1.3×1.3 mm^2 sensor, leading to a loss of about 50 photons. The conversion between channels and number of photons is obtained by considering that the peak-to-peak distance at the operating voltage and with an amplification of a factor 40 (32 dB) is 320 ADC channels, while the sodium spectra are obtained by integrating the split SiPM output signal. For the 2×2 mm^2 sensor the peak position changes by 13% with a displacement of 0.4 mm, causing a loss of about 110 photons. It is true that, even with the perfect alignment, the light collected with the small sensor is lower with respect to the number of photons detected with these other two sensors, even if not optimally aligned. However, since the main goal is finding the best conditions for enhance the light collection, the alignment of these sensors constitutes a relevant issue: a different method is required to produce the detecting unit case with a precision of 0.1 mm.
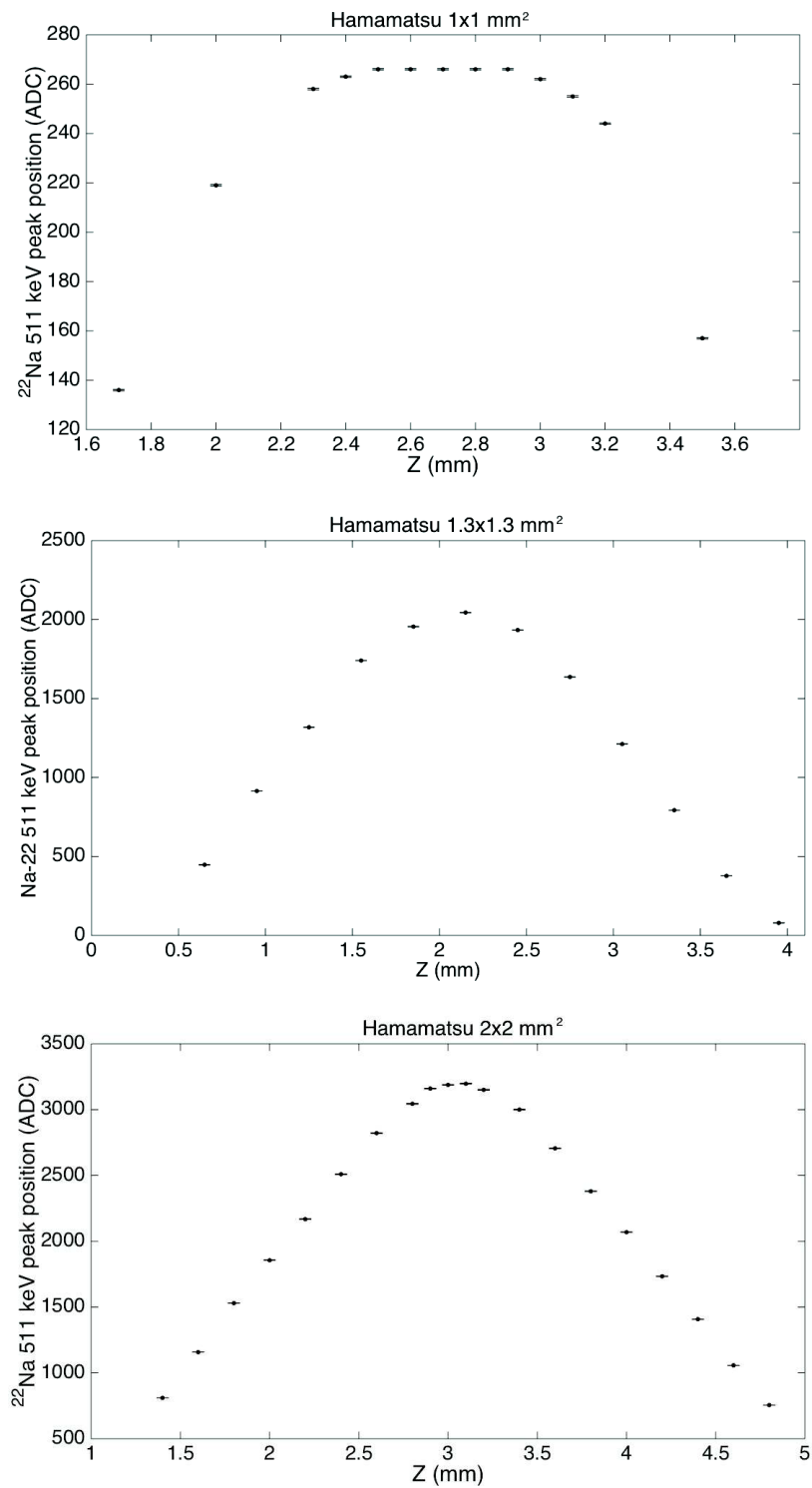
Figure 7.12: The 511 keV peak in ADC as a function of the z coordinate of the micro-metric screw adjusting the sensor position with respect to the crystal.

7.4 Crystal-sensor geometrical coupling

The figures of merit taken into account to establish which sensor provides the best performance of the detecting unit are the energy resolution, the peak-to-total ratio and the number of collected annihilation photons. The quality of the spectrum reflects the properties of the geometrical coupling between the sensor and the crystal and has an impact on the lowest possible threshold that could be set and on the number of coincidence events selected.

Figure 7.13 reportes in black the spectra acquired for 20 minutes with the three tested sensors biased at their operating voltages. The ^{22}Na source is housed in the half part of the collimator and positioned in contact with the crystal. The spectra are obtained by integrating the split SiPM output during a gate of 200 ns for the smaller area sensor and 300 ns for the other two. The optimal length of the integration gate is the one that maximizes the signal peak area without degrading the quality of the spectra. The trigger is provided by the other branch of the SiPM output, amplified 40 times and discriminated at 25 mV for the 1×1 mm^2 and the 1.3×1.3 mm^2 and at 50 mV for the the 2×2 mm^2. The threshold has been chosen as the minimum value that allow eliminating the SiPM dark count. In the next section, thanks to the determination of the conversion factor, it will be possible to express the threshold in energy. The red distributions represent the background, as they are obtained by accumulating data for 20 minutes but in absence of the radioactive source: they are due to the LYSO self-activity and represent a negligible contribution to the whole source spectra. The blue distributions are the subtraction of the background to the source spectra, and the differences with respect to the raw data are really imperceptible. The spectra are characterized by the photo-peak at 511keV, corresponding to fully absorbed photons, and a contribution from Compton scattered events. In spectra acquired with higher SiPMs area it is also possible to distinguish the 1275 keV and the backscattering peaks.

In order to determine the **energy resolution** of a photo-peak due only to the system resolution, the underlying physics processes that are considered as backgrounds have to be estimated. In fact, for γ energies below the pair production (E$_\gamma$< 1.02 MeV) the interaction with the detector is dominated by Compton scattering and photo-absorption: the experimental spectrum results in a photo-absorption peak broadening contaminated by the edge of the Compton spectrum. In order to separate the underlying background of the Compton events from the information of the photo-peak, the spectra are processed with the Sensitive Nonlinear Iterative Peak (SNIP) algorithm [160], [161], [162]. It is a flexible and widely used method, since it does not need assumption on the background shape. The iterative procedure is stopped when the estimated background is monotonically changing in the peak region or when it drops below 5% of the total area underneath the peak (for low background spectra). A more detailed description of the SNIP algorithm will be addressed in Appendix B. Figure 7.14 shows the SNIP procedure applied to the blue spectra of Figure 7.13. The Compton scattering background has been correctly subtracted as the peak sides fluctuate around zero. A fit to the resulting photo-peaks allows to measure the energy resolution at 511 keV: it corresponds to 22.02%±0.01% for the small area sensor, to 15.45%±0.01% for the intermediate area sensor and 14.83%±0.01% for the large area sensor. The latter two represent a good result, dominated by the irreducible intrinsic resolution of the LYSO crystal, of ∼15%.
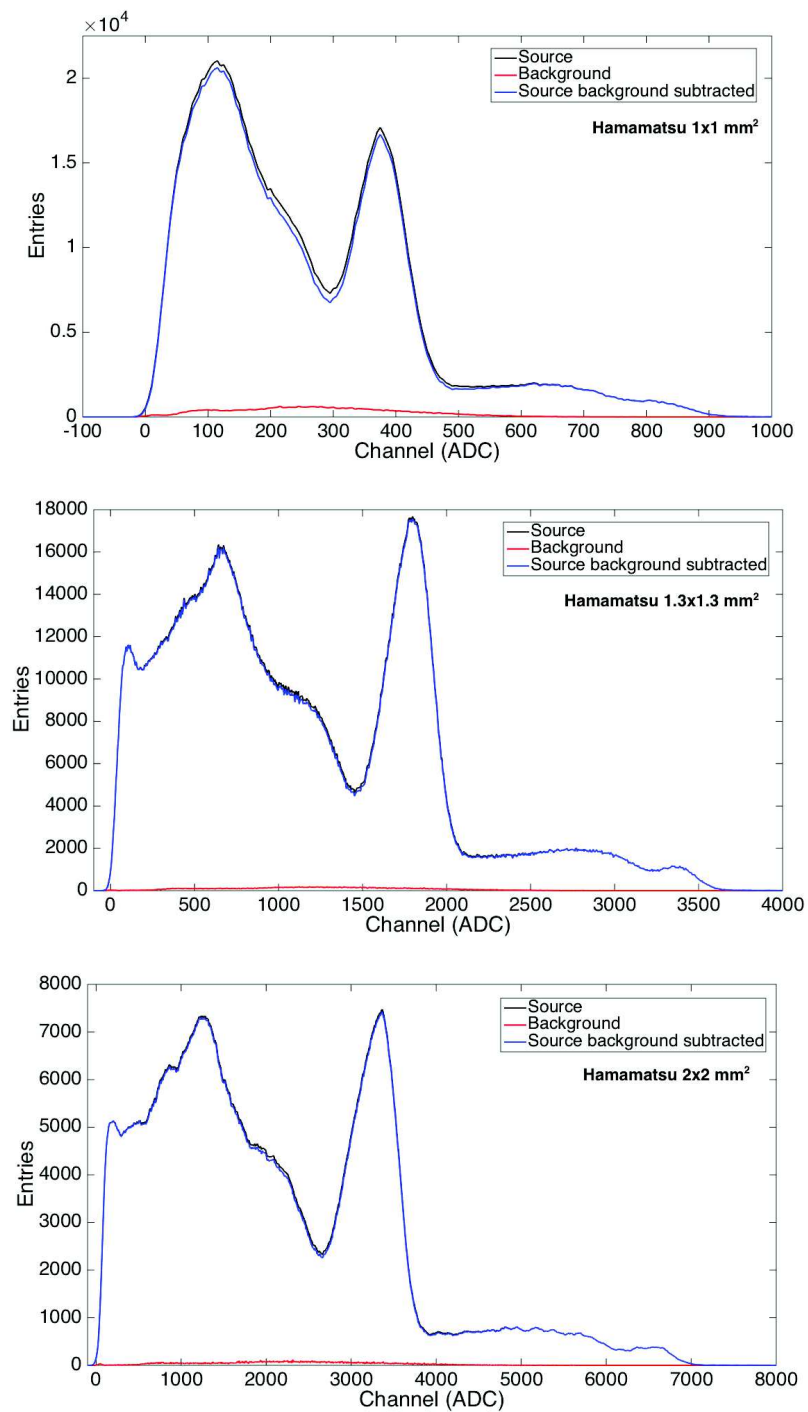
Figure 7.13: The distributions in black represent the ^{22}Na spectra acquired for 20 minutes with the three sensors considered. In red are shown the background contributions and in blu the source distribution background subtracted.
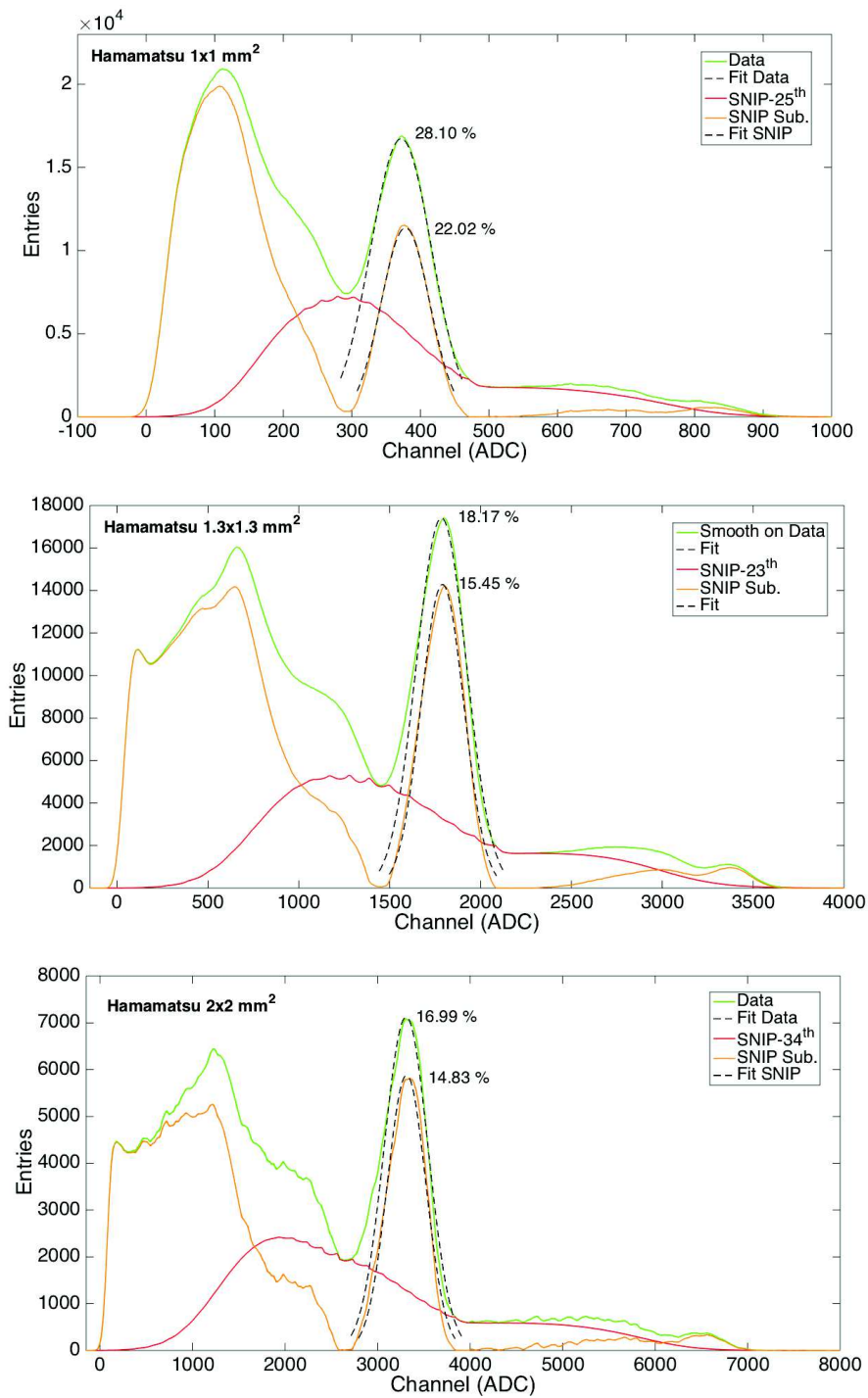
Figure 7.14: The SNIP algorithm applied to ^{22}Na spectra of the three sensors.

The **peak-to-total ratio** has been calculated by normalizing the areas underneath the 511 keV peaks to the total number of events. The peak-to-total ratio results to be 28.1%± 0.1% for the 1×1 mm^2, 25.9%± 0.1% for the 1.3×1.3 mm^2 and 25.1%± 0.1% for the 2×2 mm^2. In general, these results are in agreement with the value of 25.5% attributed to the LYSO photon fraction: it means that the fraction of the area under the photo-peak with respect to the area under the Compton continuum corresponds the ratio between the photoelectric and the Compton cross-sections in the detector material.

The last quantity that has to be measured is the **number of photons** collected in the photo-peak. Thanks to the performed SiPMs characterization, which is reported in Section 7.2, the peak-to-peak distance corresponding to one photon has already been measured in ADC channels for the three sensors. It has to be considered that in the characterization configuration the SiPM signal was amplified of a factor 40, while in the current set-up the signals that are integrated are the direct sensor output that has also been split in two branches. As a result, it is necessary to divide the peak-to-peak distance by 80 to find the number of channels corresponding to one photon in the current configuration.

For the 1×1 mm^2 it has been calculated that one photon corresponds to 1.55 ± 0.01 ADC channels: the number of fired cells for the 511 keV peak, located at 373 ± 1 ADC, is 241 ± 2. As the SiPM has 400 cells, the saturation effect on the number of photoelectrons should be considered: the correction according to Equation (1.8) lead to the value of 369 ± 6. The number of primary photons can finally be determined by taking into account the impact of the (11 ± 1)% of the OCT: it results to be 329 ± 10. This value can be compared with the estimation of the number of impinging photons. The LYSO crystal produces about 16352 photons per 511 keV: only the (25 ± 5) % of light is conveyed to the sensor, the typical percentage accounting for the light transmission of the crystal and the optical coupling grease [163], then only a fourth can be detected due to the sensor geometrical acceptance and finally the 35% is effectively detected thanks to the sensor photon detection efficiency. The expected number of incoming photons is 356 ± 72, which is in agreement with the measured value.

The 1.3×1.3 mm^2 shows a number of fired cells equal to 447 ± 2 at 511 keV because the peak corresponds to 1789 ± 2 ADC and the charge integrated for one photon is spread over 4 ± 0.01 channels. As the SiPM comprises 667 cells, the number should be corrected for the saturation. Taking into account also the (2.5 ± 0.5 %) of the OCT, the number of primary photons corresponds to 721 ± 12. The value is consistent with the expected number of 687 ± 137 impinging photons, calculated assuming the same number of generated photons from the LYSO and the light collection on the SiPM mentioned before, but reduced by a factor of 42 % to account for the ratio of the sensor and the crystal area an of 40 % to include the SiPM PDE.

Finally, with the 2×2 mm^2 the spectrum has a peak at 3378 ± 4 ADC, which corresponds to 923 ± 4 photoelectrons because of one photon is represented by 3.66 ± 0.01 channels. Considering that the sensor is composed by 1584 cells and has an OCT of (6.0 ± 0.7 %), the resulting number of primary photons is 1300 ± 20. This is in a fairy good agreement with 1635± 327, the calculated number of impinging photons from the hypothesis that the photons produced by the LYSO are scaled only for the the probability of light collection onto the sensor and of their detection method, as the area of the crystal and the sensor are perfectly matching.

The results of the measurements of the FWHM at 511 keV, of the peak-to-total ratio and of the photons collected at the photo-peak for the threes sensors under test are summarized in Table 7.4.

SiPM	FWHM	Peak-to-Total ratio	Ph.e.	Ph.
1×1 mm^2	$(22.02 \pm 0.01)\%$	$(28.1 \pm 0.1)\%$	241c	329 ± 10
1.3×1.3 mm^2	$(15.45 \pm 0.01)\%$	$(25.9 \pm 0.1)\%$	447 ± 2	721 ± 12
2×2 mm^2	$(14.83 \pm 0.01)\%$	$(25.1 \pm 0.1)\%$	923 ± 4	1300 ± 20

Table 7.4: The results of the figure of merit evaluated for the three sensors under test: the energy resolution at the peak, the peak-to-total ratio, the number of fired cells corresponding to the peak and the number of photons, obtained by correcting the number of photoelectrons for the saturation effect and the OCT.

From the comparison of the performances of the detecting unit equipped with the three different sensors in terms of light collection it can be concluded that the two SiPMs with higher areas allow to obtain a great advantage in terms of energy resolution and peak-to-total ratio with respect to the sensor currently used in the EasyPET demonstrator. Between them, the 2×2 mm^2 permits to achieve a slightly better FWHM. In terms of number of photons collected at the photo-peak the values reflect mainly their geometrical coupling with the crystal area. As a result, it is obvious that the higher number of photons detected corresponds to the spectrum acquired with the largest area sensor.

Calibration

The calibration is useful to convert in energy the threshold that are applied on the signal amplitude and it is obtained with a two-step procedure described in detail in the following paragraphs.

The correspondence between **channels** and **energy** can be established by acquiring spectra from a set of radioactive sources. The spectra of the ^{133}Ba, with gaussian fit to the peaks at 81 keV and 356 keV, of the ^{57}Co, with a gaussian fit to the peak corresponding to a mixture of 122 keV and 136 keV that can not be distinguished, and of the already shown ^{22}Na recorded with the smaller area sensor are reported in Figure 7.15. Because of the low energy resolution it is not possible to fit the peaks at energies higher than 511 keV. In addition, the low energy at about 30 keV could not be separated from the SiPM DCR contribution due to both the low number of collected photons at that energy and the low sensor gain. Figure 7.16 shows the spectra acquired for the calibration of the 1.3×1.3 mm^2 sensor with the ^{133}Ba, the ^{137}Cs and the ^{22}Na sources. The red lines represent the Gaussian fit to the peaks: it is possible to notice that the higher value of both the SiPM gain and the geometrical matching between the sensor and the crystal surface result in the extremely better quality spectra. It is possible to distinguish the 31 keV peak in the first two spectra and to fit the peaks at 662 keV and 1275 keV in the ^{137}Cs and in the ^{22}Na spectra, respectively. Finally, an even better peak resolving capability can be appreciated in Figure 7.17, where the spectra of the^{133}Ba, the ^{137}Cs and the ^{22}Na sources are acquired with the bigger area sensor.
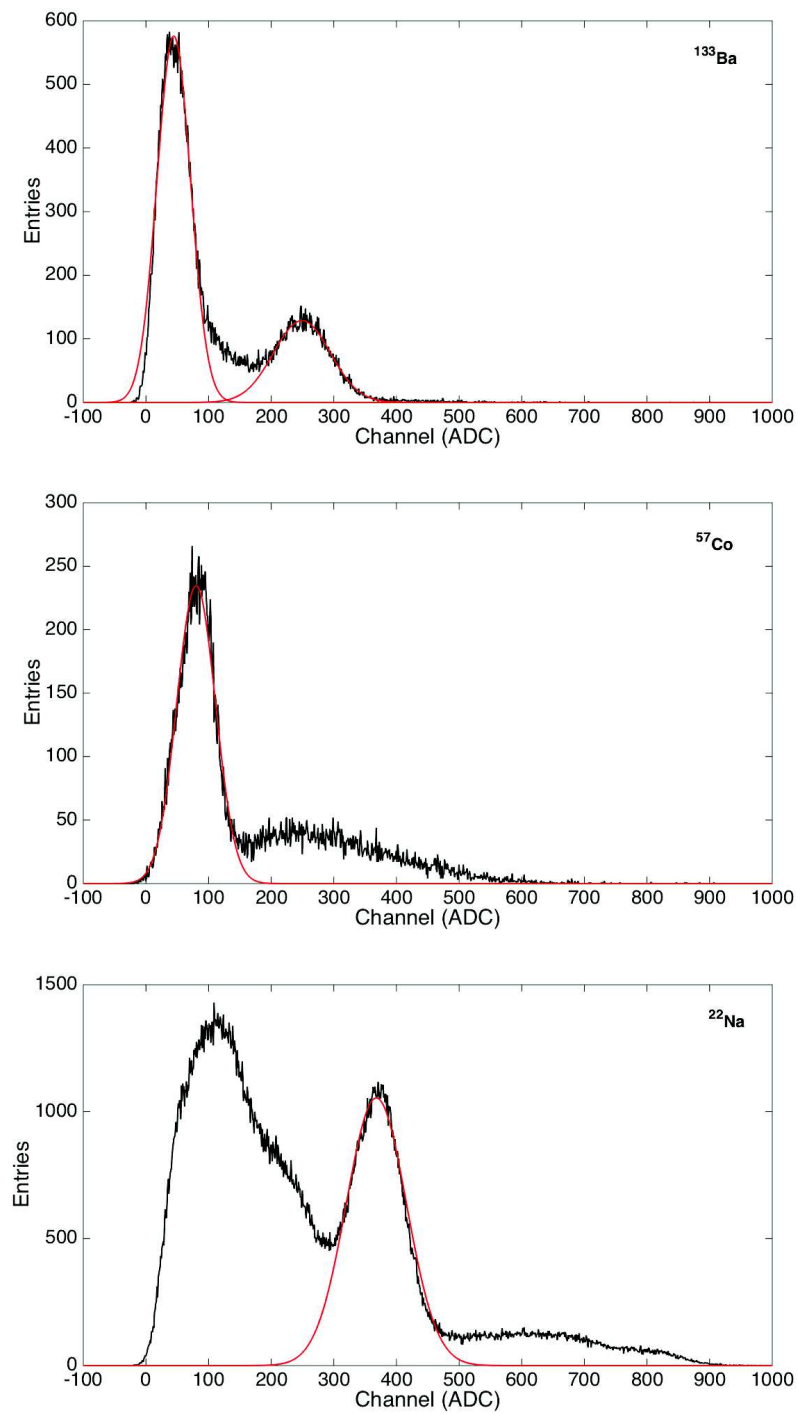
Figure 7.15: Spectra of ^{133}Ba, ^{57}Co and ^{22}Na acquired with the 1×1 mm^2.
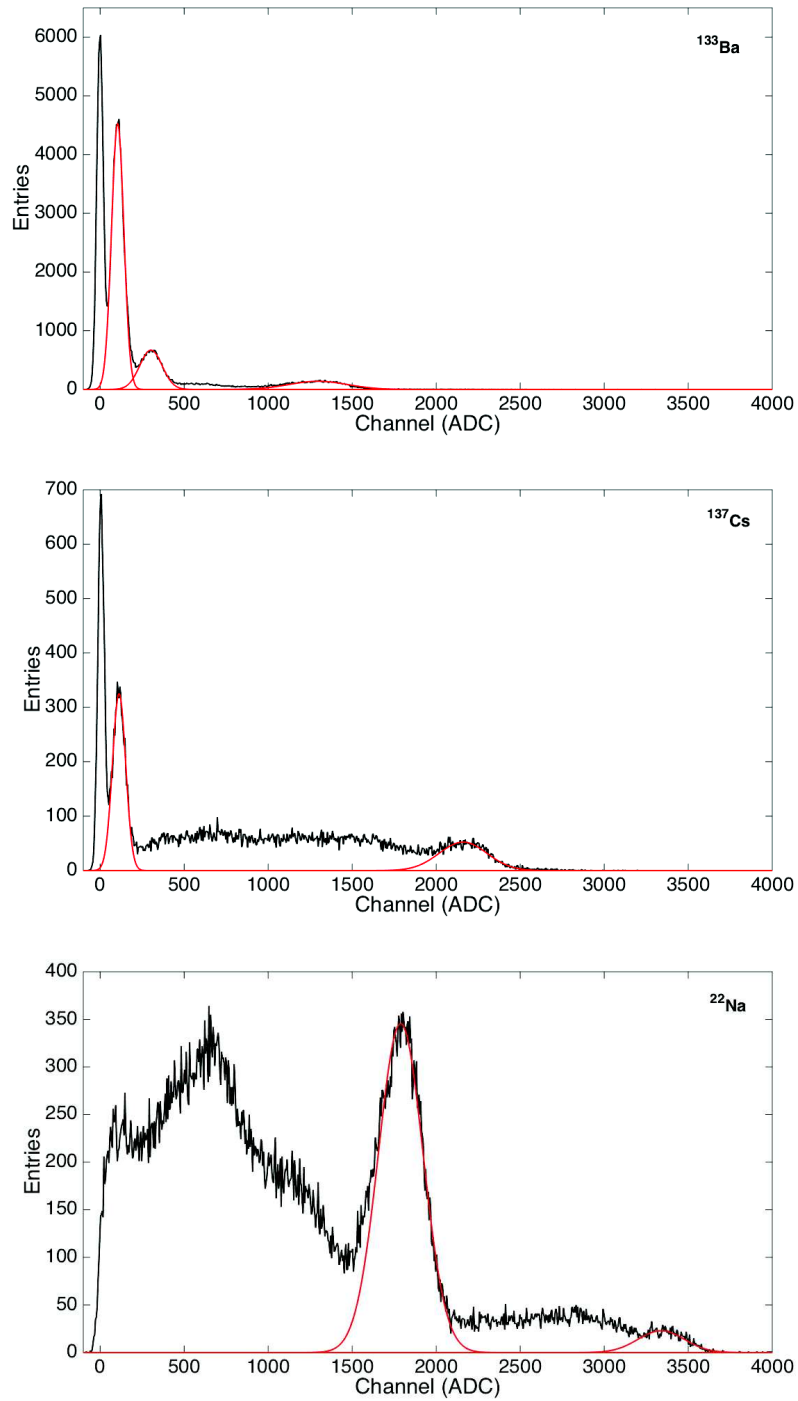
Figure 7.16: Spectra of ^{133}Ba, ^{137}Cs and ^{22}Na acquired with the 1.3×1.3 mm^2.
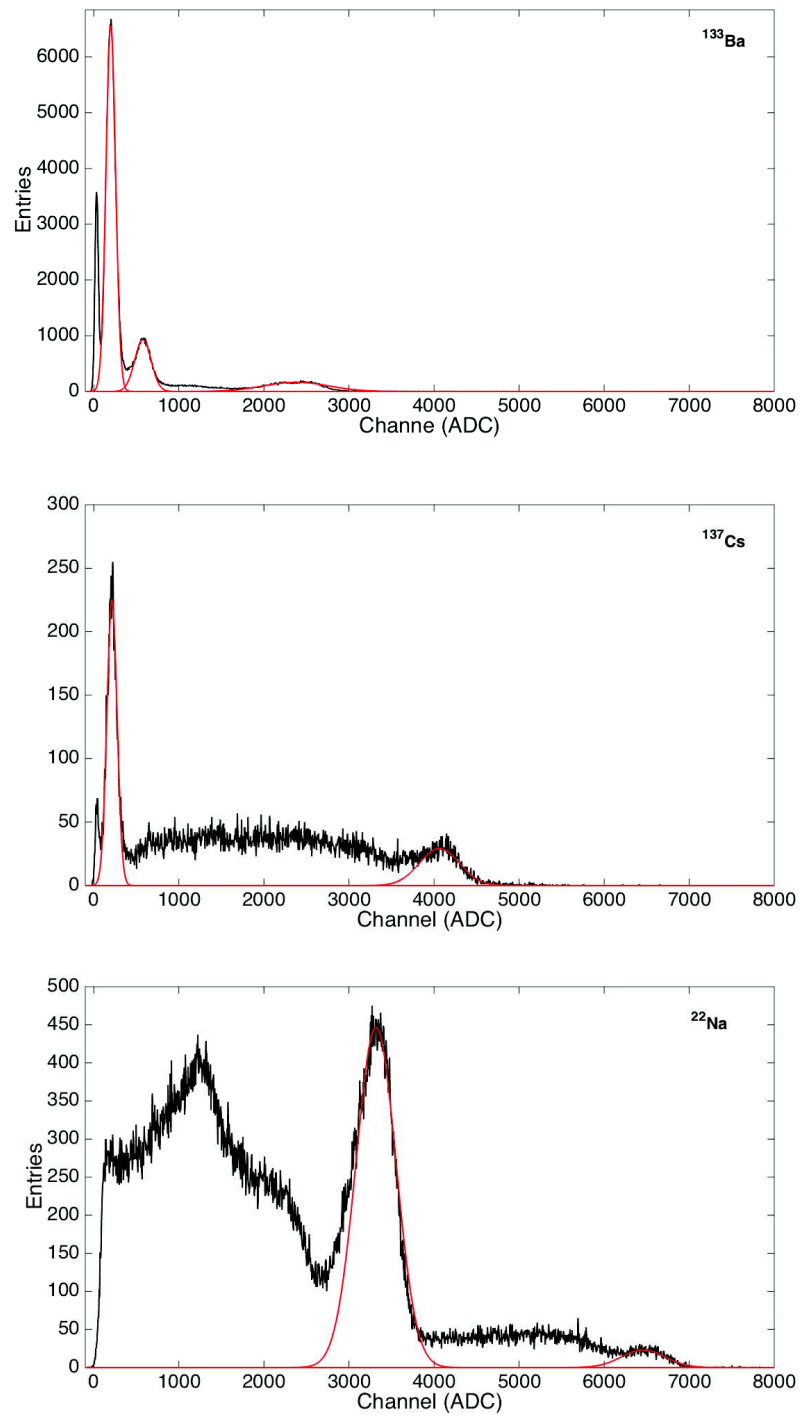
Figure 7.17: Spectra of ^{133}Ba, ^{137}Cs and ^{22}Na acquired with the 2×2 mm^2.

The mean value of the gaussian fit to the various peaks as a function of the energy is reported in Figure 7.18 for the spectra acquired with the three sensors. It is clear that, for each sensor, the effect of the saturation of the number of fired cell occurs after the 511 keV. The channels corresponding to 662 keV and 1275 keV are lower than expected and these data points have not been included in the fit procedure. The three straight lines represent the fit functions, expressed in the form: Channel = $a \cdot$ Energy $+ b$. The resulting parameters a and b are 0.75 $\pm$ 0.01 and -16 $\pm$ 8 for the 1$\times$1 mm^2, 3.48 $\pm$ 0.03 and 10 $\pm$ 10 for the 1.3$\times$1.3 mm^2 and 6.56 $\pm$ 0.04 and 26 $\pm$ 13 for the 2$\times$2 mm^2. The $\chi^2/d.o.f.$ for the three cases are, respectively, 1.2, 3.4 and 2.9, confirming the good quality of the fit.
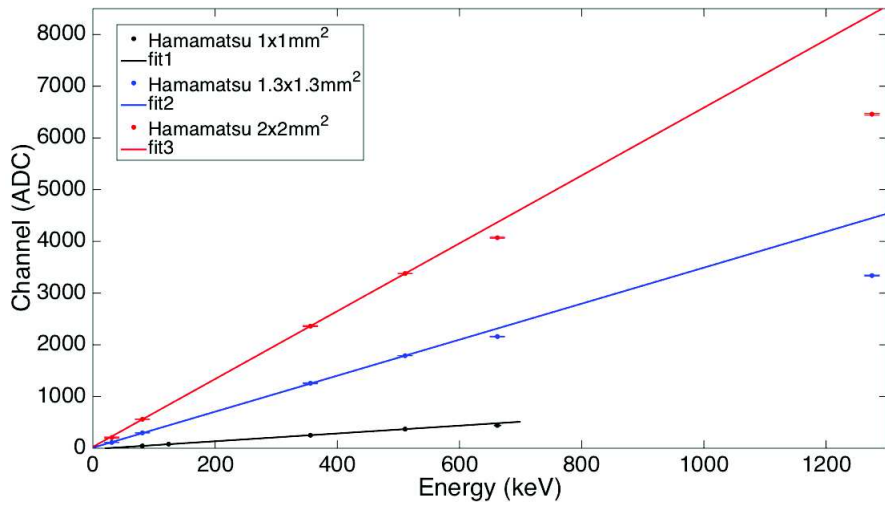
Figure 7.18: The channel energy calibration for the three sensors under test. The error-bars are the data points and the lines represent the linear fit.

The relation that allows to convert the value of the discriminator threshold expressed in **mV** in the correspondent ADC **channel** can be determined by recording a set of ^{22}Na spectra acquired by changing the events acceptance threshold and keeping fixed the total amount of time dedicated to the data acquisition. In fact, the analysis is based on the ratios between the spectra acquired with different thresholds and the reference spectrum. The latter has been obtained using the lowest possible threshold that allows to discard the noise. For this reason it is crucial that the spectra are normalized in time. Then the resulting distribution is fitted with an error-function and the position corresponding to the 90% of the plateau value is retained as a measurement in ADC channel of the set discriminator threshold.

In order to illustrate the procedure, in Figure 7.19 are reported the reference spectrum for the 1.3$\times$1.3 mm^2 SiPM, acquired with a threshold of 25 mV, a spectrum obtained selecting the events with an amplitude higher than 400 mV and the ratio of them. It is obvious that the net effect of the discriminator threshold is a shaping of the low energy region of the spectrum and the fit function, represented by the red line, describes well its behavior.
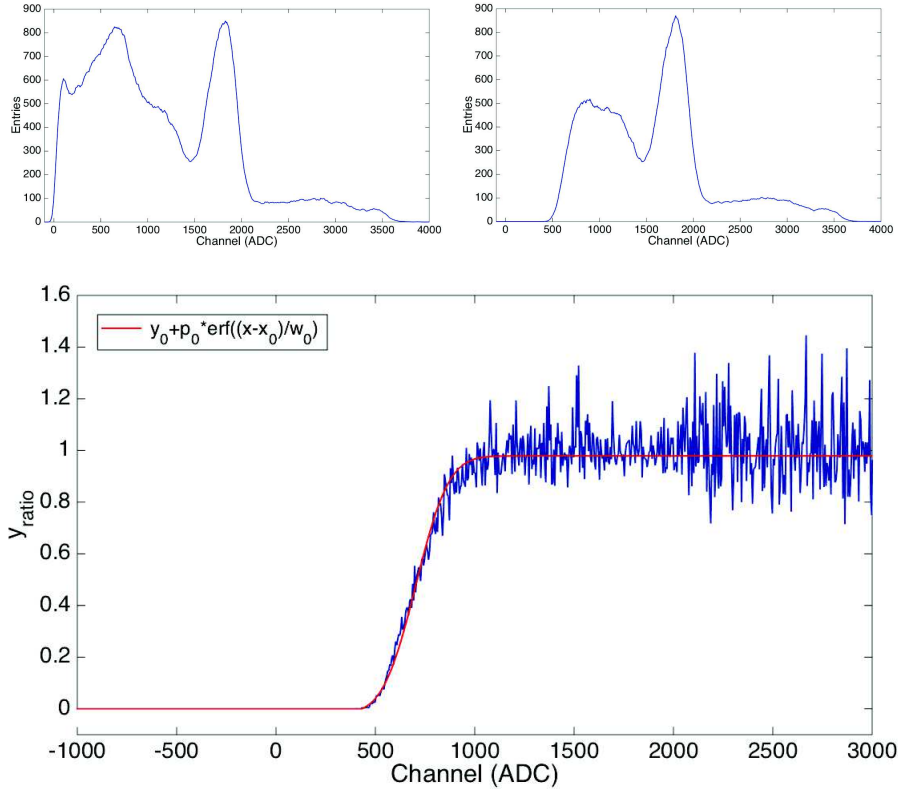
Figure 7.19: The spectra acquired with the 1.3×1.3 mm^2 SiPM applying a threshold of 25 mV (top left) and of 400 mV (top right). On the bottom the ratio of the two spectra is shown, with an error function fit (red line).

Figure 7.20 illustrates the calibration curves obtained by applying the explained procedure to the three sensors under test: the channel corresponding to the cut in the spectrum is shown as a function of the imposed threshold in mV. It is possible to notice that for the three sensors there is a proportional law between the two quantities: a linear fit is performed on each set of data, represented with the solid lines. The fit function result to be compatible for the two sensors of higher area: the obtained parameter are a=2.15±0.03 and b=-11±9 for 1.3×1.3 mm^2, and a=2.04±0.02 and b= 2.5±5.7 for the 2×2 mm^2. Instead, the slope and the intercept of the fit function to the data of the 1×1 mm^2 are 1.52±0.02 and 10±5. In fact, this difference can also be appreciated in all the shown spectra: for the smaller area sensor the shaping introduced by the threshold is really very smooth compared to the effect of the same threshold on the events acquired with the other two SiPMs. The reason could be explained by considering that the signals from the 1×1 mm^2 are very small because of the low gain of the sensor. As a consequence, the signal shapes have an high uncertainty, especially at low energies, and the selection on the signal amplitudes lead to the acceptance of events with a huge fluctuation of the signal integral.
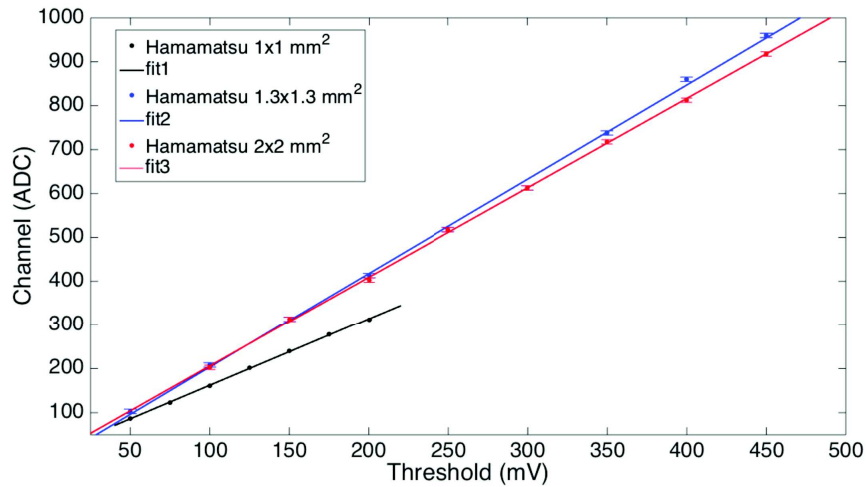
Figure 7.20: The channel energy calibration for the three sensors under test. The error-bars are the data points and the lines represent the linear fits.

7.5 Coincidence detection efficiency

The most important figure of merit for the detecting unit performance consists in the coincidence detection efficiency, as it is the basic measurement of the EasyPET. It can be defined as the fraction of detected positron annihilation events with respect to the total number of back-to-back emitted photons. It depends both on the geometrical acceptance of the crystals and on the capability of the whole detecting unit to reveal the impinging photons. This latter quantity is a function of the scintillating material, of the light collection efficiency, of the sensor features and of the electronic noise.

Since the detecting units under test are dedicated to a 2D imaging prototype, it will be not fair to measure the coincidence detection efficiency referring to the entire 3D sphere with a radius equal to the distance between the crystal front face and the system centre. For this purpose, the collimator described in Section 7.1 is used: it generates an emission cone and allows to reduce the system to a kind of toroidal region including the two crystal front faces.

The measurement of the coincidence emission hole activity, which will be used as a normalization factor for the coincidence detection efficiency, is performed by embedding the ^{22}Na source inside the collimator and using two calibrated detectors. In particular, two LYSO crystal of $6\times6\times30$ mm^3 are positioned in contact with the collimator, with their centers aligned to the emission hole and optically coupled to two Hamamatsu SiPMs of 6×6 mm^2 area, already characterized in Chapter 3. In this way, as depicted in Figure 7.21, all the photon pairs emitted by the hole will interact in the crystals and will be detected. The SiPMs are readout with the electronics of the experimental set-up and the logic output of the two discriminators, set at the lowest possible value, are fed into a coincidence logic to select only the events within a time window of 120 ns, as in the EasyPET demonstrator. Then, a counter has been used to measure the number of coincidence events above the threshold. The coincidence rate, after the subtraction of the background, result to be (112±3) Hz.
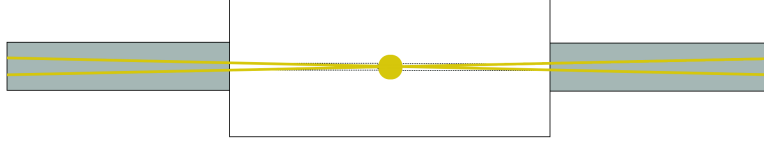
Figure 7.21: A sketch of the set-up used to measure the activity of the collimator emission hole: all the coincidence pairs of emitted photons are detected by the $6\times6\times30$ mm^3 LYSO crystals coupled to the 6×6 mm^2 Hamamatsu SiPMs.

When the coincidence rate are measured with the $2\times2\times30$ mm^3 LYSO crystals of the experimental set-up, coupled with the three sensors, lower values are expected. In fact, as explained in a pictorial manner in Figure 7.22, not all the photon pairs included in the solid angle of the crystals will be detected because they do not cross a sufficient quantity of scintillating material to interact.
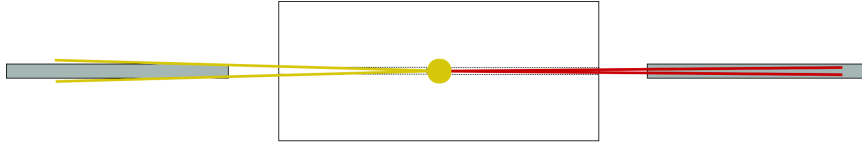
Figure 7.22: The coincidence detection efficiency are measured with the $2\times2\times30$ mm^3 LYSO crystals coupled to the various sensors under test: not all the back-to-back photon pairs emitted by hole are effectively detected due to the photon interaction probability in the LYSO.

In this scenario, the coincidence rate measurement accounts also for the effective distance that a photon has to travel inside the scintillators in order to be detected, which depends on the interaction length of the crystal material, its dimension and the energy of the photon. As a result, the coincidence detection efficiency can be interpreted as the ratio between the effective solid angle Ω_{eff} and the real solid angle covered by the crystal surface Ω:

$$\frac{\Omega_{eff}}{\Omega} = \frac{s}{(d+\Delta)^2} \cdot \frac{d2}{s}, \tag{7.3}$$

where s is the crystal surface, d is the distance between the source and the crystal and Δ accounts for the distance traveled by the photon in the crystal before interacting and being detected.

The results of the measured coincidence detection efficiency for the three considered sensors are summarized in Table 7.5. The 350 keV represents a reference, as it is the threshold usually adopted in preclinical PET systems, which have to discard the Compton scattering events to select only the true coincidences. It can be inferred that the EasyPET allows to lower the energy threshold, accepting more events and enhancing the coincidence detection efficiency. At each value of energy threshold, there is a slight effect related to the SiPM area: the bigger is the sensor area and the higher is the detection efficiency. In

fact, at fixed energy, a better spectra quality in terms of energy resolution and peak-to-total ratio ensures a better effectiveness in selecting the events above a certain threshold. The real advantage that comes from using the larger area sensor is that it allow to lower even more the energy threshold and achieve an higher coincidence detection efficiency: with the 2×2 mm^2 it is possible to select the photons with an energy higher than 10 keV, resulting in a $(9.9\pm0.9)\%$ of coincidence detection efficiency. The explanation lies in the fact that this sensor, for a fixed energy value, is capable to collect an higher amount of photons with respect to that detected by the other sensors. As a result, the same threshold of a tens of photons required to eliminate the background, corresponds to an higher energy for small sensor area and to a lower ones for sensors with areas matching the cross section of the scintillating crystals.

SiPM	350 keV	150 keV	Min. energy	Max. efficiency
1×1 mm^2	$(0.6\pm0.2)\%$	$(2.9\pm0.6)\%$	80 keV	$(4.5\pm0.7)\%$
1.3×1.3 mm^2	$(0.5\pm0.2)\%$	$(3.1\pm0.5)\%$	25 keV	$(4.7\pm0.7)\%$
2×2 mm^2	$(1.0\pm0.4)\%$	$(3.3\pm0.5)\%$	10 keV	$(9.9\pm0.9)\%$

Table 7.5: The results of the coincidence detection efficiency at 350 keV and 150 keV, together with the minimum energy threshold achievable and the correspondent maximum coincidence detection efficiency for the three sensors considered.

In addition, also from the quality of the spectra shown in Figure 7.23, obtained by placing the ^{22}Na source in between the detecting units and triggering with the coincidence signals, the superiority of the 2×2 mm^2 sensor with respect to the 1×1 mm^2 can be appreciated. The effect of the energy selection is evident. For the smaller area SiPM, the lowest achievable energy threshold introduces a shaping in the distribution, resulting in a loss of the number of events. The larger area sensor, instead, lead to a better energy resolution and it can be exploited to set a very low energy threshold without introducing any background contaminaton and maximizing the amount of selected coincidence events.
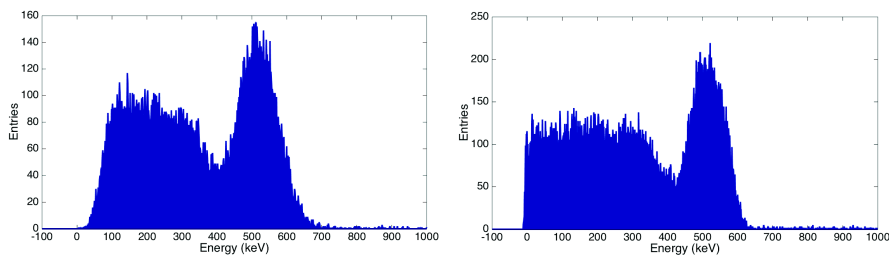
Figure 7.23: The ^{22}Na spectrum of the integration of the 1×1 mm^2 (left) and of the 2×2 mm^2 (right) SiPM output signal triggered by the coincidence of the two detecting unit discriminators.

Chapter 8

EasyPET prototype commissioning

A prototype based on the EasyPET concept has been realized in collaboration with Nuclear Instruments and Caen, starting from the previous demonstrator and including some improvements defined using the dedicated setup described in the previous Chapter. The EasyPET concept has been licensed to Caen and the prototype will become a commercial product for the education market. EasyPET constitutes an asset in high level didactic laboratories as it allows to teach by doing the basis of the SiPM characterization, the spectroscopy measurements together with the theoretical principles and the technology behind the PET imaging modality.

In this Chapter the design features of the EasyPET prototype will be explained, its functionalities will be shown and the qualification of its performances will be reported.

8.1 Prototype description and functionalities

The prototype of the commercial product for the educational market is shown in Figure 8.1 [164]. The improvements with respect to the demonstrator concern the electronic circuit on the U-shaped PCB responsible for the SiPM signal readout and for the control of the stepper motor movements (with a dedicated control board), the mechanics of the source holder and of the base and the control software. The sensors in use has not been changed with respect to the ones of the demonstrator, although the analysis carried out on the light collection and on the detection efficiency reported in the previous Chapter suggests that a significant improvement will be obtained with the use of the $2{\times}2$ mm^2 MPPC. The reason behind this decision is merely commercial: a large number of $1{\times}1$ mm^2 MPPC are already available at a very low price. As a result, for the first EasyPET production the sensors will be kept the same of the previous version.

The **electronic circuit** has been designed by Nuclear Instrument and the main idea was to introduce the improvements established with the analysis reported in the previous Chapter. For this purpose, two different branches have been implemented: one dedicated to spectroscopy and the other one for the coincidence detection. This choice is driven by the approach of the EasyPET

to lower the energy threshold and recover the limited geometrical acceptance, which requires a high gain on the signals. At the same time, it is necessary to qualify the system performances in terms of light collection, for which it is mandatory to distinguish the single photon signals generated by the SiPM. The implementation of this configuration is also advantageous considering the educational purposes related to the EasyPET because the students are guided from the SiPM characterization and the spectroscopy analysis towards the imaging principle with a unique device. The spectroscopy branch results to be very important in determining the proper energy threshold, measuring the energy resolution of the system, the threshold and channel calibration in energy units, assessing the system linearity, and in converting the light collected in number of photons.

Figure 8.1: The EasyPET prototype.

The electronic circuit of the U-shaped PCB and the control board are illustrated in Figure 8.2, while the U-shaped PCB is shown in Figure 8.3.

<div align="center">(a)   (b)</div>
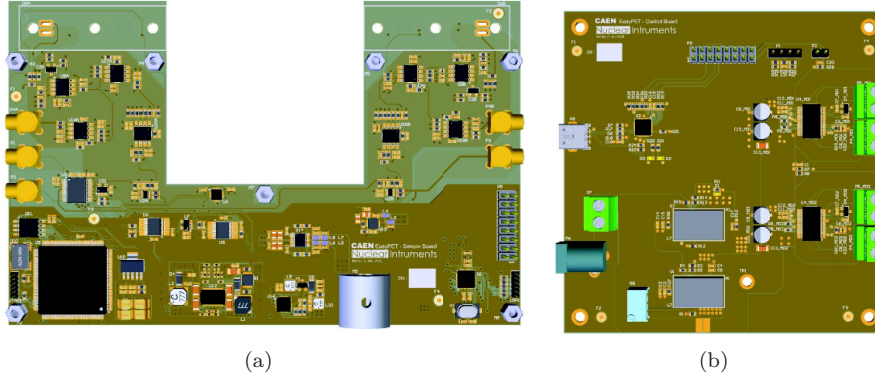
Figure 8.2: The design of the (a) U-shaped PCB and (b) control board.
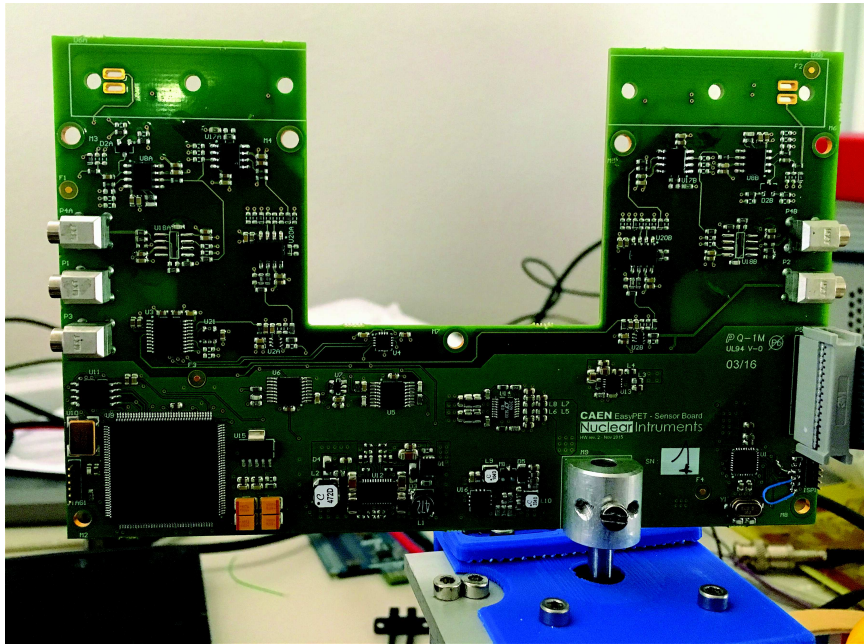
Figure 8.3: The EasyPET prototype U-shaped PCB.

The blocks of the electronic scheme are illustrated in Figure 8.4. The power supply of the SiPMs is still common for the two channels and each output passes through a first amplification stage. Then the signals are split into two branches: the one dedicated to the spectroscopy is only constituted by a second amplification stage, while the other used for the counting measurement comprises two additional amplification stage, a leading edge discriminator and a coincidence logic which is common for the two channels of this branch. The second amplification stage of the counting branching inverts the signal.
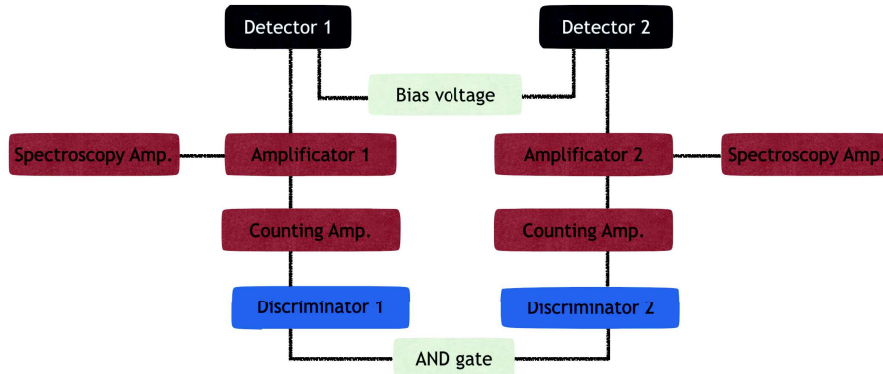
Figure 8.4: The EasyPET prototype electronic circuit scheme.

The signal splitting after the first common amplification stage avoids potential problems due to the different impedance of the two branches. In addition, the splitting of the SiPM output, which is a small signal, with respect to an amplified one will cause a worsening of the signal to noise ratio of at least a factor two.

The first amplification stage, shown in Figure 8.5 consists of a trans-impedance amplifier to convert the current produced by the SiPM into a voltage. Its gain is set by the 2.5 kΩ resistor: at the end of the first stage there is a signal of 2.5 V per each mA generated by the SiPM. This high value for the gain is dictated by the need to amplify as much as possible in this first common stage in order to reduce to a negligible level the noise of the other amplification stages in the two branches. In parallel to the resistance it has been added the so-called feedback capacitor to improve the signal stability. The choice of the operational amplifier is very important because it is characterized by some sources of internal noise that can affect the output signal to noise ratio. The main noise contributions are the input voltage noise, that can be modeled as a voltage appearing differentially across the two amplifier inputs and the input current noise, which is a current at both amplifier inputs [165]. To minimize these effects, trans-impedance amplifiers are usually designed with JFET inputs that have very low input offset voltages and provide very low bias current.
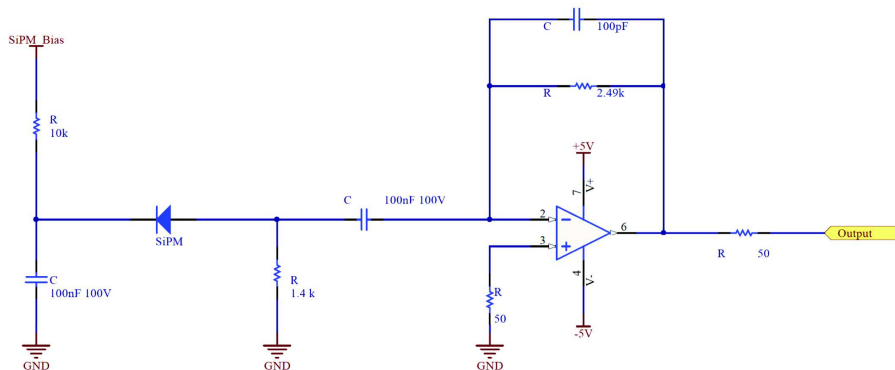
Figure 8.5: The SiPM amplification stage circuit (Schematic by CAEN ©).

The two counting amplification stages aim to saturate the signal in order to improve the coincidence detection. In fact signals with different amplitudes reach the discrimination threshold with different times, introducing the time-walk uncertainty. The saturation of signals at a low energy level minimizes the rise time of the signals, with a sensible reduction of the time-walk. As a result, the probability for two discriminated events to occur during a very short coincidence gate (ns level) is independent from their energy.

The coincidence logic is implemented with discrete components, a CMOS AND gate and two programmable monostables to set the coincidence gate length. With this kind of components it is impossible to achieve a length lower than 100 ns, which is reasonably good for the educational product. Considering further improvement towards the preclinical PET, which requires the use of multiple detector pairs, it will be important to reach 10 ns. For this reason, ad also to avoid the use of Arduino in managing more readout channels, an FPGA has been mounted on the PCB (even if not already programmed).

The spectroscopy amplifier has a gain of a factor two with respect to the first common amplification stage. In this way the output voltage is compatible with the input voltage dynamic range of a commercial multichannel analyzer or digitizer for spectroscopy applications. Moreover, it also features a high output current to be supplied to devices with an input impedance of 50 Ω or 1 kΩ.

Another important modification concerns the control of the micro-stepper motors: a dedicated **control board** has been developed and its design is shown in Figure 8.2(b). The power supply and the USB cables are connected to this board, then the information loaded by the user through the GUI control software are delivered to Arduino on the U-shaped PCB to be interpreted. The Arduino is still responsible for the settings of the SiPMs bias voltage, the discriminator thresholds, the coincidence gate length and the coincidence counting for each system position. Instead, the parameters related to the motor movements are send to the control board, which allows to steer the stepper motor by providing ramp voltage signals to activate alternatively one or two coils. In this way all the movements of 0.9° are very smooth and the oscillations and vibration of the U-shaped PCB are minimized. This improvement provides an higher precision on the detecting unit position during the coincidence counting and as a consequence, a better coincidence detection efficiency.

The mechanical re-engineering regards the source holder and the **base**. This latter has been enclosed in a box to protect the motors control board against accidental cables removal. The box is equipped with the power button and with a slotted hole to allow the end of the flat cable connected to the U-shaped PCB to rotate together with the top motor but keeping the other end of the cable fixed to the control board, without stressing it. Also the bottom motor is enclosed in the box but one side has been kept open in order to dissipate the heat generated by the stepper motor.

The **source holder** is connected to two metallic arms to decouple the different types of movement. On the vertical arm a threaded nut with micro-metric step is used to set the vertical position of the source and it can be hold in the chosen position by using the correspondent pivot. In the back side of the horizontal arm a pivot allows to arrange its position with respect to the other arm by describing an arc of circumference. The horizontal arm is also equipped with a micro-metric screws and a pivot in order to change and fix the radius of the x-y circular movement.

Finally, the **control software** has been improved by adding some new functionalities. The programming language has been changed from MATLAB ® to Visual Basic and the versatility of the .NET development framework has been exploited. In this way an executable of the control software will be provided to the user and no specific and licensed software installation is required.

A first new functionality is the "Oscilloscope" operation mode which introduces the possibility to visualize the analog signal of the spectroscopy branch (Figure 8.6). This requires the additional use of the Caen DT5770 Digitizer [167]. By adjusting the acquisition parameters (mainly dependent to the signal decay time and amplitude) it is possible to observe both the signals from the SiPM DCR and the ones induced by the LYSO self emission in no illumination condition and of course the signals produced by the photons emitted by the source.
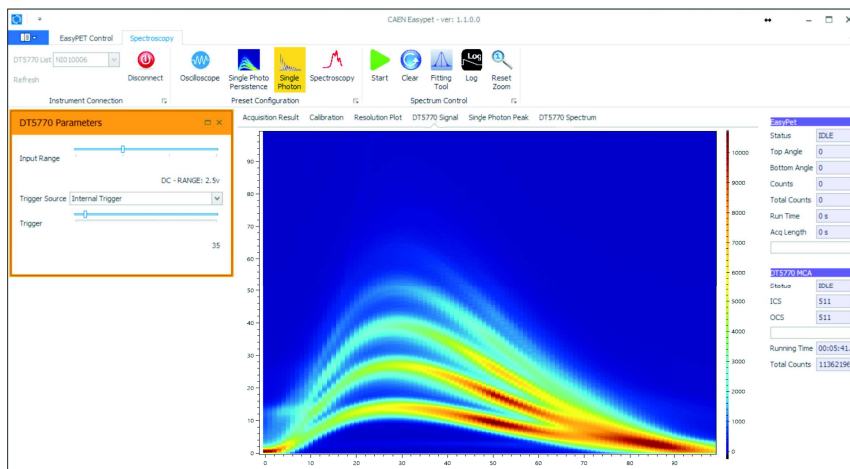
Figure 8.6: The EasyPET GUI Scope function for online signal visualization.

Another new functionality, "Spectroscopy" shown in Figure 8.7, has been introduced in the control software. By exploiting the same digitizer it is possible to integrate the signals through the trapezoidal filter [168], [169] and also in this case different pre-settings of the acquisition parameters allow to visualize the Multi-Photon Spectrum generated by the DCR or by the source.

These new functionalities allow students to learn the basic features of the SiPMs and the techniques to characterize them with the dark conditions, as described in Chapter 2. In addition they permit a linearity study of the detected energy, the calibration between ADC channels and energy (with the implemented Fitting Tool) and from the discriminator threshold expressed in mV to the correspondent ADC channel and the measurement of the peaks resolution as a function of the energy. In addition, from the Multi-Photon spectrum it is possible to calculate the peak-to-peak distance and determine the number of photons collected at different energies during the acquisition of the radioactive source spectra. This enables a measurement of the light collection and of the light detection efficiency, as performed in the previous Chapter. Finally, by considering the coincidence spectrum of the Sodium, it is possible to determine the proper threshold which eliminates the noise contribute and allows to take into account only the true coincidences.
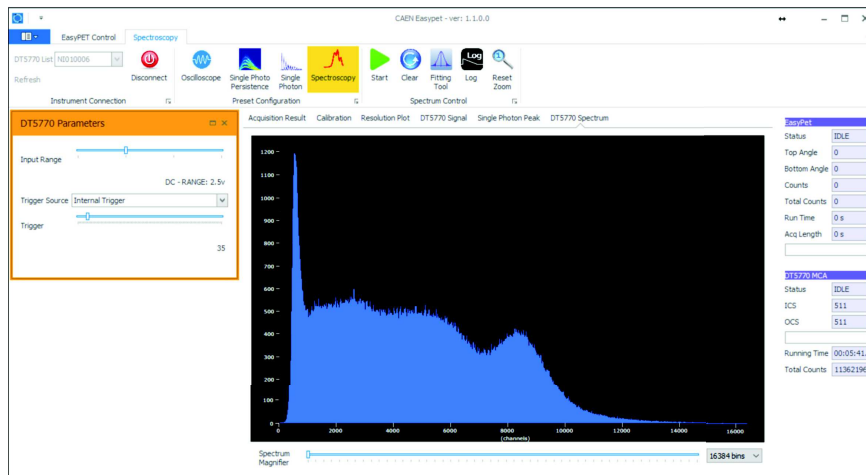
Figure 8.7: The EasyPET GUI Spectroscopy function for spectrum acquisition.

As already implemented in the previous version, the "Calibration" function can be used to determine the best position of the source and as a cross check on the choice of the discriminator threshold. In fact, by comparing the coincidence rates in absence and in presence of the Sodium source the student is introduced to the importance of the energy discrimination in selecting the events.

Once these preliminary measurements have been performed it is possible to start with the dedicated imaging studies and, as shown in Figure 8.8, the real-time image reconstruction by back-projecting the acquired number of coincidence events at each position can be assessed. On the menu to the lefthand side all the image acquisition parameters can be set and are applied immediately, adding more versatility to the image data acquisition.
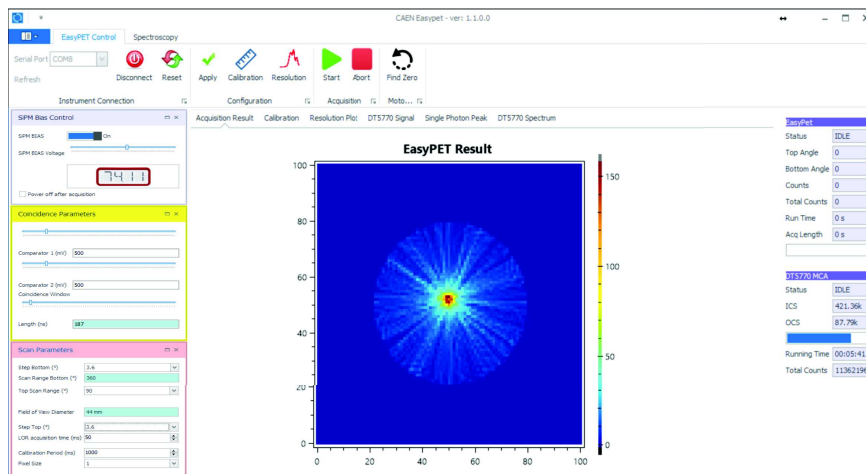
Figure 8.8: The EasyPET GUI Imaging function for online image visualization.

The operational mode for the spatial resolution measurement has been maintained the same as the previous software. In this case too it is possible to change online the parameters related to this data acquisition (Figure 8.9).
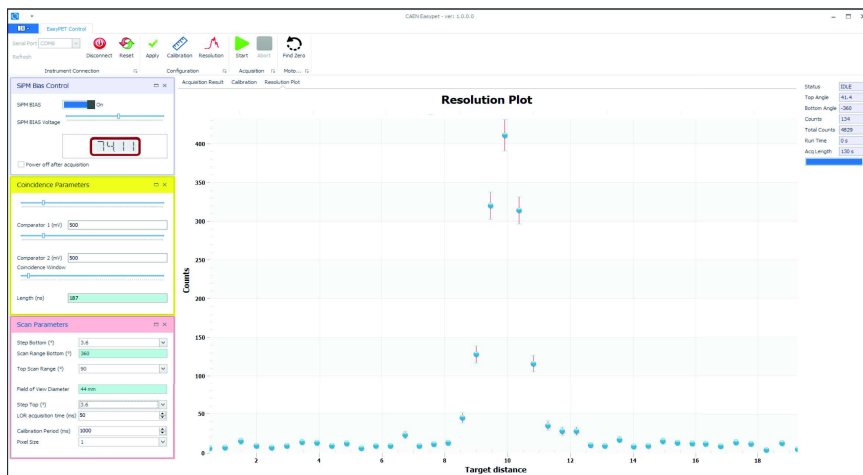
Figure 8.9: The EasyPET GUI Resolution function for resolution measurement.

8.2 Prototype commissioning

8.2.1 Signal quality

The first feature that can be considered in evaluating the performances of the prototype is the signal quality. Figure 8.10 shows the analog signals from the spectroscopy output.
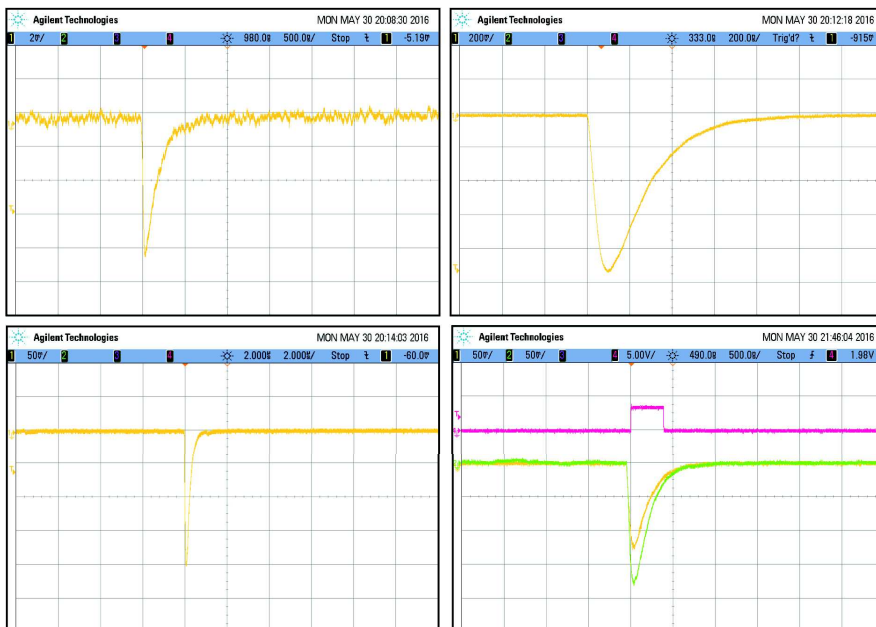
Figure 8.10: The EasyPET spectroscopy analog output from DCR (first) and radioactive source (second to last). In the last scope screenshot the two analog output are triggered with the coincidence logic signal.

The signals are negative because of the inverting stage implemented on the counting branch. In the first scope image it can be seen a signal corresponding to a DCR event: it is obtained in a condition of no-illumination, triggering the signal itself at low voltages in order to have an higher probability to see a thermal signal with respect to the LYSO self-activity signal. It can be appreciated that the electronic noise has been drastically reduced at the level of 1 mV. The second and the third scope images show the signal due to the presence of a radioactive source at different time scales. It is possible to see that the signal quality is really good: there is no trace of ripples or of overshoots. The signal does not saturate and reaches a maximum amplitude of about 1 V: this is in agreement with the fact the spectroscopy amplifiers have a gain of a factor two with respect to the signal after the first common amplification stage, which has been measured with a probe to be at maximum 500 mV. The last picture represents an event coincidence: the spectroscopy output of both detecting units have been triggered with the coincidence output. It can be inferred that the above consideration for the signal quality hold for both spectroscopy outputs. Furthermore the two channels feature a signal with the same time decay constant which is of the order to 250 ns, making the signals to last for about 800 ns. Instead, the signals after the second and third stage of amplification, which is also inverting, of the counting branches have been visualized at the scope by using a probe. It is possible to see that they are saturated at 3.3 V, limiting the highest possible discriminator thresholds that can be selected. The correspondence between this value in mV and the energy can be assessed by acquiring the radioactive source energy spectra, as shown in the next section. The output of the discriminators are logic signals of 4 V amplitude, with 4 ns of rise/fall time and a length corresponding to the chosen coincidence time. Finally, the coincidence output is the same logic signal but with a fixed duration of 400 ns.

Thanks to very low electronic noise level, the low number of photons that are thermally generated by the SiPM can be easily distinguished, as shown in Figure 8.11. Here an image of the signal persistence obtained with an oscilloscope with 1 mV per division allows to measure a 3 mV separation between signals corresponding to one photon with respect to two photons and so on. This allows the study of the various figure of merit of the sensor and a more precise and quantitative qualification of the system, as described in the following section.
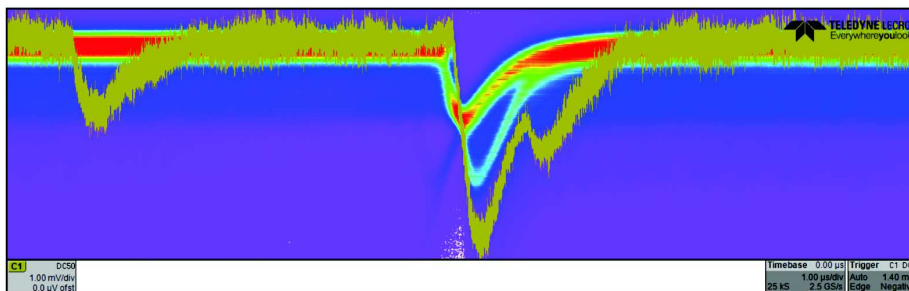
Figure 8.11: The EasyPET spectroscopy analog output from DCR acquired with the persistence modality: single photon signals are clearly distinguishable.

8.2.2 Spectroscopy measurements

The spectroscopy measurements are performed by using the Caen Educational Kit DT5720A Digitizer. In fact, even if the control software has been specifically developed for the DT5770 Digitizer, the spectroscopy branch has a 1 V output range, which results to be compatible with the ±1 V input range of the DT5720A.

First the Multi-Photon spectrum has been acquired by using the spectroscopy branch and triggering with the discriminator output set with a threshold of 50 mV. In Figure 8.12 can be seen the peaks of the events occurring in the condition of no illumination corresponding to one, two and three photoelectrons. The Gaussian fit to the first two peaks is superimposed to the spectra and is used to measure the peak-to-peak distance. A value of 188.5 ± 0.1 ADC channels has been obtained, corresponding to the integrated area of one photon signal. It has been proved that on the single channel a threshold of 450 mV is required to reduce to a negligible level the contribution of the DCR, which is equivalent to select signals exceeding three photoelectrons.
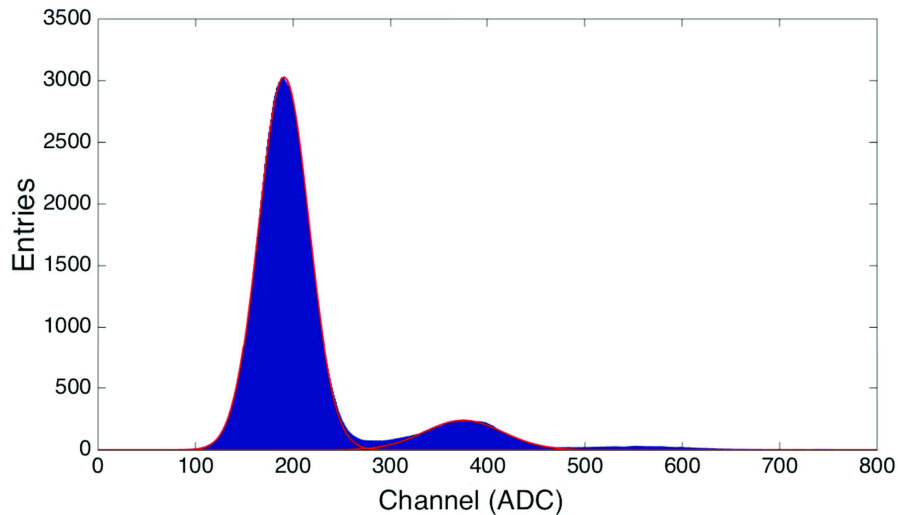
Figure 8.12: The Multi-Photon spectrum of the SiPM in dark condition.

In fact, by setting this threshold on the discriminator and integrating signals from the spectroscopy output of the single channel in dark conditions, the spectrum of Figure 8.13 has been obtained. Ithe spectrum corresponds to the typical energy distribution of the LYSO self-activity.

Then the ^{22}Na source has been positioned in the centre of the FOV and the spectroscopy signal of one channel has been integrated by triggering with the discriminator output at 450 mV threshold (Figure 8.14). By fitting the peak correspondent to 511 keV it can be inferred that the energy resolution is (25 ± 1) %, the peak-to-total ratio result to be (30.6 ± 0.1) % and the number of photons collected are 200 ± 3. In comparison with the demonstrator performances the energy resolution has been improved thanks to the better signal quality, while the peak-to-total ratio is worse. This can be due to the fact that the number of photons in the peak are less with respect to the maximum achievable value
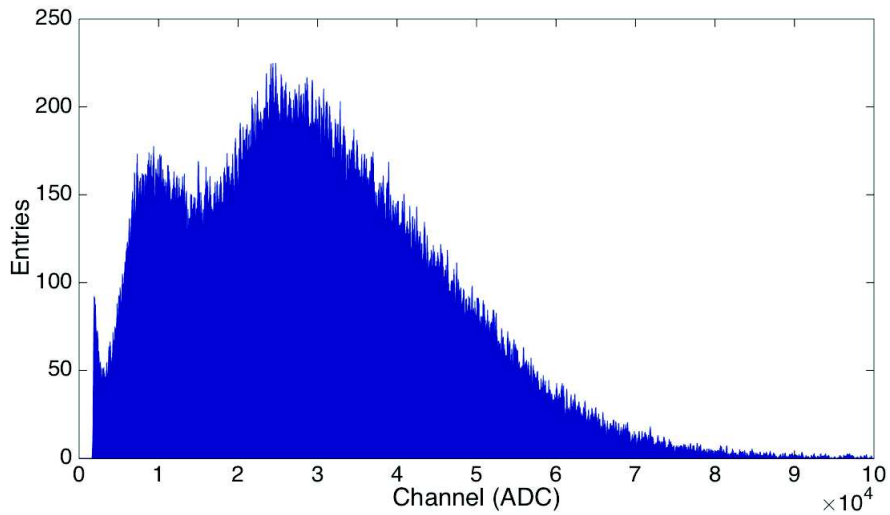
Figure 8.13: The energy spectrum of the LYSO self-emission.

determined with the perfect crystal-sensor alignment. As it has also been proved that the alignment is not so critical for 1×1 mm^2 MPPC, the reason of this inefficiency in light collection can be assigned to a non perfect optical grease adopted to optically couple the crystal to the sensor. Instead a direct comparison with the number of photons collected with the demonstrator is not allowed as the single photon signal could not be distinguished from the electronic noise. In addition it is possible to affirm that the spectroscopy signals are not saturated till 1275 keV, as some counts are visible at that energy in the spectrum.
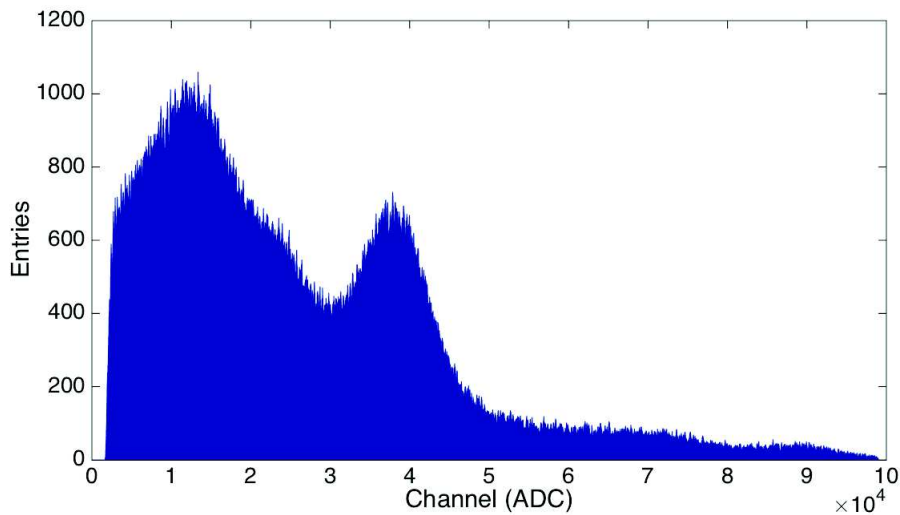
Figure 8.14: The ^{22}Na spectra for the single channel.

Figure 8.15 displays the spectrum of the coincidence events: also in this case the spectrum is betterthan the one acquired with the demonstrator, but the ratio between the peak and the Compton scattering contribution is lower. It has been determined that a threshold of 200 mV is enough to eliminate all the random noise and select only true coincidences. Considering that the energy distribution is cut at 300 ADC channels, the discriminator threshold corresponds to 1.5 photons. As expected, triggering with the coincidence with respect to the single channel discriminator allows to loose the acceptability criteria. In order to express the threshold in energy unit a calibration is necessary.
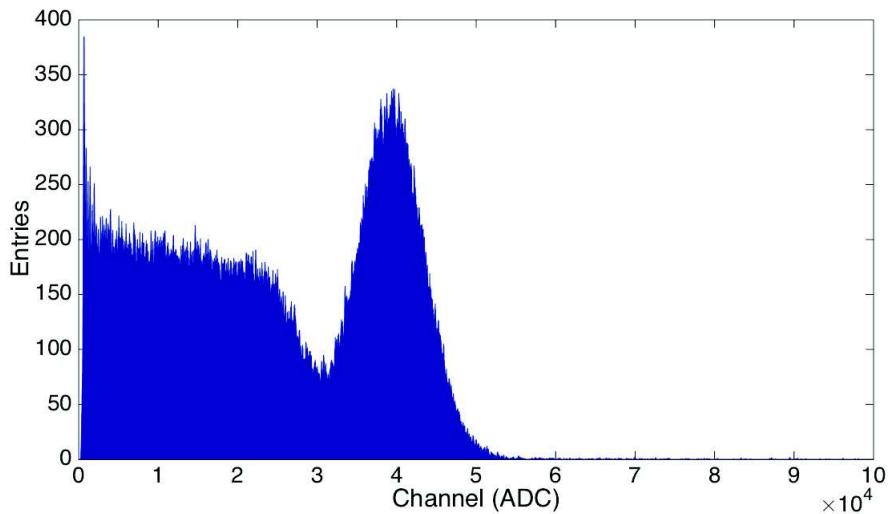
Figure 8.15: The ^{22}Na spectra for the coincidence.

However, due to the low light collection, the energy-channel calibration results to be impossible to be determined. In fact, Figure 8.16 reports the spectra acquired with the single channel with the ^{133}Ba and ^{137}Cs sources and the effects of the light collection inefficiency are evident. It can be noticed that in the case of the high energy of the ^{133}Ba (356 keV) and of the ^{137}Cs (662 keV) the peaks feature a very low peak-to-total ratio and their determination is very imprecise. Instead the low energy peaks, 31 keV for ^{137}Cs and 32 keV and 81 keV for the ^{133}Ba, can not be detected because they corresponds to few photons. In fact, in the left region of both spectra the single photons are clearly distinguishable. As a result it is not possible to perform a calibration measurement. However, assuming a linear energy system response and considering the 511 keV peak position expressed in ADC channel, it can be calculated that the threshold of 200 mV required to accept coincidences corresponds to 15 keV, while the maximum settable threshold of 3.3 V result to cut the events above 250 keV. This means that the minimum allowed threshold is not constrained by the electronic noise but only by the DCR. The signal quality has been optimized as much as possible and further improvements can only come by optimizing the light collection efficiency and the sensor performances, as pointed out in the previous Chapter.

This hypothesis is confirmed by considering the set-up used to analyze the effects of the crystal-sensor alignment and geometrical coupling equipped with
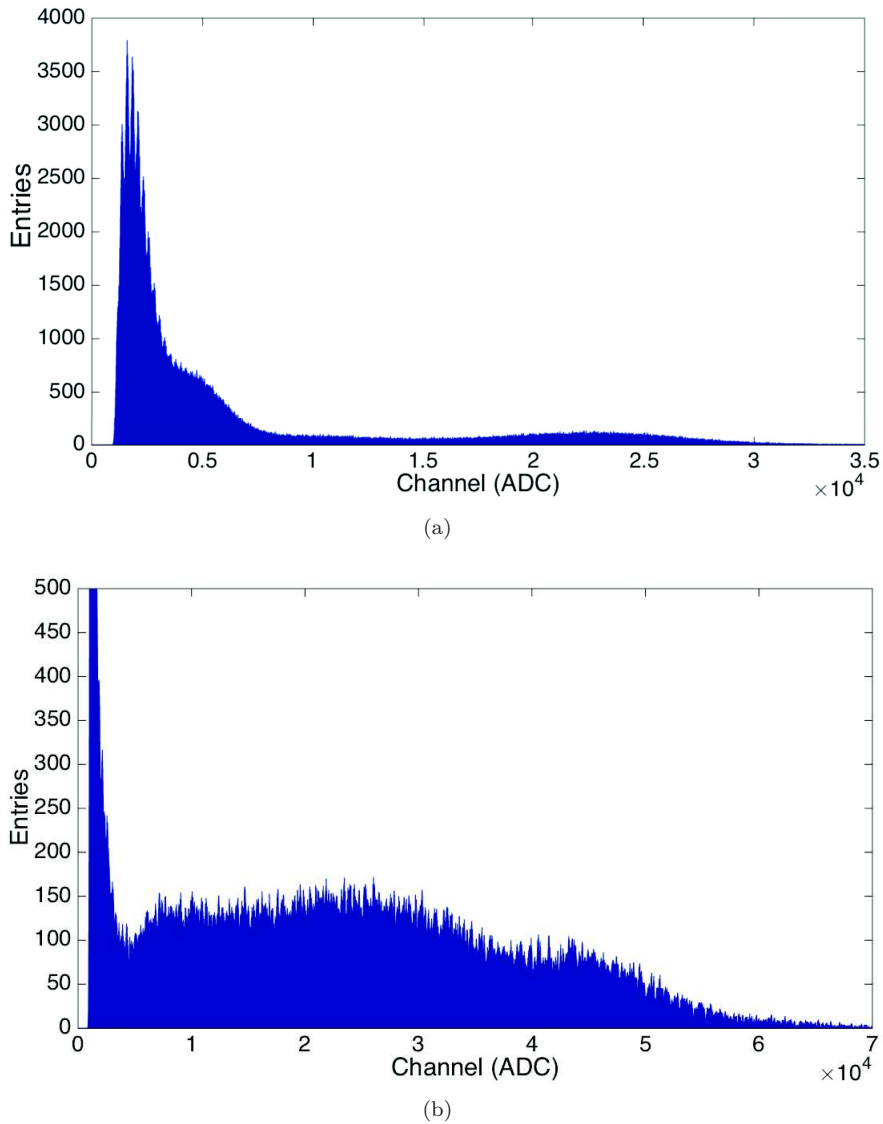
Figure 8.16: The ^{133}Ba (a) and ^{137}Cs (b) sources single channel spectra.

the 1×1 mm^2 MPPC. In this case the signal quality is worse and the electronic noise is higher than the one obtained with this prototype, leading to a minimum threshold of 50 keV. Despite of this conditions, the perfect alignment and the correct optical grease allow to get an energy resolution which is better of a factor two, dominated by the intrinsic LYSO resolution, and a peak-to-total ratio which is exactly the LYSO photon fraction. As a result it can be concluded that a good electronic scheme is not enough and to achieve higher performances the light collection efficiency plays a crucial role.

8.2.3 Temperature

An important issue that has been noticed during the prototype commissioning is the U-shaped PCB heating: at a room temperature of 22° the part of the board in which are housed the case containing the detecting unit reaches a temperature of 35°, measured with a thermic camera. This amount of heat is considered quite normal for this type of boards but represent a real problem for the SiPMs working conditions stability. The main component responsible for this warming is the Logic Level Shifter which is required by the presence of the FPGA. In fact, the Arduino UNO operates at 5 V and imposes the same operational voltage to the whole board. However, the FPGA operates at 3.3 V and as a consequence, requires a logic level translator in input to reduce the comparator output voltages, and in output in order to deliver the signals to the other part of the circuit. The Logic Level Shifter in use is the SN74ALVC164245DL from Texas Instruments, which has 16 channels featuring very high performances, which cause the temperature growth of the board [170]. Even if the board is manufactured with FR-4 substrate, which is a relatively good thermal insulator, copper power supply and ground layers diffuse the heat throughout the U-shaped board. In order to prove this hypothesis the level translator has been disconnected and the board temperature has been measured again with the thermic camera and a room temperature of 22°. The images of Figure 8.17 show that in average the board reaches a temperature of about 28°, but the heat is mainly concentrated in the lower part, generated by the components that provide the bias voltages to all the circuit. Considering the arms of the U-shape the temperature lowers to about 24° and the warming is mainly due to the components responsible for the three stages of amplification on the two different branches. This means that near the SiPM housing the temperature is almost the same of the room. As a result, in order to overcome the temperature problem in the commercial product, the Logic Level Shifter will be replaced with the SN74LV1T34 of the Texas Instruments, which is equipped with only one channel and will result in quite standard performances but will not affect the board temperature [171].
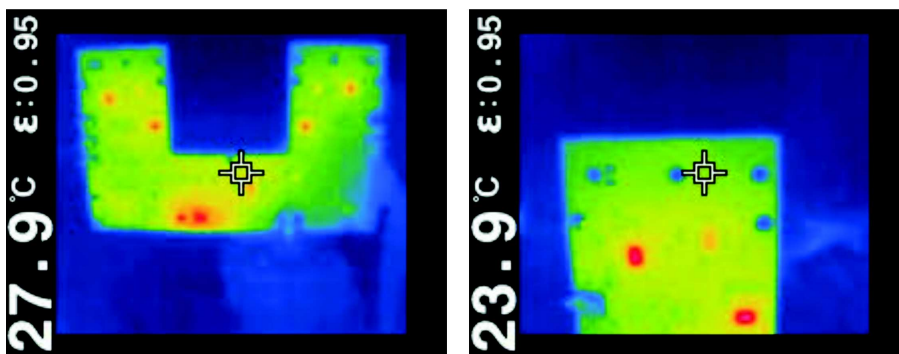
Figure 8.17: The EasyPET prototype temperature control.

Chapter 9

Conclusions and Outlook

The research activities described in this thesis aimed to a deep knowledge of the Silicon Photomultiplier technology and lead to their application in an innovative Positron Emission Tomography system. The SiPMs characterization methods that have been developed result to be fundamental in order to analyze the performance of the sensors under test and determine the best choice for the targeted application.

In particular, the first characterization method that has been taken into account, based on the staircase and the Multi-Photon spectrum analysis, offers information on the sensor Dark Count Rate and Optical Cross-Talk probability. Then, these technique have also been implemented in an offline analysis, based on the waveform events acquisition and exploiting the post-processing of data. This characterization procedure allows to achieve all the SiPM figures of merit with a semi-automatic, efficient and robust analysis. It has been validated using a simulation of waveform events and a perfect consistency between the input SiPM parameters and the analysis results has been obtained. The implemented characterization procedure has also been tested with real data of very well known sensor: the results obtained from the waveform analysis have been in fact cross checked with the standard procedure measurements. The agreement between the outcome of the two characterization methods allow to be confident that also the analysis of 6×6 mm^2 area sensors, that can not be performed with standard procedures due to their high noise, lead to reliable results.

The main focus of this thesis concerns the development of a SiPM based Positron Emission Tomography scanner. The innovative EasyPET concept, patented by the Aveiro University, aims to make the PET technology accessible to research laboratories and health universities through a low cost and simple preclinical system. The EasyPET is based on a single pair of collinear detector and a two rotational axes mechanical movement. An EasyPET demonstrator was realized collaborating with the Aveiro University to assess the concept. The commissioning of the device allowed to appreciate its imaging capability and to measure a spatial resolution of 1±0.1 mm FWHM, at the level of the pre-clinical systems currently on the market, uniform over all the Field of View. These remarkable results are mainly due to the small size of the crystals, their single readout and their collinearity during all the data acquisition, which ensure an intrinsic immunity against the acollinear photon emission, the scatter radiation and the parallax error.

The outreach activity with the EasyPET demonstrator led to the arising of the interest of two companies, which joined the project. The concept has been licensed to Caen S.p.a and with the collaboration of Nuclear Instrument the electronics, the mechanics and the control software have been improved. As a great result, the EasyPET has become a commercial product for the educational market, targeted to high level didactic laboratories to teach by doing the principle of the PET imaging. The first prototype has already been produced and qualified and it will be commercially available by the end of the year.

The easyPET potential has not been fully exploited yet and some improvements can still be developed. In fact, the weakness of the EasyPET concept lies in its sensitivity, which is expected to be low with respect to commercial preclinical PET due to both the reduced geometrical acceptance and the not optimized coincidence detection efficiency. For this purpose, specific studies have been dedicated to the alignment between the SiPM and the scintillating crystal and to their geometrical coupling. It has been demonstrated that the best performance of the detecting unit in terms of energy resolution, light collection efficiency and coincidence detection efficiency have been obtained with the use of the Hamamatsu 2×2 mm^2 area. In particular, the adoption of this high gain sensor with a perfect dimension matching with the crystal allows to lower the energy threshold down to 10 keV, reaching a coincidence detection efficiency of (9.9 ± 0.9) %, higher of a factor two with respect to the value achievable with the current 1×1 mm^2 SiPM with a minimum energy threshold of 80 keV. The alignment plays a crucial role: with this larger area sensor it has been measured that a 0.4 mm displacement from the optimal position causes a loss of 13% of collected light. An additional enhancement is expected from an optimization of the crystals aspect ratio and coating material.

In terms of geometry, the use of multiple pairs of detectors is considered a possible solution to improve the solid angle coverage implementing 3D imaging functionality without compromising the system simplicity. Also in this case the system should keep the readout of single pairs of collinear detector to automatically reject the background events and guarantee a good image quality even with a very large photon energy range acceptance.

Aveiro University has just realized a first 3D EasyPET imaging demonstrator, whose layout is depicted in Figure 9.1. It is based on two array of 16 detecting units composed of $2\times2\times30$ mm^3 LYSO crystals coupled to 2×2 mm^2 SiPMs, moving in a 60 mm diameter circumference to cover a 50 mm trans-axial FOV and a 34 mm axial FOV. The first measurements of spatial resolution and sensitivity, performed according to the NEMA NU 4-2008 standard protocols, are very promising and motivate a feasibility study for a scaled up version of the EasyPET for preclinical purposes. The GATE environment is used to simulate a system with two modules of 50×5 LYSO scintillators with $1.5\times1.5\times20$ mm^3 size and the measurement of sensitivity and position resolution using a 0.25 mm diameter sphere ^{22}Na source. The results, reported in Figure 9.2, indicate that using only about one hundred of the detecting units of a usual preclinical system is possible to obtain a good spatial resolution and a sensitivity of one tenth with respect to other small animal PET scanner. In conclusion, exploiting the EasyPET concept it is possible to reduce the complexity and the cost of the preclinical apparatus while keeping the performances at a very good level.
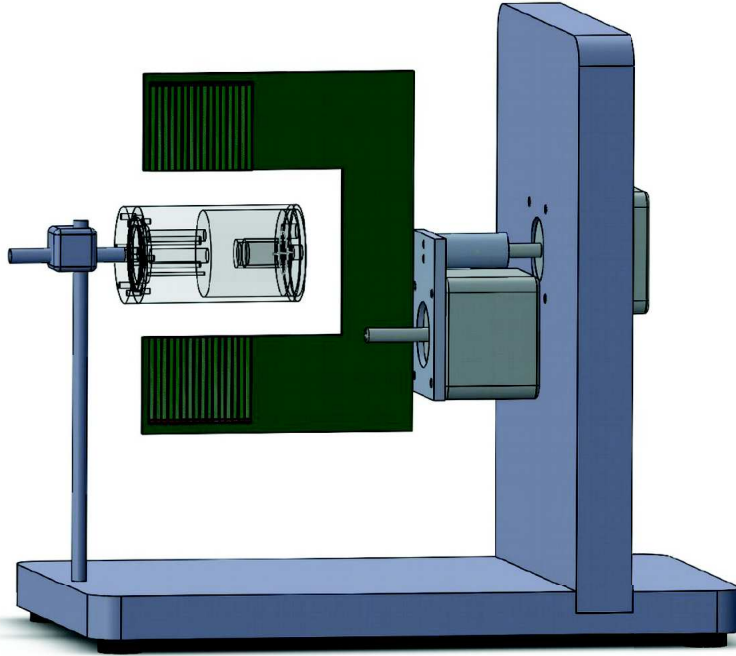
Figure 9.1: The sketched layout of the preclinical easyPET demonstrator with 16 detector pairs covering a 50 mm trans-axial FOV and a 34 mm axial FOV.
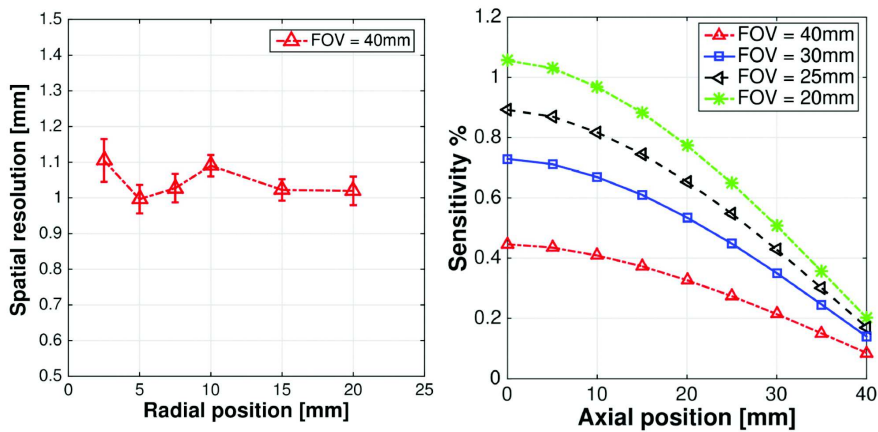
Figure 9.2: GATE simulation results of the trans-axial spatial resolution for a trans-axial FOV of 40 mm (left) and sensitivity of a function of the axial position for various trans-axial FOV (right) of a preclinical easyPET scanner with $50{\times}5$ LYSO crystals of $1.5{\times}1.5{\times}20$ mm^3 in each side.

Appendix A

In this appendix the confidence region of two variables is demonstrated to assume the shape of an ellipse. Moreover, the relation between the parameters describing the ellipse, the standard deviation of the variables and their correlation is established.

The joint probability density of two variables $x^T = [x_1, x_2]$ gaussian distributed may be written as:

$$P(x) = k \cdot \exp\left\{ -\frac{1}{2}(x - \mu)^T C^{-1}(x - \mu) \right\},$$ (A.1)

where k is a normalization constant, $\mu^T = [\mu_1 \mu_2]$ is the vector of the mean values of x and C is the covariance matrix:

$$C = E\{(x - \mu)(x - \mu)^T\} = \begin{bmatrix} \sigma_1^2 & \sigma_{12} \\ \sigma_{21} & \sigma_2^2 \end{bmatrix}.$$

The diagonal elements of C are the variances of the variables x_i and the off-diagonal elements represent their covariance, which can be expressed as:

$$\sigma_{12} = \rho \sigma_1 \sigma_2,$$

where ρ is the correlation coefficient.

Curves of constant probability are determined by requiring the exponent of the equation (A.1) to be constant:

$$(x - \mu)^T C^{-1}(x - \mu) = c$$ (A.2)

$$\frac{(x_1 - \mu_1)^2}{\sigma_1^2} - 2\rho \frac{(x_1 - \mu_1)}{\sigma_1} \frac{(x_2 - \mu_2)}{\sigma_2} + \frac{(x_2 - \mu_2)^2}{\sigma_2^2} = c',$$

where $c' = c(1 - \rho^2)$. This equation represents an ellipse with the center located at (μ_1, μ_2) and the semi-axes placed at an angle θ with respect to the x_1, x_2 axes.

As shown in the following, the equation (A.2) can be re-written as a sum of squares of two stochastically independent variables, which results to be χ^2 distributed with two degrees of freedom:

$$\frac{\xi_1^2}{a^2} + \frac{\xi_2^2}{b^2} = \chi^2.$$ (A.3)

This relation describes an ellipse centered in the origin of the reference system and with the semi-axes of length a, b parallel to the ξ_1, ξ_2 axes.

As a first step, the origin of the reference system is translated in the center of the ellipse, resulting in equation:

$$\tilde{x}^T C^{-1} \tilde{x} = c, \tag{A.4}$$

where $\tilde{x} = x - \mu$.

As a second step, axes are rotated in order to coincide with the (ξ_1, ξ_2) reference system by the transformation:

$$\tilde{x} = Q^T \xi,$$

where

$$Q = \begin{bmatrix} \cos\theta & \sin\theta \\ -\sin\theta & \cos\theta \end{bmatrix}.$$

As a consequence, equation (A.4) is turned to the form:

$$\xi^T Q C^{-1} Q^T \xi = c,$$

corresponding to the equation (A.3) as long as:

$$Q C^{-1} Q^T = \begin{bmatrix} \frac{1}{a^2} & 0 \\ 0 & \frac{1}{b^2} \end{bmatrix},$$

or, equivalently,

$$Q C Q^T = \begin{bmatrix} a^2 & 0 \\ 0 & b^2 \end{bmatrix}.$$

The vector of the mean values and the covariance matrix of ξ results to be:

$$\begin{aligned}
\mu_\xi &= E\{\xi\} = QE\{x\} = Q\mu \\
C_\xi &= E\{(\xi - \mu_\xi)(\xi - \mu_\xi)^T\} \\
&= QE\{(x - \mu)(x - \mu)^T\}Q^T \\
&= QCQ^T.
\end{aligned} \tag{A.5}$$

So it can be noticed that the eigenvalues of the covariance matrix C_ξ correspond to the squared semi-axes of the canonical ellipse (A.3).

Because of the symmetry of the covariance matrix, C can be diagonalized exploiting its decomposition in eigenvalues and eigenvectors:

$$C = U \Lambda U^T,$$

where Λ is the diagonal matrix of eigenvalues and U is the rotation matrix constituted by eigenvectors. Comparing this formula with the expression (A.5) and using the properties of the rotation matrix ($QQ^T = Q^T Q = I$, $\det Q = 1$) it can be inferred that:

$$U = Q^T \qquad \Lambda = C_\xi.$$

As a consequence, the eigenvalues of C can be obtained through the quadratic equation:

$$\det(C - \lambda I) = 0,$$

whose solutions are:

$$\lambda_{1,2} = \frac{1}{2}\left[(\sigma_1^2 + \sigma_2^2) \pm \sqrt{(\sigma_1^2 + \sigma_2^2)^2 - 4\sigma_1^2\sigma_2^2(1 - \rho)}\right].$$

The lengths of the ellipse semi-axes result to be the square root of the eigenvalues multiplied by the two degrees of freedom χ^2 value:

$$a = \sqrt{\chi^2 \lambda_1} \qquad b = \sqrt{\chi^2 \lambda_2}. \tag{A.6}$$

The eigenvectors of C can be found with the following equation:

$$(C - \lambda_i I)u_i = 0, \quad \text{with} \quad i = 1, 2.$$

For $i = 1$:

$$\begin{bmatrix} \sigma_1^2 - \lambda_1 & \rho\sigma_1\sigma_2 \\ \rho\sigma_1\sigma_2 & \sigma_2^2 - \lambda_1 \end{bmatrix}\begin{bmatrix} u_{1,1} \\ u_{1,2} \end{bmatrix} = 0,$$

and the solution is:

$$u_1 = \alpha_1 \begin{bmatrix} -\rho\sigma_1\sigma_2 \\ \sigma_1^2 - \lambda_1 \end{bmatrix},$$

where α_1 is a normalization constant. In the case of $i = 2$:

$$\begin{bmatrix} \sigma_1^2 - \lambda_2 & \rho\sigma_1\sigma_2 \\ \rho\sigma_1\sigma_2 & \sigma_2^2 - \lambda_2 \end{bmatrix}\begin{bmatrix} u_{2,1} \\ u_{2,2} \end{bmatrix} = 0,$$

and the solution is:

$$u_2 = \alpha_2 \begin{bmatrix} \sigma_2^2 - \lambda_2 \\ -\rho\sigma_1\sigma_2 \end{bmatrix},$$

where α_2 is the normalization constant. Using the eigenvalues definition, it can be proved that $\sigma_2^2 - \lambda_2 = -(\sigma_1^2 - \lambda_1)$. As a result, the U matrix turns out to be equal to Q^T, with $\cos\theta = -\rho\sigma_1\sigma_2$ and $\sin\theta = \sigma_1^2 - \lambda_1$. From these identities it is possible to calculate the angle θ between the ellipse axis, which lies on ξ_i, and the x_i axis:

$$\tan\theta = -\frac{\sigma_1^2 - \lambda_1}{\rho\sigma_1\sigma_2}.$$

As θ belongs to the range [-π/2, π/2] and the above expression is quite complex, it is more convenient to estimate the $\tan 2\theta$:

$$\tan 2\theta = \frac{2\tan\theta_1}{1 - \tan^2\theta_1} = \frac{2\rho\sigma_1\sigma_2}{\sigma_1^2 - \sigma_2^2}. \tag{A.7}$$

The angle θ measures the rotation which brings the (x_1, x_2) coordinate system in the (ξ_1, ξ_2) reference system, which represent the rotation undergone by the ellipse. The rotation matrix Q has been completely determined and the ellipse has been entirely defined.

The covariance ellipse of the bivariate normal distribution assumes a particular importance when $\chi^2 = 1$ and its features can be analyzed in two extreme cases:

- if the variables are not correlated ($\rho = 0$), then $\theta = 0$, $a = \sigma_1$ and $b = \sigma_2$, which means that the ellipse axes are parallel to x_i and equal to the variable standard deviations,

- if the correlation is maximum ($\rho = \pm 1$), then the ellipse degenerates into a straight line of lenght $a = \sqrt{\sigma_1^2 + \sigma_2^2}$ (in fact $b = 0$).

In all the intermediate cases the ellipse is inscribed in a rectangle of center (μ_1, μ_2) and sides $2\sigma_1$ and $2\sigma_2$. The projections on the x_i axes of the four intersection points between the ellipse and the rectangle represent the 68% confidence interval for the parameter centered in the mean value μ_i.

All these characteristics of the covariance ellipse can be demonstrated exploiting the conic equations. The general quadratic equation:

$$Ax_1^2 + Bx_1x_2 + Cx_2^2 + Dx_1 + Ex_2 + F = 0 \qquad (A.8)$$

represents the canonical ellipse if $B = 0$ and $AC > 0$. It is always possible to find a new coordinate system, rotated by an angle θ with respect to the x_i axes, in which the equation does not involve the mixed variable product. Calling ξ_i the new set of axis, the x_i variables can be expressed as:

$$x_1 = \xi_1 \cos\theta - \xi_2 \sin\theta \quad x_2 = \xi_1 \sin\theta + \xi_2 \cos\theta.$$

Substituting these relations in (A.8) and collecting the similar terms a new equation in ξ_i can be obtained:

$$
\begin{aligned}
&\xi_1^2(A\cos^2\theta + B\cos\theta\sin\theta + C\sin^2\theta)+ \\
&\xi_1\xi_2(-2A\cos\theta\sin\theta + B(\cos^2\theta - \sin^2\theta) + 2C\sin\theta\cos\theta)+ \\
&\xi_2^2(A\sin^2\theta - B\cos\theta\sin\theta + C\cos^2\theta)+ \\
&\xi_1(D\cos\theta + E\sin\theta) + \xi_2(-D\sin\theta + E\cos\theta) + F = 0.
\end{aligned}
\qquad (A.9)
$$

In order to eliminate the $\xi_1\xi_2$ term, the angle θ has to satisfy:

$$-2A\cos\theta\sin\theta + B(\cos^2\theta - \sin^2\theta) + 2C\sin\theta\cos\theta = 0.$$

Simplifying the equation:

$$2(A - C)\cos\theta\sin\theta = B(\cos^2\theta - \sin^2\theta)$$

$$\frac{2\sin\theta\cos\theta}{\cos^2\theta - \sin^2\theta} = \frac{B}{A - C} \qquad (A.10)$$

$$\tan 2\theta = \frac{B}{A - C}.$$

In the specific case corresponding to equation (A.2),

$$A = \frac{1}{\sigma_1^2} \quad B = -\frac{2\rho}{\sigma_1\sigma_2} \quad C = \frac{1}{\sigma_2^2}.$$

As a consequence the expression (A.10) assume the form of the relation (A.7). Finally, the coefficients of the second order variables in equation (A.9) have to be interpreted as the inverse square of the semi-axes lengths. Replacing the definition of A, B and C and solving for a and b gives:

$$a = \sqrt{\frac{\sigma_1^2\sigma_2^2(1 - \rho^2)}{\sigma_2^2\cos^2\theta - 2\rho\sigma_1\sigma_2\cos\theta\sin\theta + \sigma_1^2\sin^2\theta^2}}$$

$$b = \sqrt{\frac{\sigma_1^2\sigma_2^2(1 - \rho^2)}{\sigma_2^2\sin^2\theta - 2\rho\sigma_1\sigma_2\cos\theta\sin\theta + \sigma_1^2\cos^2\theta^2}}.$$

Expressing θ as a function of ρ and σ_i it is possible to obtain for the semi-axes the same definition as found previously in equation (A.6).

Appendix B

The SNIP algorithm [160] has been introduced with the aim to separate useless information (i.e.: background, noise and detector artifacts) from useful information contained in the peak. The SNIP algorithm is capable of estimate the background due to linear and/or nonlinear component under the peaks using the source spectrum.

The core procedure of the SNIP requires a pre-processing step, called the log square root (LLS) operator, where the count $y(i)$ in channel $i-th$ is transformed into $v(i)$ according to:

$$v(i) = log(log(\sqrt{y(i)+1}+1)+1). \tag{B.1}$$

The square-root operator enhances small peaks while the double log operator was introduced to cope with complex spectra with relative intensities over several orders of magnitude, compressing the range of counts. In the algorithm, the background under the peak is evaluated in an iterative way, shown in Figure **??**.
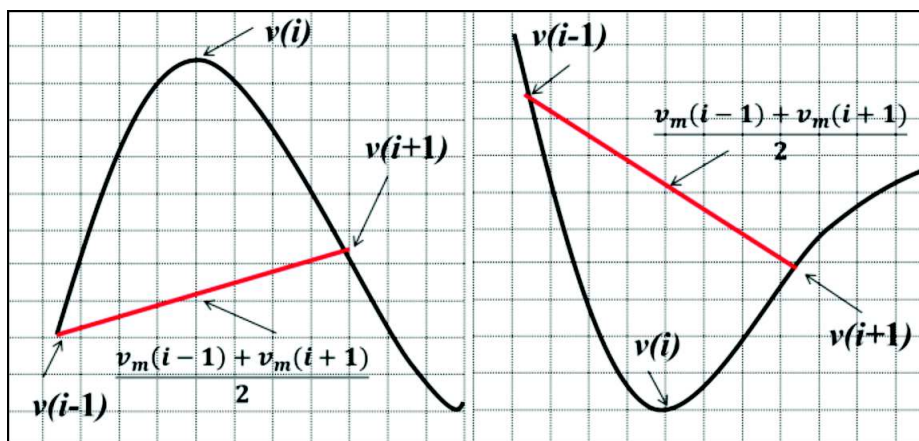
Figure B.1: Illustration of the SNIP algorithm applied to the peak region (left plot) and to a valley of the spectrum (right plot) [161].

The minimum of the average of counts at each end of a sampling interval and the channel count at the center of the interval replace the count in each channel.

215

This sampling interval is arbitrary and is called the clipping window M. The M is the product of the bin width and the number of iterations m. For the $m - th$ iteration, the content of the transformed bin $v_m(i)$ is compared to the mean of the values at distance equals to $\pm M$ and the updated spectrum is evaluated as:

$$v_{m+1}(i) = min \left\{ v_m(i), \frac{v_m(i - M) + v_m(i + M)}{2} \right\} \tag{B.2}$$

As a result, in proximity of peaks, as long as the distance is comparable to the peak width, the updated spectrum will result by the shape of the side bands. On the other hand, valleys will be essentially unchanged (see Figure **??**). The process is repeated for every channel over m iterations. The estimated background $B(i)$ is simply obtained from the final updated $v_m(i)$ by applying the inverse LLS operator.

Morhac et al. extended the SNIP algorithm to multidimensional data [161] in such a way that the algorithm can recognize useless information (background and the combination of coincidences of the background with peak ridges) from useful information contained in n-fold coincidence peaks of an n-dimensional histogram.

The main advantage of the SNIP algorithm is the capability to cope with a large variety of background shapes. Its potential weakness is in the absence of a built-in convergence criterion. For the specific application explained in this thesis, the iterative procedure is stopped as long as the estimated background is monotonically changing in the peak region. As a complementary condition, essentially applied for low background spectra where the statistical fluctuations are dominating, the procedure is stopped as long as the background drops below 5% of the total area underneath the peak.

Bibliography

[1] P. Buzhan, B. Dolgoshein, A.Ilyin, *Silicon photomultiplier and its possible applications*, Nuclear Instruments and Methods in Physics Research A, 2003, 504;48-52.

[2] B. Dolgoshein et al., *Status report on silicon photomultiplier development and its applications*, Nuclear Instruments and Methods in Physics Research A, 2006; 563:368-376.

[3] D. Renker, *Geiger-mode avalanche photodiodes, history, proprieties and problems*, Nuclear Instruments and Methods in Physics Research A, 2006; 567:48-56.

[4] P. Eckert et al., *Characterisation Studies of Silicon Photomultipliers*, Nuclear Instruments and Methods in Physics Research A, 2010, 620; 217-226.

[5] V. Arosio, M. Caccia et al., *An Educational Kit Based on a Modular Silicon Photomultiplier System*, arXiv:1308.3622v2, June 2014.

[6] A. Vacheret et al.,*Characterization and simulation of the response of Multi-Pixel Photon Counters to low light levels*, Nuclear Instruments and Methods in Physics Research A, 2011, 656, 69.

[7] C. M. Sparrow, *On spectroscopic resolving power*, Astrophys. J. 1916, 44;7686.

[8] P. Buzhan, B. Dolgoshein, A.Ilyin, *An advanced study of silicon photomultiplier*, ICFA Instrumentation Bulletin 2001.

[9] K. Sato et al., *The reliability and reproducibility of MPPC*, IEEE NSS-MIC 2013.

[10] T. L. Jackson, T.E. Murphy, *Methods of fabrication of semiconductor dice having back side redistribution layer accessed using through-silicon vias and assemblies thereof*, U.S. Patent No. 6,962,867. 8 Nov. 2005.

[11] www.hamamatsu.com

[12] C. Piemonte, *A new silicon photomultiplier structure for blue light detection*, Nuclear Instruments and Methods in Physics Research A, 2006; 568:224-232.

[13] E. Hergert, S. Piatek, *Testing Detectors: Understanding key parameters of silicon photomultipliers*, LaserFocusWordl, 11 April 2014.

[14] S.Gundacker et al., *SiPM time resolution: From single photon to saturation*, Nuclear Instruments and Methods In Physics Research A, 2013, http://dx.doi.org/10.1016/j.nima.2013.01.047.

[15] F. Acerbi at al., *Characterization of Single-Photon Time Resolution: From Single SPAD to Silicon Photomultiplier*, IEEE 10.1109/TNS.2014.2347131, August 2014.

[16] E. Martinenghi et al, *Spectrally Resolved Single-Photon Timing of Silicon Photomultipliers for Time-Domain Diffuse Spectroscopy*, IEEE Photonics Journal, Vol. 7, No. 4, August 2015.

[17] Y. Musienko, *Advances in multipixel Geiger-mode avalanche photodiodes*, Nuclear Instruments and Methods in Physics Research A, 2009; 598:213-216.

[18] K. Yamamoto, *HPK: 2nd SiPM Advanced Workshop*, March 2014.

[19] W. Oldham, R.R. Samuelson, P. Antognetti, *Triggering phenomena in Avalanche Diodes*, IEEE, 1972, 9;1056-1060.

[20] N. Dinu et al., *Temperature and Bias Voltage Dependence of the MPPC Detectors*, IEEE 2010, 10.1109/NSSMIC.2010.5873750.

[21] C R. Crowell, S.M. Sze, *Temperature dependence of avalanche multiplication in semiconductors*, Applied Physics Letters 1996.

[22] N. Dinu, A. Nagai, A. Para, *Studies of MPPC detectors down to cryogenic temperatures*, Nuclear Instruments and Methods in Physics Research A, 2015; 787:275-279.

[23] M. Ramilli, *Characterization of SiPM: Temperature dependencies*, IEEE, November 2008.

[24] F. Licciulli et al., *A Novel Technique for the Stabilization of SiPM Gain against Temperature Variations*, IEEE TNS-00232-2012.

[25] P. Dorosz et al., *Silicon photomultipliers gain stabilization by bias correction for compensation of the temperature fluctuations*, Nuclear Instruments and Methods in Physics Research A, 2013, 718;202-204.

[26] B. Dolgoshein, *Silicon Photomultipliers in Particle Physics:. Possibilities and Limitations*, Innovative Detectors for Supercolliders Conference Proceedings, 2004.

[27] P. Eckert, R. Stamen and H. C. Schultz-Coulon, *Study of the response and photon counting resolution of silicon photomultipliers using a generic simulation framework*, arXiv:1206.4154v1, Jun 2012.

[28] A Stoykov et al., *On the limited amplitude resolution of multipixel Geiger-mode APDs*, arXiv:0706.0746, June 2007.

[29] G. Collazuol, *Studies of silicon photomultipliers at cryogenic temperatures*, Nuclear Instruments and Methods in Physics Research A, 2011, 628;389-392.

[30] A. L. Lacaita et al., *On the bremsstrahlung origin of hot carrier induced photons in silicon devices*, IEEE Transactions on electron devices, 1993; 40.3:577-582.

[31] I. Rech et al., *Optical crosstalk in single photon avalanche diode arrays: a new complete model*, Optics Express, 2008.

[32] S. Vinogradov et al.*Analytical models of probability distribution and excess noise factor of solid state photomultiplier signals with crosstalk*, Nuclear Instruments and Methods in Physics Research A, 2012; 695:247- 251.

[33] V. Golovin, M. Tarasov, G. Bondacenko, Russian patent 2142175, 1998.

[34] D. McNally et al., *Review of Solid-state Photomultiplier Developments by CPTA and Photonique SA*, Elsevier, 2008.

[35] C. Piemonte et al., *Characterization of the First Prototypes of Silicon Photomultiplier Fabricated at ITC-irst*, IEEE Transactions on Nuclear Science, Vol. 54, N.1, 2007.

[36] Y. Du, F. Retiere, *After pulsing and cross-talk in multi-pixel photon counters*, Nuclear Instruments and Methods in Physics Research A, 2008, 596;396-401.

[37] S. Vinogradov et al., *Probability Distribution and Noise Factor of Solid State Photomultiplier Signals with Cross-Talk and Afterpulsing*, Nuclear Instruments and Methods in Physics Research A, 2012, 695, 247.

[38] S. Vinogradov et al., *Efficiency of Solid State Photomultipliers in Photon Number Resolution*, IEEE, 2009.

[39] L.M.P Fernandes, J.A.M Lopes, J.M.F Dos Santos *Excess noise factor in large area avalanche photodiodes for different temperatures*, Nuclear Instruments and Methods in Physics Research A, 2004; 531:566-568.

[40] Y. Musienko et al., *The gain, photon detection efficiency and excess noise factor of multi-pixel Geiger-mode avalanche photodiodes*, Nuclear Instruments and Methods in Physics Research A, 2006, 567;57-61.

[41] S. Gundacker et al., *Time of flight positron emission tomography towards 100ps resolution with L(Y)SO: an experimental and theoretical analysis*, 2013 JINST 8 P07014.

[42] S. Espana et al., *Performance evaluation of SiPM photodetectors for PET imaging in the presence of magnetic fields*, Nuclear Instruments and Methods in Physics Research Section A, 613(2):308-316, 2010.

[43] J. Anderson, for the CMS Hcal Collaboration, *Upgrade of the CMS hadron calorimeter for an upgraded LHC*, Journal of Physics: Conference Series 404, 2012, 012019.

[44] B.D. Leverington, *The LHCb Upgrade Scintillating Fibre Tracker*, Proceedings of Science, TIPP 2014,113.

[45] E. Garutti, R. Klanner, S. Laurien, *Silicon Photomultiplier characterization and radiation damage investigation for high energy particle physics applications*, IOP Science for Sissa MEDIALAB, 2013.

[46] portal.cta-observatory.org/Pages/Home.aspx

[47] A. Bouvier et al., *Photosensor Characterization for the Cherenkov Telescope Array: Silicon Photomultiplier versus Multi-Anode Photomultiplier Tube*, arXiv:1308.1390v1 [astro-ph.IM], Aug 2013.

[48] R. Rando et al., *Silicon Photomultiplier Research and Development Studies for the Large Size Telescope of the Cherenkov Telescope Array*, arXiv:1508.07120v1 [astro-ph.IM], Aug 2015.

[49] www.kromek.com

[50] www.mirion.com

[51] www.lns.infn.it

[52] www.weightron.com/weighbridge-peripheries/radiation-detection

[53] M. Caccia et al., *Silicon Photomultiplier readout of a scintillating noble gas detector for homeland security*, 10.1109/ANIMMA.2013.6727974, 2013.

[54] www.dfa.unict.it/it/content/muon-portal

[55] mu-ray.fisica.unina.it

[56] M. Caccia, R. Santoro, V. Arosio et al., *Development of a Silicon Photomultiplier toolkit for Science and Education*, Journal of Instrumentation, Volume 10, July 2015.

[57] www.caen.it

[58] R. D. Martin, D. J. Thomson , *Robust-resistant spectrum estimation*, Proceeding of the IEEE, 70;1097-1115, 1982.

[59] M. Ramilli et al., *Photon-number statistics with silicon photomultipliers*, Journal of the Optical Society of America B Optical Physics, 2010, 27, 852.

[60] I. Afek, A. Natan, O. Ambar, Y. Silberberg, *Quantum state measurements using multipixel photon detectors*, Phys. Rev. A, 2009, 79; 043830.

[61] L. Lyons, *Statistics For Nuclear And Particle Physicists*, Cambridge,Uk, Univ. Pr., 1986.

[62] P. R. Bevington, D. K. Robinson, *Data reduction and error analysis for the physical sciences*, 3rd ed., 2003.

[63] W. H. Press, *Numerical Recipes in C: The Art of Scientific Computing*, Cambridge University Press; 2nd ed., 1992.

[64] G. Cowan, *Statistical Data Analysis*, Clarendon Press, Oxford Science Publications, 1998.

[65] it.mathworks.com/help/econ/filtering.html

[66] S.W. Smith, *The Scientist and Engineer's Guide to Digital Signal Processing*, California Technical Publishing, San Diego, Second Edition, 1999.

[67] G. F. Knoll, *Radiation Detection and Measurement*, John Wiley and Sons, 2010.

[68] S.H. Byun, *Radioisotopes and Radiation Methodology*, Lecture Notes, Department of Medical Physics and Applied Radiation Sciences, McMaster University, Ontario, 2016.

[69] it.mathworks.com/help/signal/ref/zpk.html?searchHighlight=zpk

[70] romualdo talk

[71] J.T. Bushberget al., *The essential physics of medical imaging*, 2nd edition, Lippincott Williams & Wilkins, 2002, chapters 1 and 22.

[72] A. Luna et al., *Functional Imaging in Oncology*, vol. I-II, Springer, 2014.

[73] M.E. Juweid, B.D. Cheson, *Positron-emission tomography and assessment of cancer therapy*, N. Engl. J. Med. 2006, vol. 354,496-507.

[74] G.K. Von Schulthess, H.C. Steinert, T.F. Hany, *Integrated PET/CT: current applications and future directions*, Radiology, 2006, vol. 238, 405-422.

[75] T. Beyer, David W. Townsend, et al., *A Combined PET/CT Scanner for Clinical Oncology*, The Journal of Nuclear Medicine, 2000, vol. 41 no. 8, 1370-1379.

[76] G. B. Saha, *Basics of PET imaging, Physics, Chemistry and Regulations*, Springer 2005, chapters 2-5.

[77] H. Jadvar, J.A. Parker, *Clinical PET and PET-CT*, Springer, 2005, chapter 2.

[78] M. Schwaiger, H.J. Wester, *How Many PET Tracers Do We Need?*, J Nucl Med 2011; 52:36S-41S.

[79] S. Fanti, M. Farsad, L. Mansi, *Atlas of PET-CT, A Quick Guide to Image Interpretation*, Springer, 2009.

[80] A.F.L. Schinkel, D. Poldermans, A. Elhendy, J. J. Bax, *Assessment of Myocardial Viability in Patients with Heart Failure*, J Nucl Med July, 2007, vol. 48, no. 7, 1135-1146.

[81] www.norcalscans.org

[82] www.petsyselectronics.com

[83] H. Anger, *A new instrument for mapping gamma-ray emitters*, Biology and Medicine Quarterly Report UCRL, 1957, 3653: 38.

[84] H. Anger, *Scintillation camera with multichannel collimators*, Journal of nuclear medicine, 5: 515-31, 1964.

[85] S. R. Deans, *The Radon Transform and Some of Its Applications*, New York, 1983, John Wiley & Sons.

[86] F. Natterer, *The Mathematics of Computerized Tomography*, New York, 1986, John Wiley & Sons.

[87] H. Erdogan, *Statistical Image Reconstruction Algorithms Using Paraboloidal Surrogates for PET Transmission Scans*, PhD Thesys, University of Michigan, 1999.

[88] www.humanhealth.iaea.org

[89] A.J. Reader, H. Zaidi, *Advances in PET Image Reconstruction*, Elsevier, PET Clin 2, 2007, 173-190.

[90] G. Tarantola et al., *PET instrumentation and reconstruction algorithms in whole-body application*, The Journal of Nuclear Medicine, 2003; 44:756-769.

[91] W.W. Moses, *Fundamental limits of spatial resolution in PET*, Nuclear Instruments and Methods in Physics Research A, 2011; 648:s236-s240.

[92] J.S. Lee, *Technical advances in current PET and hybrid imaging systems*, The Open Nuclear Medicine Journal, 2010; 2:192-208.

[93] M. Schmand, L. Eriksson, M.E. Casey et al., *Performance results of a new DOI detector block for a High Resolution PET-LSO Research Tomograph HRRT*, IEEE Trans Nucl Sci 1998; 45(6): 3000-6.

[94] J. Seidel et al., *Depth identification accuracy of a three layer phoswich PET detector module*, IEEE Trans Nucl Sci 1999; 46(3): 485-90.

[95] Y.F. Yang, Y.B. Wu, J.Y. Qi et al., *A prototype PET scanner with DOI-encoding detectors*, J Nucl Med 2008; 49(7): 1132-40.

[96] Y.H. Chung et al., *New design of a quasimonolithic detector module with DOI capability for small animal pet*, Nucl Instrum Meth A 2008; 593(3): 588-91.

[97] S. Surti et al., *Optimizing the performance of a PET detector using discrete GSO crystals on a continuous lightguide*, IEEE Trans Nucl Sci. 2000;47:1030-1036.

[98] L.E. Adamet al., *Performance of a whole-body PET scanner using curve-plate NaI(Tl) detectors*, J Nucl Med. 2001;42:1821-1830.

[99] D.L. Bailey et al., *ECAT ART: a continuously rotating PET camera-performance characteristics, initial clinical studies and installation considerations in a nuclear medicine department*, Eur J Nucl Med. 1997;24:6-15.

[100] D. Brasse et al., *Correction methods for random coincidences in 3D whole body PET imaging*, IEEE Nucl Sci Symp Med Imaging Conf Rec. 2001;4:2080-2084.

[101] V. Bettinardi et al., *An automatic classification technique for attenuation correction in positron emission tomography*, Eur J Nucl Med. 1999;26:447-458

[102] F.H. van Velden, R.W. Kloet, B.N. van Berckel et al., *HRRT versus HR+ human brain PET studies: an interscanner test-retest study*, J Nucl Med 2009; 50(5): 693-702.

[103] R.R. Raylman, S. Majewski, M.F. Smith et al., *The positron emission mammography/tomography breast imaging and biopsy system (PEM/PET): design, construction and phantom-based measurements*, Phys Med Biol 2008; 53(3): 637-53.

[104] S. Surti, J.S. Karp, *Design considerations for a limited angle, dedicated breast, TOF PET scanner*, Phys Med Biol 2008; 53(11):2911-21.

[105] S.L. Bowen, Y. Yang, Y. Wu et al., *Monte Carlo simulation study of several camera designs for the PET component of a dedicated breast PET/CT scanner*, 2006 IEEE Nuclear Science Symposium Conference Record 2006; 6: 3920-4.

[106] Y. Zhang et al., *Performance characteristics of a high resolution oncologic transformable PET in brain/breast and whole-body modes*, 2007 IEEE Nuclear Science Symposium Conference Record 2007; 5: 3684-7.

[107] A. Alessio, P. Kinahan, *PET Image Reconstruction*, appeared in Henkin et al. Nuclear Medecine 2nd edition, 2006.

[108] A. C. Kak, M. Slaney, *Principles of Computerized Tomographic Imaging*, New York, IEEE Press, 1988.

[109] R. Leahy, J. Qi, *Statistical Approaches in Quantitative PET*, Statistics and Computing, vol. 10, 2000.

[110] L.A. Shepp, Y. Vardi, *Maximum Likelihood Reconstruction for Emission Tomography*, IEEE transaction on medical imaging, vol. MI-1, no. 2, 1982.

[111] H. M. Hudson, R. S. Larkin, *Accelerated image reconstruction using ordered subsets of projection data*, IEEE Trans Med Imaging, vol. 13, pp. 601-609, 1994.

[112] P. E. Kinahan, J. G. Rogers, *Analytic 3D image reconstruction using all detected events*, IEEE Trans Nuclear Science, vol. 36, pp. 964-968, 1989.

[113] M. E. Daube-Witherspoon, G. Muehllehner, *Treatment of axial data in 3D PET*, J Nucl. Med., vol. 28, pp. 1717-1724, 1987.

[114] M. Defrise et al., *Exact and Approximate Rebinning Algorithms for 3D PET Data*, IEEE Trans Med Imaging, vol. 16, pp. 145-158, 1997.

[115] M. Conti, *State of the art and challenges of time-of-flight PET*, Physica Medica, 2008; 25: 1-11.

[116] S. Vandenberghe, *Recent developments in time-of-flight PET*, EJNMMI Physics20163:3.

[117] J.S. Karpet al., *Benefit of time-of-flight in PET: experimental and clinical results*, J Nucl Med 2008; 49(3):462-70.

[118] A. Boss, *Hybrid PET/MRI of Intracranial Masses: Initial Experiences and Comparison to PET/CT*, J Nucl Med August 1, 2010 vol. 51 no. 8 1198-1205.

[119] A. Almuhaideb, N. Papathanasiou, J. Bomanji, *18F-FDG PET/CT Imaging In Oncology*, Ann Saudi Med. 2011 Jan-Feb; 31(1): 3-13.

[120] D.W. Townsend, T. Beyer, P.E. Kinahan et al., *The SMART scanner: a combined PET/CT tomograph for clinical oncology*, IEEE Nucl Sci Symp Med Imaging Conf Rec. 1998;2:1170-1174.

[121] G.W. Goerres et al., *PET-CT image co-registration in the thorax: influence of respiration*, Eur J Nucl Med. 2002;29:351-360.

[122] B. Pichler, H.F. Wehrl, A. Kolb, M.S. Judenhofer, *PET/MRI: the next generation of multi-modality imagingS?*, Semin Nucl Med. 2008 May; 38(3): 199-208.

[123] C. Catana et al., *PET/MRI for Neurologic Applications*, J Nucl Med December 1, 2012 vol. 53 no. 12 1916-1925.

[124] A. Daftary, *PET-MRI: Challenges and new directions*, Indian J Nucl Med. 2010 Jan-Mar; 25(1): 3-5.

[125] S.J. Hong, I.C. Song, M. Ito et al., *An investigation into the use of Geiger-mode solid-state photomultipliers for simultaneous PET and MRI acquisition*, IEEE Trans Nucl Sci 2008; 55(3): 882-8.

[126] J.S. Lee, S.J. Hong, *Geiger-mode avalanche photodiodes for PET/MRI*, Iniewski K, Eds. Electronic Circuits for Radiation Detection. CRC Press LLC; 2010:179-200.

[127] A.M. Grant et al., *NEMA NU 2-2012 performance studies for the SiPM-based ToF-PET component of the GE SIGNA PET/MR system*, Med. Phys. 43, 2334, 2016.

[128] S.R. Cherry, S.S. Gambhir, *Use of positron emission tomography in animal research*, ILAR J., 2001, 42:219-32.

[129] R. Yao, R. Lecomte, E. S. Crawford, *Small-Animal PET: what is it, and why do we need it?*, Journal of Nuclear Medicine Technology, 2012; 40: 157-165.

[130] C. Kuntner, D. Stout, *Quantitative preclinical PET imaging: opportunities and challenges*, Frontiers in physics, 2014.

[131] M. Larobina, A. Brunetti, M. Salvatore, *Small Animal PET: a review of commercially available imaging system*, Current Medical Imaging Reviews, 2006; 2: 187-192.

[132] G.D. Hutchins, M.A. Miller, V.C. Soon, T. Receveur, *Small Animal PET Imaging*, ILAR Journal, 2008, 49 (1): 54-65.

[133] R. Prasad, H. Zaidi, *Scatter characterization and correction for simultaneous multiple small-animal PET imaging*, Mol Imaging Biol., 2013, doi:10.1007/s11307-013-0683-2.

[134] M. Bergeron, J. Cadorette, C. Bureau-Oxton, *Performance evaluation of the LabPET12, a large axial FOV APD-based digital PET scanner*, IEEE Nuclear Science Symposium, 2009; 4017-4021.

[135] F. Sanchez et al., *ALBIRA: a small animal PET/SPECT/CT imaging system*, Medical Physics 40(5):051906, May 2013.

[136] P. S. Roldan,*Raytest ClearPET^{TM}, a new generation small animal PET scanner*, Nuclear Instruments and Methods in Physics Research A, Volume 571, Issues 1-2, 1 February 2007, Pages 498-501.

[137] www.perkinelmer.com

[138] NEMA Standards Publications, *NEMA NU 4-2008 Performance Measurements of Small Animal Positron Emission Tomographs (PETs)*, 2008.

[139] A.L. Goertzen et al., *NEMA NU 4-2008 Comparison of preclinical PET imaging systems*,The Journal of Nuclear Medicine, 2012; 53:1300-1309.

[140] A.K. Alstrup, D.F. Smith, *Anaesthesia for positron emission tomography scanning of animal brains*, Lab Anim., 2013, 47:12-8

[141] C. Suckow, C. Kuntner, P. Chow, R. Silverman, A. Chatziioannou, D. Stout, *Multi-modality rodent imaging chambers for use under barrier conditions with gas anesthesia*, Mol Imaging Biol., 2009, 11:100-6.

[142] J.M. David, S. Knowles, D.M. Lamkin, D.B. Stout, *Individually ventilated cages impose cold stress on laboratory mice:a source of systemic experimental variability*, J Am Assoc Lab Anim Sci., 2013, 52:738-44.

[143] M.C Kreissl et al., *Influence of dietary state and insulin on myocardial, skeletal muscle and brain F-fluorodeoxyglucose kinetics in mice*, EJNMMI Res., 2011, 1:8.

[144] S.K. Pandey, M. Saijad, Y. Chen et al., *Comparative positron-emission tomography (PET) imaging and phototherapeutic potential of 124I-labeled methyl-3-(19-iodobenzyloxyethyl) pyropheophorbide-a vs the corresponding glucose and galactose conjugates*, J Med Chem., 2009; 52:445-455.

[145] R. Lecomte, E. Croteau, M.E. Gauthier et al., *Cardiac PET imaging of blood flow, metabolism, and function in normal and infarcted rats*, IEEE Trans Nucl Sci., 2004;51:696-704.

[146] S.J. Liow et al., *Effect of a P-glycoprotein inhibitor, cyclosporin-A, on the disposition in rodent brain and blood of the 5-HT1A receptor radioligand, [C-11](R)-(2)-RWAY*, Synapse, 2007;61:96-105.

[147] D. Schulz, P. Vaska, *Integrating PET with behavioral neuroscience using RatCAP tomography*, Rev. Neurosci., Vol. 22(6), 2011.

[148] A. Kyme, S. Se, S. Meikle, W. Ryder, K. Popovic, R. Fulton, *Markerless motion tracking enabling motion-compensated PET in awake rats*, Nuclear Science Symposium and Medical Imaging Conference (NSS/MIC) ,2012, p. 3825-8.

[149] K. Nagy et al., *Performance evaluation of the small-animal nanoScan PET/MRI system*, J Nucl Med. 2013 Oct;54(10):1825-32.

[150] G.B. Ko et al., *Simultaneous Multiparametric PET/MRI with Silicon Photomultiplier PET and Ultra-High-Field MRI for Small-Animal Imaging*, J Nucl Med. 2016 Aug;57(8):1309-15.

[151] A.L. Geortzen et al., *First Results From a High-Resolution Small Animal SiPM PET Insert for PET/MR Imaging at 7T*, IEEE Transactions on Nuclear Science, Volume: 63, Issue: 5, Oct. 2016.

[152] M. Hoehn, U. Himmelreich, K. Kruttwig, D. Wiedermann, *Molecular and cellular MR imaging: potentials and challenges for neurological applications*, J Magn Reson Imaging. 2008;27:941-954.

[153] M.S. Judenhofer et al., *Simultaneous PET-MRI: a new approach for functional and morphological imaging*, Nat Med. 2008 Apr;14(4):459-65.

[154] www.kinheng-crystal.com

[155] www.astrosyn.com

[156] www.arduino.cc

[157] www.adafruit.com/product/1438

[158] www.spectrumtechniques.com/radioisotopes.htm

[159] B. Hasegawa, *Physics of Medical X-Ray Imaging*, Chapter 6, Medical Physics Pub Corp; 2 edition, 1987.

[160] C. G. Ryan, E. Clayton, W. L. Griffin, S. H. Sie, D. R. Cousens, *SNIP, a statistics-sensitive background treatment for the quantitative analysis of PIXE spectra in geoscience applications*, Nuclear Instruments and Methods in Physics Research Section B, 1998, Volume 34, Issue 3, p. 396-402.

[161] M. Morhac, J. Kliman, V. Matousek, M. Veselsky, I. Turzo, *Background elimination methods for multidimensional coincidence X-ray spectra*, Nuclear Inst. and Methods in Physics Research A, 1997, Volume 401, Issue 1, p. 113-132.

[162] M. Caccia, A. Ebolese, M. Maspero, R. Santoro, *Background removal procedure based on the SNIP algorithm for γ-ray spectroscopy with the CAEN Educational Kit*.

[163] A.N. Otte, J. Barral, B. Dolgoshein, *A test of silicon photomultipliers as readout for PET*, Nuclear Instruments and Methods in Physics Research A, 2005; 545:705-715.

[164] www.caen.it/csite/CaenProd.jsp?parent=61&idmod=1025

[165] www.analog.com/media/en/training-seminars/tutorials/MT-047.pdf

[166] www.ti.com/lit/ds/symlink/opa656.pdf

[167] www.caen.it/csite/CaenProd.jsp?parent=14&idmod=935

[168] V. Radeka, *Trapezoidal filtering of signals from large germanium detectors at high rates*, Nuclear Instruments and Methods, Volume 99, Issue 3, 15 March 1972.

[169] V. T. JordanoV, G. F. Knoll, A. C. Huber and J. A. Pantazis, *Digital techniques for real-time pulse shaping in radiation measurements*, Nuclear Instruments and Methods in Physics Research A, 353, 1994.

[170] www.ti.com/lit/ds/symlink/sn74alvc164245.pdf

[171] www.ti.com/lit/ds/symlink/sn74lv1t34.pdf